Observation, Evidence and Origin of Magnetodielectric Effect in Mn/Fe Doped $LaGaO_3$

A THESIS

Submitted in partial fulfillment of the requirements for the award of the degree of

DOCTOR OF PHILOSOPHY

By

Hari Mohan Rai

DISCIPLINE OF PHYSICS
INDIAN INSTITUTE OF TECHNOLOGY INDORE
June 2017

INDIAN INSTITUTE OF TECHNOLOGY INDORE

CANDIDATE'S DECLARATION

I hereby certify that the work which is being presented in the thesis entitled "**OBSERVATION, EVIDENCE AND ORIGIN OF MAGNETODIELECTRIC EFFECT IN Mn/Fe DOPED $LaGaO_3$"** in the partial fulfillment of the requirements for the award of the degree of **DOCTOR OF PHILOSOPHY** and submitted in the **DISCIPLINE OF PHYSICS, INDIAN INSTITUTE OF TECHNOLOGY INDORE**, is an authentic record of my own work carried out during the time period from July 2012 to June 2017 under the supervision of Dr. Pankaj R. Sagdeo, Associate Professor, Discipline of Physics, and Dr. Rajesh Kumar, Associate Professor, Discipline of Physics, IIT Indore.

The matter presented in this thesis has not been submitted by me for the award of any other degree of this or any other institute.

Signature of the student with date
Hari Mohan Rai

This is to certify that the above statement made by the candidate is correct to the best of our knowledge.

Signature of Thesis Supervisor #1 with date — Signature of Thesis Supervisor #2 with date

Dr. Pankaj R. Sagdeo — **Dr. Rajesh Kumar**

Hari Mohan Rai has successfully given his Ph.D. Oral Examination held on……..

Signatures of Thesis Supervisors
Date:

Signature of External Examiner
Date:

Convener, DPGC
Date:

Signature of PSPC Member #1
Date:

Signature of PSPC Member #2
Date:

Signature of chairman (OEB)
Date:

Dedicated to My Parents

Acknowledgement

This thesis is an end of my journey in procuring PhD degree. This journey was not possible without motivation, encouragement and constant support of some people. Here, I would like to pay special thankfulness, warmth and sincere appreciation to those who have made this thesis successful and supported me in one way or the other during this period of time.

At this moment of accomplishment, I am greatly indebted to my research mentors, Dr. Pankaj R. Sagdeo and Dr. Rajesh Kumar, whose stimulating motivation and valuable ideas kept me on track during this journey. I am thankful to both of them for their kind help, encouragement and constant support at professional and also at personal level. Their valuable advices, constructive criticism and extensive discussion helped me in accomplishing my PhD.

I would like to express my gratitude to Prof. Pradeep Mathur. He always goes out of the way to help students of IIT Indore. His energy and enthusiasm towards research always motivated me.

I would like to express my sincere gratitude to my parents, my sisters, brother in-laws, their kids and my wife for all the sacrifices they made on my behalf. My mother and father was always been a source of encouragement and inspiration to me throughout my life. My sisters and brother in-laws were always with me during my hard times. This thesis was not possible without their support and help.

I am highly grateful to Shri Rama Sankar Singh (Chairman), Mrs. Kanupria Singh Rathore, (Chairperson), Mrs. Ruchi Singh Chauhan (Vice-Chairperson) Shri Ravindra Pratap Singh Rathore, (Director) and Shri Daulat Singh Chauhan (Executive Director), ITM Universe, Gwalior, for their kind support.

I want to give special thanks to Archana Madam and Khusboo Madam for homely comfort and care during my PhD.

I would like to express my gratitude towards Prof. P. N. Puntambekar, Dr. N.P Lalla and Prof. Gustau Catalan for scientific discussion/communication and kind guidance.

I sincerely pay my gratitude to Dr. Biswarup Pathak and Dr. Sudeshna Chattopadhyay for their support, encouragement valuable suggestions and words of appreciation.

I gratefully acknowledge Dr. Panakj Srivastava (ABV-IIITM Gwalior), Dr. Neeraj K. Jaiswal (PDPM-IIITDM Jabalpur), Mr. Uday Pratap Gahlaut (ITM Gwalior) and Mr. Hariom Pandey (ITM Gwalior) for motivating me to join PhD program.

I would like to thank my friends Dr. Rituraj Sharma and Mr. Pawan Patidar for their help and support. I extend my thank to Dr. Mahesh Bhatt (IIT Delhi), Dr. Fozia Aziz and Dr. Sunil Kumar for scientific discussions and valuable suggestions.

Raja Ramanna Centre for Advanced Technology (RRCAT) Indore and Sophisticated Instrumentation Center (SIC) , IIT Indore are acknowledged for experimental facility.

I thank all our collaborator for providing experimental or simulation facility at their Lab. Our collaborators are – Dr. Biswarup Pathak and Dr. Vipul Singh (IIT Indore); Dr. A. K. Sinha, Dr. S.N. Jha, Dr. S.M. Gupta, Dr. Archana Sagdeo, Mr. Anuj Upadhyay, Mr. Manvendra Singh and Mr. Adityanaryan Pandey (RRCAT); Dr. Parasmani Rajput, Mr. Ashok K. Yadav and Ms. Chandrani Nayak (BARC); Dr. K.V. Adarsh and Dr. Rituraj Sharma (IISER Bhopal); Dr. A.K. Shukla and Dr. Sujeet Choudhary (IIT Delhi); Dr. Kaustav Mukherjee (IIT Mandi); Dr. Panakj Srivastava (ABV-IIITM Gwalior); Dr. Neeraj K. Jaiswal (PDPM-IIITDM Jabalpur); Dr. A.K. Nigam, Dr. Rajib Mondal and Dr A. Thamizhave (TIFR, Mumbai); Dr. A. Banerjee, Dr. V. R. Reddy, Dr. Vasant Sathe and Dr. U.P. Deshpande (UGC-DAE-CSR, Indore).

I take this opportunity to sincerely acknowledge Dr. Krushna R. Mavani and Dr. Preeti A. Bhobe, for providing experimental facilities whenever we needed. I would like to thank Ms. Indrani Cohoudhuri for DFT calculations whereas Dr Aga Shahee and Ms. Sonam Mandani for helping in iodometric titration.

I want to thank whole Physics department of IIT Indore which was like a family during my PhD. I never felt alone due to pleasant atmosphere at Physics department.

Writing PhD thesis without the help of colleagues is not possible. I sincerely thank my friends Dr. Gayatri Sahu, Dr. Shailendra Kumar Saxena, Vikas Mishra, Ravikiran Late, Dr. Swarup Roy, Kamal Warsi, Preetam Singh, Anil Kumar, Sandep Jain, Pooja, Priyanka Yogi, Suryakant Mishra, Deepika, Rupnayan, Balal and Haardik for providing friendly and pleasant environment in the Lab. In particular, I want to thank, Dr. Shailendra Kumar Saxena with whom I started my work and I admire his helping nature.

I cannot forget to thanks some of my best buddies who were always there in my bad and good times during this period; Priyadarshani, Surbhi, Tulika, Shanu, Pritpal, Pooja pareek, Smriti, Ankita, Dr. Adityanath Miashra, Dr. Ajay Kumar, Ajay Pratap, Krishna Dayal Shukla, Ankit Agrawal, Najimuddin, Ravi Kancharla, Sudeep Ghosh, Ashish Yadav, Tejendra Dixit, Shivendra Pandey, Yogesh Singh, Dr. Kshitij, Dr Prakhar Garg, Surjendu, kavita and Ankit Soni.

I sincerely thank Dr. Abhishek Srivastava, Dr. Ashisha Kumar, Dr. Akhil Jha, and Dr. Raghunath Sahoo for kind guidance, encouragement and words of appreciation.

I would like to thank Mr. Ujwal Kulkarni Mr. Kinny Pandey, Mr. Nitin Uppadhaya, Sarita Batra madam and Mr. Ghanshyam for their support.

I want to express my gratitude towards Dr. Shilpa Raut, Dr. P. Matkar and other medical staff members of IIT dispensary who kept me physically fit.

Last but not least, I want to thank all staff member of IIT Indore for providing all comfort and convenience. Beside this, several people have knowingly and unknowingly helped me in successful completion of my thesis.

I also acknowledge MHRD for providing me financial assistance.

Hari Mohan Rai

LIST OF PUBLICATIONS

(A) Peer reviewed journals (thesis)

[1] **H.M. Rai**, R. Late, S.K. Saxena, V. Mishra, A. Sagdeo, R. Kumar, P.R. Sagdeo, Room temperature magnetodielectric studies on Mn-doped $LaGaO_3$**,** Mater. Res. Express 2 (2015) 096105-096112.

[2] **H.M. Rai**, S.K. Saxena, R. Late, V. Mishra, P. Rajput, A. Sagdeo, R. Kumar, P.R. Sagdeo, Observation of large dielectric permittivity and dielectric relaxation phenomenon in Mn-doped lanthanum gallate, RSC Adv. 6 (2016) 26621–26629.

[3] **H.M. Rai**, S.K. Saxena, V. Mishra, A. Sagdeo, P. Rajput, R. Kumar, P.R. Sagdeo, Observation of room temperature magnetodielectric effect in Mn-doped lanthanum gallate and study of its magnetic properties, J. Mater. Chem. C 4 (2016) 10876–10886.

[4] **H.M. Rai**, P. Singh, S.K. Saxena, V. Mishra, M.K. Warshi, R. Kumar, P. Rajput, A. Sagdeo, I. Choudhuri, B. Pathak, P.R. Sagdeo, Room-Temperature Magneto-dielectric Effect in $LaGa_{0.7}Fe_{0.3}O_{3+\gamma}$; Origin and Impact of Excess Oxygen, Inorg. Chem. 56 (2017) 3809–3819.

[5] **H.M. Rai,** S.K. Saxena, V. Mishra, R. Kumar, P.R. Sagdeo, Importance of Frequency Dependent Magnetoresistance Measurements in Analyzing the Intrinsicality of Magnetodielectric Effect: A Case Study, J. Appl. Phys. 122 (2017) 054103.

[6] **H.M. Rai**, S.K. Saxena, V. Mishra, M. Kamal Warshi, R. Kumar, P.R. Sagdeo, Effect of Mn Doping on Dielectric Response and Optical Band Gap of $LaGaO_3$ Advances in Materials and Processing Technologis (AMPT) 3 (2017) 1-11

[7] **H.M. Rai**, S.K. Saxena, V. Mishra, R. Kumar, P.R. Sagdeo, Magneto-expansion/compression Mediated Room Temperature Magnetodielectric Effect in $LaGa_{1-x}Mn_xO_{3+\gamma}$, Adv. Mater. **(communicated).**

(B) Peer reviewed journals (other than thesis)

[8] **H.M. Rai**, S.K. Saxena, V. Mishra, R. Late, R. Kumar, P.R. Sagdeo, N.K. Jaiswal, P. Srivastava, Possibility of spin-polarized transport in edge fluorinated armchair boron nitride nanoribbons, RSC Adv. 6 (2016) 11014–11022.

[9] **H.M. Rai**, S.K. Saxena, V. Mishra, R. Late, R. Kumar, P.R. Sagdeo, N.K. Jaiswal, P. Srivastava, Half-metallicity in armchair boron nitride nanoribbons: A first-principles study, Solid State Commun. 212 (2015) 19–24.

(C) Peer reviewed journals (other than thesis: as a contributory author)

[1] R. Late**, H.M. Rai**, S.K. Saxena, R. Kumar, A. Sagdeo, P.R. Sagdeo, Effect of Hf doping on the structural, dielectric and optical properties of $CaCu_3Ti_4O_{12}$ ceramic, J. Mater. Sci. Mater. Electron. 27 (2016) 5878.

[2] R. Late, **H.M. Rai**, S.K. Saxena, R. Kumar, A. Sagdeo, P.R. Sagdeo, Probing structural distortions in rare earth chromites using Indian synchrotron radiation source, Indian J Phys. 90 (2016) 1347-1354.

[3] P. Singh, I. Choudhuri, **H.M. Rai**, V. Mishra, R. Kumar, B. Pathak, A. Sagdeo, P.R. Sagdeo, Fe doped $LaGaO_3$: good white light emitters, RSC Adv. 6 (2016) 100230-100238.

[4] S.K. Saxena, R. Borah, V. Kumar, **H.M. Rai**, R. Late, V. g. Sathe, A. Kumar, P.R. Sagdeo, R. Kumar, Raman spectroscopy for study of interplay between phonon confinement and Fano effect in silicon nanowires, J. Raman Spectrosc. 47 (2016) 283–288.

[5] S.K. Saxena, P. Yogi, P. Yadav, S. Mishra, H. Pandey, **H.M. Rai**, V. Kumar, P.R. Sagdeo, R. Kumar, Role of Metal Nanoparticles on porosification of silicon by metal induced etching (MIE), Superlattices Microstruct. 94 (2016) 101-107.

[6] S.K. Saxena P. Yogi, , S. Mishra, **H.M. Rai**, R. Late, V. Kumar, B. Joshi, P.R. Sagdeo, R. Kumar, Interplay between phonon confinement and Fano effect on Raman line shape for semiconductor nanostructures: Analytical study, Solid State Commun. 230 (2016) 25–29.

[7] R. Kumar, G. Sahu, S.K. Saxena, **H.M. Rai**, P.R. Sagdeo, Qualitative Evolution of Asymmetric Raman Line-Shape for Nanostructures, Silicon 6 (2014) 117–121.

[8] V. Mishra, A. Sagdeo, V. Kumar, M. Kamal Warshi, **H.M. Rai**, S.K. Saxena, D.R. Roy,V. Mishrs, R. Kumar, A. Sagdeo, P.R. Sagdeo, Electronic and optical properties of BaTiO3 across tetragonal to cubic phase transition: An experimental and theoretical investigation, J. Appl. Phys. 122 (2017) 065105.

Contents

List of Figures

Figure C-2: Schematic situation-I; octahedral arrangement of Oxygen ions around a cation (say La). One of the two electrons of each oxygen ion is bonded with the shown central cation and remaining one is connected to other cation site. Situation -II; shows that due to the removal of La ion (considered La-defect) the up spin Oxygen electron becomes unbound (or the corresponding Oxygen bond remains unsaturated/dangling).

List of Tables

Abbreviations

Room temperature	RT
Magnetodielectric	MD
Magnetoelectric	ME
Magnetocapacitance	MC
Magnetoloss	ML
Dielectric constant	ε′
Loss tangent	tanδ
Magnetoresistance	MR
Frequency dependent magnetoresistance	FDMR
Magnetoresistance impedance spectroscopy	MRIS
Jahn-teller	JT
Asymmetric stretching	AS
Symmetric stretching	SS
Jahn-Teller asymmetric stretching	JTAS
X-Ray diffraction	XRD
X-Ray absorption near edge structure	XANES
Extended X-ray absorption fine structure	EXAFS
Vibrating sample magnetometer	VSM
Superconducting quantum interference device	SQID
Charge coupled device	CCD
Transition metal	TM
Ferromagnetic	FM
Paramagnetic	PM
Anti ferromagnetic	AFM
Ferroelectric	FE
Field cooled	FC
Zero field cooled	ZFC
Polarization - electric field	P-E
Magnetization - magnetic field	M-H

Density functional theory	DFT
Density of states	DOS
Vienna abinitio simulation package	VASP
Local spin density approximation	LSDA
$LaGaO_3$	LGO
$LaGa_{1-x}M_xO_3$	LGMO
$LaGa_{1-x}Fe_xO_3$	LGFO
$LaGa_{0.8}Mn_{0.2}O_{3+\gamma}$	LGM2O
$LaGa_{0.4}Mn_{0.6}O_{3+\gamma}$	LGM6O
$LaGa_{0.7}Fe_{0.3}O_{3+\gamma}$	LGF3O

Chapter 1

Introduction

1.1 Preamble: magnetodielectric (MD)/magnetoelectric (ME) materials and/or multiferroics

Magnetodielectric (MD)/magnetoelectric (ME) materials and/or multiferroics are of very high research interest due to their potential possible applications and interesting physics. Multiferroics are the materials which exhibit coexistence of at least two primary ferroic orders[$] (amongst ferroelectric, ferromagnetic and ferroelastic orderings) in a single phase compound [1–19]. However, single-phase multiferroic materials are rarely exist [1,11] and multiferroicity has been reported also in composites or two-phase materials [1,16,20–23]. Similar to the work which reveals that magnetic order can create superconductivity [1,24], it has also been reported that magnetic ordering may also induce ferroelectricity [1,13] and vice versa. Multiferroics can be expanded also to include non-ferroic magnetic orderings such as ferrimagnetism and antiferromagnetism. Further, multiferroics are divided into two groups [8]. The first group, which can be categorized as type-I multiferroics, covers those materials in which magnetism and ferroelectricity has different origin and appears independently of one another, though there may be a little (weak) coupling between them. Type-I multiferroics usually exhibit relatively a large spontaneous polarization P (of the order of $10 - 100\ \mu C/cm^2$)

[$] Appendix A-II

and in these materials, ferroelectricity appears generally at higher temperatures than that of the magnetic ordering. Examples include $YMnO_3$ (P ~ 6μC/cm^2, T_N = 76 K, T_{FE} ~ 914 K) and $BiFeO_3$ (P ~ 90μC/cm^2, T_N = 643 K, T_{FE} ~ 1100 K) [8]. The second category, which can be named as type-II multiferroics, comprises the materials [8,13,25], which exhibit strong coupling between ferroelectric and magnetic orders (e.g.; transition temperatures corresponding to ferroelectric (T_{FE}) and magnetic (T_M) orderings are same), as in these materials, ferroelectricity is induced due to magnetic ordering itself [8,13,25]. However, the polarization in these materials is usually much

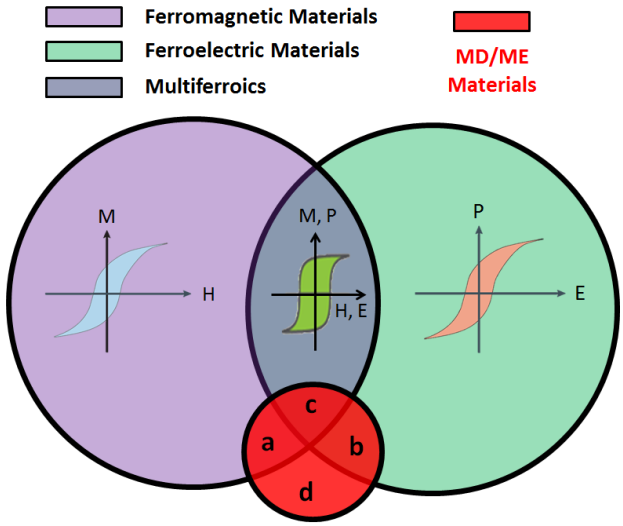

Figure-1.1: A rough comparison of number of existing/reported ferromagnets, ferroelectrics, multiferroics, MD/ME materials along with an interconnection between them. The left side circle (light violet) represents ferromagnets, right side circle (light green) includes ferroelectrics and the intersection part (gray shaded) comprises the materials that are multiferroic. The materials, exhibit MD/ME coupling belongs to small red circle; a) MD/ME materials with only magnetic ordering, b) MD/ME materials with only ferroelectric ordering, c) MD/ME multiferroics and d) completely independent MD materials [1]. Note-the shape, size and colors of depicted hysteresis loops are chosen randomly and do not signify anything other than hysteresis.

smaller (~10^{-2}μC/cm^2) [8]. Ultimately, materials belonging to type-I and type-II categories can be recognized on the basis of the values of transition temperature of ferroic orderings [8]. In type-I multiferroics, the transition temperature of ferroelectric ordering (T_{FE}) is generally

higher as compared to that of the magnetic ordering (T_M) whereas T_{FE} and T_M are same in case of type-II multiferroics [8].

Distinctly, the controlling of magnetization (electric polarization) through external electric (magnetic) field i.e. coupling between ferroelectric and magnetic ordering or in other words coupling of external magnetic (electric) field with electric dipoles (magnetization) is known as ME/MD effect. Materials showing such an effect are formally called as magnetoelectrics/magnetodielectrics. Moreover, MD/ME effect is an independent phenomenon though, it may coexist along with multiferroicity in specific compounds [1,26] as shown in the Venn diagram depicted in Figure 1.1. It is clear from this logic diagram and its caption that the materials which display either only magnetic or electric (polarization) ordering, or even neither of them, can also exhibit MD/ME phenomenon [1,27–29].

1.2 Compatibility of polarization and magnetization in a single phase compound

From the point of view of symmetry consideration it is difficult for a single phase compound to offer coexistence (or/and coupling) of spontaneous polarization and magnetization because ferroelectricity (polarization) needs broken spatial inversion symmetry while the time reverse symmetry can be invariant, on the contrary broken time-reversal symmetry is the prerequisite for magnetization (spin ordering) while invariant spatial-inverse symmetry applies for most conventional magnetic materials in use (but this is not a prerequisite) [1,4,11,30]. Likewise, technologically important ferroelectrics such as $BaTiO_3$ and $(Pb,Zr)TiO_3$ are transition metal (TM) oxides with perovskite /perovskite-like structure (ABO_3). ABO_3 usually constitutes a small B-site cation at the center of an octahedral cage of oxygen ions and a relatively large A-site cation at the unit cell corners [31,32]. In parallel, several magnetic oxides are reported with a perovskite or a perovskite-like structure. It is worth mentioning that attempts to search (or to

synthesize) multiferroics have mainly concentrated on this class of compounds. It is known that all conventional ferroelectric perovskite oxides contain TM ions with a formal configuration d^0, such as Ti^{4+}, Ta^{5+}, W^{6+}, at B-sites (i.e. the TM ions with an empty *d*-shell). The empty *d*-shell appears to be a prerequisite for generating ferroelectricity, although this does not imply that all perovskite oxides with empty *d*-shell TM are ferroelectric [5]. Magnetization, in contrast, requires TM ions at the B-site with partially filled shells (always *d*- or *f*-shells), such as Cr^{3+}, Mn^{3+}, Fe^{3+}, because the spins of electrons occupying the filled shell completely gives zero magnetic moment as they do not participate in magnetic ordering. The different prerequisites in filling the d-shells of TM ion at the B-site considering polarization and magnetism, makes these two ordered states mutually exclusive. As far as magnetic and crystallographic symmetry is concern, amongst all 233 Shubnikov magnetic point groups, only 13 point groups (i.e. 1, 2, 2′, *m*, *m*′, 3, 3*m*′, 4, 4*m*′*m*′, *m*′*m*2′, *m*′*m*′2′, 6 and 6*m*′*m*′) allow the simultaneous appearance of spontaneous polarization and magnetization [5,11]. This constrain in the crystallographic symmetry is responsible for the fact that the coexistence of polarization and magnetization is rare in nature [1,5,11,30]. It is noticeable that, in practice, some compounds belonging to these 13 point groups do not show any simultaneous appearance of polarization and magnetization. Ultimately, in spite of there being hundreds of ferroelectric oxides and magnetic oxides, there is practically very rare overlap between them [1,5,11,30]. Therefore, an approach other than only symmetry consideration may be helpful to achieve and understand such an overlap in single phase compounds. As stated above, ferroelectric perovskite oxides need B-site TM ions with an empty *d*-shell to form ligand hybridization with the surrounding anions. This type of electronic structure likely excludes magnetism. However, not all experimental and theoretical results support the argument that ferroelectricity and magnetism are absolutely incompatible, and an integration of them seems to be possible. First, the well-known

Maxwell equations which govern the dynamics of magnetic field, electric field and electric charges, express that rather than being two independent phenomena, electric and magnetic fields are intrinsically and tightly coupled to each other. A varying magnetic field generates an electric field, whereas motion of charge i.e. electric current, produces a magnetic field. Second, the formal equivalence of the equations governing the electrostatics and magnetostatics in polarizable media; describes the similarities in the physics of ferromagnetism and ferroelectricity, such as their hysteresis behaviour in response to the external field and anomalies (thermal, structural, mechanical, dielectric and magnetic) at the critical temperature. These coupling phenomena or/and similarities in terms of the electric dipoles and spins endorse the integration of ferroelectricity and magnetism into single phase materials and hence the possibility of MD/ME effect. This effect can be linear or/and non-linear with respect to the external fields, and can be described in terms of ME coupling coefficients which are given in the following equations. Thermodynamically, the ME effect can be understood in terms of expansion of free energy within the framework proposed in Landau-Devonshire theory;

$$F(E,H) = F_0 - P_i^s E_i - M_i^s H_i - \frac{1}{2}\varepsilon'_0\,\varepsilon'_{ij}\,E_i E_j - \frac{1}{2}\mu_0\mu_{ij}H_i H_j - \alpha_{ij}E_i H_j - \frac{\beta_{ijk}}{2}E_i H_j H_k - \frac{\gamma_{ijk}}{2}H_i E_j E_k + \ldots. \quad (1.1)$$

here, F_0 is the ground state free energy, P_i^s and M_i^s are the components of spontaneous polarization P^s and magnetization M^s, subscripts (i, j, k) stand for three components of a variable in spatial coordinates, E_i and H_i are the components of electric field E and magnetic field H, respectively, μ_0 and ε_0 are magnetic and dielectric susceptibilities in vacuum, ε_{ij} and μ_{ij} are the second-order tensors of dielectric and magnetic susceptibilities whereas ε_{ijk} and μ_{ijk} are referred as the third-order tensor coefficients. Importantly, α_{ij} is the component of tensor α which is designated as linear ME coupling coefficient (or simply linear

ME effect) and corresponds to the induction of magnetization by an electric field or polarization by a magnetic field. The rest of the other such coupling coefficients in the preceding equation are corresponding to the high-order ME effects parameterized by tensors γ and β [1,3]. The partial differentiation of equation 1.1, w.r.t. H_i will lead to magnetization

$$M_i(E,H) = -\frac{\partial F}{\partial H_i} = M_i^s + \mu_0\mu_{ij}H_j + \alpha_{ij}E_i + \beta_{ijk}E_iH_j + \frac{\gamma_{ijk}}{2}E_jE_k + ... \quad (1.2)$$

whereas the differentiation of F w.r.t. E_i leads to polarization

$$P_i(E,H) = -\frac{\partial F}{\partial E_i} = P_i^s + \varepsilon'_0\,\varepsilon'_{ij}\,E_j + \alpha_{ij}H_j + \frac{\beta_{ijk}}{2}H_jH_k + \gamma_{ijk}H_iE_j + ... \quad (1.3)$$

These above equations 1.1 to 1.3, are treated as the theoretical framework that describe ME coupling and provide correlation between polarization (magnetization) and external magnetic (electric) field.

It is vital to note that observation of ME coupling needs recording the effect of an electric field on magnetization or, conversely, that of a magnetic field on ferroelectric polarization. A difficulty arises in both of these situations as many of the candidates for being magnetoelectrics are indeed poor insulators which makes it difficult for them to sustain such a high electric field necessary (for realizing the effect) to switch/align the polarization/dipoles [1,9,16,33–35]. By keeping this in view, a relatively simple and widely accepted alternative method is used; in which capacitance (C) or dielectric constant (ε') is measured as a function of temperature (T) and/or applied magnetic field (H). Examples of such MD response (from literature) are shown in Figure 1.2 and 1.9. It is to be noted that the ε' is not measured directly, but, calculated from following formula (1.4) by measuring the capacitance in parallel plate capacitor arrangement

$$\varepsilon' = C/C_0 \quad (1.4)$$

here, C_0 is the capacitance measured when plates are separated by vacuum, whereas, C is the capacitance of material measured by placing it between same plates.

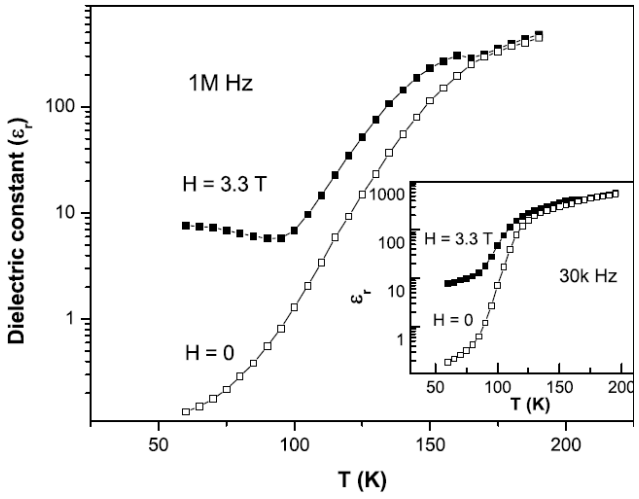

Figure-1.2: Temperature variation of the dielectric constant (1 MHz) of $Nd_{0.5}Ca_{0.5}MnO_3$ in the absence and presence of a magnetic field (H = 3.3 T). The inset shows data at 30 kHz [36].

In a magnetoelectric material, the magnetic order is coupled to polarization and hence also with ε' by obeying the equation 1.5;

$$\varepsilon' = \frac{P}{\varepsilon_0 E} + 1 \qquad (1.5)$$

Here, P is total polarization, E is applied electric field whereas ε_0 = 8.8542 x 10^{-12} F/m is the permittivity of vacuum. Thus, appearance of change in ε' (indirectly in P) due to the application of magnetic field is called as MD effect. Ultimately, MD phenomenon/terminology is observationally distinguishable from ME effect, as, it represents magnetic field induced change in dielectric permittivity (ε') whereas ME effect shows electric (magnetic) field induced change in magnetization (electric polarization). The intriguing MD/ME coupling and/or multiferroicity and the underlying physics endorse the suitability of these materials for different technological applications in various multifunctional devices such as multistate memory devices, non-volatile memories, spintronic devices, tunable filters, magnetic sensors, etc. [1,7,16,37–42]. As an specific example, considering

electrical power consumptions, multiferroics or MD/ME materials may be useful in enhancing the storage density of a RAM (random access memory) device with tremendously low power consumption (comparing to DRAM i.e. dynamic RAM which uses a pair of one capacitor and one transistor to read or write a single bit '0'/'1') in reading and writing cycle. Additionally, FeRAMs (ferroelectric RAMs) represent a typical device for ferroelectric applications in recent years, favored by 5 ns access speed and 64 MB memory density. The disadvantage of these FeRAMs is their destructive read and reset operation. On the other side, MRAMs (Magnetoresistive RAMs) have been lagging far behind FeRAMs, mainly because of the slow and high-power read/write operation though storage density is higher. Multiferroics or ME/MD materials, in this regard, offer a possibility to combine the advantages of FeRAMs and MRAMs in order to compete with EEPROMs (electrically erasable programmable read-only memories). Owing to all these reasons, currently, MD/ME/multiferroic systems are drawing enormous attention from scientific community.

1.3 Background and major challenges with existing MD/ME materials and/or multiferroics

Since last decade, research activities in the field of multiferroics and /or ME/MD materials have been invigorated for different materials [1,3–5,7,8,13,17,18,25,30,37,43–52] after the first experimental realization of ME coupling in Cr_2O_3 [53] and subsequent low temperature (LT) observations in $DyPO_4$ [54], $BaMnF_4$ [55], $YMnO_3$ [56] etc.. It is noticeable that MD effect can be observed also in some magnetic materials which do not exhibit spontaneous polarization [27–29]. In such systems, MD effect may appear due to the presence of some kind of coupling between their dielectric properties and magnetization [27–29]. Observation of MD effect has been reported in different single phase materials [13,25,43,44,57–59]. But, there are following major issues with existing/reported MD/ME materials-

(a) The MD effect is generally witnessed with the application of high magnetic field of the order of several tesla [13,25,43,44,58,59] and/or below room temperature (RT) which inhibits low-field and RT applications of these materials. For example – the observation of 13% change in ε' at 0.5 T and 10 K in $Y_3Fe_5O_{12}$ [60], 3% for H = 0.2 T below 30 K in $Tb_3Fe_5O_{12}$ [61], 1% in $CaMn_7O_{12}$ at 10 K [59], at 28 K in $TbMnO_3$ [13], at 230 K in CuO [62], at 25 K in $EuMnO_3$ [63] and also in other MD materials [42,64–66]. Two such examples from literature are shown in Figure 1.2 and 1.3 respectively for $Nd_{0.5}Ca_{0.5}MnO_3$ (well below 200K with H=3.3T) and Se/$TeCuO_3$ (across 30K/10K with 1kOe) [67]. However, for MD effect to be used in above-mentioned devices, only low magnetic field MD materials, which exhibit this effect near/at RT are important.

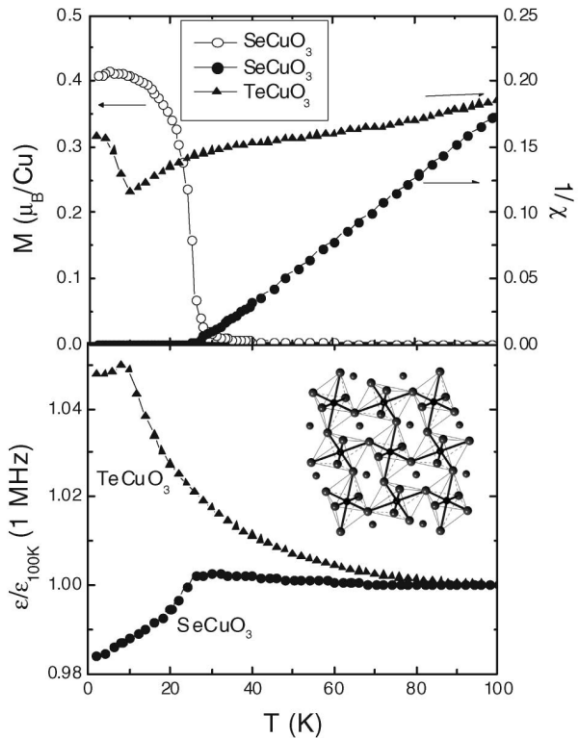

Figure-1.3: Magnetization of $SeCuO_3$ and $TeCuO_3$ versus temperature in the 1 kOe field (upper) and dielectric constant of $SeCuO_3$ and of $TeCuO_3$ versus temperature in the zero applied field (lower). The inset shows the structure of $SeCuO_3$ [67].

(b) Intrinsicality (intrinsic nature) of the observed MD effect is also important from basic physics as well as application point of view as the MD effect may appear also due to extrinsic effects like

magnetoresistive artifacts [9,29]. G. Catalan [9] provided a way through theoretical calculations to judge the intrinsicality (basically resistive origin) of observed MD effect. The approach has been widely accepted and followed by others [1,10,46,68–76]. However, to the best of our knowledge, the experimental studies for recognizing the resistive and MR (magnetoresistance) free contributions present in MD response have not been reported so far.

(c) Even though MD/ME materials and/or multiferroics exhibit fascinating properties, the mechanism responsible for the appearance of MD/ME phenomenon and/or multiferroicity is still not very clear and no such generalized mechanism has been established till now. For example-(i) the ME coupling in $TbMnO_3$, $Ni_3V_2O_8$, $MnWO_4$ and $BaNiF_4$ [30,77–86] has been attributed to inverse Dzyaloshinskii-Moriya (DM) effect, which works in systems with non-collinear spin structures (usually spiral magnetic structures; in which spins rotate around an axis perpendicular to the propagation vector of the spiral) and needs the direct action of the spin-orbit interaction [3,4,30,77–86]. (ii) Magnetostriction gives rise to ME phenomenon in $HoMnO_3$ via periodic collinear ‘up-up-down-down’ type spin arrangement that can induce electric polarization via exchangestriction mechanism [3,4]. The mechanism based on magneto-striction does not require the presence of spin-orbit coupling as a compulsion and can occur in collinear magnetic structures. (iii) Magnetic reversal of ferroelectric polarization or dynamical and/or resonant coupling between magnetic and electric dipoles is reported in $CoCr_2O_4$ [87,88]. Both ferroelectric and magnetic order parameters were supposed to be changed simultaneously across these multiferroic domain walls (MFDWs). The multiferroic nature of $CoCr_2O_4$ is depicted in Figure 1.4 and it has been understood in terms of the dynamics of MFDWs and the electromagnon or electrically driven magnetic resonance. The ferroelectricity in particular, has been attributed to conical spin

modulation for $CoCr_2O_4$ [87]. (iv) Simultaneous occurrence of long-range ferroelectric and incommensurate magnetic order has been

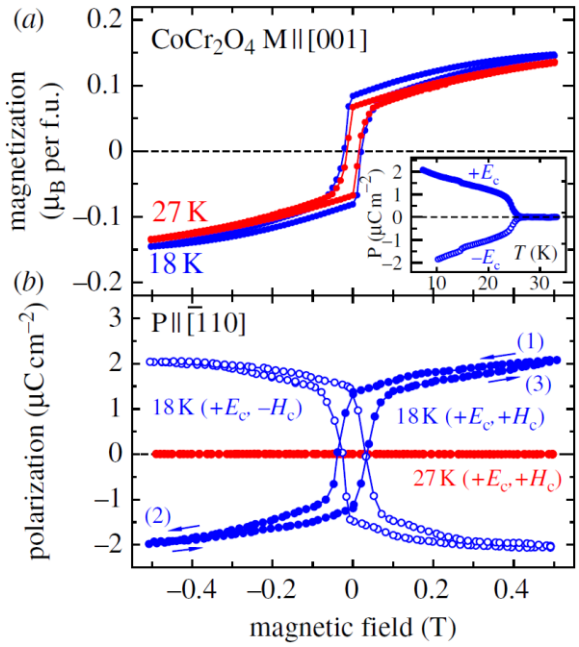

Figure-1.4: Magnetic field dependence of (a) magnetization and (b) electric polarization measured for $CoCr_2O_4$ above (27K) and below (18K) the ferroelectric transition temperature (T_S=26K). For measurements of polarization, the magnetic field was scanned between $+H_c$ and $-H_c$, for each magnetoelectrically cooled state prepared with (E_c,H_c) and (E_c,$-H_c$), as represented by closed and open circles. Ec (=400kVm−1) and Hc (=0.5 T) stand for the cooling electric and magnetic fields, respectively. The inset of (a), shows the temperature dependence of spontaneous polarization in the cases of the magnetoelectric cooling with positive and negative Ec [87,88].

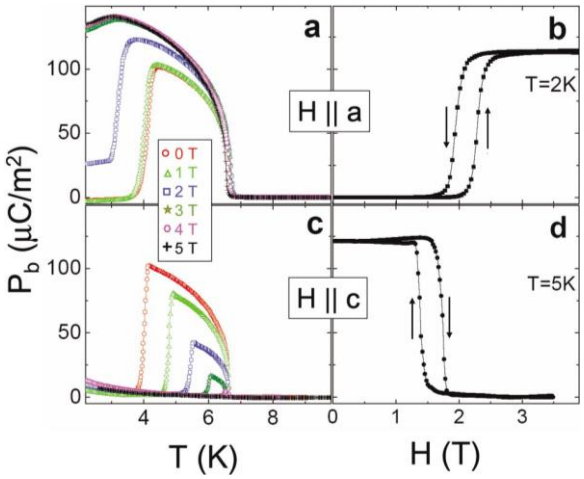

Figure-1.5: Promotion and suppression of electric polarization by applying magnetic fields in NVO. Temperature and magnetic-field dependence of electric polarization along the *b* axis for **H** along the *a* [frames (a) and (b)] and *c* [frames (c) and (d)] axes [89].

observed across phase transition in $Ni_3V_2O_8$ [89] as shown in Figure 1.5. The observed ferroelectricity was considered to be appeared only in the phase for which magnetic ordering breaks inversion symmetry and hence assigned as magnetically driven. (v) Order-disorder ferroelectricity (ferroelectric domain boundary motion) and MD response is reported in $LuFe_2O_4$ [21,90]. A para to ferroelectric transition (under pyroelectric measurements) along with temperature dependent dielectric dispersion has been observed in $LuFe_2O_4$ as depicted in Figure 1.6 and 1.7 respectively. The appearance of

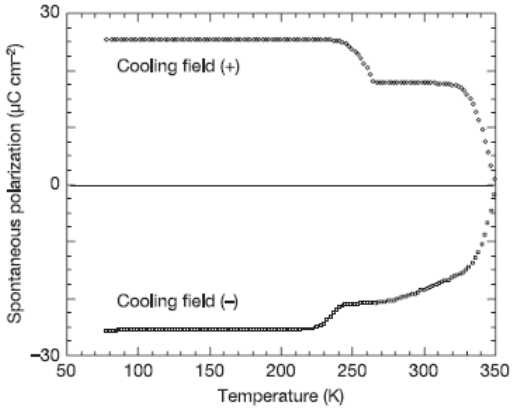

Figure-1.6: Polarization as a function of temperature under pyro-electric current measurement for LuFe2O4 [90].

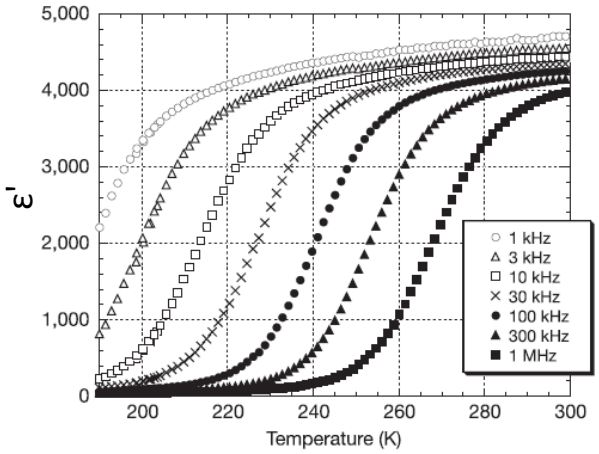

Figure-1.7: Temperature dependent dielectric response of $LuFe_2O_4$ for frequencies ranging from 1kHz to 1MHz [90]. Subramanian *et al.* [21] have also reported the similar dielectric dispersion for $LuFe_2O_4$.

ferroelectricity has been explained in terms of ordering of iron multivalence (Fe^{2+} and Fe^{3+}) [90] whereas the observed dielectric dispersion has been attributed to change in polarizability associated

with the ordering of coexisting Fe charge sates and charge fluctuations on Fe sites [21]. Similar to $LuFe_2O_4$ (Figure 1.6) [90], $YFeO_3$ also shows improved ferroelectric polarization at lower temperature [48] as depicted in Figure 1.8 and its inset.

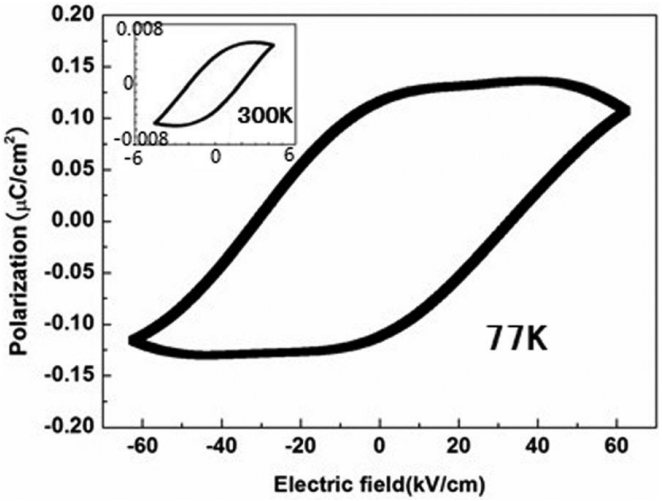

Figure-1.8: The P–E hysteresis loops were measured at 77K (main panel) and 300K (inset) respectively; showing polarization improvement at lower temperature [48].

(vi) Additionally, in various multiferroic perovskite systems, the appearance of magnetism or magnetic order has been attributed to the presence of transition metal (TM) ions whereas the evolution of ferroelectricity is accounted for different mechanisms in different compounds like- lone pair (at Bi ions) driven in $BiFeO_3$ [15], $BiMnO_3$ [14] , and $Bi_{1-x}Nd_xFeO_3$ [91]; geometrically driven in $YMnO_3$ [92] whereas charge ordering (CO) driven in $PrCaMnO_3$ [93]. Thus lacking of a generalized mechanism makes it difficult to prepare the multifunctional compounds which can exhibit desired MD/ME properties without any extrinsic contribution.

1.4 Present research work

It is clear from above background that from application (e.g. RAM-random access memory, capacitance based tuning circuit etc.) perspective, in a MD material, it is extremely important that the MD effect–

(i) should appear at/around room temperature (RT),

(ii) should appear due to a low magnetic field and

(iii) should not be MR (magnetoresistance) originated.

The already existing/reported MD materials do not satisfy all these three key requirements simultaneously and enormous efforts are being made worldwide for searching a MD material with desired key features. Therefore, we decided to prepare a MD material and to analyze and explore its intinsicality and possible origin of MD coupling.

1.4.1 Selection of material and a brief modus operandi

As far as intrinsic MD coupling is concern, ideally it can be realized in a material with magnetically switchable net electric dipole moment and such systems are barely formed [11] . Nonetheless, it can be achieved by making a compound which expands/shrinks in response to an externally applied magnetic field as the ε' or ultimately capacitance *C*, is directly related to sample's dimensions by the relation $C \propto A/d$ (here, *C* is the capacitance of a dielectric material, *A* the area and *d* is he thickness of dielectric).

By keeping this in view, $LaGaO_3$ (LGO) was doped with Mn at Ga site with an expectation of RT (near RT) MD coupling because, the strain evolved due to significant difference in Ga-O (1.97 Å) and Mn-O (2.18Å long bond/1.90Å short bond) distances [94], is supposed to be magnetically switchable as the magnetic field retransforms [94] or rerotates [95] Mn spin moments and hence the Mn-orbitals [94,95] (magnetic field induced re-rotation of spin coupled Mn-orbitals is possible [94,95], as in such systems spin and orbital degrees of freedoms are strongly coupled with each other). With similar approach LGO is separately doped also with Fe at Ga site. This magnetically switchable reorientation/retransformation of Mn/Fe-orbitals [94,95] may result into shrinking/expanding of material and hence, may lead to a change in capacitance (according to $C \propto A/d$) i.e., occurrence of an

intrinsic MD effect. There is an additional advantage of selecting the said compound that is, for $LaMn_{1-x}Ga_xO_3$, sufficient literature on- its structure (neutron diffraction) [96], its lattice modes (Raman spectroscopy) [97,98], local geometry around its MnO_6 octahedron (extended X-ray absorption fine structure i.e., EXAFS measurements) [99], arrangement of Mn orbitals (orbital ordering) and their transformation on replacing Mn with Ga [94] etc., is already available which can be helpful in identifying the structure and understanding the mechanism of MD effect. However, this compound had not been explored from dielectric or magnetodielectric purpose. Ultimately, under present research work, two series namely $LaGa_{1-x}Mn_xO_3$ (LGMO) and $LaGa_{1-x}Fe_xO_3$ (LGFO) were prepared by solid state reaction method.

Present research work mainly covers an observation of RTMD effect in LGMO samples with x=0.2 (LGM2O) and x=0.6 (LGM2O) and LGFO sample with x=0.3 (LGF3O) along with a systematic study on the intrinsicality of the observed MD coupling. It is noteworthy that this MD coupling has been realized under a low or moderate magnetic field (for LGM2O, at only 0.4 tesla). Further, a known technique – 'impedance spectroscopy (IS)' has been used and emphasized first time to identify and separate intrinsic and resistive contributions present in the observed MD coupling. Our analysis reveals that in order to estimate the resistive contributions, frequency dependent MR (FDMR) measurements are more sensitive and useful than that of measuring only dc MR, therefore, we have proposed 'impedance spectroscopy (IS)' as a tool for recognizing and separating intrinsic and resistive parts/factors contributing in MD effect. The intrinsicality of observed MD phenomenon has been validated also through a non-electrical technique. For this purpose, Raman measurements have been performed at RT in the absence and presence of magnetic field. On the basis of magnetic field dependent Raman data, presently observed MD effect has been validated as an intrinsic property and attributed to magnetostriction phenomenon. We proposed that the studied

LG(M/F)O can be used as MD material as it satisfies all three core criteria. The temperature dependent dielectric and magnetization measurements have also been performed with an expectation of a direct signature of MD coupling i.e., appearance of an anomaly in ε'-T and M-T curves at same temperature; an example from literature, is shown in Figure 1.9. Additionally, the same set of LGMO samples has been probed also for multiferroic properties by means of P-E, M-H and M-T (in ZFC-*zero field cooled* and FC-*field cooled* modes) measurements. The presently studied LGMO exhibit magnetic ordering below RT (at low temperatures) with leaky P-E loops. The appearance of magnetic ordering at different temperatures for different LGMO compositions has been understood on the basis of average number of Mn^{3+} and Mn^{4+} (not on the relative percentage of Mn^{3+} and Mn^{4+}).

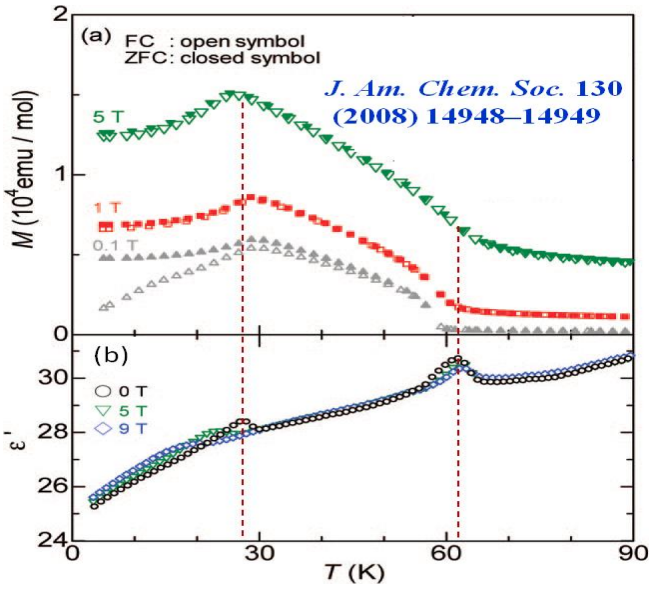

Figure-1.9: Temperature dependent (a) magnetization and (b) dielectric constant of $(BiMn_3)Mn_4O_{12}$ perovskite measured at different magnetic fields. The magnetic and dielectric anomalies appeared at almost same temperature (indicated by dashed vertical lines of red color) exhibits MD coupling in A-site ordered $(BiMn_3)Mn_4O_{12}$ perovskite [95].

The research work reported in present thesis has been accomplished systematically in following manner

(i) Sample preparation and analysis of structural phase purity

(ii) Observation of RTMD effect and its understanding

(iii) Analysis of resistive and intrinsic contribution of MD effect
(iv) Evidence and origin of intrinsic nature of MD coupling
(v) Large dielectric permittivity and dielectric dispersion
(vi) Investigation for the possibility of multiferroicity

The remaining chapters of thesis are summarized as follows:

Chapter 2: Experimental Details; this chapter covers - procedure used for the synthesis of LG(M/F)O samples, basic description of characterization techniques, discussion on the formation of material's structural phase by analyzing XRD results and selection of specific LG(M/F)O compositions for further studies. Presently used techniques includes, Lab source and synchrotron based x-ray diffraction (XRD), x-ray absorption near edge structure (XANES), dielectric and impedance spectroscopy, Raman spectroscopy, magnetic measurements etc.. The basic working principle along with the schematic representation of used set-ups and attachments is discussed in detail.

Chapter 3: Observation and Analysis of Room Temperature Magnetodielectric Effect in $LaGa_{1-x}Mn_xO_{3+\gamma}$ (x=0.2 and 0.6); this chapter presents an observation of RTMD effect in $LaGa_{0.8}Mn_{0.2}O_{3+\gamma}$ (LGM2O) and $LaGa_{0.4}Mn_{0.6}O_{3+\gamma}$ (LGM6O). An initial analysis of observed RTMD effect is presented in terms of trends of magnetic field dependent change of dielectric constant (ε')/capacitance (C) and loss tangent ($tan\delta$). The oxygen excess (coexistence of Mn^{3+} and Mn^{4+}) has been validated through titration and XANES analysis. The excess of oxygen has been understood by means of density functional theory (DFT) based first principles calculations.

Chapter 4: Analysis of Resistive and Intrinsic Contributions: Magnetodielectric Effect in $LaGa_{1-x}Mn_xO_{3+\gamma}$ (x=0.2 & 0.6);This chapter provides an analysis of resistive contributions (of observed MD effect) by means of *dc* (direct current) and frequency dependent magnetoresistance (FDMR) measurements. In case of LGM6O, the

observed MD effect is found to be intrinsic over the entire range of probing frequencies. In case of LGM2O, at frequencies corresponding to bulk contribution (>10^5Hz), the MD effect is intrinsic whereas at lower frequencies (<10^5Hz) it is dominated by magnetoresistive artifacts. The intrinsic nature of MD effect has been validated by analyzing the magnetic field dependent Raman spectra.

Chapter 5: Room Temperature Magnetodielectric Study on $LaGa_{0.7}Fe_{0.3}O_{3+\gamma}$: Impact and Origin of Excess Oxygen; In this chapter, an observation of room temperature magnetodielectric (RTMD) behavior of $LaGa_{0.7}Fe_{0.3}O_{3+\gamma}$ (LGF3O) is presented. The resistive contribution of observed MD effect is analyzed by means of FDMR whereas the intrinsic nature of MD phenomenon is evidenced in terms of magnetic field dependent Raman measurements.

Chapter 6: Large Dielectric Permittivity, Dielectric Dispersion and Possibility of Multiferroicity in Mn doped $LaGaO_3$; The first part of this chapter covers an observation of large dielectric permittivity and temperature dependent dielectric dispersion in LGMO samples. The second part covers RT and temperature dependent magnetic studies, which includes *M-H* and *M-T* (in ZFC- FC modes) measurements, along with RT *P-E* hysteresis loops for selected LGMO compositions.

Chapter-7: Conclusions and Future Research Scope; This chapter summarizes the results of present research work with concluding remarks. The possible future scope of present study has also been discussed.

Chapter 2

Experimental Details

This chapter provides basic information about the synthesis procedure (sample preparation) and characterization techniques used in present research work. Additionally, discussion on the formation of material's structural phase by analyzing XRD results and selection of specific LG(M/F)O compositions for further studies is also presented. All presently studied samples have been prepared through sloid state reaction method. As far as characterization techniques are concern, (i) X-ray diffraction (XRD) is used to confirm the formation of structural phase, (ii) dielectric/impedance spectroscopy is used to record the dielectric and MD response, (iii) Raman spectroscopy (in the absence and presence magnetic field) has been employed to check the intinsicality of presently observed MD effect, (iv) XANES and iodometric titration have been used to estimate the oxidation state of Mn or to check the oxygen stoichiometry (v) SQUID-VSM (superconducting quantum interference device-vibrating sample magnetometer) has been employed for magnetic measurements. Further, more specific details about synthesis of samples and characterization techniques are discussed accordingly in the '*experimental*' section of each forthcoming chapter.

2.1 Sample preparation

Polycrystalline samples of $LaGa_{1-x}Mn_xO_3$ (LGMO) and $LaGa_{1-x}Fe_xO_3$ (LGFO); x=0 to x=1 with an increment of 0.1, have been prepared through conventional solid-state reaction route. It is notable that some intermediate LG(M/F)O compositions have also been prepared.

2.1.1 Solid state reaction method

Solid state reaction is a commonly used method for synthesis of oxides [100]. In general, it is a solvent free reaction method in which reactants are mixed in molar ratio homogeneously and allowed to react in powder form. The reaction rate is determined by various parameters such as temperature, surface area of reactants and rate of nucleation. Large surface area of contact is obtained by making very fine grains and homogeneous mixture of the constituents. The homogeneous mixture is prepared by grinding the powder mixture either manually by using a pestle mortar or mechanically by means of Ball milling. For present research work, the constituent oxides are grinded manually by using agate pestle-mortar. It is to be noted that in present work, propanol has been added for homogeneous mixing of oxides. Moreover, it is known that the solids do not react at room temperature; therefore, in order to initialize the reaction the grinded powder is heated at high temperature (well below the melting temperature of the compounds but above calcination temperature) in air or gas. The rate of diffusion increases at higher temperatures. This process is known as calcination, in which, thermal decomposition of initial/constituent oxides takes place to form the new desired phase. In order to improve the crystal quality of desired phase, the powder mixture is heated at a further higher temperature (generally preferred in steps and termed as intermediate heating) well above the calcination temperature but lower to the melting temperature of any of the constituent oxides. This post calcination heat treatment is generally known as sintering. This solid state reaction procedure can be summarized in the following steps:

- Weighing and mixing of constituent oxides in stoichiometric proportion.
- Grinding the powders to prepare a homogeneous mixture by making larger area of contact between reactants.
- Calcinations and final sintering of grounded powder at high temperature.

2.1.2 Preparation of circular pellets

First of all, the phase purity of as prepared powder samples has been examined by means of XRD experiments. XRD data has then been refined by using FullProf Rietveld refinement package [101]. It is to be noted that particularly for dielectric measurements pellets with very high density (i.e., low porosity) are needed. Hence, in order to further enhancing the intimate bonding between crystallites (i.e. minimizing the porosity), the pure phase powder is pressed in the form of a circular pellet by means of a hydraulic press and a suitable die set. Then the pellet is again heated/sintered at high temperature (well above to calcination temperature), but, below the melting point. This post-calcination sintering (below melting point), helps in (i) improving the crystal quality by minimizing defects, (ii) enhancing grain growth by reducing the total area of grain boundary (GB), and (iii) attaining the maximum possible density. Moreover, as far as present research work is concern, the pure phase LG(M/F)O powder samples have been pelletized at a pressure of 15 ton to form 1 mm thick circular discs of 12 mm diameter. These pellets were sintered in air at 1400 $^{\circ}$C for 24 hours. Further, after being coated with silver paint these pellets were fired at 300° C for 30 min. These pellets are then used for, almost, rest of all the measurements carried out under present research work.

2.2 Characterization techniques

2.2.1 X-Ray Diffraction

X–rays diffraction (XRD) is one of the most suitable and reliable tool to probe the structure of a material as the wavelength of X-rays (it is of the order of *Å*) is comparable to the interatomic distances. The non-destructiveness is an additional advantage of XRD method. In XRD, an X-ray falls on the material at some incidence angle, gets diffracted through different set of atomic planes present in the crystal structure. When, both, *d* (spacing between successive atomic planes; also called as *d*-spacing) and θ (the angle of incidence of X-ray), satisfies the Bragg relation $2dsin\theta=n\lambda$ (here, *d* is the inter-planer distance, λ is wavelength of incident X-ray and *n* is an integer), a constructive interference takes place between the diffracted waves. The Bragg condition i.e., the basic of XRD can be understood with help of a schematic ray diagram depicted in Figure 2.1.

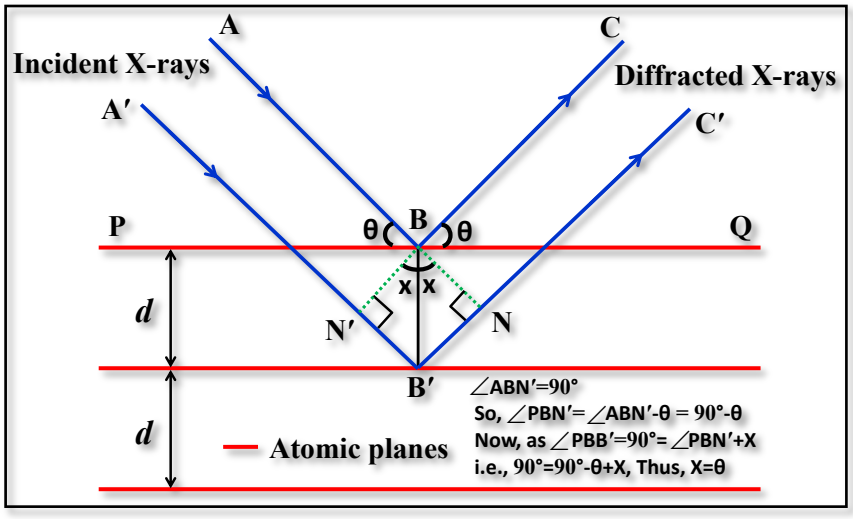

Figure-2.1: Diffraction of X-rays through lattice/atomic planes of a crystal.

According to Figure 2.1, the geometrical path difference between ABC and A′B′C′ (say Δ) = N′B′+B′N

$$=BB'Sin\theta+BB'Sin\theta$$

$$\Delta=2BB'Sin\theta = 2dSin\theta \qquad (2.1)$$

For the constructive interference, the path difference is always an integer multiple of wavelength, i.e.,

$$\Delta = n\lambda \qquad (2.2)$$

Thus, from equations 2.1 and 2.2, the Bragg's condition for constructive interference of diffracted X-rays is $2dSin\theta = n\lambda$, where n is an integer. The diffracted X-ray photons are then detected, processed and counted. In this way, with the satisfaction of Bragg's condition, a peak, across the corresponding θ value appears in the intensity versus angle (2θ) curve. Conversion of the diffraction peaks to d-spacing enables the identification of the material under investigation. It is wort mentioning

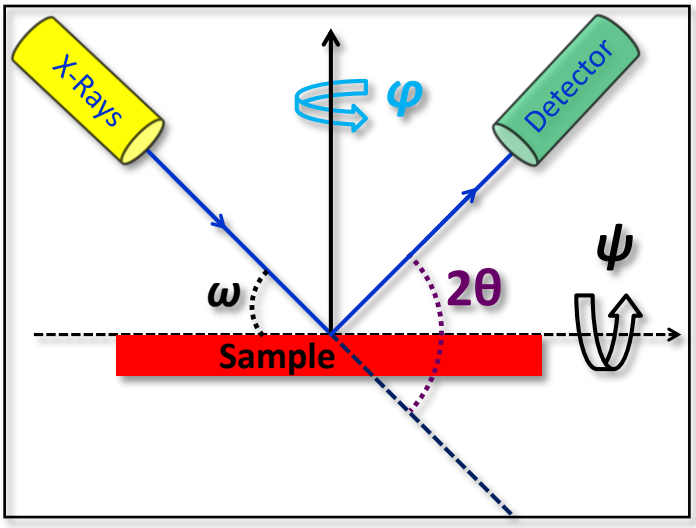

Figure-2.2: Schematic of XRD setup with different angles of rotation.

that the XRD pattern of each element/material is unique and can be considered as a signature of its structural phase. This uniqueness enables the XRD to identify and validate the purity of a structural phase for given a material. XRD pattern contains almost complete information about the crystal structure, like-lattice parameters, bond angles, grain size, strain etc... For structural studies, the samples in the form of powder or pellet or film can be probed by means of XRD. Schematic of a typical XRD set up is shown in Figure 2.2. Here, 2θ is the angle between incident beam and diffracted beam, φ is angle of

rotation about a plane perpendicular to the surface, ψ is angle about the line parallel to the surface, whereas, ω is the angle between incident X-ray beam and sample surface. In 'θ-2θ' scanning, angle ω is treated as θ. Depending upon the type of information to be extracted; XRD can be operated in different scanning modes.

2.2.2 Iodometric titration

In ABO_3 (B: transition metal=TM) perovskite systems, some specific physical properties are evolved mainly due to the relative concentration of multi-valent transition metal ions (e.g, Mn^{3+} and Mn^{4+} in manganites) [102]. Thus, determination of average charge state of TM ion/exact oxygen content (i.e., oxygen stoichiometry) becomes essential for such systems. This is usually realized by redox volumetric analysis, which is essentially an iodometric titration method [103,104]. In iodometric titration, the volume (say V_1; to be measured) of *titrant* (known solution with known concentration N_1), is required to react with a measured volume of an unknown solution *(titrand).* By measuring V_1, the value of γ in $ABO_{3\pm\gamma}$ is calculated with the help of normality relation $N_1V_1=N_2V_2$ and

$$z = (N_1V_1 \times y)/x \qquad (2.3)$$

here, z is the charge transfer in the reaction, y is the molecular weight whereas, x is the weight of the sample. Note that the z is determined through reaction balancing and can be different for different samples/reactions. Gamma (γ) is included well within the z, for example (for LGM2O i.e. $LaGa_{0.8}Mn_{0.2}O_{3+\gamma}$)

$$z = 2 \times (0.1 + \gamma) \qquad (2.4)$$

An example of z determination through reaction balancing (for LGM2O) is given here;

$$LaGa_{0.8}Mn_{0.2}O_{3+\gamma} + 5.8HCl \rightarrow LaCl_3 + 0.8GaCl_3 + 0.2MnCl_2 + 2.9H_2O + (0.1+\gamma)O$$

$(0.1+\gamma)O$ is the nascent oxygen which further reacts with KI and HCl in following manner

$$(0.1+\gamma)[2KI + 2HCl \rightarrow 2KCl + I_2 + H_2O]$$

here, the multiple of I i.e., $2\times(0.1+\gamma)$ represents total charge transferred in the reaction (z). In this way by means of reaction balancing, z can be determined for different samples. Titration method is based on *redox* reaction. In a *redox* (reduction-oxidation) reaction, one material (reducing agent which is oxidized in the reaction) donates an electron whereas the other (oxidizing agent that is reduced in the reaction) accepts one electron. In this way, the reactive species are electrons which are transferred from reducing agent to oxidizing agent. Iodine is commonly used as an oxidizing agent in redox titrations (despite, it is considerably less oxidizing than that of the other agents like $KMnO_4$ or $K_2Cr_2O_7$). The process or reaction which involves the inter-conversion of elemental iodine and I^- ions [$I_2+2e^- \leftrightarrow 2I^-$] i.e., iodine liberated during oxidation, is known as *iodometric titration* or simply *iodometry*. Since, the solution of sodium thiosulphate does not

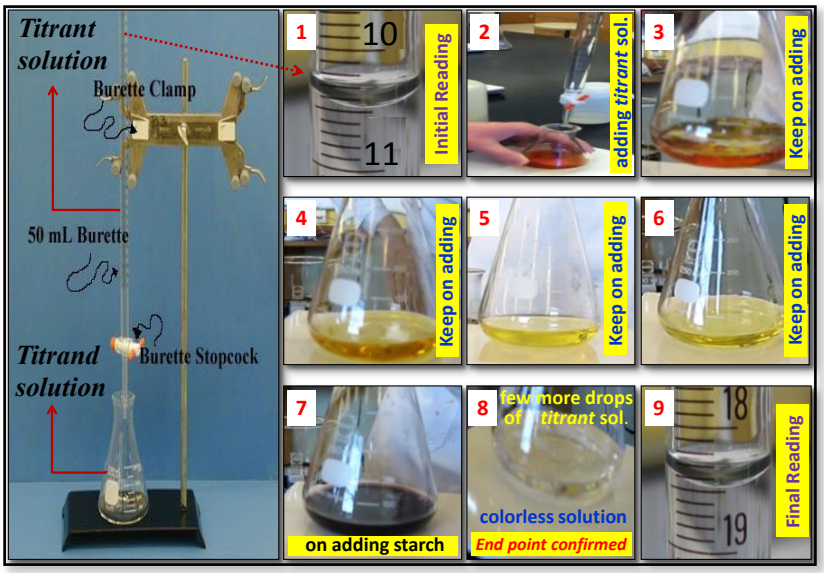

Figure-2.3: Experimental arrangement for titration along with a sequential picture display of different steps involved in the titration process (like stepwise color changing of titrand solution). Note- after adding the titrant solution, each time, a gentle shaking of the titrand solution (in conical flask) is neccessary.

remain stable for a long period of time, it is usually standardized with primary standards, e.g., solution of oxidizing agents like $KMnO_4$ and $K_2Cr_2O_7$. The titration process involves following reactions-

when potassium dichromate of known normality and volume reacts with KI, iodine is liberated;

$$K_2Cr_2O_7 + 6KI + 14HCl \rightarrow 3I_2 + 8Kcl + 2CrCl_3 + 7H_2O$$

the liberated iodine is titrated with thiosulphate via following reaction

$$2Na_2S_2O_3 + I_2 \rightarrow 2NaI + Na_2S_4O_6$$

$$2S_2O_3^{2-} + I_2 \rightarrow 2I^- S_4O_6^{2-}$$

i.e., when sodium thiosulphate reacts with iodine molecule, it gives sodium tetrahionate ($Na_2S_4O_6$), where two $S_2O_3^{2-}$ ions, with four excess electrons, are converted into a single $S_4O_6^{2-}$ ion with only two excess electrons. It is to be noted that due to thiosulphate solution (*titrant*), the entire iodine is used to make the solution (sample+Hcl+KI) colorless at the *endpoint*. Freshly prepared 1% starch solution is used as an indicator for an accurate determination of *end point*, as its inclusion makes a dark blue complex on reacting with iodine in the solution and makes *end point* detection easier. As far as the titration procedure is concern, first of all, initial solutions of thiosulphate, $K_2Cr_2O_7$, KI and starch are prepared. The determination of γ in $ABO_{3\pm\gamma}$, is realized by dissolving the sample along with KI in an acidic solution (sample+Hcl+KI) and titrating it (adding thiosulphate drop by drop) till the *end point*. In association with the experimental arrangement, a sequential picture display of different steps involved in the titration (like stepwise color changing of *titrand* solution) process is shown in Figure 2.3.

2.2.2.1 Charge state determination via iodometric titration

The difference of initial and final reading (in Figure 2.3) gives the volume V_1. By substituting the values of V_1, N_1, x and y, the value of z can be determined with the help of equation 2.3. Further, by equating this value of z with the one obtained through reaction balancing (an example shown in equation 2.4), γ is determined. For $A(TM)O_3$ perovskites having multivalence TM ions; with this value of γ, the

average charge state of TM (like Mn/Fe) and individual percentage of each among two valence (like $Mn^{3+}/Fe^{3+}$and $Mn^{4}/Fe^{4+)}$ can be calculated by using the charge neutrality condition . An example of such a calculation by using the value of γ and charge neutrality condition is given here;

Example:-Calculation for determining charge state of Mn and percentage of Mn^{3+} and Mn^{4+} in $LaGa_{0.8}Mn_{0.2}O_{3+\gamma}$ by using the results of iodometric titration (say γ=0.015):-

(i) Mn Charge state (say x)

For the considered sample, by charge neutrality condition,

$$La^{3+}Ga^{3+}_{0.8}Mn^{x}_{0.2}O^{2-}_{(3+\gamma)} = La^{3+}Ga^{3+}_{0.8}Mn^{x}_{0.2}O^{2-}_{(3+0.015)} = 0$$

Here, x is the charge state of Mn in the considered sample and γ = 0.015 (by titration),
Thus,

$$(3\times1)+(3\times0.8)+0.2x+(-2\times3.015)=0$$
$$3+2.4+0.2x-6.030=0$$
$$5.4+0.2x-6.030=0$$
$$0.2x-0.63=0$$
$$x=\frac{0.63}{0.2}$$
$$x=3.15$$

Thus, through iodometric titration, the charge state of Mn in the considered $LaGa_{0.8}Mn_{0.2}O_{3+\gamma}$ sample is found to be 3. 15.

(ii) Percentage of Mn^{3+} and Mn^{4+}

For the presently considered sample, by charge neutrality condition,

$$LaGa_{0.8}Mn_{0.2}O_{(3\pm\gamma)} = La^{3+}Ga^{3+}_{0.8}Mn^{3+}_{0.2(1-x)}Mn^{4+}_{0.2x}O^{2-}_{(3\pm\gamma)}$$

Here, x is the amount of Mn^{4+} in the total Mn present in the sample. Since, through titration experiment the value of γ is taken as 0.015, therefore, according to charge neutrality condition

$$La^{3+}Ga^{3+}_{0.8}Mn^{3+}_{0.2(1-x)}Mn^{4+}_{0.2x}O^{2-}_{(3+\gamma)}$$

$$= La^{3+}Ga^{3+}_{0.8}Mn^{3+}_{0.2(1-x)}mn^{4+}_{0.2x}O^{2-}_{(3+0.015)} = 0$$

$$(3\times1)+(3\times0.8)+[3\times0.2(1-x)]+(4\times0.2x)+(-2\times3.015)=0$$

$$3+2.4+0.6-0.6x+0.8x-6.030=0$$

$$6+0.2x-6.030=0$$

$$0.2x-0.030=0$$

$$x=\frac{0.030}{0.2}$$

$$x=0.15$$

Thus Mn^{4+} is 15% out of total Mn present in the considered sample whereas remaining 85% is Mn^{3+}.

2.2.3 X-ray absorption spectroscopy (XAS)

X-ray absorption spectroscopy (XAS) is widely used to determine local geometric and/or electronic structure of matter. The experiments are usually performed at synchrotron radiation source, which provides intense and tunable X-ray beam. X-rays are ionizing radiation with energies ranging from ~ 500 eV to 500 keV or wavelengths ranging from ~ 25° A to 0.25A ° and thus, have potential to eject an electron from a core level of an atom. When a substance is scanned for X-ray energies across the binding energy of a core shell, an abrupt increase in absorption cross-section takes place. This gives rise to an absorption edge in the absorption versus photon energy plot. The XAS study only across absorption edge is termed as X-ray absorption near edge structure (XANES) or as near edge X-ray absorption fine structure (NEXAFS), whereas, with an additional extended range of X-ray energy it is categorized as extended X-ray absorption fine structure (EXAFS). The edges for an atom can be named according to the principle quantum number of the electron that is, K for n=1, L for n=2, M for n=3, etc. The core–electron binding energy increases with increasing atomic number, ranging from 284 eV for the C (carbon) K-edge to 115606 eV for the U (uranium) K- edge, with the L-edges at

significantly lower energies than that of the corresponding K-edge. In XAS, an x-ray photon is absorbed by an electron in a tightly bound quantum core level (such as the 1*s* or 2*p* level) of an atom (Fig 2.4). In order for a particular electronic core level to participate in the absorption, the binding energy of this core level must be less than the energy of the incident x-ray. If the binding energy is greater than the energy of the x-ray, the bound electron will not be perturbed from the well-defined quantum state and will not absorb the x-ray. If the binding energy of the electron is less than that of the x-ray, the electron may be removed from its quantum level. In this case, the x-ray is destroyed (i.e., absorbed) and any energy in excess of the electronic binding energy is given to a photo-electron that is ejected from the atom. This

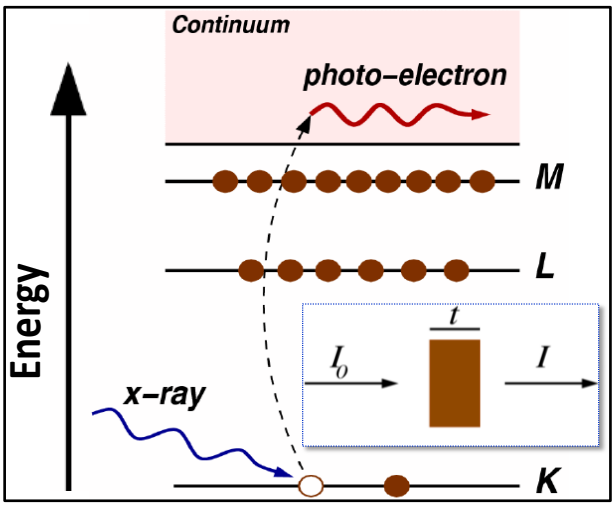

Figure-2.4: The photoelectric effect; an x-ray is absorbed and a core level electron is promoted out of the atom. Inset shows schematic for x-ray absorption measurements: An incident beam of monochromatic x-rays of intensity I_0 passes through a sample of thickness t, and the transmitted beam has intensity *I*.

process has been well understood for nearly a century (Einstein received the Nobel Prize for describing this effect). The full implications of this process when applied to molecules, liquids, and solids will give rise to XAFS. When discussing x-ray absorption, we are primarily concerned with the absorption coefficient μ, which gives the probability that x-rays will be absorbed according to Beer's Law:

$$I = I_0 e^{-\mu t} \qquad (2.4)$$

where, I_0 is the x-ray intensity incident on a sample, t is the sample thickness, and I is the intensity transmitted through the sample, as shown in the inset of Fig 2.4. The x-ray intensity is proportional to the number of x-ray photons. The absorption coefficient μ is a smooth function of energy, with a value that depends on the sample density ρ, the atomic number Z, atomic mass A, and the x-ray energy E roughly as

$$\mu \approx \frac{\rho Z^4}{AE^3} \qquad (2.5)$$

The strong dependence of μ on both Z and E is a fundamental property of x-rays, and is the key to why x-ray absorption is useful for different applications.

In XAS, when the incident x-ray has an energy equal to that of the binding energy of a core-level electron, a sharp rise in absorption takes place; an absorption edge in μ versus E curve appears corresponding to the promotion of this core level electron to the continuum (Figure 2.4). An XAFS measurement is simply a measure of the energy dependence of μ at and above the binding energy of a known core level of a known atomic species. Since every atom has core-level electrons with well-defined binding energies, the x-ray energy can be tuned according to the absorption edge of a selected element. The edge energies vary with atomic number roughly as Z^2. Following an absorption event, the atom is said to be in an excited state, with one of the core electron levels left empty (a so-called core hole) and a photo-electron comes out (Figure 2.4). The excited state will eventually decay typically within a few femtoseconds of the absorption event. Note that this decay does not affect the x-ray absorption process. After an x-ray absorption event, there are two main mechanisms for the decay of the excited atomic state. The first of these is x-ray fluorescence (Fig 2.5 (a)), in which a higher energy core-level electron fills the deeper core hole, ejecting an x-ray of well-defined energy. The fluorescence energies emitted in this way are characteristic

of the atom, and can be used to identify the atoms in a system, and to quantify their concentrations. For example, an L or M shell electron dropping into the K level gives the K fluorescence line (Figure 2.5 (a)).The second process for de-excitation of the core hole is the Auger Effect (Figure 2.5 (b)), in which an electron drops from a higher electron level and a second electron is emitted into the continuum (and possibly even out of the sample). In the hard x-ray regime (> 2 keV), x-ray fluorescence is more likely to occur than Auger emission, but for lower energy x-ray absorption, Auger processes dominate. Either of

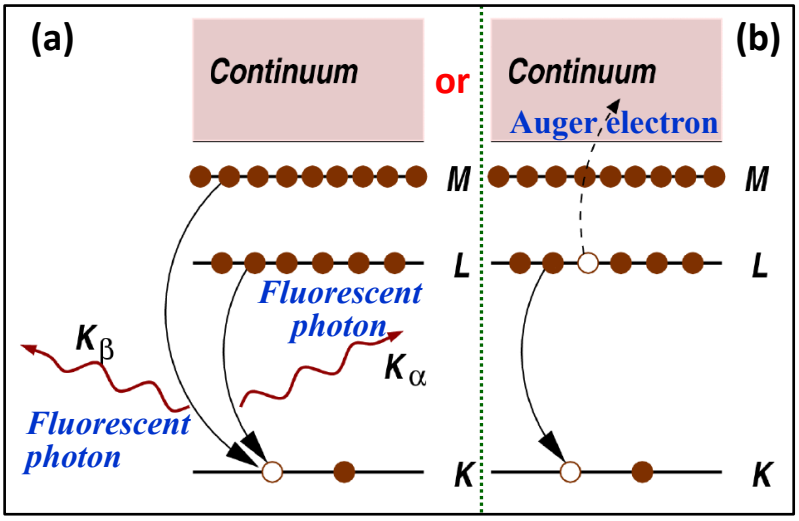

Figure-2.5: Decay of the excited state: (a) x-ray fluorescence and (b) the Auger effect. In both cases, the probability of emission (x-ray or electron) is directly proportional to the absorption probability.

these processes can be used to measure the absorption coefficient μ, though the use of fluorescence is somewhat more common. XAFS/XANES can be measured either in transmission or fluorescence geometries as shown in the inset of Figure 2.4. The geometry for Auger measurements is typically the same as for fluorescence, except the position of detector, as in fluorescent mode it is at at a right angle to the incident beam (Figure 2.6) unlike to transmission mode, where, the detector is placed inline with the beam (inset of Figure 2.4). The fluorescence is emitted isotropically, whereas the other scatter is actually not emitted isotropically because the x-rays from a synchrotron are *polarized*. The polarization means that elastic scatter is

greatly suppressed at 90 degree, thus in fluorescence mode, detectors are normally placed at a right angle to the incident beam to the

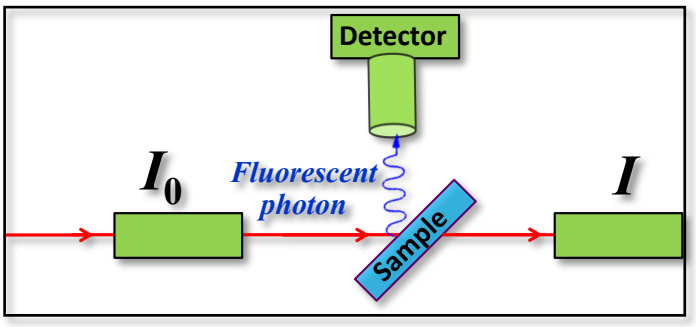

Figure-2.6: Schematic of XAFS/XANES setup in fluorescence mode; fluorescence detector at a right angle with the incident x-ray beam.

incident beam, in the horizontal plane. Eventually, the energy dependence of the absorption coefficient $\mu(E)$ can be measured either in transmission as

$$\mu(E) = \log(I_0/I) \qquad (2.6)$$

or in x-ray fluorescence mode as

$$\mu(E) \propto (I_f/I_0) \qquad (2.7)$$

where, I_f is the monitored intensity of a fluorescence line (or, again, electron emission) associated with the absorption process. For present research work, Mn/Fe K-edge XANES measurements were performed in fluorescence geometry to determine the charge state of Mn/Fe as the charge state determination by means of XANES is already being used [105–108].

2.2.4 Dielectric and magnetodielectric (MD) measurements

The main objective of present research work is to study the coupling between electrical polarization and magnetic ordering for the material under investigation. This can be achieved by measuring the change in electrical polarization upon the application of a magnetic field, or alternatively indirectly by measuring the change in the capacitance upon the application of a magnetic field. The dielectric susceptibility χ, of a material is related to the electrical polarization by $dP/dE = \varepsilon'.\chi$.

Thus, the slope of a plot of P vs E is proportional to the dielectric constant of the material, via $\varepsilon'=1+\chi$, which is proportional to capacitance. The capacitance of a dielectric in parallel-plate geometry (Figure 2.7) is defined as

$$C = \varepsilon_0 \varepsilon' (A/d) \qquad (2.8)$$

where ε_0 is the permittivity of free space, ε' is the dielectric constant, A is the area of the contact plates, and d is the thickness of the sample (Figure 2.7). The dielectric constant is a unitless quantity.

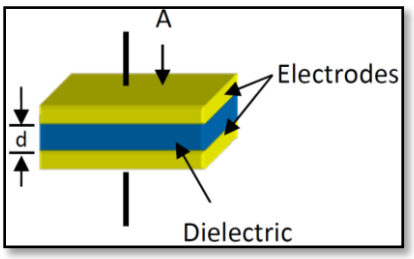

Figure-2.7: Schematic of parallel plate capacitor geometry.

2.2.4.1 Experimental arrangement

For present research work, the experimental arrangement used to record the dielectric and MD response is depicted in Figure 2.8.

LCR meter: All the dielectric and MD measurements were performed by means of a precision impedance analyzer (LCR meter)-6500B of Wayne Kerr company (marked as 1 in (a); Figure 2.8) with a measurement accuracy of ±0.05%.

Electromagnet: For MD measurements an electromagnet capable to exert a maximum magnetic field of 2 tesla at a pole to pole separation of 1 cm (shown in (c) and marked as 2 in (a); Figure 2.8) was used. A regulated power supply (lower box in (d)) and a gauss meter (upper box in (d)) are equipped to produce and measure the magnetic field. The gauss meter is equipped with a Hall probe (a red brown strip marked as 8 in (d)), which is used as a sensor to measure the strength of magnetic field around its position. It is to be noted that a Hall probe contains an indium compound semiconductor crystal such as *indium*

antimonide, mounted on an aluminum backing plate, and encapsulated in the probe head.

Temperature controller: A cryogenic temperature controller-CTC100 (marked as 4 in (a); Figure 2.8) of SRS (stanford research systems) company was used to record the temperature dependent dielectric response under zero magnetic field (similar to Figure 1.7) and temperature dependent MD response (similar to Figure 1.9).

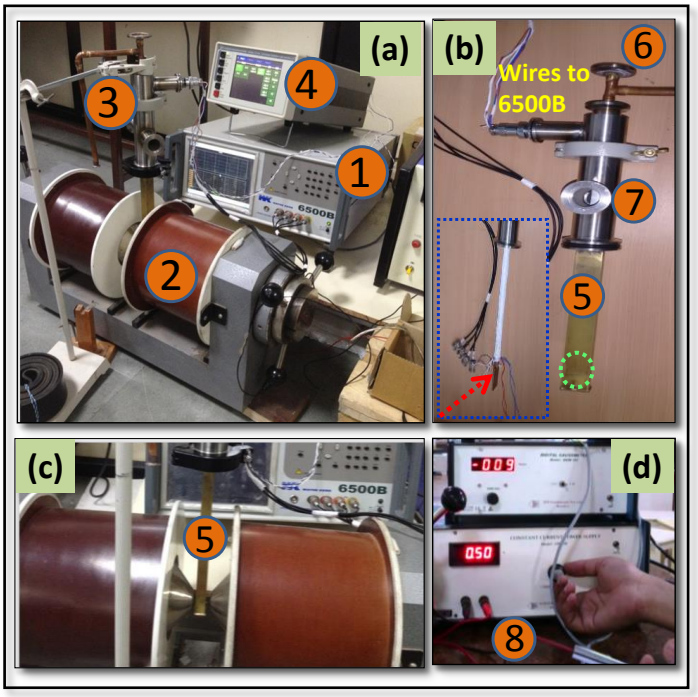

Figure-2.8: Experimental arrangement used for dielectric and MD measurements. Description of each marked part/equipment is given in main text.

Sample holder: A homemade (designed in our own laboratory) sample-holding assembly (marked as 3 in (a) and shown in (b) and (c); Figure 2.8) with the provision of cooling upto cryogenic temperatures and vacuum upto 10^{-3} mbar (or even lower), was used to place the sample. In Figure 2.8, the inset of (b) shows the sample holder which is kept inside a brass hollow rectangular box (marked as 5 in (b) and (c)). The sample is mounted by using silver paint at a Cu strip shown by the head of a dotted arrow in (b). The length of this sample holder is chosen such that when inserted in the rectangular hollow box (brass), the sample automatically finds its place (also marked by a dotted circle

in (b)) exactly in between the two poles of the electromagnet as shown in Figure 2.8 (c). The circular openings marked as 6 an7 in Figure 2.8 (b), are the pathways respectively for inserting the cooling agent (liquid N_2 for present research work) and creating vacuum in sample chamber.

In addition to above mentioned parts/equipments, a data acquisition unit, a liquid N_2 (nitrogen) container and a turbo Vacuum pump (Pfeiffer vacuum company), were also used for recording RT and temperature dependent dielectric/MD response.

2.2.4.2 Working

When a dielectric material is placed in an alternating electric field and its dielectric response is recorded through a LCR meter, a phase lag or lead may appear between the applied field (voltage) and the response (current) of the system depending upon the type of component (*capacitor* or *inductor*). It is to be noted that unlike to capacitive or inductive counterparts, a *resistor*, does not induce any phase shift between the applied voltage and measured current as illustrated (for ideal L, C, and R elements) in the top and bottom panel of Figure 2.9 and more elaborately in Figure 2.10 ((a) and (b) for ideal R and L). However, when an unknown element/material is kept in an alternating electric field, an arbitrary/unknown phase shift can be expected; an example of which is illustrated in Figure 2.10 (c). For present research work, sample is kept in parallel plate geometry as shown in Figure 2.7, with a difference that all the sample were circular in shape and hence the electrode plates on both the sides were also circular in shape as they were just coating of silver paint on both the faces of circular pellet. Note that in an impedance analyzer (LCR meter) the capacitance (indirectly ε')/impedance is recorded by measuring the

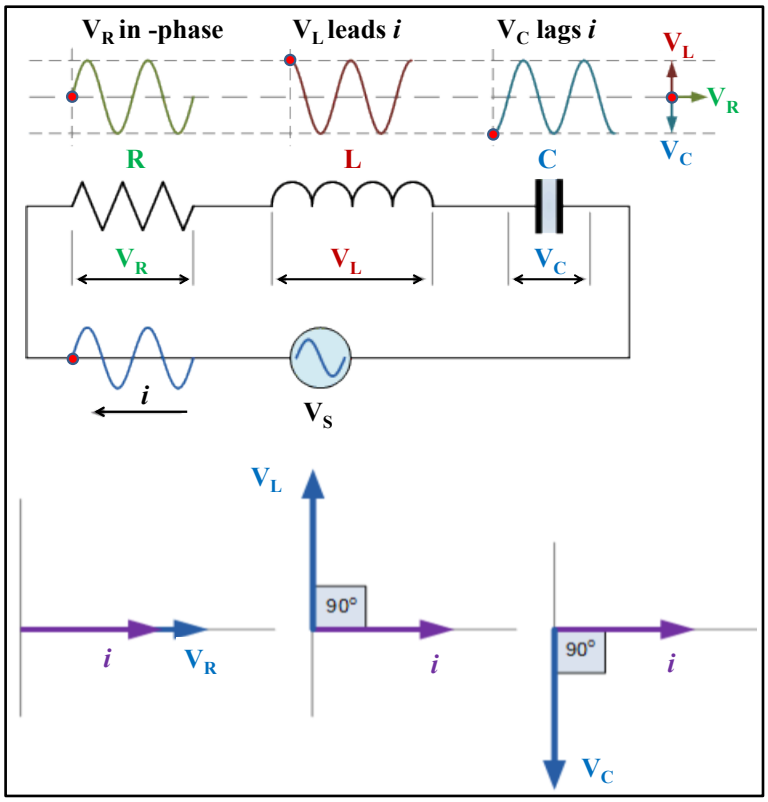

Figure-2.9: Schematic illustration of LCR circuit (middle panel) in association with the phase diagram between voltage and current individually for L, C and R (top and bottom panel).

above discussed phase shift. The basic theoretical formulation for these measurements is given below. The impedance in its standard definition means quotient of vector voltage and vector current calculated from small single sinusoidal measurement. When an *ac* signal is applied to a system, the impedance of the system obeys Ohm's law, as ratio of voltage to current in the time domain [109].

$$V(t) = V_0 \exp(j\omega t) \qquad (2.9)$$

$$I(t) = I_0 \exp(j\omega t - \phi) \qquad (2.10)$$

The impedance is a complex quantity, having both magnitude $|Z|$ & phase angle (ϕ) and expressed as

$$Z(\omega) = |Z| \exp(-j\phi) \qquad (2.11)$$

$$Z(\omega) = |Z| \cos\phi - j|Z| \sin\phi \qquad (2.12)$$

$$Z^* = Z' - jZ'' \qquad (2.13)$$

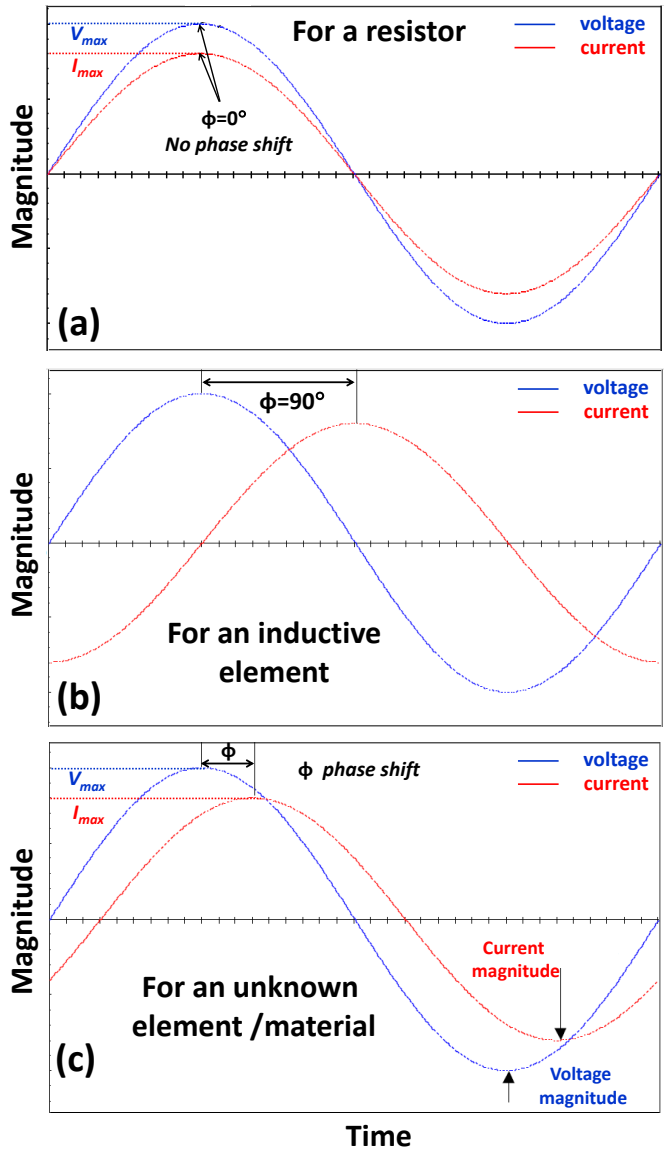

Figure-2.10: Examples of phase diagram between voltage and current, drawn individually for an ideal (a) resistive element, (b) inductive element and (c) for an unknown element/material.

where Z' and Z'' are the real and imaginary parts of complex impedance whereas j=√-1. In impedance technique, the real and imaginary parts of impedance for the sample under study are measured simultaneously as a function of frequency. The measured impedance data can be converted in the other three forms, using following conversion relations

$$\varepsilon^* = \varepsilon' - j\varepsilon'' = 1/j\,\omega\,C_0 Z^* \qquad (2.14)$$

$$\mathrm{Y}^* = \mathrm{Y}' + j\mathrm{Y}'' = 1/Z^* \qquad (2.15)$$

$$M^* = M' + jM'' = j\,\omega\,C_0 Z^* \qquad (2.16)$$

where ε^*, Y* and M* are complex permittivity, complex admittance and complex modulus respectively. ε' is the real or relative permittivity or dielectric constant, ε'' is the imaginary equivalent or dielectric loss. Similarly remaining quantities with a single prime are real whereas double primed ones are corresponding imaginary counterparts. C_0 is the vacuum capacitance (or capacitance of free space) and $\omega = 2\pi f$ is the angular frequency [109].

2.2.4.3 Dielectric response

As far as dielectric permittivity is concern, it is a characteristic of a short-range electrical conduction of a material under the influence of an applied electric field [109–112]. When a field (or voltage V) is applied across a material, it displaces the charges within the material and results in the accumulation of charge at the interface, creating dipoles with a moment p = Q.*dl*, where Q is the charge and *dl* is the separation distance between two charges. The capacitance *C* has following relations with voltage and dielectric permittivity

$$Q = CV \qquad (2.17)$$

$$C = C_0 \varepsilon' \qquad (2.18)$$

C_0, is the capacitance of free space (vacuum); measured when plates are separated by vacuum, and *C* is the capacitance of material measured by placing it between same plates. The capacitance *C* and sample dimensions are related as follows given by

$$C \propto A/d \qquad (2.19)$$

In a material, if field (or voltage V) varies with time, then the induced charge is given by

$$Q = \varepsilon^* V_0 \exp(j\omega t) \qquad (2.20)$$

The complex dielectric permittivity ε^* can be expressed also in terms of impedance [110,113] i.e,

$$\varepsilon^* = 1/j\,\omega\,C_0 Z^* \qquad (2.21)$$

Now, by uing equations 2.8, 2.14, 2.18, 2.19 and 2.21, one can write

$$\varepsilon' = (t/\omega A\varepsilon_0)\,[Z''/(Z'^2 + Z''^2)] \qquad (2.22)$$

$$\varepsilon'' = (t/\omega A\varepsilon_0)\,[Z'/(Z'^2 + Z''^2)] \qquad (2.23)$$

$$tan\delta = \varepsilon''/\varepsilon' \qquad (2.24)$$

Here, *tanδ* is called as loss tangent or sometimes dielectric loss. In accordance to 2.24, *tanδ* is defined as the ratio of lossy permittivity ε'' and lossless permittivity ε' (i.e., Energy lost per cycle/Energy stored per cycle) and is parametrized by an angle δ (in the permittivity/impedance complex plane) either between the permittivity vector and lossless permittivity axis (Figure 2.11 (a)) or between the capacitor's impedance vector and the negative reactane axis (Figure 2.11 (b)). It is obvious from above equations (2.22, 2.23 and 2.24) that

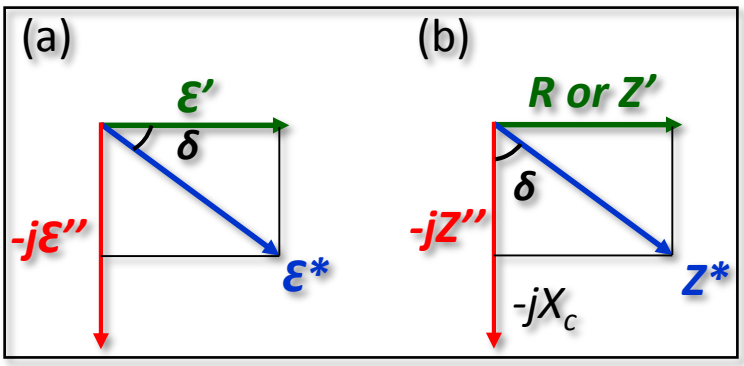

Figure-2.11: Dielectric permittivity and impedance complex planes; defining angle *δ*.

for a given material, the dielectric parameters ε', ε'' and *tanδ*, are determined by measuring impedance (or above discussed phase shift) by means of a LCR meter (impedance analyzer). A graphical comparison of frequency dependent response of ε', ε'' and *tanδ* for a given material is shown in Figure 2.12. Appearance of such an anomaly (peak) in ε' (ε'' or *tanδ*) is a signature of dielectric relaxation and it provides a hint that the material may exhibit temperature dependent dielectric dispersion. Moreover, such a diffusiveness (broadening) of ε' -anomaly (ε'' or *tanδ* peak) indicates distribution of relaxation time. This frequency dependent dielectric

behavior/relaxation is explained on the basis of following equations. The frequency dependent dielectric function can be written as following Cole-Cole relation [57,110,114]

$$\varepsilon(\omega)^{*} = \varepsilon'_{\infty\infty} + \frac{\varepsilon'_{s} - \varepsilon'_{\infty}}{1+(i\omega\tau)^{1-\alpha}}; 0 \le \alpha \le 1 \qquad (2.25)$$

where, ε_s' and ε'_∞ are the values of the dielectric constant in the low-frequency (static) and high-frequency limit respectively, ω is the angular frequency, τ is the mean relaxation time and ε^* is the complex permittivity. The change ε_s'-ε'_∞=$\Delta\varepsilon'$ is the strength of dielectric relaxation and α is the exponent parameter which is a measure of relaxation broadening (i.e., sharpness/diffusiveness in the step-like feature in ε' or broadening in ε'' or *tanδ* peak (Figure 2.12). α varies between 0 and 1; for α=0, Cole-Cole expression (2.25) reduces to following *Debye* relation [110,114]

$$\varepsilon(\omega)^{*} = \varepsilon'_{\infty} + \frac{\varepsilon'_{s} - \varepsilon'_{\infty}}{1+i\omega\tau} \qquad (2.26)$$

In terms of real and imaginary parts,

$$\varepsilon' = \varepsilon'_{\infty} + \frac{\varepsilon'_{s} - \varepsilon'_{\infty}}{1+\omega^{2}\tau^{2}} \qquad (2.27)$$

$$\varepsilon'' = \frac{(\varepsilon'_{s} - \varepsilon'_{\infty})\omega\tau}{1+\omega^{2}\tau^{2}} \qquad (2.28)$$

and

$$\tan\delta = \frac{\varepsilon''}{\varepsilon'} = \frac{(\varepsilon'_{s} - \varepsilon'_{\infty})\omega\tau}{(\varepsilon'_{s} + \varepsilon'_{\infty}\omega^{2}\tau^{2})} \qquad (2.29)$$

These equations (4.27- 4.29) also, are known as *Debye* equations. In Figure 2.12, the sudden increase in ε' with decreasing frequency can be attributed to the contribution of charge accumulation at the sample--electrode interface [110,114]. This leads to a net polarization of the ionic medium, which contributes to ε'. Whereas at high frequencies, the periodic reversal of the field takes place so rapidly such a way that no charge accumulation takes place at the sample electrode interface,

resulting in almost constant ε′ value [110,114–120] as depicted in Figure 2.12 (a).

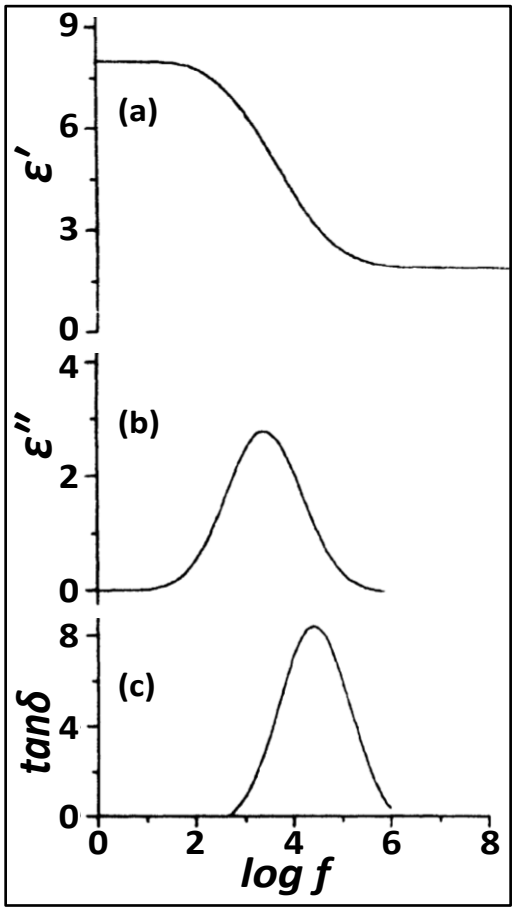

Figure-2.12: Response of dielectric parameters (a) *ε′*, (b) *ε″* and (c) *tanδ* as function of frequency for an ideal material (*Debye* relaxation) [110,114].

In Figure 2.12 (b), ε″ exhibits a maximum at ω=2πf = 1/τ, where the oscillating charges are coupled with the oscillating field and absorbs a maximum electrical energy. In Figure 2.12 (c), *tanδ* as a function of frequency exhibits symmetric *Debye* behavior with a loss tangent maximum at its characteristic frequency f_{max}, where $\omega\tau = (\varepsilon_s'/\varepsilon'_\infty)^{1/2}$ [121]. In practice, many materials exhibit a non-*Debye* dielectric behavior characterized by a broader asymmetric loss peak and by a constant loss tangent at a frequency higher than the loss peak, where the relaxation effects of the sample begin. Cole-Cole, Davidson-Cole and empirical expression proposed by Havriliak-Negami, could describe the non-*Debye* behavior of the material [122–124].

2.2.4.4 Impedance complex plane

The complex plane analysis is a mathematical technique involving real & imaginary parts of the complex electrical quantities like complex impedance (Z^*), complex admittance (Y^*), complex permittivity (ε^*) and complex modulus (M^*). In present research work complex plane (Nyquist plot or Cole-Cole plot) for only impedance has been analyzed to detect the contribution of magnetoresistance (MR) in the observed MD response. The complex impedance spectrum of a system in Figure 2.13 shows semicircle intersecting the real axis at a point R and origin. This complex impedance spectrum can be fitted with an equivalent circuit consisting of a parallel combination of R and C as shown in the same Figure. It is to be noted that such a spectrum can be expected in a systems having no effect/contribution of grain boundaries (GB) and sample-electrode interface i.e., space charge polarization (SCP). In practice, for a polycrystalline material, generally two or three semicircular arcs are appeared in the Z'-Z'' plot. If SCP contribution is

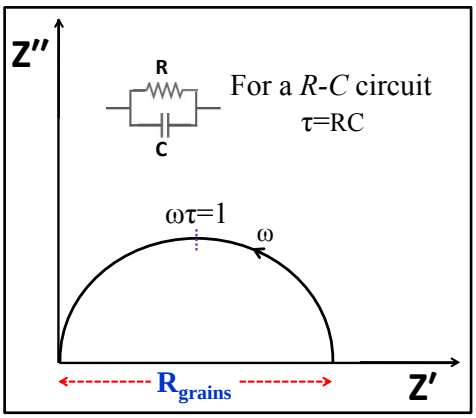

Figure-2.13: Impedance Nyquist plot for an ideal system with only grains contribution. This Z'-Z'' data can be fitted by using a parallel R-C circuit, shown in the Figure. Since the semicircular arc is not depressed and has only a single curvature throughout, therefore a *Debye* type relaxation can be expected for this material.

completely absent and the polycrystalline sample has well defined grain boundaries then only two semicircular arcs, each with a single curvature, are expected; out of that higher frequency semicircle is accounted for grain (bulk) contribution whereas the low frequency

semicircle for GB contribution. If SCP is also contributing for the same material then ideally three semicircular arcs, each with a single curvature, should be appeared. In such a case, semicircle corresponding to higher probing frequencies represents grains contribution, semicircle corresponding to mid-range of probing

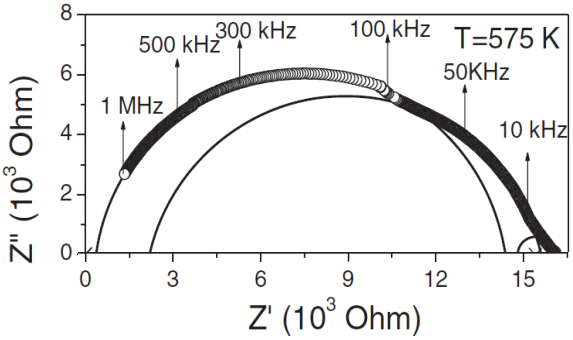

Figure-2.14: Cole-Cole plot of complex-impedance ($Z^*=Z'-Z''$) at 575 K in the frequency range of 100 Hz to 1 MHz. Symbols are experimental data points, while the smooth semicircular arcs are the fitted depressed semicircles [71].

frequencies represents GB contribution whereas the semicircle corresponding to lower range of probing is accounted for SCP contribution. The difference of x-axis intersects of corresponding semicircular arc gives the value of resistance associated with particular contribution (grains, GB and SCP); in Figure 2.13, R_{grains} represents the resistance corresponding to bulk/grains. In Z'-Z'' semicircle a depression may also appear, which indicates a deviation from *Debye* relaxation [110,114] for that case. In some cases depressed semicircles with two or more curvatures are also appeared; an example of which is reported by Singh *et al.* [71] as depicted in Figure 2.14. In such situations fitting or even simulation of Z'-Z'' data becomes mandatory to identify the frequency segments corresponding to specific contributions (i.e., grains, GB and SCP).

2.2.5 Micro Raman spectrometer

Jobin-Yvon Horiba micro Raman spectrometer was used for Raman measurements. The micro-Raman spectrometer setup consists of - an argon ion laser as light source, spatial filters, microscope and sample compartment, a monochromator (to disperse the signal into its

constituent wavelengths), CCD (charge coupled device) detector, instrumental control and acquisitions unit as shown schematically in the Figure 2.15. Details of the all these components used in the present study are discussed in the following Sections.

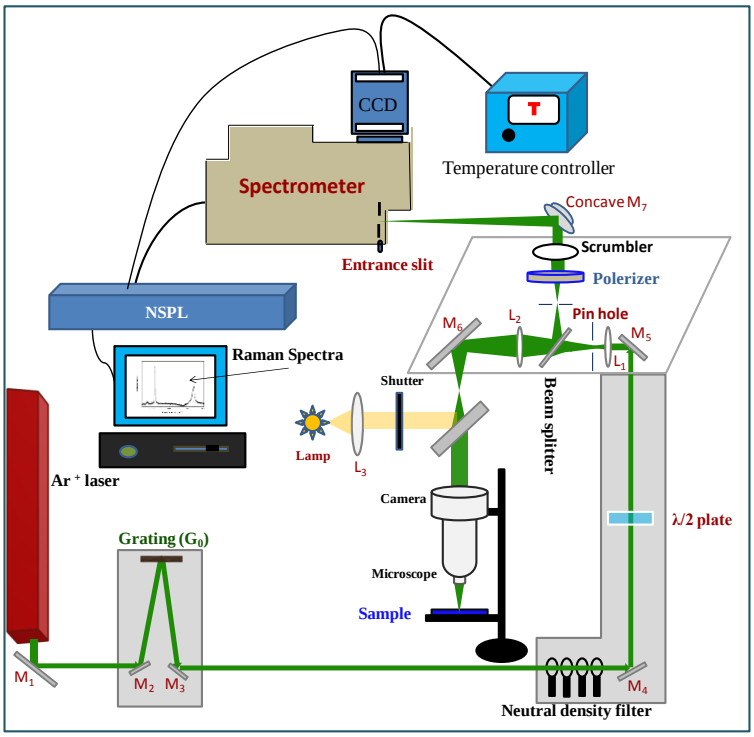

Figure-2.15: Block diagram of the major components in a micro-Raman spectrometer setup.

2.2.5.1 Laser and spatial filters

An argon-ion laser (Coherent Innova 90-5 model) was used as an excitation source for Raman scattering experiments. Laser emission was accompanied by many false spontaneous emission lines originating in the plasma discharge, known as plasma lines, which must be eliminated to avoid interference with the Raman emissions. Therefore, a laser-filter monochromator with a band pass of 1.0 nm (and transmission of 75 %) was used to eliminate the undesired plasma lines. This consists of grating (G0), mirror M1 and mirror M2 as shown in Figure 2.15.

2.2.5.2 Microscope and sample compartment

The Raman setup is equipped with BX40 microscope; three planoachromatic objectives (10X, 50X and 100X) were provided. Other objectives with lower magnification can be used without a correct aperture adaptation which might introduce some vignetting effect. With the microscope, incident and scattered optical axis are identical i.e. back scattering geometry. The operator has just to place a sample under the objective of the microscope and brings it to focus with the help of the TV camera. In this manner, the elastic radiation remains outside this range, in fact, that is the main purpose of the pre-monochromators. The polychromatic radiation selected by the pre-monochromators is dispersed by the grating of the spectrograph and is directed by mirrors to the lateral exit of the spectrograph. The T64000 is equipped with three holographic 1800 grooves/mm gratings, defining a mechanical range of 0-950 nm.

2.2.5.3 CCD detector and data acquisition

A charge-coupled device (CCD) detector, air cooled by Peltier effect down to about 215K, is used to offer the highest performance to the system. Spectrometer is controlled by LabSpec software. The computer controlled scan range, integration time, scan speed and different scan units are available with the software.

2.2.6 Magnetic measurements

For present research work, the temperature dependent magnetic state of the sample i.e. magnetization versus temperature (M-T) data as well as field dependent magnetic response (*M-H*) at a fixed temperature has been recorded using superconducting quantum interference device (SQUID) vibrating sample magnetometer (VSM) of Quantum Design. Working principle of a SQUID VSM is briefly described below.

SQUID VSM: A conventional VSM is based on the Faraday's laws of induction to measure the magnetic moment of a sample. In VSM, a magnetic sample vibrates inside a detection coil in the presence of

magnetic field. Consequently, due to the change in flux through the coil the voltage of coil changes. This change in voltage is proportional to the magnetic moment of the sample. Schematic of VSM is shown in Figure 2.16. On the other hand, principle of SQUID is based on the change in the persistence current in a superconducting detection circuit due to change in flux in the detection coil by magnetic moment of the sample. This change results in voltage variation in the SQUID output which is proportional to the moment of the sample. The SQUID is a very sensitive magnetometer and it can detect magnetic moments as low as

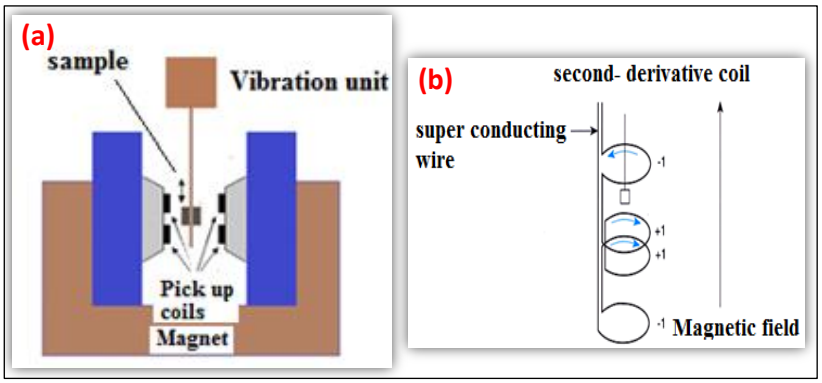

Figure 2.16: Principle of (a) VSM magnetometer and (b) SQUID [125–127].

10^{-7} emu [125–127]. Interestingly, a SQUID VSM combines the high sensitivity of conventional SQUID magnetometer and fast scan speed of a VSM. The major components of a SQIUD VSM are:

Superconducting Magnet: The magnet is in the form of a solenoid and constructed in the form of a close superconductor loop. Once the loop is charged up to a critical current the magnet can be used in a persistent mode without the need of external power source [125–127].

Superconducting detection unit: This is the most important and sensitive part of the magnetometer. It consists of a single superconducting wire which is wound in a second order gradiometer geometry containing three set of coils (Figure 2.16 (b)).

Sample space and Temperature controller: The sample space is a tube of 9 mm inner diameter. The temperature is controlled precisely by means of a temperature controller in association with a heater and

two thermocouples placed at the bottom of the sample space. The SQUID VSM can be operated from 2K to 450 K. However, high temperature susceptibility measurements up to 1100 K can be performed by using a VSM oven option [125–127]. In present research work, following magnetic measurements were performed on the bulk samples.

(a) Temperature dependent Magnetization (*M-T* measurements): *M-T* measurements are important for observation of different magnetic phase transitions and for finding the corresponding transition temperature. These measurements can be performed in two modes. (i) Zero Field Cooled (ZFC) measurement; in this mode, the sample is cooled to the lowest available temperature and the magnetic moment is measured in presence of a low magnetic field (like 100 Oe) while heating the sample. (ii) Field Cooled (FC) measurement; in this mode, the sample is cooled to the lowest temperature in the presence of a fixed magnetic field and the moment is measured under heating cycle again in the same field.

2) Magnetization Isotherm (*M-H* measurement): At a constant temperature magnetization is measured as a function of applied magnetic field. This measurement gives information about the magnetic state and hysteresis behavior in high fields at that particular temperature.

Important Note:- The basic information about all experimental details related to present research work has been provided in this chapter. Further and more specific details about synthesis of samples (synthesis parameters like name and formula of reactants) and characterization techniques are discussed accordingly in the '*experimental*' section of each forthcoming chapter.

2.3 XRD data and selection of specific LG(M/F)O compositions

For present research work, two series namely $LaGa_{1-x}Mn_xO_3$ (LGMO) and $LaGa_{1-x}Fe_xO_3$ (LGFO); x=0 to x=1 with a step of 0.1, were prepared by solid state reaction method. As a representative of both the series (LGMO and LGFO), XRD data for LGMO series is shown in Figure 2.17, whereas the corresponding representative refined powder XRD patterns for polycrystalline samples of $LaGa_{0.8}Mn_{0.2}O_3$ and $LaGa_{0.4}Mn_{0.6}O_3$ are depicted in Figure 3.1(chapter 3). Similar XRD

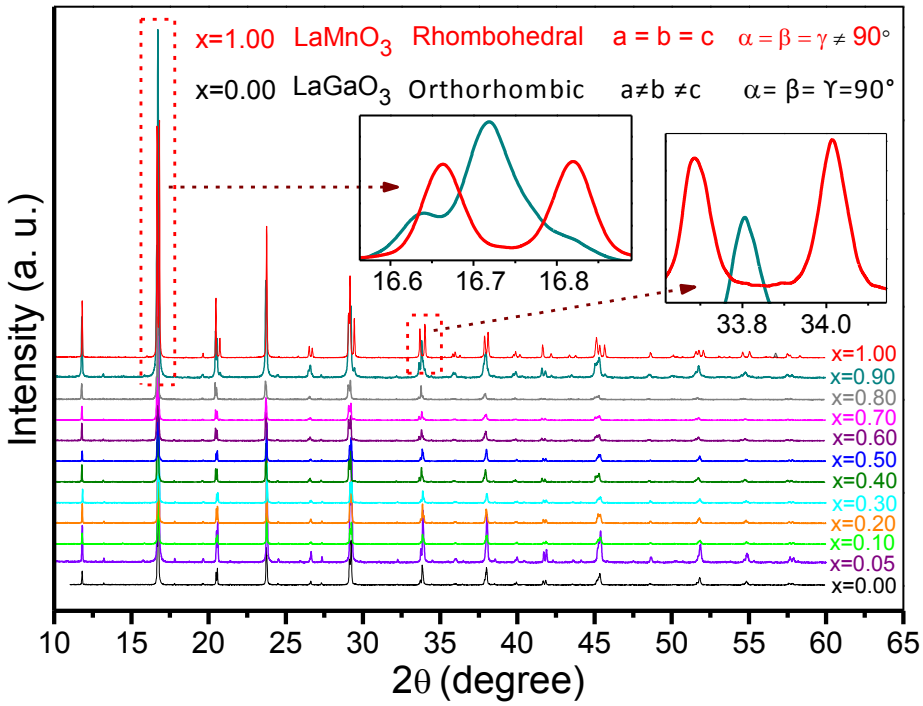

Figure 2.17: X-ray diffraction (XRD) data for $LaGa_{1-x}Mn_xO_3$ (LGMO) series recorded at the Indus-2 synchrotron radiation source. Insets show the magnified view of selected peaks (2θ ranges) indicating a structural phase transition (orthorhombic to rhombohedral) at and beyond x=0.9. Note- as representatives of LGMO series, Rietveld refined XRD patterns of $LaGa_{0.8}Mn_{0.2}O_3$ and $LaGa_{0.4}Mn_{0.6}O_3$ powder samples are shown in Figure 3.1(chapter 3).

data for LGFO series is shown in Figure A-2, as unpublished results (Appendix A-III), whereas the corresponding representative refined powder XRD pattern for polycrystalline sample of $LaGa_{0.7}Fe_{0.3}O_3$ is depicted in Figure 5.1(chapter 5). The XRD patterns for all LG(M/F)O samples were refined with the help of FullProf package by considering

orthorhombic structure with *Pnma* space group. The absence of any unaccounted peak in the refined XRD pattern (see the refined XRD patterns for representative LG(M/F)O compositions in Figure 3.1 and 5.1), confirms the phase purity of all the samples. In LGMO, a structural transition from orthorhombic to rhombohedral symmetry is taking place for x≥0.9, as can be seen from Figure 2.17 and its insets. Note that Lawes *et al.* [67] pointed out that MD response may appear significantly near structural transition. Thus for compositions x≥0.9, a significant MD effect can be expected. However, when the loss tangent (*tanδ*) of all LG(M/F)O has been measured the lowest value of *tanδ* is found for x=0.2 composition in case of LGMO samples whereas for x=0.3 composition in case of LGFO samples. Since for MD effect to be used at device level the loss (*tanδ*) of that material should be as low as possible. Thus among all prepared LG(M/F)O samples only $LaGa_{0.8}Mn_{0.2}O_3$ and $LaGa_{0.7}Fe_{0.3}O_3$ were mainly probed for MD purpose as the value of *tanδ* for all other compositions is too high. However, despite the large value of *tanδ,* a specific LGMO composition i.e., $LaGa_{0.4}Mn_{0.6}O_3$, was also probed from MD perspective, because, across Ga:Mn ratio of 60:40/40:60, in $LaMn_{1-x}Ga_xO_3$, two different phases (orbitally, disordered *O-phase* and ordered *O′*-phase) appears within the *Pnma* orthorhombic structure [20,21]. Ultimately, only three samples namely, $LaGa_{0.8}Mn_{0.2}O_3$, $LaGa_{0.4}Mn_{0.6}O_3$ and $LaGa_{0.7}Fe_{0.3}O_3$ were selected / probed for rest of the other investigations.

Chapter 3

Observation and Analysis of Room Temperature Magnetodielectric Effect in $LaGa_{1-x}Mn_xO_{3+\gamma}$ (x=0.2 and 0.6)

In this chapter, an observation of room temperature (RT) magnetodielectric (MD) effect in $LaGa_{0.8}Mn_{0.2}O_{3+\gamma}$ (LGM2O) and $LaGa_{0.4}Mn_{0.6}O_{3+\gamma}$ (LGM6O) is presented. The observed MD effect has been analyzed (by considering the pair of neighboring Mn^{3+} and Mn^{4+} as a local dipole) in terms of trends of magnetic field dependent change of dielectric constant (ε')/capacitance (C) and loss tangent ($tan\delta$). The coexistence of Mn^{3+} and Mn^{4+} (or oxygen excess) has been validated through titration and XANES analysis. The excess of oxygen has been understood by means of density functional theory (DFT) based first principles calculations. Results presented in this chapter are published in peer reviewed journals.[*†]

[*] *H.M. Rai et al., J. Mater. Chem. C* **4** *(2016) 10876-10886.*
[†] *H.M. Rai et al., Mater. Res. Express* **2** *(2015) 096105-096112.*

3.1 Introduction

As discussed in chapter 1, Magnetoelectric (ME)/ magnetodielectric (MD) materials are of very high research interest due to their potential possible applications and interesting physics [1,3–6,8,9,16,45,95,128–131]. The ME effect i.e., intriguing coupling of magnetization (electric polarization) with external electric field (magnetic field), opens new possibilities in microelectronic storage systems. The intriguing MD coupling and its underlying physics [1,9,27,48,67,132] endorse the suitability of MD materials for different technological applications such as multistate memory devices, non-volatile memories, spintronic devices (magnetic read heads, tunnel junction spin-filtering etc), magnetically modulated/spin-charge transducers, ultrafast optoelectronic devices tunable filters, magnetic sensors, etc. [1,4,7,39]. Observation of MD effect has been reported in different single phase materials [13,25,43,58,59]. But, this effect is witnessed with the application of high magnetic field of the order of several tesla [13,25,43,58,59] and/or below room temperature (RT). For example - 3% (change in ε') with H = 0.2 T below 30 K in $Tb_3Fe_5O_{12}$ [61], 13% at 0.5 T and 10 K in $Y_3Fe_5O_{12}$ [60], 1% in $CaMn_7O_{12}$ at 10 K [59], at 25 K in $EuMnO_3$ [63], at 230 K in CuO [62], at 28 K in $TbMnO_3$ [13], and also in other MD materials [1,57,65,66]. However, for MD effect to be used in above-mentioned devices, only low magnetic field MD materials, which exhibit this effect near/at RT are important. Recently, RTMD effect (~3% change in ε' due to the application of magnetic field of ~0.9 T) has been reported in 'Z-type hexaferrite - $Sr_3Co_2Fe_{24}O_{41}$' which is a polycrystalline ceramic sintered in oxygen [19]. This RTMD effect has been observed at a probing frequency of 100 kHz (as only grain contribution is expected at such high frequencies) and its origin has been attributed to the cycloidal spiral spin arrangement [19].

As far as intrinsic MD coupling is concern, ideally it can be realized in a material with magnetically switchable net electric dipole

moment and such systems are barely formed [11]. Nonetheless, it can be achieved by making a compound which expands/shrinks in response to an externally applied magnetic field as the ε' or ultimately capacitance *C*, is directly related to sample's dimensions by following relation-

$$C \propto \frac{A}{d} \qquad (3.1)$$

where, *C* is the capacitance of a dielectric material, *A* the area and *d* is he thickness of dielectric. By keeping this alternative in view, for present work, $LaGaO_3$ (LGO) is doped with Mn at Ga site with an expectation of RT (near RT) MD coupling because, the strain evolved due to significant difference in Ga-O (1.97 Å) and Mn-O (2.18Å long bond/(1.90Å short bond) distances [94], is supposed to be magnetically switchable as the field can retransform/rerotate Mn spin moments and hence the Mn-orbitals (magnetic field induced re-rotation of spin coupled Mn-orbitals is possible, as in such systems spin and orbital degrees of freedoms are strongly coupled with each other). This magnetically switchable rerotation/retransformation of Mn-orbitals may result into shrinking/expanding of material (*A*/*d*, in relation (3.1)) and hence, may result in an intrinsic MD effect. For present research work, $LaGaO_3$ (LGO) compound has been chosen as a host matrix to realize RTMD coupling by means of TM doping.

3.2 Experimental

Polycrystalline samples of $LaGa_{1-x}Mn_xO_3$ (LGMO) with x=0.2, and 0.6 have been prepared through conventional solid-state reaction route by following the process described in section **2.1.1** (chapter 2). Specifically, La_2O_3 (99.999%), Ga_2O_3 (99.999%), and MnO_2 (99.99%) were used as starting materials. These starting reactants were mixed in proper stoichiometric amount and grounded thoroughly with Propanol as a mixing medium. The resulting homogenous mixture was calcined in air ambient at 850 ^oC, 1050 ^oC, and 1200 ^oC each time for 24 hours

and final sintering was carried out at 1400 ^{o}C in air for 24 hours with intermediate grindings. It has already been mentioned (section **2.3**) that LGMO sample with x=0.2 and x=0.6 were selected purposefully, because x=0.2 LGMO composition exhibits lowest loss tangent (*tanδ*) among all Mn doped LGO samples, whereas, across Ga:Mn ratio of 60:40/40:60, in $LaMn_{1-x}Ga_xO_3$, two different phases (orbitally, disordered *O-phase* and ordered *O′*-phase) appears within the *Pnma* orthorhombic structure [97,98]. It may be interesting to check the MD response across such a circumstance because in that situation (transformation from *O* to *O′* phase) the cell volume (or strain) is supposed to be changed significantly. Thus, significant MD effect can be expected in LGMO sample with x=0.6. Additionally, for $LaMn_{1-x}Ga_xO_3$, the compositions with x=0.2 and x=0.6, have already been reported as distinctly composed of symmetric (x=0.6) and asymmetric (x=0.2) octahedral geometries respectively [97]. The purity of structural phase for all the prepared samples is validated by using x-ray diffraction (XRD) experiments carried out at BL-12 XRD beam line on Indus-2 synchrotron radiation source using Huber 5020 diffractometer in angle dispersive mode. XRD data is refined by using FullProf Rietveld refinement package [101,133]. For further measurements (using the methods and techniques described in chapter 2), these single phase powdered samples were pelletized at a pressure of 15 ton to form 1 mm thick circular discs of 12 mm diameter. These pellets were sintered in air at 1400 $^{\circ}$C for 24 hours. After being coated with silver paint these pellets were fired at 300° C for 30 min. For all as prepared pellets, RT capacitance is measured in the absence and presence of magnetic field by means of a precision impedance analyzer. These measurements were performed by applying an oscillator voltage of ±1 V and the data was recorded for probing frequencies ranging from 20 Hz to 10 MHz (1 MHz) for LGMO with x=0.2 (x=0.6). The direction of applied field (H) was kept along the applied electric field to ensure the complete absence of contributions, which, may arise in MD measurements due to Hall-effect geometry. Further, to understand the

observed MD response iodometric titration (section **2.2.2**) and XANES measurements (section **2.2.3**) have been performed. Specifically, for titration, sodium thio-sulphate ($Na_2S_2O_3.5H_2O$) solution is used as titrant whereas the analyte (LGMO) is dissolved in HCl solution and KI is added in that solution to get an end point as a result of redox. The titrant (in Burette) is added drop by drop in the Analyte+HCL+KI solution until it becomes colorless i.e., end point (Figure 2.3). The end point is confirmed by using starch as an indicator. The volume of used titrant is recorded and the value of γ (amount of excess oxygen) is determined by using normality relation, equation 2.3 and equation 2.4 (section **2.2.2**). The Mn K-edge XANES spectra were carried out on ~1 mm thick circular pellets in the fluorescence mode using Vortex energy dispersive detector (VORTEX-EX) at BL-9, Scanning EXAFS Beamline of Indus-2 synchrotron radiation source at the RRCAT (Raja Ramanna Centre for Advanced Technology) Indore, India[134]. The beamline consists of Rh/Pt coated meridional cylindrical mirror for collimation and Si (111) based double crystal monochromator (DCM) to select excitation energy. The energy range of DCM was calibrated using standard Fe foil. Fe K-edge XANES data normalization and self-absorption correction were processed using ATHENA software[135] Moreover, in order to understand the presence of mixed charge state of Mn in present LGMO samples, DFT (density functional theory) based first principles calculations have also been performed by using Vienna Ab initio simulation package–'VASP' (computational methodology along with results is discussed in detail in the forthcoming section **3.3**).

3.3 Results and discussion

Here, before presenting the RTMD response, structural phase purity along with the validation and understanding of coexistence of Mn^{3+} and Mn^{4+} (oxygen access) in LGMO samples is discussed to prepare the background for describing the MD behavior.

3.3.1 XRD

Figure 3.1 (a) and (b) shows the refined powder XRD pattern for polycrystalline samples of $LaGa_{0.8}Mn_{0.2}O_3$ and $LaGa_{0.4}Mn_{0.6}O_3$

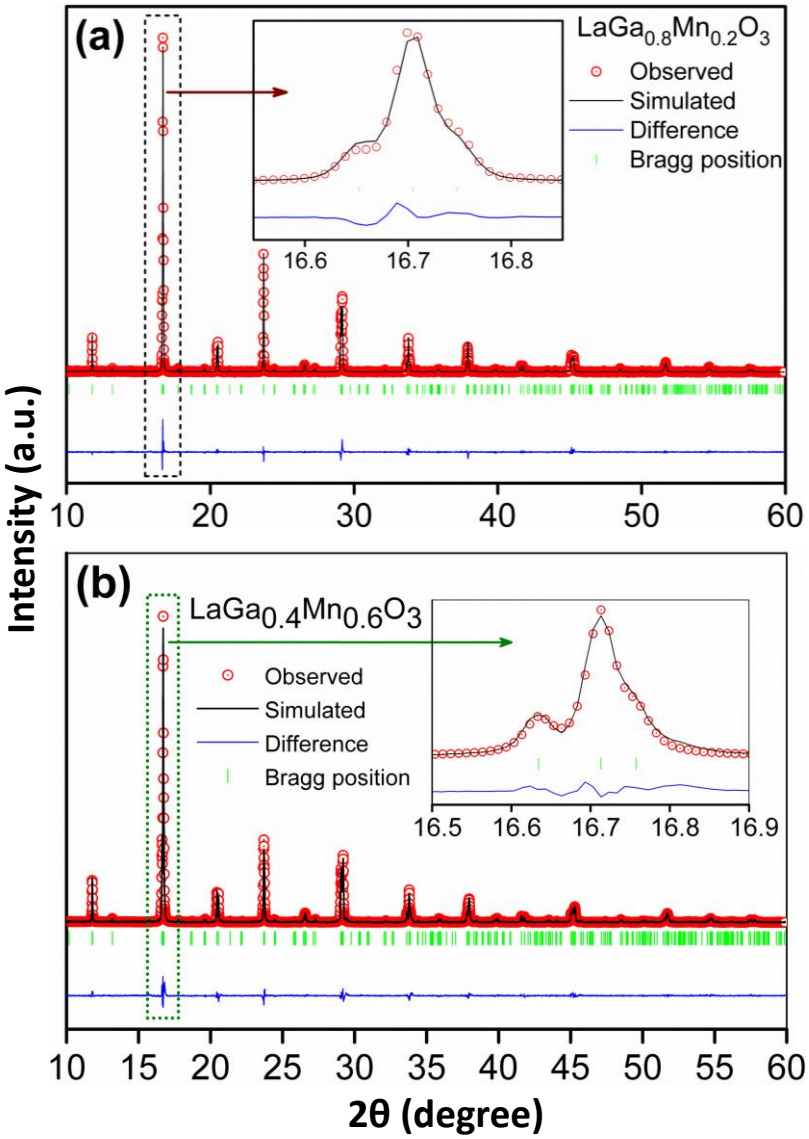

Figure 3.1: Rietveld refined X-ray diffraction data of (a) $LaGa_{0.8}Mn_{0.2}O_3$ and (b) $LaGa_{0.8}Mn_{0.2}O_3$ powder samples recorded at the Indus-2 synchrotron radiation source. Inset shows magnified view of most intense peak; reflecting the quality of fitting.

respectively. These XRD patterns were refined with the help of FullProf package by considering orthorhombic structure with *Pnma* space group. The value for the goodness of fit (i.e., χ^2) was found to be ~1.5 for both the samples. The absence of any unaccounted peak in the refined XRD pattern, confirms the phase purity of these samples.

3.3.2 Iodometric titration

In order to check the oxygen stoichiometry of presently studied $LaGa_{0.8}Mn_{0.2}O_3$ and $LaGa_{0.4}Mn_{0.6}O_3$ samples, iodometric titration experiments [136] have been carried out. Presently studied both LGMO compounds were found to be oxygen off-stoichiometric with an excess of oxygen i.e., $LaGa_{0.8}Mn_{0.2}O_{3+\gamma}$ and $LaGa_{0.4}Mn_{0.6}O_{3+\gamma}$, because gamma ($\gamma$) has been found to be positive as calculated by using the well-known equation of normality ($N_1V_1=N_2V_2$). The value of γ in $LaGa_{0.8}Mn_{0.2}O_{3+\gamma}$ ($LaGa_{0.4}Mn_{0.6}O_{3+\gamma}$), has been estimated as 0.15 (0.042). By using the value of γ in charge neutrality condition, the charge state of Mn and percentage of Mn^{3+} and Mn^{4+} in $LaGa_{0.8}Mn_{0.2}O_{3.015}$ (LGM2O), has already been calculated in an example under section **2.2.2.1.** Whereas for $LaGa_{0.4}Mn_{0.6}O_{3.042}$ (LGM6O), the same has been calculated as following

(i) Mn Charge state (say x)

For LGM6O sample, by charge neutrality condition,

$$La^{3+}Ga^{3+}_{0.4}Mn^{x}_{0.6}O^{2-}_{(3+\gamma)} = La^{3+}Ga^{3+}_{0.4}Mn^{x}_{0.6}O^{2-}_{(3+0.042)} = 0$$

Here, x is the charge state of Mn in LGM6O sample and $\gamma = 0.042$ (by titration),

Thus,

$$(3\times1)+(3\times0.4)+0.6x+(-2\times3.042)=0$$

$$3+1.2+0.6x-6.084=0$$

$$4.2+0.6x-6.084=0$$

$$0.6x-1.884=0$$

$$x=\frac{1.884}{0.6}$$

$$x=3.14$$

Thus, through iodometric titration, the charge state of Mn in LGM6O sample is found to be 3. 14.

(ii) Percentage of Mn^{3+} and Mn^{4+}

For LGM6O sample, by charge neutrality condition,

$$LaGa_{0.4}Mn_{0.6}O_{(3\pm\gamma)} = La^{3+}Ga^{3+}_{0.4}Mn^{3+}_{0.6(1-x)}Mn^{4+}_{0.6x}O^{2-}_{(3\pm\gamma)}$$

Here, x is the amount of Mn^{4+} in the total Mn present in the sample.

Since, through titration experiment the value of γ is found to be 0.042, therefore, according to charge neutrality condition

$$La^{3+}Ga^{3+}_{0.4}Mn^{3+}_{0.6(1-x)}Mn^{4+}_{0.6x}O^{2-}_{(3+\gamma)} = La^{3+}Ga^{3+}_{0.4}Mn^{3+}_{0.6(1-x)}Mn^{4+}_{0.6x}O^{2-}_{(3+0.042)} = 0$$

$$(3\times1)+(3\times0.4)+[3\times0.6(1-x)]+(4\times0.6x)+(-2\times3.042)=0$$

$$3+1.2+1.8-1.8x+2.4x-6.084=0$$

$$6+0.6x-6.084=0$$

$$0.6x-0.084=0$$

$$x=\frac{0.084}{0.6}$$

$$x=0.14$$

Thus in LGM6O, Mn^{4+} is 14% out of total Mn present in the sample whereas remaining 86% is Mn^{3+}. In this way, the charge state of Mn along with percentage of Mn^{3+} and Mn^{4+} in LGM2O and LGM6O has been calculated and summarized in Table 3.1.

Table 3.1: Charge state of Mn, amount of excess oxygen and percentage of Mn^{3+} and Mn^{4+} in $LaGa_{0.8}Mn_{0.2}O_{3+\gamma}$ and $LaGa_{0.4}Mn_{0.6}O_{3+\gamma}$ estimated through iodometric titration.

Sample Name	Mn charge state	value of γ	% of Mn^{3+}	% of Mn^{4+}
$LaGa_{0.8}Mn_{0.2}O_{3+\gamma}$	3.15	0.015	85	15
$LaGa_{0.4}Mn_{0.6}O_{3+\gamma}$	3.14	0.042	86	14

The coexistence of Mn^{3+} and Mn^{4+} in LGM2O and LGM6O is evident from above Table 3.1.

3.3.3 XANES

This coexistence of Mn^{3+} and Mn^{4+} has been supported through XANES measurements (as the charge state determination by means of XANES is already being used [105–108]) carried out at Mn K-edge energy of 6539 eV and the obtained data is plotted in Figure 3.2 for LGM2O as a representative of LGMO samples. The energies

corresponding to absorption edge of - pure Mn metal foil (Mn^0) and powders of MnO (Mn^{2+}), Mn_2O_3 (Mn^{3+}) and MnO_2 (Mn^{4+}) have been used as references/standards. The oxygen stoichiometry of powders

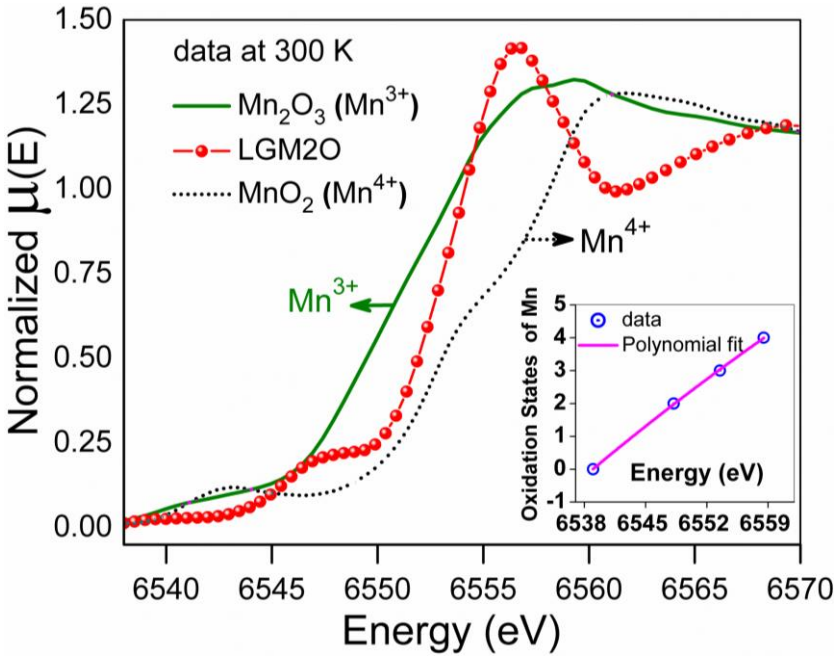

Figure 3.2: Mn K-edge XANES spectra of LGM2O along with Mn^{3+} and Mn^{4+} standards. To clearly visualise the position of LGM2O absorption edge relative to 3+ and 4+ standards, the XANES data of Mn metal foil (Mn0) and Mn^{2+} standard is not shown. Inset shows oxidation states of Mn references (i.e., 0, 2+, 3+ and 4+) as a function of the corresponding K-edge energies.

(standards) has been validated through iodometric titration before using them as standards. XANES measurements for all these standards along with LGM2O and LGM6O samples are performed with same experimental settings at RT. Figure 3.2 compares the normalized XANES spectra of LGM2O with Mn^{3+} and Mn^{4+} references. With an obviously noticeable chemical shift, absorption edge of LGM2O sample is found to be situated between Mn^{3+} and Mn^{4+} which points towards the presence of mixed Mn charge states [105–107] in this LGM2O sample. The absorption edge (K-edge) energies of Mn metal foil (Mn^0), MnO (Mn^{2+}), Mn_2O_3 (Mn^{3+}), MnO_2 (Mn^{4+}) and LGM2O are determined by plotting the first derivative of the corresponding absorption μ(E) versus energy E curves [137] as shown in Figure 3.3 for LGM2O (as a representative). The value of energy corresponding

to first maximum (exclude the one corresponding to pre-edge) on this first derivative curve gives the position of the inflection point and hence the position of the absorption edge [137].

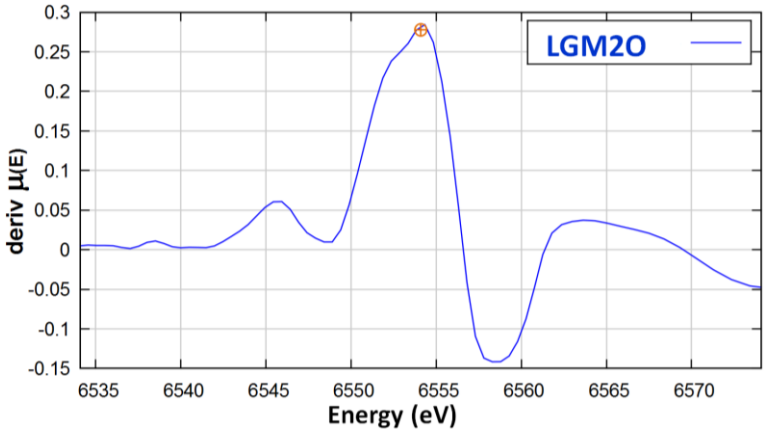

Figure 3.3: Estimation of absorption edge energy; first derivative of *μ(E)-E* curve for LGM2O sample. The energy coordinate of small circle represents corresponding K-edge energy.

The calculated K-edge energy of LGM2O is found to be greater (less) than that of the Mn_2O_3 i.e. 3+ (MnO_2 i.e. 4+) indicating coexistence of Mn^{3+} and Mn^{4+} in LGM2O sample. In order to obtain a precise value of oxidation setae of Mn in LGM2O, the oxidation states of Mn references (i.e., 0, 2+, 3+ and 4+) are plotted as a function of corresponding K-edge energies as shown in the inset of Figure 3.2. This data is fitted with a 2nd order polynomial [105] and by using fitting parameters, oxidation state of Mn in LGM2O is estimated between +3 and +4 (i.e., 3.15), signifying the coexistence of Mn^{3+} and Mn^{4+}. In the same manner, the oxidation state of Mn in LGM6O was estimated as 3.14. By using this value of Mn oxidation state (e.g., 3.15 for LGM2O) in the following charge neutrality condition –

$$La^{3+}Ga^{3+}_{0.8}Mn^{3.15+}_{0.2}O^{2-}_{(3+\gamma)} = 0$$

$$(3\times1)+(3\times0.8)+(3.15\times0.2)-2\times(3+\gamma)=0$$

$$\text{OR} \qquad 3+2.4+0.63-6-2\gamma=0$$

$$\text{OR} \qquad 0.03-2\gamma=0$$

$$\text{OR} \quad \gamma = \frac{0.03}{2} = 0.015$$

the value of gamma (γ) for LGM2O is found to be 0.015, which is consistent with the titration results. Similar, consistency is found also for LGM6O. Ultimately, the value of Mn charge state and concentration of Mn^{3+}/Mn^{4+} (for LGM2O and LGM6O) determined through titration, have been found closely consistent with XANES results. The coexistence of Mn^{3+} and Mn^{4+} in present LGM2O and LGM6O samples is appearing due to oxygen off-stoichiometry (oxygen excess).

3.3.4 Origin of excess oxygen

We propose that the excess oxygen in LGM2O and LGM6O samples can be attributed to (i) oxygen adsorption at the surface [138,139] and/or (ii) vacancies at A (La) and/or B (Ga/Fe) cation sites considering ABO_3 structure [139,140]. The first situation is discussed in detail elsewhere for other ABO_3 structures [138,139]. In order to understand the second situation (vacancy at cation site) [139,140], we have determined the Bader charge on La, Mn, Ga and Oxygen ions using DFT (density functional theory) based first principles calculations. For this purpose, we have investigated 50% Mn-doped $LaGaO_3$ i.e., $LaGa_{0.5}Mn_{0.5}O_3$ (as for present LGM2O and LGM6O systems, 20% or 60% Mn doping involves large number of atoms whereas doping of 50% Mn is achieved only with 20 atoms in a supercell) system. We have used spin-polarized DFT calculations as implemented in the Vienna Ab initio Simulation Package (VASP) [141]. Projector augmented wave (PAW) method [142,143] is employed using an energy cut-off of 470 eV to describe the electronic wave functions. The local density approximation (LDA) + U method [144] is used to account the strong on-site correlated electrons in the partially filled *d* orbitals. We have employed correlation energy (U) of 4 eV and exchange energy (J) of 1 eV for Mn *d*-orbitals. These U and J values have been well tested and used in similar systems [145,146]. A

20 atom (2×2×1) supercell is considered to study pure and defected $LaGa_{0.5}Mn_{0.5}O_3$ system. The Monkhorst-pack [147] generated set of 7×7×7 (for 20 atoms supercell) K-points are used to optimize the structures. The convergence criteria for energy and force are set at 10^{-6} eV and 10^{-3} eV/Å respectively. We have calculated La, Ga and Mn defect formation energy in $LaGa_{0.5}Mn_{0.5}O_3$ system to understand that which cation-defect, among La, Ga and Mn, is most favorable. Figure 3.4 shows the structure with La-defect as a representative case.

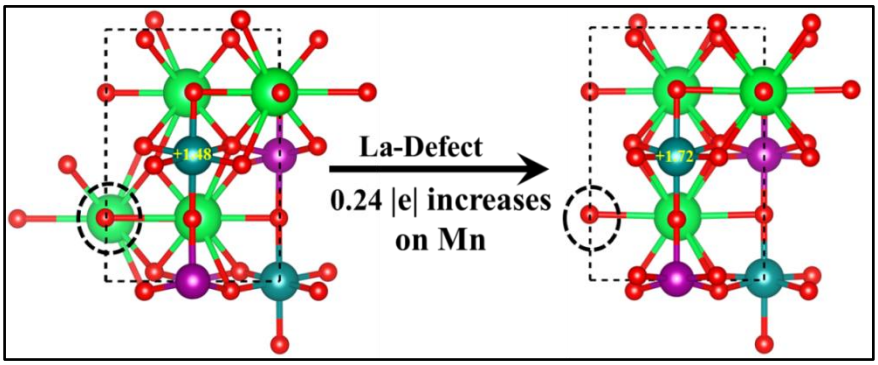

Figure 3.4: The change in Bader charge on Mn atom due to the La-defect in $LaGa_{0.5}Mn_{0.5}O_3$. Here, green, blue, purple and red colour balls denote La, Ga, Mn and O atoms, respectively.

The defect formation energy (E_f) is calculated using the following equation:

$$E_f = [E_D + E_\mu] - E_p$$

where, E_D and E_P represent total energies of defected and pure $LaGa_{0.5}Mn_{0.5}O_3$ systems. E_μ represents chemical potential of lanthanum (μ_{La}), gallium (μ_{Ga}) and manganese (μ_{Mn}) in their respective bulk structures. The chemical potential energy is calculated from their most stable crystal structure [148,149]. Present defect formation energy calculations reveal that La-defect (E_f = 1.02 eV) formation is energetically favorable compared to Ga (7.85 eV) or Mn defects which is consistent with the previous report [150]. Therefore, the La-defected structure is considered for the Bader charge analysis. The Bader charge analysis [150,151] is performed using the Henkelman programme

[152] with near-grid algorithm refine-edge method. From our Bader charge analysis, we find that Mn losses 0.24|*e*| (Table 3.2) due to the La-defect (Figure 3.4), whereas charges on other atoms are almost

Table 3.2: Average Bader charges (total electrons) on La defected $LaGa_{0.5}Mn_{0.5}O_3$ structure. Net effective charges (average) are given in parenthesis.

Pure (No defect)	Defect (cation vacancy)
La= 8.95 (+2.05)	La= 8.92 (+2.08)
Ga= 1.31 (+1.69)	Ga=1.32 (+1.68)
Mn = 6.51 (+1.48)	Mn = 5.28 (+1.72)
O = 7.21 (-1.21)	O = 7.09 (-1.09)

unchanged. Thus, Mn gains more positive charge due to the La-vacancy. In this way, the La-defect formation appears to be responsible for making the oxidation state of Mn more than 3+. Note that, this cation vacancy based theoretical analysis of excess oxygen is reasonable and neutron diffraction measurements will be very useful in its experimental validation because the oxygen excess in $LaMnO_{3.12}$ has already been studied by using neutron diffraction data [139,140] and explained in terms of cation vacancies [139,140].

3.3.5 Room temperature magnetodielectric (RTMD) response

Figure 3.5 and 3.6 shows the RT frequency dependence of ε'/capacitance along with MC% (defined in Figure 3.5 and 3.6) for LGM2O and LGM6O respectively. This data is recorded in the absence (H=0T) and presence (uoto H=0.4T for LGM2O and upto H=2.35T for LGM6O) of magnetic field. It is to be noted that the magnetocapacitance (MC) can be calculated in terms of ε' or simply capacitance *C* and generally it is parameterized as MC% or MD%. Here, we are using ε' for LGM2O whereas *C* for LGM6O and the used formula for MC% is given in the corresponding Figure (Figure 3.5 and 3.6). Note that similar frequency dependent dielectric behavior under zero magnetic field, is discussed in detail in the upcoming chapter 6 for $LaGa_{1-x}Mn_xO_3$ (x=0, 0.05, 0.1, 0.2 and 0.3) samples (section **6.3.3**). As far as present magnetic field dependent data is concern, for LGM2O

(LGM6O), the ε' (C) is found to be increased (decreased) over the entire range of probing frequencies due to the application of magnetic field as depicted in Figure 3.5 (3.6) and corresponding insets. Further, the MD effect is expected to be magnetoresistance (MR) free

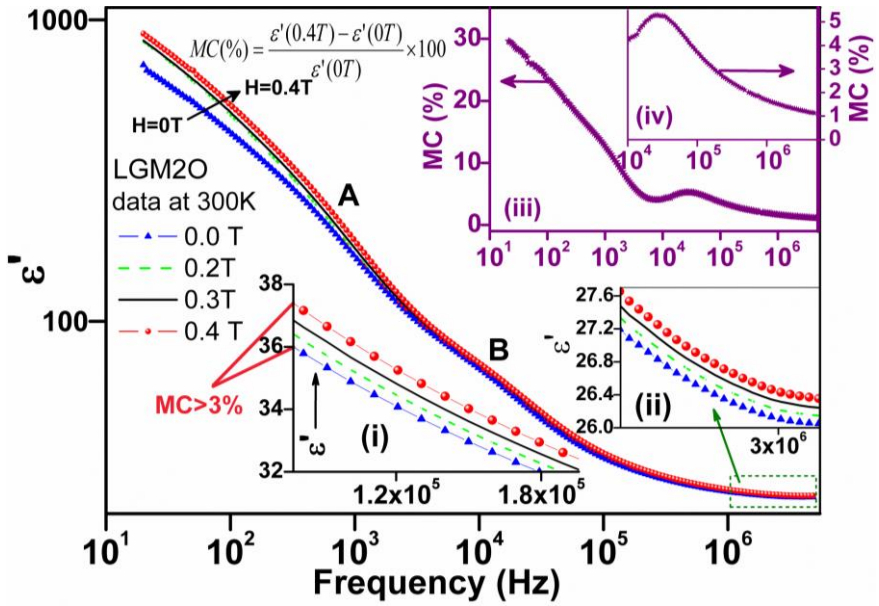

Figure 3.5: Room temperature dielectric constant (ε') as a function of frequency, measured in the absence (H=0T) and presence (upto H=0.4T) of magnetic field for LGM2O. Inset (i) and (ii) shows magnified view of data at corresponding frequency ranges. In the inset (iii), MC% is plotted as a function of frequency. The MC% been calculated by using the formula shown in the Figures. Where, ε' (0) and ε' (0.4 T) are the values of ε', recorded correspondingly in the absence (H=0 T) and presence of magnetic field (H=0.4 T). Inset (iv) shows the magnified view of MC% versus frequency data for clarity.

or intrinsic when it is measured at probing frequencies corresponding to grains contribution (generally at ≥ 100 kHz) [9,115]. Since, at such high probing frequencies, the hopping charge transport (common in perovskites having TM i.e., transition metal, ions with mixed valence) gets suppressed as the carriers have no chance to jump between hopping cites [9,115] (presently Mn^{3+} and Mn^{4+}), therefore, only grain contribution is expected over these high frequencies. This is the reason, the MD data recorded around 100kHz or higher frequencies, is generally emphasized [19,35,153,154] for MD analysis. In other words, an intrinsic MC/MD effect appears at probing frequencies

higher to characteristic/relaxation frequency (frequency range corresponding to broad *tanδ* peak or anomaly in ε'/C when plotted as a function of frequency) because at such high probing frequencies charge carriers do not have time to respond to applied ac electric field [1,9,10,35,46,68,71,75]. Thus, as far as the intrinsic nature

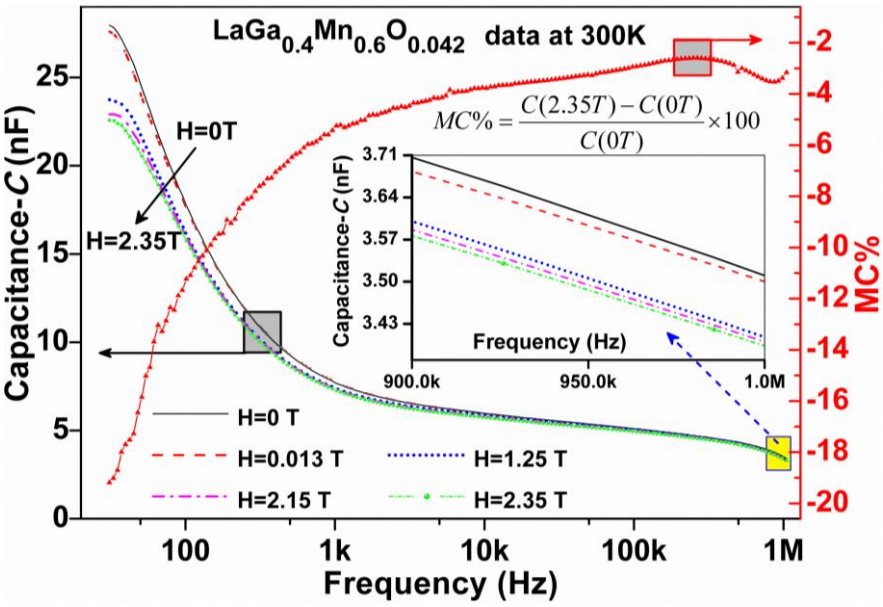

Figure 3.6: Room temperature capacitance *C* as a function of frequency (measured in the absence (H=0T) and presence (upto H=2.35T) of magnetic field) and magnetocapacitance (MC%) as a function of frequency. Inset shows the magnified view of data across 1MHz. MC% has been calculated by using the formula shown in the Figure. Where, *C*(0) and *C*(2.35 T) are the values of *C*, recorded correspondingly in the absence (H=0 T) and presence of magnetic field (H=2.35 T).

(intrinsicality) of MD coupling is concern, MC should be measureable at such high frequencies [9,35]. Presently, a significant RTMD effect (i.e., MC%) of about 3%/-3% is observed in LGM2O/LGM6O sample when measured at a probing frequency of 100kHz/1MHz (Figure 3.5/3.6 and corresponding insets). This MD behavior is consistent with the trends of frequency dependent MC% reported for other systems [29,35,71]. Presently observed MD effect is strong at low frequencies and significant even at higher probing frequencies as the MC% is ~1.8% for LGM2O (inset (iv) of Figure 3.5) and -3% for LGM6O (red curve in Figure 3.6) which is expected to be intrinsic as it has been

measured at high frequency [9,35]. Since MC% is positive/negative for LGM2O/LGM6O, presently observed MD effect can be MR affected only with negative/positive MR [9,46,128]. The magnitude of MC% (see insets (iii) and (iv) in Figure 3.5, and red curve in Figure 3.6) is comparable with the MD effect reported by others at same/lower probing frequency in different materials [19,46,47,59,155], but, with the application of equivalent [155]/relatively higher magnetic fields [19,46,47,59,155]. It should be noted that the presently observed MC%

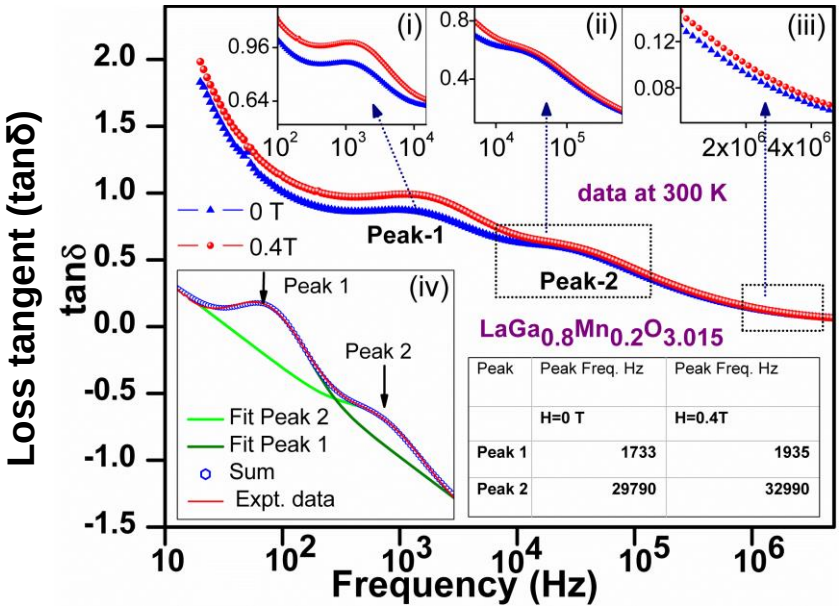

Figure 3.7: Room temperature frequency dependence of loss tangent (tanδ) recorded in the absence (H=0T) and presence (H=0.4T) of magnetic field for LGM2O. Insets (i) to (iii) show the magnified view of data across the corresponding range of probing frequencies. Inset (iv) shows the fitting of two broad peaks observed in *tanδ* to determine the shift of *tanδ*-peak(s) under the influence of magnetic field. The observed shift is summarized in the enclosed Table. *Note*- For clarity, data corresponding to H=0.2T and H=0.3T is not shown in the Figure, but it is in the trend with presented data.

is well above the sum of instrumental and statistical error bar, even at the highest probing frequency. Figure 3.7/3.8 shows the RT frequency dependence of loss tangent (*tanδ*) for LGM2O/LGM6O; the data was recorded in the absence (H=0T) and presence (upto H=0.4T)/(upto H=2.35T) of magnetic field. For clarity, data corresponding to H=0.2T and H=0.3T is not shown in the Figure 3.7, but, that data also follow the magnetic field dependent trend of increase in *tanδ* over the entire

range of probing frequencies. Two broad *tanδ*-peaks were observed for LGM2O as depicted in Figure 3.7 and indexed as peak-1 and peak-2. These characteristic *tanδ*-peaks are corresponding to the diffusive anomalies in ε' (indicated by A and B in the Figure-3.5) observed across the same

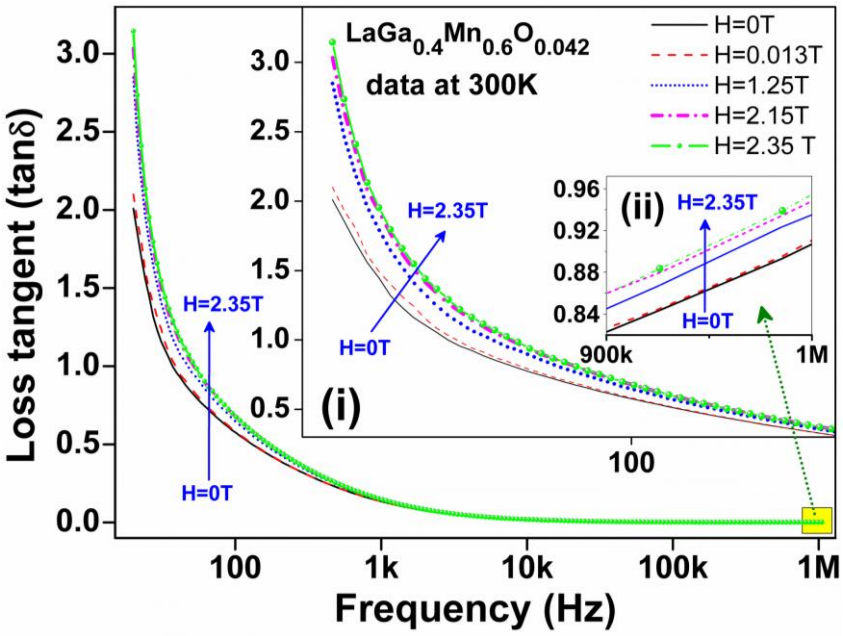

Figure 3.8: Room temperature frequency dependence of loss tangent (*tanδ)* recorded in the absence (H=0T) and presence (upto H=2.35T) of magnetic field for LGM6O. Insets (i) and (ii) shows the magnified view of data across low and high frequency range.

range of probing frequencies. These two peaks (diffusive anomalies) in tanδ (ε'), indicate the presence of two dielectric relaxation processes which might be corresponding to grain (peak-2) and grain boundary (peak-1) contributions as the similar peaks in Z″ versus frequency data have been assigned for such contributions by Kakarla et al. [156]. It may be interesting to explore these peaks in future from relaxation perspective. These relaxation loss peaks are possibly associated with the oxygen off-stoichiometry (coexistence of Mn^{3+} and Mn^{4+}) observed in LGM2O sample (section **3.3.2 and 3.3.3**) as the appearance of similar loss peaks has been attributed to oxygen vacancies in different systems [29,46]. Similarly, corresponding to a diffusive anomaly in *C* (Figure 3.6), an anomaly in *tanδ* is observed also for LGM6O (Figure

3.8). This *tanδ* anomaly (LGM6O) or *tanδ*-peak (LGM2O) is found to be shifted towards higher frequency due to the application of magnetic field. This effect is clearly visible for LGM6O (Figure 3.8 and its insets), whereas, observed clearly after fitting (inset (iv) and enclosed Table in Figure 3.7) for LGM2O. Additionally, over the entire range of probing frequencies, *tanδ* is found to be increased due to the application of magnetic field for both the LGMO samples (Figure 3.7, 3.8 and corresponding insets). This effect of magnetic field on frequency dependence of *tanδ* can be understood in the following manner-

The loss tangent can be expressed by following relation (derived from Maxwell's 4th equation of electromagnetism)

$$\tan\delta = \frac{\omega\varepsilon'' + \sigma}{\omega\varepsilon'} \qquad (3.2)$$

where, ω is the frequency of applied electric field and ε'' is the imaginary component of permittivity attributed to bound charge and dipole relaxation phenomena (associated with the dipolar oscillations), which gives rise to energy loss and hence also known as dielectric loss. This energy loss is indistinguishable from the loss due to the free charge conduction quantified by σ. The component ε' represents the lossless permittivity (dielectric constant). In presently studied LGM2O and LGM6O samples, coexistence of $Mn^{3+}$and Mn^{4+} has been evidenced (section **3.3.2 and 3.3.3**). A pair of neighbouring $Mn^{3+}$and Mn^{4+} ions connected via an intermediate oxygen ion at 180˚ provides a net localized dipole moment (p=charge x Mn-O distance) as the chemical potential (or charge) of Mn^{3+} (ionic radius is 0.64 Å)[157] is different from Mn^{4+} (ionic radius is 0.53 Å)[157] and hence 'Mn^{3+}-O-Mn^{4+}' (or simply 'Mn^{3+}- Mn^{4+}') can be considered as a localized dipole (as depicted schematically in Figure 3.9). This mismatch of chemical potential facilitates, electron hopping between neighbouring Mn^{3+} (say site X) and Mn^{4+} (say site Y) sites via Mn^{3+}-O- Mn^{4+} path. Now, we imagine following three situations for the distribution of such

dipoles – (i) There only one such pair of neighbouring $Mn^{3+}$and Mn^{4+} is present in the sample kept between two electrodes as shown in Figure 3.10 (a). In this case, after first jump from Mn^{3+} to Mn^{4+}, 'site X' becomes Mn^{4+} and 'site Y' becomes Mn^{3+}, therefore, electron hope

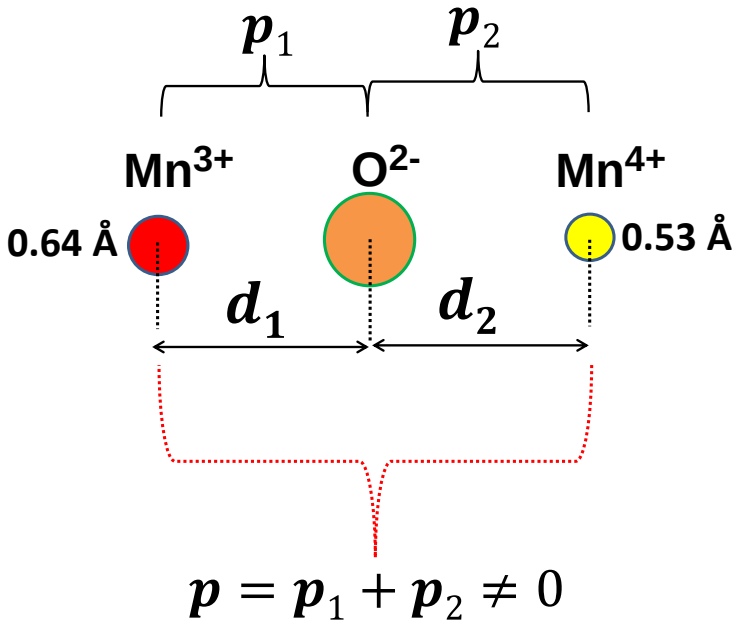

Figure 3.9: Schematic presentation of a pair of neighbouring Mn^{3+} and Mn^{4+} connected via oxygen ion forming 'Mn^{3+}-Mn^{4+}' dipole (net electric dipole moment ***p***) as the chemical potential (charge) and ionic radii of Mn^{3+} and Mn^{4+} are different.

back to 'site X' to make it 'Mn^{3+} and again to 'site Y' to do the same and so on i.e., 'Mn^{3+}- Mn^{4+}' dipole oscillates locally with some characteristic frequency due to charge (chemical potential) imbalance. When this frequency matches with the frequency of applied ac electric field, a sharp resonance peak is expected to be appeared in *tanδ* versus frequency plot. It is to be noted that in general, such a situation with only one pair is not possible to attain practically. (ii) When many such localized dipoles are present in the system (Figure 3.10 (b)) and each of them oscillates with its own characteristic frequency (owing to distinct local surrounding), a distribution of relaxation time τ ($1/f$) appears in the form of a broad *tanδ* peak as observed in case of LGM2O (peak-1 and peak-2 in Figure 3.7). Note that in case of LGM6O, such a broad *tanδ* peak is about to appear in the form of an

anomaly (as can be seen in Figure 3.8) and expected to be appeared at further low frequencies (<20 Hz). (iii) When there a complete chain of such dipoles is present throughout the material (as shown in Figure 3.10 (c) or in any random manner to allow the electron transport between electrodes; one such example is shown in Figure 3.10 (d)),

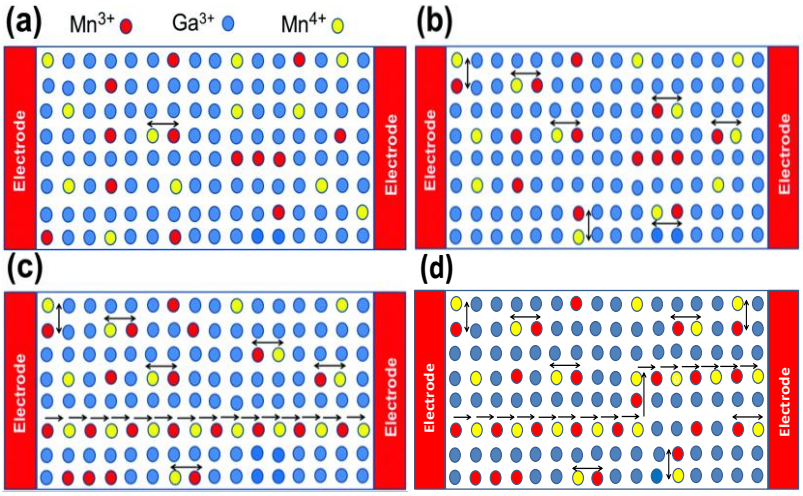

Figure 3.10: Schematic representation of main three possible distributions of 'Mn^{3+}/Mn^{4+}' dipoles within the material (LGM2O/LGM6O sample) sandwiched between two electrodes in parallel plate geometry. (a) There is only one local 'Mn^{3+}/Mn^{4+}' dipole. (b) Dipoles are arranged randomly in such a way that each diploe can oscillate (electron hopping between Mn^{3+} and Mn^{4+}) locally. (c) and (d) shows two examples of the possible arrangements of dipoles for electron transport; the 'Mn^{3+}/Mn^{4+}' dipoles form a series of consecutive pairs of Mn^{3+} and Mn^{4+} which allows electron transport between end electrodes by means of electron hopping via Mn^{3+}-Mn^{4+}- Mn^{3+} …… path. The double head arrow indicates a pair of Mn^{3+} and Mn^{4+} whereas as single head arrow shows the direction of electron transport. For simplicity lanthanum and oxygen ions are not shown whereas Ga^{3+}, Mn^{3+} and Mn^{4+} ions are represented by blue, red and yellow circular spots respectively.

electron transport takes place between the electrodes via electron hopping. Since, Mn^{3+} is a Jahn-Teller (JT) active/distorted ion [158] this electron transport can be termed as JT polaron transport/hopping because, when an electron hops from Mn^{3+} to Mn^{4+} ion, it carries JT distortion i.e. the octahedron around the donor (acceptor) Mn ion only shrinks (expands) as a whole, while its shape remains normal, mimicking the movement of breathing. It is important to note here, that, such electron transport is a matter of conduction percolation

threshold as discussed in detail by Krishnan et al.[159] in terms of double (Mn^{3+}–O–Mn^{4+}) and super exchange (Mn^{3+}–O–Mn^{3+}) interactions for $LaMn_{1-x}Al_xO_{3+\gamma}$. Now coming back to presently observed results, the magnetic field (H) facilitates this electron exchange further easier between $Mn^{3+}$and Mn^{4+} by making all the spins parallel to H. Consequently 'Mn^{3+}-Mn^{4+}' dipoles oscillate faster under H and hence the shifting of broad *tanδ* peaks or anomaly towards higher frequency (Figure 3.7 and 3.8) appears reasonable. Moreover, *tanδ* is also increasing due to H (Figure 3.7 and 3.8) which can be understood in terms of increased leakage associated with the above discussed charge (electron) transport (σ in equation 3.2).

3.4 Summary

In summary, following four major observations are noticeable from above discussed MD response (Figure 3.5 to 3.8)-

(i) A significant positive/negative RTMD effect is appearing even at high frequencies in both LGM2O/LGM6O. Note that MC% is positive/negative for LGM2O/LGM6O, thus, presently observed MD effect can be MR affected only with negative/positive MR [9,46,128].

(ii) According to the trend convention considered by Mao *et al.* [46], the same trend, i.e. both ε' and *tanδ* are increasing over the entire range of probing frequencies due to H, indicating that the observed low field RTMD effect should be an intrinsic property of LGM2O sample as the same is suggested [9]/pointed out [46]/shown [46,47,155] also by others. Whereas, in case of LGM6O the opposite trends of *C* (decreasing with H) and *tanδ* (increasing with H) indicate the dominance resistive contribution according to the trends convention in literature [9,46,47,155].

(iii) For LGM2O/LGM6O, the position of broad peak(s)/anomaly in tanδ is found to be shifted towards higher frequency due to the

application of magnetic field. Similar shifting is shown by G. Catalan for negative MR (90%) affected MD effect [9]. And

(iv) For both LGM2O and LGM6O, *tanδ* is increasing due to the application of magnetic field over the entire range of probing frequency, indicating a negative MR owing to increased leakage or conductivity (see equation 3.2).

In case of LGM2O, both *ε′* and *tanδ* are increasing with magnetic field indicating a MR free RTMD coupling (according to trends convention by Mao *et al.* [46]), but conversely, last two observations indicates the MR origin. Similarly, in case of LGM6O, according to trends convention by Mao *et al.* [46], the opposite trends of H dependent change in *C* and *tanδ* indicates MR affected MD coupling, whereas, negative MC% and so called negative MR (due to increased *tanδ* or conductivity σ) suggest the appearance of an intrinsic MD effect with the suppression of MR. Ultimately, as far as the consideration of trend convention (considering *ε′*/*C* and *tanδ*) [9,46] is concern, the observed trends are providing contradictory information. On the basis of above analysis, we proposed that "the contribution of MR in MD coupling should not be judged only on the basis of trends of H dependent change in *ε′*/*C* and *tanδ*". To further support our argument, RTMD effect observed in Fe doped $LaGaO_3$ has also been analyzed systematically and discussed in detail in chapter 5. Nonetheless, for LGM2O and LGM6O samples, a systematic and conclusive analysis to identify MR/intrinsic contribution is required for commenting concretely about the actual origin or mechanism responsible for the observed MD effect. Thus, to identify and validate the resistive/intrinsic contributions and to understand the origin of intrinsic MD coupling in LGM2O and LGM6O, an in depth and systematic analysis is given in chapter 4.

Chapter 4

Analysis of Resistive and Intrinsic Contributions: Magnetodielectric Effect in $LaGa_{1-x}Mn_xO_{3+\gamma}$ (x=0.2 & 0.6)

An observation of room temperature (RT) magnetodielectric (MD) effect in $LaGa_{0.8}Mn_{0.2}O_{3+\gamma}$ (LGM2O) and $LaGa_{0.4}Mn_{0.6}O_{3+\gamma}$ (LGM6O) has been presented in previous chapter 3. Present chapter provides an analysis of resistive contributions by means of *dc* (direct current) and frequency dependent magnetoresistance (FDMR) measurements. Our analysis reveals that at frequencies corresponding to bulk contribution (>10^5Hz), the MD effect is intrinsic for LGM2O whereas at lower frequencies (<10^5Hz) it is dominated by magnetoresistive artifacts. In case of LGM6O, the observed MD coupling is found to be intrinsic over the entire range of probing frequencies. The intrinsic nature of MD coupling has been validated by analyzing the magnetic field dependent Raman spectra. In LGM2O/LGMO6O sample, the observed MD effect has been attributed to magneto-compression/expansion associated with reorientation of spin coupled Mn-orbitals as evidenced in the form of magnetic field mediated hardening of symmetric stretching (*SS*) MnO_6 octahedral Raman modes. Results presented in this chapter are published (communicated).[‡§]

[‡] *H.M. Rai et al., J. Mater. Chem. C* **4** *(2016) 10876-10886.*
[§] *H.M. Rai et al., Adv. Mater. (communicated).*

4.1 Introduction

Magnetoresistance (MR) is always a major suspect responsible for magnetodielectric (MD) effect. Magnetoelectric (ME) coupling needs recording the effect of an electric field on magnetization or, conversely, that of a magnetic field on ferroelectric polarization. A difficulty arises in both of these situations, as many of the contenders (especially perovskites having transition metal (TM) ions with mixed charge states) for being magnetoelectrics are indeed poor insulators, which makes it difficult for them to sustain such a high electric field necessary for realizing the effect i.e. to switch (align) the polarization (dipoles) [1,9,16,33–35]. By keeping this in view, a relatively simple and widely accepted alternative method is used; in which, capacitance (C) or ε' is measured as a function of applied magnetic field (H). The intrinsicality of magnetocapacitance (MC)/MD effect observed through this indirect approach, is always a major concern, because, in many materials, it appears without any intrinsic ME coupling [1,9,29,128,160–163]. Generally, in such systems, MC arises due to extrinsic artifacts like- MR [1,9,29,128,160–163]. In this regard, through some excellent theoretical modelling, G. Catalan [9] provided a way to judge the intrinsicality of MD effect which has been accepted widely [1,4,10,29,35,46,68,71,75,128,154,160–164]. Catalan has suggested that measuring MR (considering dc measurements), provides sufficient information about resistive origin of MC [9]. Whereas, others [46,128] have suggested that the trends of H dependent change in ε'/C and $tan\delta$ can provide the information about MR free (both ε'/C and $tan\delta$ change in same trend) or MR affected (ε'/C and $tan\delta$ change oppositely) [46] MD effect.

However, in practice, MC/MD measurements are performed by applying an electric field with varying frequency upto MHz or even higher range [1,4,10,29,35,46,68,71,75,128,154,160–164]. Thus, measuring only dc MR is not an effective way to check and validate MR contribution as the frequency of applied electric field is crucially

important in MD measurements. Additionally, our analysis (Chapter 3) on MD effect in $LaGa_{0.8}Mn_{0.2}O_{3+\gamma}$ (LGM2O) and $LaGa_{0.4}Mn_{0.6}O_{3+\gamma}$ (LGM6O), suggests that only trends of H dependent change in ε'/C and $tan\delta$ are not sufficient to judge the resistive origin of MD effect. Therefore, the MD effect observed in these LGMO samples, has been examined by systematically analyzing dc MR and frequency dependent MR (FDMR). Our analysis reveals that the FDMR measurements are more effective than that of measuring only dc MR or only analyzing the trends of H dependent change in ε'/C and $tan\delta$ and hence should necessarily be employed to check and validate the resistive contribution of MC. Further, magnetic field dependent Raman spectra have been analyzed to validate the intrinsic nature of MD effect.

4.2 Experimental

In addition to the experimental details discussed in section **3.2**, MR measurements (dc MR) were performed in the absence and presence of magnetic field in standard four-probe geometry using nano voltmeter and source meter. Frequency dependent MR (FDMR) measurements (i.e., magnetic field dependent change in real and imaginary parts of impedance), on circular pellets of LGM2O and LGM6O, were performed by means of a precision impedance analyzer. These measurements were performed by applying an oscillator voltage of ±1 V and the data was recorded for probing frequencies ranging from 20Hz to 10MHz for LGM2O and upto 1MHz for LGM6O. The direction of applied magnetic field was kept along the applied electric field to ensure the complete absence of contributions, which, may arise in MD measurements due to Hall-effect geometry. The magnetic field dependent RT Raman spectra on highly dense LGMO pellets were recorded from 300 to 1200 cm^{-1} by using a Horiba Lab RAM high-resolution (~0.4 cm^{-1}) micro Raman spectrometer in confocal mode equipped with 30 mW air cooled He-Ne laser (632.8nm) as the excitation source and a charge-coupled device (CCD) detector. The

spectra were recorded by using 50x standard objective with a spot size of ~5 μm whereas the laser power was kept at 15 mW.

4.3 Results and discussion

This section is divided into three parts; first part presents the analysis of resistive origin (MR contribution) by means of dc and FDMR studies. In second part an evidence of intrinsic nature of observed RTMD effect (chapter 3), in the form of magnetic field dependent Raman spectra, has been presented. In third part, the mechanism responsible for intrinsic RTMD (for LGM2O and LGM6O) is discussed.

4.3.1 *dc* MR and impedance spectroscopy (FDMR):Analysis of resistive (MR) contribution

In order to examine that whether the presently observed MD effect (chapter 3) is MR dominated or it is completely MR free, firstly, RT dc MR has been recorded for both LGMO samples by means of *I-V* measurements as plotted in the Figure 4.1. According to the observed

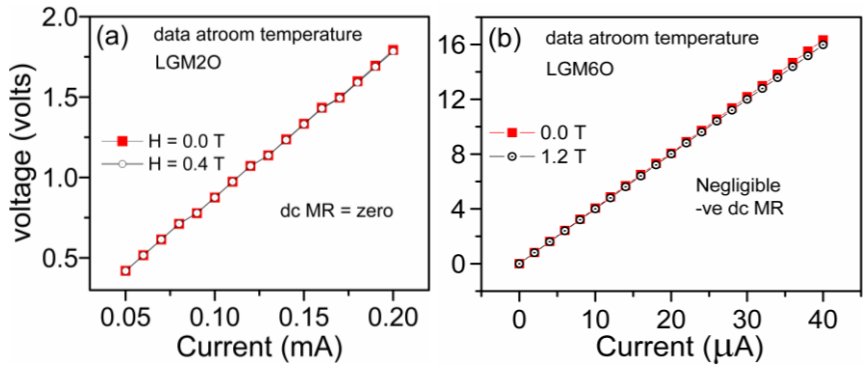

Figure 4.1: Room temperature current-voltage (*I-V*) graph of LGM2O (a)/ LGM6O (b), plotted by measuring the voltage for different currents in the absence (H=0T) and presence (H=0.4T/H=1.2T) of magnetic field using the four-probe method. This data reveals that there is no significant negative dc magneto resistance (MR) is present in either LGMO sample.

RTMD response, negative dc MR is expected in LGM2O whereas for LGM6O the situation was contradictory (observations (i) to (iv) discussed in section **3.4**). However, it is clearly evident from Figure

4.1 (a) and (b) that no significant dc MR is taking place either in LGM2O or inLGM6O. The absence of any significant dc MR indicates that the observed MD effect for both the investigated LGMO compositions is unaffected from dc MR. However, increase in *tanδ* and shifting of *tanδ*-peak (LGM2O) or *tanδ*-anomaly (LGM6O) due to magnetic field (Figure 3.7 and 3.8) indicates resistive origin [9]. These contradictory observations suggest that measuring only dc MR is not

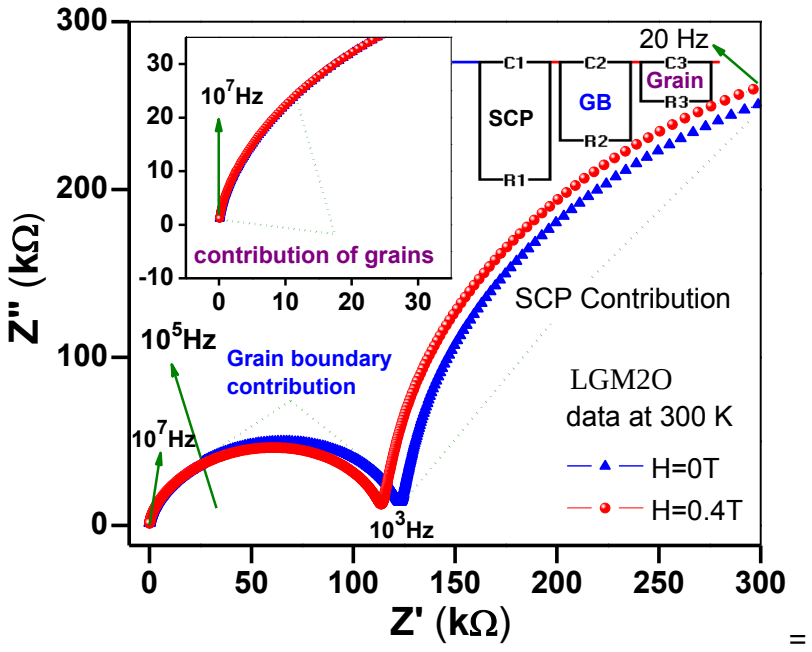

Figure 4.2: Room temperature Cole-Cole diagram of $LaGa_{0.8}Mn_{0.2}O_{3.015}$ (LGM2O) plotted for frequencies ranging from 20 Hz to 10 MHz. The data is measured in the absence (▲) and presence (●) of magnetic field. The inset shows that the impedance does not change due to magnetic field at high frequencies corresponding to grain contributions. Frequency segments corresponding to different contributions like, space charge polarization (SCP), grain boundary (GB) and grains are identified by fitting and simulating this data with the displayed circuit model. For clarity, data corresponding to H=0.2T and H=0.3T is not shown. *Note*- For convenience, the data on y-axis is multiplied by minus one.

sufficient to identify and validate the origin (resistive/intrinsic) of observed MD coupling. As we have already mentioned that the MD measurements are performed by applying an electric field with varying frequency upto MHz or even higher range [1,4,10,29,35,46,68,71,75,128,154,160–164], therefore, measuring FDMR is expected to be more useful than that of the *dc* counterpart.

Thus, to get a better insight about the contribution of MR in the observed MD effect, FDMR has been analyzed by means of MRIS (MR via impedance spectroscopy) measurements. These RT measurements for LGM2O/LGM6O were performed in the absence (H=0.0T) and presence of magnetic field (upto H=0.4T/2.35T) to record the real (Z′) and imaginary (Z″) part of impedance. For clarity, present impedance analysis has been divided into following two segments. First part covers the discussion on LGM2O, whereas in later part, results corresponding to LGM6O are discussed. The results of MRIS measurements for LGM2O are shown as a Cole-Cole (Nyquist) plot in Figure 4.2.

LGM2O: It is clear from Figure 4.2 that at the frequencies corresponding to space charge and grain boundary contributions i.e. at low and mid-range of probing frequencies ($<10^5$ Hz for LGM2O), the value of *Z′* (resistance) is decreasing significantly due to the application of magnetic field. This suggests that the large MD effect observed at these frequencies (Figure 3.5 and its insets) is FDMR affected/dominated in this range of probing frequency (20 Hz to $<10^5$ Hz). This frequency dependent negative MR can be attributed to the hopping of electrons between Mn^{3+} and Mn^{4+} via intermediate oxygen by following the double exchange mechanism (as discussed in section **3.3.5**). As the magnetic field makes this exchange further easier [29], *Z′* and *Z″*, both, decrease i.e., negative FDMR takes place, which, appears to be responsible for presently observed large (significant) MD effect at low (mid) frequencies in LGM2O[9]. Moreover, as the magnetic field makes the said exchange further easier, therefore, the dynamic dipole of *'Mn^{3+}/Mn^{4+}'* (section **3.3.5**) starts oscillating with a higher frequency and hence *tanδ*-peak(s) corresponding to this characteristic frequency is (are) observed to be shifted towards higher frequency side due to the application of magnetic field (Figure 3.7 and its insets). Ultimately in case of LGM2O, the increase in *tanδ* and shifting of *tanδ*-peak(s) due to magnetic field (Figure 3.7 and its

insets), can be credited to negative FDMR. Nevertheless, as we have already mentioned that the MD effect is expected to be MR free or even intrinsic when it is measured at probing frequencies higher (for LGM2O, ≥ 100 kHz) to characteristic frequency [9] (the frequency of electron hopping between Mn^{3+} and Mn^{4+} sites) because at such high probing frequencies the hopping charge transport (ultimately FDMR) gets suppressed as the carriers have no chance to jump between hopping cites [9,115] (Mn^{3+} and Mn^{4+}), therefore, at these frequencies, only grain contribution is expected [115]. Further, as shown in Figure

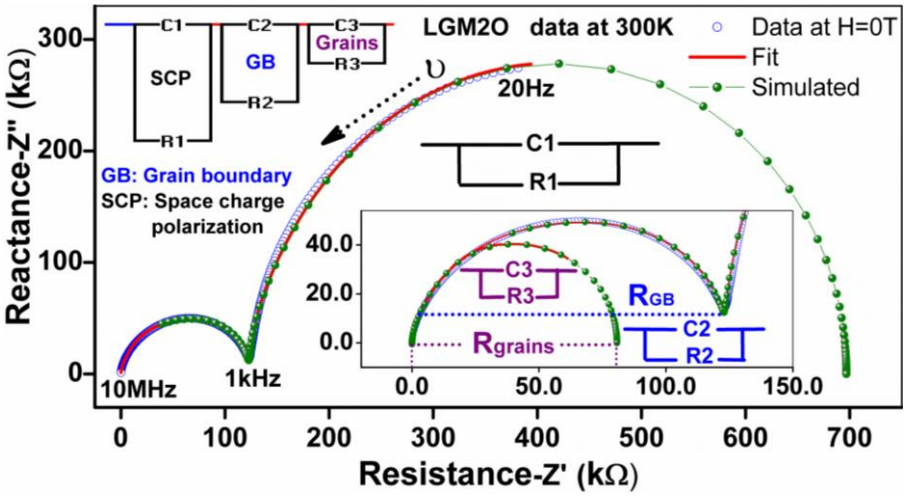

Figure 4.3: Fit of Cole-Cole plot for $LaGa_{0.8}Mn_{0.2}O_{3.015}$ (LGM2O) by using the circuit model shown in the figure. The open blue symbols (circles) are representing experimental data whereas solid red line and green balls are presenting fitted and simulated pattern respectively. The large semicircle (main panel) is corresponding to SCP. Inset shows the magnified view of first small semicircle consisting two curvatures. A further smaller semicircle is also shown in the same inset which is drawn for a high frequency segment corresponding to grains contribution. The circuit components (C1-R1, C2-R2 and C3-R3) are also positioned independently in their most suitable semicircular arc according to frequency segments of their dominance. *Note*- For convenience, the data on y-axis is multiplied by minus one.

4.2, at frequencies corresponding to grain contributions i.e., for $\geq 10^5$ Hz, neither part of impedance is changing due to the application of magnetic field. This discards any contribution of any type of MR in the observed MD effect (>3% at ≥100 kHz; Figure 3.5 and its insets) at these high frequencies. Further, the different frequency segments corresponding to SCP (space charge polarization), GB (grain

boundary) and grains contribution are identified by fitting and simulating Z′ -Z″ data for H=0T and H=0.4T with the circuit model depicted in Figure 4.2. The data is fitted and simulated with the help of EIS (Electrochemical Impedance Spectroscopy) Spectrum Analyzer software by considering the circuit model shown in Figure 4.2. The results of fitting are shown in Figure 4.3 only for the data (Z′-Z″) corresponding to H=0T as a representative. The data is fitted over the entire range of probing frequency considering a series of three capacitors (each having a resistance in parallel individually). The contributions of grains, GB and bulk-electrode interface/SCP have been separated with the help of this fitted and simulated data (Figure 4.3). It is known that SCP appears at low frequencies, therefore, the first parallel combination (C1-R1) is representing SCP region as low frequency (20 Hz to 1 kHz) semicircular arc (second and large semicircle in main panel) is fitted and simulated by varying the values of mainly C1 and R1. It appears that the first small semicircle (in main panel) has only a single curvature but actually it consists of two curvatures and it is alone fitted with a series combination of two capacitors; each having a resistance in parallel individually (C2-R2 and C3-R3). In this regard, a segment of this arc was fitted and simulated separately for a parallel combination of a capacitor and a resistor (C3-R3). Consequently, a new smaller semicircle, corresponding to ‘C3-R3’, is observed as shown in the inset. Since, this small segment is corresponding to higher range of probing frequency (100 kHz to 10 MHz) hence it has been recognized as the region corresponding to grains contribution. The remaining segment corresponding to midrange of probing frequency (1 kHz to 100 kHz), fitted mainly with the variation in C2 and R2, has been assigned as the GB region. In this way, in LGM2O sample, three different capacitance regions have been identified. These were separated on the basis of corresponding frequency range and hence recognized as SCP (C1-R1), GB (C2-R2) and grains (C3-R3) contributions accordingly. It can be clearly seen from Figure 4.3 that grains are less insulating (Note-the difference of

x-axis intersects of corresponding semicircular arc gives the value of resistance associated with particular contribution) as compare to GB. In LGM2O compound, oxygen off-stoichiometry (i.e. coexistence of Mn^{3+} and Mn^{4+}) can be considered as one of the causes responsible for low resistivity of grains (owing to already discussed hopping charge transport; Figure 3.10 (c) and (d) demonstrate two examples probable transporting paths) as the similar enhancement of grains conductivity has been attributed to oxygen vacancies in different compounds [21,55,56]. The grains of LGMO samples with better oxygen stoichiometry ((i.e. with γ=zero or very close to zero) are expected to be more insulating with reduced leakage. Now, as far as the effect of magnetic field is concern, the resistance corresponding to grain contribution (R_{grain}) is found to be almost equal in the absence (H=0 T) and presence (H=0.4 T) of magnetic field, suggesting that the MD coupling at frequencies $\geq 10^5$ Hz for LGM2O is unaffected from MR. Whereas, the resistance corresponding to both SCP and GB is lower in the presence of magnetic field which is clearly distinguishable also in Figure 4.2 and its inset. Since, the comparison of resistance in the absence (H=0T) and presence (H=0.4T) of magnetic field is the main concern of present MRIS study, therefore, present EIS analysis is limited only upto the identification of above mentioned regions (i.e. SCP (C1-R1), GB (C2-R2) and grains (C3-R3)) which are contributing to observed magneto capacitance at corresponding frequencies. Eventually for LGM2O, at frequencies corresponding to grains contribution ($\geq 10^5$ Hz), the observed MD effect is completely unaffected from any kind of MR, whereas, it is MR (ac) dominated at lower frequencies ($<10^5$ Hz).

LGM6O: The results of MRIS measurements for LGM6O are shown as a Cole-Cole plot in Figure 4.4. It is clear from this Figure that at frequencies $\leq 10^5$Hz, the resistance (Z') and reactance (Z''), both are

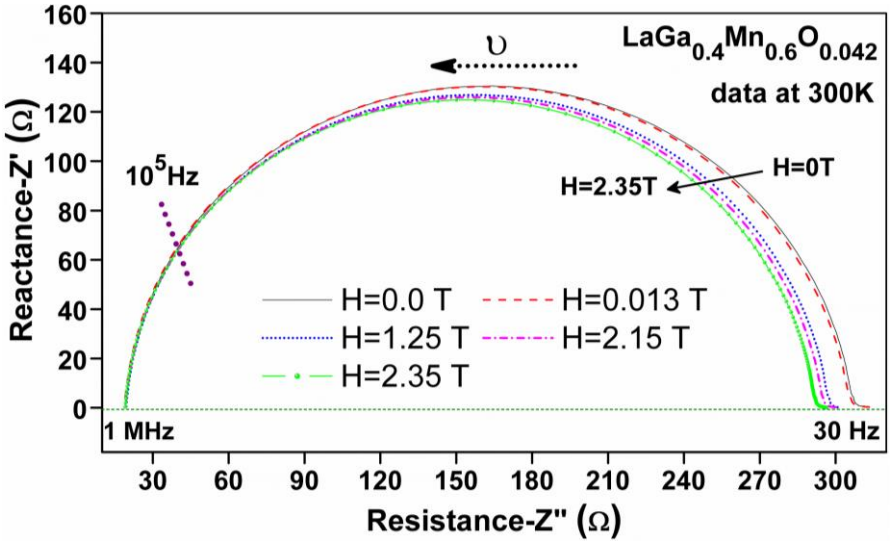

Figure 4.4: Room temperature Cole-Cole diagram of $LaGa_{0.4}Mn_{0.6}O_{3.042}$ (LGM6O) plotted for frequencies ranging from 30 Hz to 1 MHz. The data is recorded in the absence (H=0T) and presence (upto H=2.35T) of magnetic field. *Note*- For convenience, the data on y-axis is multiplied by minus one.

decreasing significantly due to external magnetic field (upto H=2.35 T) which signifies negative FDMR over these probing frequencies. This frequency dependent negative MR can be attributed to the hopping of electrons between Mn^{3+} and Mn^{4+} via intermediate oxygen by following the double exchange mechanism (as discussed in section **3.3.5**). As the magnetic field makes this exchange further easier [29], the dynamic dipole of *'Mn^{3+}/Mn^{4+}'* (section **3.3.5**) starts oscillating with a higher frequency and hence *tanδ*-anomaly corresponding to this characteristic frequency is observed to be shifted towards higher frequency side due to the application of magnetic field (Figure 3.8 and its insets). Moreover, as the magnetic field makes the said exchange further easier, Z' and Z'', both, decrease or conductivity σ increases therefore, the increase in *tanδ* (Figure 3.8 and its insets) appears reasonable in accordance to the equation 3.2. Nevertheless, at frequencies $\geq 10^5$Hz, neither part of impedance is changing due to the application of external magnetic field. It is important to note that the observed negative FDMR ($<10^5$Hz) is not affecting the negative MD effect observed in LGM6O (Figure 3.6 and its insets), because, any kind (dc or ac) of negative MR, leads to a positive MD response[9]. Thus, it seems that the MD coupling in LGM6O is completely MR

unaffected and very strong too as it is appearing by suppressing the effect of negative FDMR even at low frequencies. This is the reason, the identification of different segments (SCP, GB and grains) in case of LGM6O was not required and hence the corresponding Z'-Z'' data has not been fitted. Ultimately, LGM6O exhibits RTMD effect without any resistive contribution over the entire range of probing frequencies.

This MRIS analysis reveals that for LGM2O the observe RTMD effect is found to be MR free at frequencies corresponding to grains contribution ($\geq 10^5$ Hz) whereas, it is FDMR dominated at lower frequencies ($<10^5$ Hz). On the other side, LGM6O exhibits a negative RTMD effect without any resistive contribution over the entire range of probing frequencies. On the basis of this analysis, we propose that instead of measuring only dc MR or analyzing only magnetic field dependent trends of change in IS (FDMR) alone can be used as an effective experimental technique to identify and analyze the intrinsic and resistive parts contributing in MD effect. Further, in case of LGM2O, there is a possibility that at lower frequencies ($<10^5$ Hz), the intrinsic part of RTMD might have gone suppressed due the dominance of negative FDMR because, MR (ac and dc both) and MD response are recorded through electrical measurements, where, this superposition of resistance (MR) and capacitance (MD) is possible. Thus, magnetic field dependent measurements (even, also for LGM6O sample) using non-electrical characterization techniques (where, electrical resistance does not contribute in signal) may provide additional and concrete information about the intrinsic nature and mechanism of MD coupling in presently studied samples. For this purpose magnetic field dependent Raman measurements were performed and the obtained results are discussed below.

4.3.2 Magnetic field dependent Raman spectroscopy: Evidence and origin of intrinsicality (intrinsic nature) of observed MD coupling

Magnetic field dependent Raman spectra for LGM2O/LGM6O were recorded between 300 to 1200 cm^{-1} and the results are shown in Figure

4.5/4.6. Note that similar to most of the manganitelike ABO_3 systems, the observed Raman spectrum is basically dominated by the MnO_6 octahedral vibrational modes [97,98,165,166]. Using previous conventions, the broad features observed around 500 cm^{-1} and above

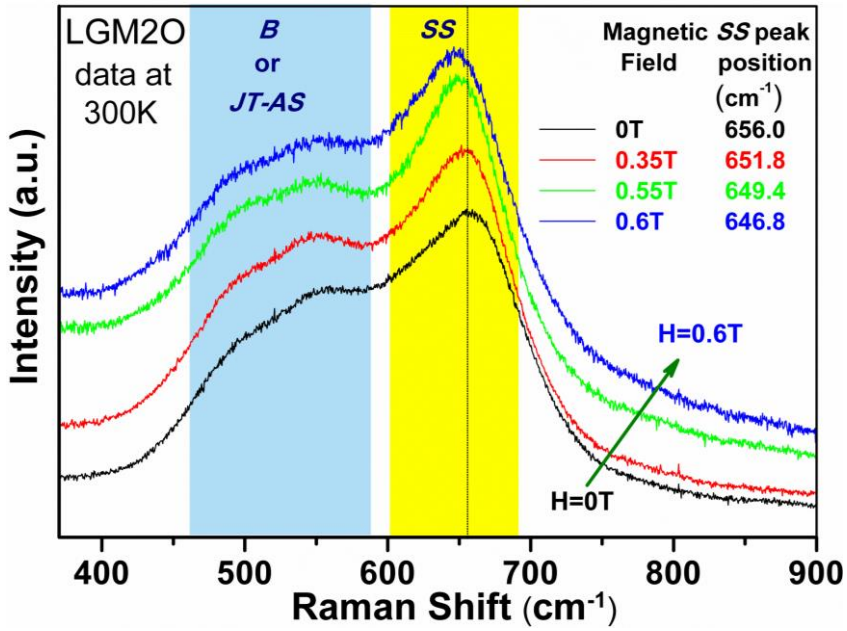

Figure 4.5: Room temperature Raman spectra of LGM2O, recorded in the absence (H=0T) and presence (upto H=0.6T) of magnetic field. A vertical dotted line is drawn to show the shifting of *SS* MnO_6 octahedral Raman mode due to the application of magnetic field. The x-axis intersect of this dotted line represents the peak position (656 cm^{-1}) of *SS* mode under zero magnetic field. The peak position of this *SS* mode for H=0T to H=0.6T, are tabulated in the Figure itself.

600 cm^{-1} (Figure 4.5 and 4.6) were respectively assigned as bending (*B*) or Jahn-teller asymmetric stretching (*JT-AS*) and symmetric stretching (*SS*) MnO_6 octahedral Raman modes [97,98,167,168]. Interestingly, with the application of a very low magnetic field of ≤0.6 T, the peak position of *SS* mode is found to be significantly shifted toward lower frequency side for LGM2O (Figure 4.5) whereas towards higher frequency for LGM6O (Figure 4.6). For LGM2O (LGM6O), a shift of 4.2 cm^{-1} (5.1 cm^{-1}) between the peak positions corresponding to zero field and lowest applied field (i.e., H= 0.35) is clearly evident from Figure 4.5 (4.6) and enclosed Table. For LGM6O, this difference is additionally marked with the help of a vertical line and two arrows

(Figure 4.6). Further, For LGM2O/LGM6O, a backward/forward shift of 9.2 cm^{-1}/7.2 cm^{-1} is observed for highest available field of H=0.6T as evident from Figure 4.5/4.6. This magnetic field dependent backward/forward (LGM2O/LGM6O) shifting is a signature of softening/hardening of *SS* MnO_6 octahedral Raman modes, indicating expansion/compression of material [97] due to magnetic field. As a result of this volume expansion/compression (considering uniform expansion/compression for circular pellets), presently observed increase (LGM2O)/decrease (LGM6O) in ε'/capacitance i.e., positive/negative MC%, appears justified and intrinsic in accordance to relation (3.1) as in case of a circular pellet sample, C (or ε') scales with A (for uniform magnetic expansion /compression).

Now, As far as the origin of presently observed significant positive/negative MC% in LGM2O/LGM6O (or magnetic softening/hardening of Raman modes) is concern, it can be understood as follows. In presently studied LGM2O/LGM6O system 85%/86% of total Mn is in its 3+ state which is JT distorted [158] due to that Mn^{3+} forms two long Mn-O bonds (2.18 Å) [94] and four short Mn-O bonds (1.90 Å) [94] with octahedrally connected oxygens. Further, the ionic radius of Ga^{3+} (0.62 Å) is a little smaller than that of the Mn^{3+} (0.64Å) [94,96,157] whereas Ga-O distances (1.97 Å) is slightly higher than Mn-O short bond (1.90 Å) and significantly smaller to Mn-O long bond (2.18 Å) [94]. The evolution of orthorhombic strain in $LaMn_{1-x}Ga_xO_3$ is already predicted by Farrell et al. [94] in terms of transformation/rotation of Mn - $(3x^2 - r^2)/(3y^2 - r^2)$ orbital into the $(3z^2 - r^2)$ state due to the replacement of Mn^{3+} with Ga^{3+}. The evolution of such orthorhombic strain can be considered in present LGMO samples, by means of alignment of Mn orbitals transforming due to the replacement of non-JT Ga^{3+} ions with JT distorted Mn^{3+} ions [94]. Further, as the application of magnetic field (upto H=0.4T for LGM2O and H=2.35T for LGM6O) aligns/rotates magnetic moments related to Mn ions, therefore, readjustment or reorientation

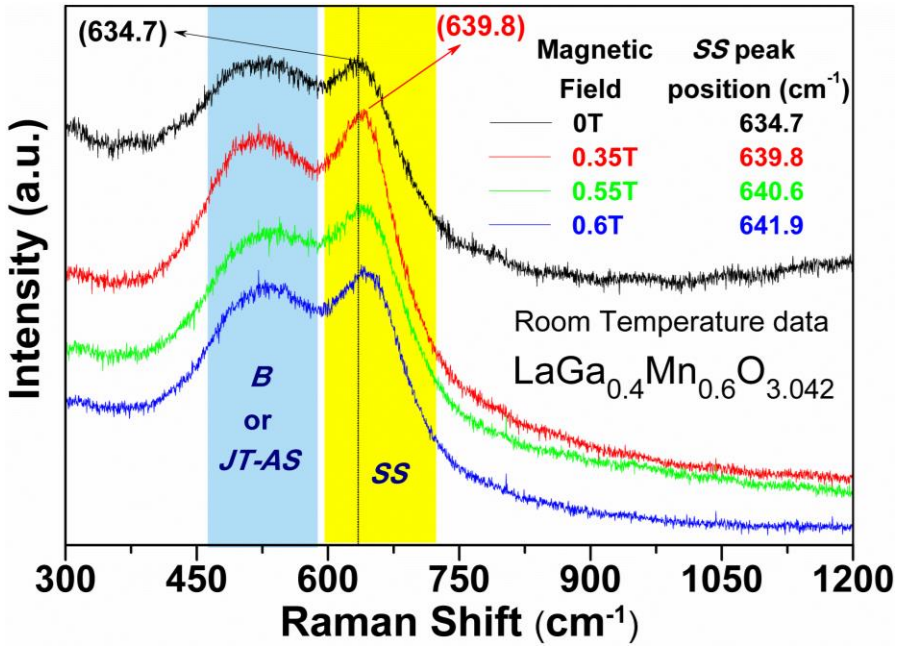

Figure 4.6: Room temperature Raman spectra of LGM6O, recorded in the absence (H=0T) and presence (upto H=0.6T) of magnetic field. A vertical dotted line is drawn to show the shifting of *SS* MnO_6 octahedral Raman mode due to the application of magnetic field. The x-axis intersect of this dotted line represents the peak position (634.7 cm^{-1}) of *SS* mode under zero magnetic field. The peak position of this *SS* mode for H=0T to H=0.6T, are tabulated in the Figure itself.

[95] of such already transformed Mn orbitals appears possible (as for such correlated systems, spin and orbital degrees of freedoms are strongly coupled) which may lead to a change in the above discussed orthorhombic strain (i.e., expansion or compression of material; presently expansion for LGM2O whereas compression for LGM6O) and hence in capacitance (or ε') according to relation 3.1.

4.4 Summary

In summary, resistive contribution/origin of room temperature MD (RTMD) effect, observed in LGM2O and LGM6OO (chapter 3), has been examined by analyzing the results of dc and FDMR measurements. The intinsicality of the effect has been evidenced by means of magnetic field dependent Raman spectroscopy. The MD coupling in LGM2O found to be MR unaffected for frequencies $\geq 10^5$ Hz as revealed through a systematic analysis of *dc* and FDMR. However, at lower frequencies, the presently observed MD

phenomenon for LGM2O was found MR dominated (due to which intrinsic contribution might have gone suppressed at these lower frequencies) which has been attributed to the electron hopping between Mn^{3+} and Mn^{4+} sites. As far as the observed RTMD coupling in LGM6O (chapter 3) is concern, present analysis of dc and FDMR reveals that the observed negative MD effect in LGM6O is completely unaffected from any kind of MR over the entire range of probing frequencies. The results of magnetic field dependent Raman spectroscopy suggest that the observed MD coupling is intrinsic and magnetostriction meditated in both LGM2O and LGM6O (magneto expansion in LGM2O and compression in LGM6O). This magnetic expansion (LGM2O)/compression (LGM6O) has been attributed to the reorientation/retransformation of spin-coupled Mn orbitals. Thus our assumption (section **3.4**) that in case of LGM2O, as for MD and MR being electrical measurements the intrinsic part of observed MD coupling at low frequencies might have gone suppressed due to the dominance of FDMR appears correct. It is clear form present study (chapter 3 and 4) that for analyzing resistive origin of MD coupling, measuring only dc MR or investigating only trends of magnetic field dependent change in ε'/C and $tan\delta$, are not sufficient. FDMR measurements in this regard provide better information and hence should necessarily be employed to analyze the resistive contribution in MD effect. The intrinsicality/mechanism of a genuine MD effect should (can) be evidenced/understood by means of a non-electrical characterization technique (where, electrical resistance does not contribute in signal) like magnetic field dependent XRD, XANES or Raman spectroscopy. Eventually, the Present in depth analysis (chapter 3 and 4) reveals that intrinsic MD coupling can be realized in a compound which expands/shrinks in response to an externally applied magnetic field. In order to further support our conclusive argument (s), Fe doped $LaGaO_3$ has also been prepared and probed from MD perspective. A detailed MD study on this Fe doped $LaGaO_3$ system is provided in next chapter.

Chapter 5

Room Temperature Magnetodielectric Study on $LaGa_{0.7}Fe_{0.3}O_{3+\gamma}$: Impact and Origin of Excess Oxygen

To provide an additional support for our concluding arguments or proposals given in chapter 3 and 4, an observation with a systematic study on room temperature magnetodielectric (RTMD) behavior of $LaGa_{0.7}Fe_{0.3}O_{3+\gamma}$ is presented in this chapter. Results of this chapter are published in the literature.[**]

[**] *H.M. Rai et al., Inorg. Chem.* **56** *(2017) 3809-3819.*

5.1 Introduction

Similar to Mn doping in $LaGaO_3$ (LGO) at Ga site (section **3.1**), doping of other TM (transition metal) ion at Ga site in LGO may also lead to magneto compression/magneto expansion mediated magnetodielectric (MD) coupling. Keeping this in view, we have doped Fe at Ga site in LGO with an expectation of RT (near RT) MD coupling because, the strain evolved due to Fe doping (considering the difference in ionic radii of Ga and Fe ions), is supposed to be magnetically switchable as it is correlated with the arrangement of orbitals/moments of TM ions [94] (since in such systems, spin and orbital degrees of freedoms are strongly coupled). Here, we report an observation of RTMD effect in $LaGa_{0.7}Fe_{0.3}O_{3+\gamma}$ with the application of low magnetic field of about 1T (maximum 1.2T) and < 1T. The observed results have been explained using impedance spectroscopy (IS) by considering the pair of nearest $Fe^{3+}$and Fe^{4+} jointly as a dynamic dipole ('Fe^{3+}-Fe^{4+}') [29,155]. The coexistence of $Fe^{3+}$and Fe^{4+} is validated through iodometric titration and XANES experiments. The contribution of resistive sources in the observed RTMD effect has been analyzed via systematic study of magneto-capacitance (MC%), magneto-loss (ML%), dc MR (magnetoresistance) in four probe geometry and frequency dependent MR (FDMR) via impedance spectroscopy (MRIS). MRIS analysis reveals that at frequencies corresponding to grain contribution ($\geq 10^6$ Hz), the observed MD phenomenon, is MR-unaffected whereas at lower probing frequencies, it appears to be MR dominated possibly due to the coexistence of Fe^{3+} and Fe^{4+}. The origin of excess oxygen or positive value of γ (i.e, coexistence of Fe^{3+} and Fe^{4+}) and its impact on RTMD properties of $LaGa_{0.7}Fe_{0.3}O_{3+\gamma}$ has been investigated by means of 'bond-valance-sum' analysis and DFT (density functional theory) based first principles calculations. The cation vacancies at La/Ga site (or at La and Ga both) have been proposed as one of the possible reason for excess oxygen in $LaGa_{0.7}Fe_{0.3}O_{3+\gamma}$. The intrinsic nature of observed MD coupling in $LaGa_{0.7}Fe_{0.3}O_{3+\gamma}$ has been

evidenced by means of magnetic field dependent Raman spectroscopy and explained in terms of modified volume strain governed by magnetic field induced rerotation/retransformation of spin coupled Fe-orbitals.

5.2 Experimental

Polycrystalline sample of $LaGa_{0.7}Fe_{0.3}O_3$ was prepared through conventional solid-state reaction route by following the process described in section **2.1.1**. The phase purity of the prepared sample has been examined by means of powder x-ray diffraction (XRD) experiments carried out on Lab source diffractometer. XRD data has been refined by using FullProf Rietveld refinement package [101]. For dielectric measurements single phase powdered samples were pelletized at a pressure of 15 ton to form 1 mm thick circular discs of 12 mm diameter. These pellets were sintered in air at 1400 $^{\circ}$C for 24 hours. Further, after being coated with silver paint these pellets were fired at 300° C for 30 min. For all as prepared pellets, RT capacitance and frequency dependent MR (FDMR) i.e. magnetic field dependent change in real and imaginary parts of impedance are measured in the absence and presence of magnetic field by using a precision impedance analyzer. These measurements were performed by applying an oscillator voltage of ±1 V and the data was recorded for probing frequencies, ranging from 20 Hz to 10 MHz. The direction of applied magnetic field was kept along the applied electric field to ensure the complete absence of contributions which may arise in MD measurements due to Hall-effect geometry. In order to find out the Fe charge state in $LaGa_{0.7}Fe_{0.3}O_{3+\gamma}$ compound, iodometric titration experiment has been carried out. For this purpose sodium thio-sulphate ($Na_2S_2O_3.5H_2O$) solution is used as titrant whereas the analyte ($LaGa_{0.7}Fe_{0.3}O_{3+\gamma}$) is dissolved in HCl solution and KI is added in that solution to get an end point as a result of redox. The titrant (in Burette) is added drop by drop in the Analyte+HCL+KI solution until it becomes colorless (end point). The end point is confirmed by using

starch as an indicator. The volume of used titrant is recorded and ultimately gamma (γ) in $LaGa_{0.7}Fe_{0.3}O_{3+\gamma}$ is calculated by usng the well-known equation of normality ($N_1V_1=N_2V_2$). The coexistence of $Fe^{3+}$and Fe^{4+} in $LaGa_{0.7}Fe_{0.3}O_{3+\gamma}$ as recognized through iodometric titration method is further validated by XANES measurements performed at Fe K-edge. The Fe K-edge XANES spectra were carried out on ~1 mm thick circular pellets in the fluorescence mode using Vortex energy dispersive detector (VORTEX-EX) at BL-9, Scanning EXAFS Beamline of Indus-2 synchrotron radiation source at the RRCAT (Raja Ramanna Centre for Advanced Technology) Indore, India [134]. The beamline consists of Rh/Pt coated meridional cylindrical mirror for collimation and Si (111) based double crystal monochromator (DCM) to select excitation energy. The energy range of DCM was calibrated using standard Fe foil. Fe K-edge XANES data normalization and self-absorption correction were processed using ATHENA software [135]. The resistivity and magneto-resistance measurements (dc MR) were performed in the absence (0 T) and presence of magnetic field (0.7 T and 1.2 T) in standard four-probe geometry using nano voltmeter and source meter. Moreover, 'bond-valance-sum' calculations have been carried out in FullProf suit to estimate the average charge of Fe in presently studied $LaGa_{0.7}Fe_{0.3}O_{3+\gamma}$ sample. In order to understand the presence of mixed charge state of Fe in $LaGa_{0.7}Fe_{0.3}O_{3+\gamma}$ (i.e., stability of Fe^{4+}), DFT based first principles calculations have been performed by using Vienna Ab initio simulation package–'VASP' (computational methodology is discussed in detail in the 'results and discussion' section). The magnetic field dependent RT Raman spectra on highly dense $LaGa_{0.7}Fe_{0.3}O_{3+\gamma}$ pellet were recorded from 300 to 3000 cm^{-1} by using a Horiba Lab RAM high-resolution (~0.4 cm^{-1}) micro Raman spectrometer in confocal mode equipped with 30 mW air cooled He-Ne laser (632.8nm) as the excitation source and a charge-coupled device (CCD) detector. The spectra were recorded by using 50x standard objective with a spot size of ~5 μm whereas the laser power was kept at 15 mW.

5.3 Results and discussions

This section is divided into seven subsections; first three parts present the analysis for structural phase purity by XRD, along with the validation of oxygen access (coexistence of Mn^{3+} and Mn^{4+}) in the sample by means of iodometric titration and XANES analysis. The observed RTMD response and analysis for resistive contribution (by means of dc MR and MRIS) are disused respectively in fourth and fifth segment. In last two subsections, impact of excess oxygen along with its origin and evidence of intrinsic nature of observed MD coupling along with its understanding are discussed respectively.

5.3.1 XRD

Figure 5.1 shows the refined powder XRD pattern for polycrystalline sample of $LaGa_{0.7}Fe_{0.3}O_3$. This XRD pattern is refined with the help of FullProf package by considering orthorhombic structure with *Pnma* space group. The value for the goodness of fit (i.e., χ^2) was found to be ~1.4. The absence of any unaccounted peak in the refined XRD pattern

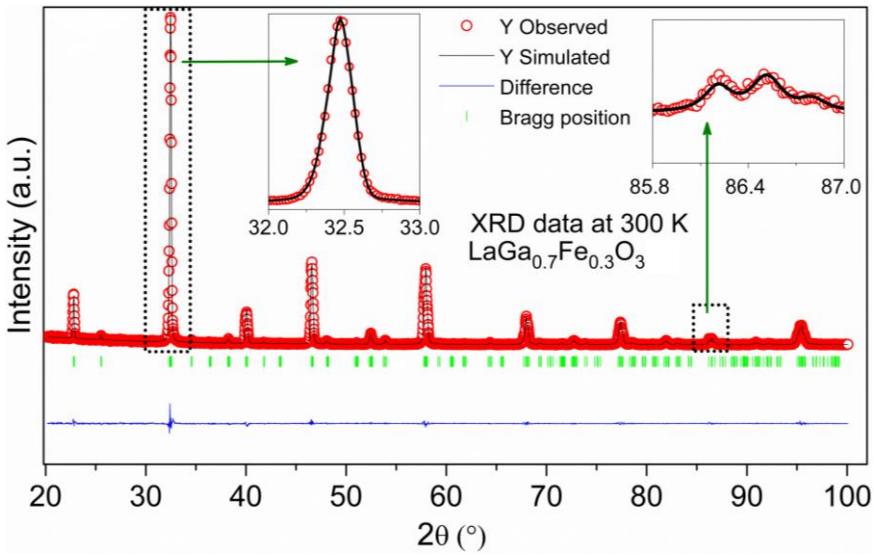

Figure 5.1: Rietveld refined X-ray diffraction data for $LaGa_{0.7}Fe_{0.3}O_3$. The absence of any unaccounted peak confirms the purity of the structural phase of the prepared sample. Insets display the magnified view of selected peaks to show the quality of fitting.

confirms the phase purity of prepared sample. This pure phase $LaGa_{0.7}Fe_{0.3}O_3$ sample was used for rest of the other measurements.

5.3.2 Iodometric titration

In order to check the oxygen stoichiometry of presently studied $LaGa_{0.7}Fe_{0.3}O_3$ sample, iodometric titration experiments [136] have been carried out. The sample was found to be oxygen off-stoichiometric with some excess oxygen (i.e., coexistence of $Fe^{3+}$and Fe^{4+}) and hence named here and after as $LaGa_{0.7}Fe_{0.3}O_{3+\gamma}$ (or as LGF3O). In $LaGa_{0.7}Fe_{0.3}O_{3+\gamma}$, the value of γ is found to be 0.044. Further, with this value of γ, the charge state of Fe and percentage of $Fe^{3+}$and Fe^{4+} has been calculated in the following manner by using the charge neutrality condition.

(i) Fe charge state (say x)

For the present sample, by charge neutrality condition,

$$La^{3+}Ga^{3+}_{0.7}Fe^{x}_{0.3}O^{2-}_{(3+\gamma)} = La^{3+}Ga^{3+}_{0.7}Fe^{x}_{0.3}O^{2-}_{(3+0.044)} = 0$$

Here, x is the charge state of Fe in present sample and γ = 0.044 (by titration), thus,

$$(3\times 1)+(3\times 0.7)+0.3x+(-2\times 3.044)=0$$

$$3+2.1+0.3x-6.088=0$$

$$5.1+0.3x-6.088=0$$

$$0.3x-0.988=0$$

$$x=\frac{0.988}{0.3}$$

$$x=3.29$$

Thus, through iodometric titration, the charge state of Fe in present sample is found 3. 29.

(ii) Percentage of Fe^{3+} and Fe^{4+}

For the present sample, by charge neutrality condition,

$$LaGa_{0.7}Fe_{0.3}O_{(3\pm\gamma)} = La^{3+}Ga^{3+}_{0.7}Fe^{3+}_{0.3(1-x)}Fe^{4+}_{0.3x}O^{2-}_{(3\pm\gamma)}$$

Here, x is the amount of Fe^{4+} in the total Fe present in the sample. Since, through titration experiment the value of γ is found to be 0.044, therefore, according to charge neutrality condition

$$La^{3+}Ga^{3+}_{0.7}Fe^{3+}_{0.3(1-x)}Fe^{4+}_{0.3x}O^{2-}_{(3+\gamma)} = 0$$

$$La^{3+}Ga^{3+}_{0.7}Fe^{3+}_{0.3(1-x)}Fe^{4+}_{0.3x}O^{2-}_{(3+0.044)} = 0$$

$$(3\times1)+(3\times0.7)+[3\times0.3(1-x)]+(4\times0.3x)+(-2\times3.044)=0$$

$$3+2.1+0.9-0.9x+1.2x-6.088=0$$

$$6+0.3x-6.088=0$$

$$0.3x-0.088=0$$

$$x=\frac{0.088}{0.3}$$

$$x=0.29$$

Thus, Fe^{4+} is 29% out of total Fe present in the $LaGa_{0.7}Fe_{0.3}O_{3+\gamma}$ sample whereas remaining 71% is Fe^{3+} and the charge state of Fe has been estimated as 3.29.

5.3.3 XANES

The coexistence of Fe^{3+} and Fe^{4+} has been further supported through XANES measurements (as the charge state determination by means of XANES is already being used [105–108]) carried out at Fe K-edge energy of 7112 eV. The obtained XANES data is plotted in Figure 5.2. The energies corresponding to absorption edge of - pure Fe metal foil (Fe^0) and powders of FeO (Fe^{2+}) and Fe_2O_3 (Fe^{3+}) have been used as standards. The oxygen stoichiometry of powders (standards) has been validated through iodometric titration before using them as standards.

It is notable that XANES measurements for $LaGa_{0.7}Fe_{0.3}O_{3+\gamma}$ and also for all these standards are performed with same experimental settings at RT. Figure 5.2 compare the normalized XANES spectra of LGF3O

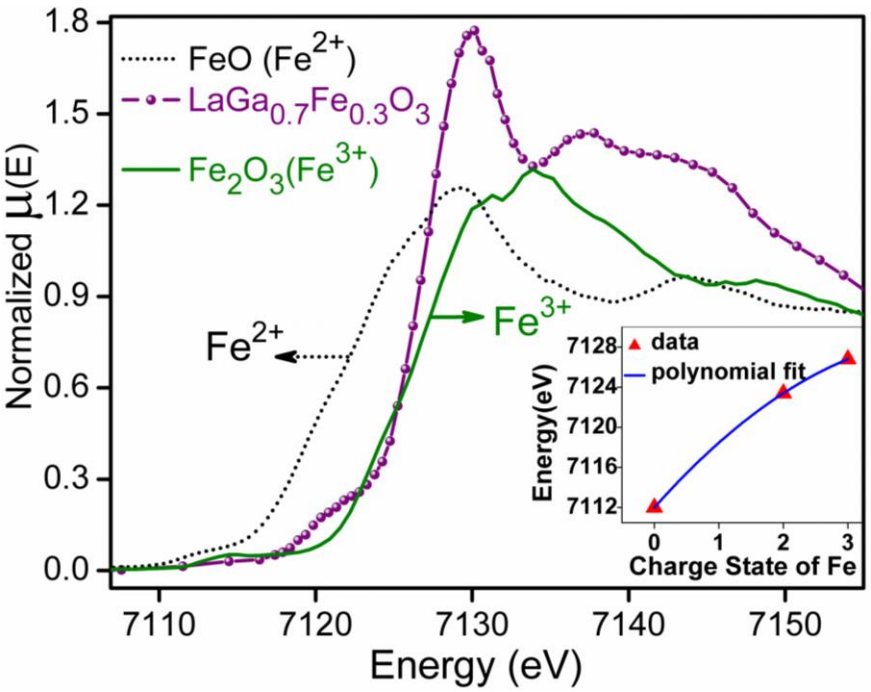

Figure 5.2: Fe K-edge XANES spectra of $LaGa_{0.7}Fe_{0.3}O_{3+\gamma}$ (LGF3O) with Fe^{2+} and Fe^{3+} standards. Since the absorption edge of Fe-metal foil (Fe^0) appears at a relatively low energy side (7112 eV), therefore, to clearly visualise the relative shift in the position of LGF3O absorption edge with (2+ and 3+), the XANES data of Fe^0 is not shown. Inset shows K-edge energies as a function corresponding oxidation states of Fe standards (i.e., 0, 2+ and 3+).

with Fe^{2+} and Fe^{3+} standards. The absorption edge (K-edge) energies of FeO (Fe^{2+}), Fe_2O_3 (Fe^{3+}) and $LaGa_{0.7}Fe_{0.3}O_{3+\gamma}$ are determined with the help of already reported convention [137], by plotting the first derivative of the corresponding μ(E) versus E curves as shown in Figure 5.3 for $LaGa_{0.7}Fe_{0.3}O_{3+\gamma}$ and used standards. The value of energy corresponding to first maximum (exclude the one corresponding to pre-edge) on this first derivative curve gives the position of the inflection point and hence the position of the absorption edge [137]. In this way, the calculated K-edge energy of $LaGa_{0.7}Fe_{0.3}O_{3+\gamma}$ is found to be greater than that of the Fe_2O_3 (3+),

indicating coexistence of Fe^{3+} and Fe^{4+} in the sample. The estimated K-edge energies of sample and standards are summarized in Table 5.1.

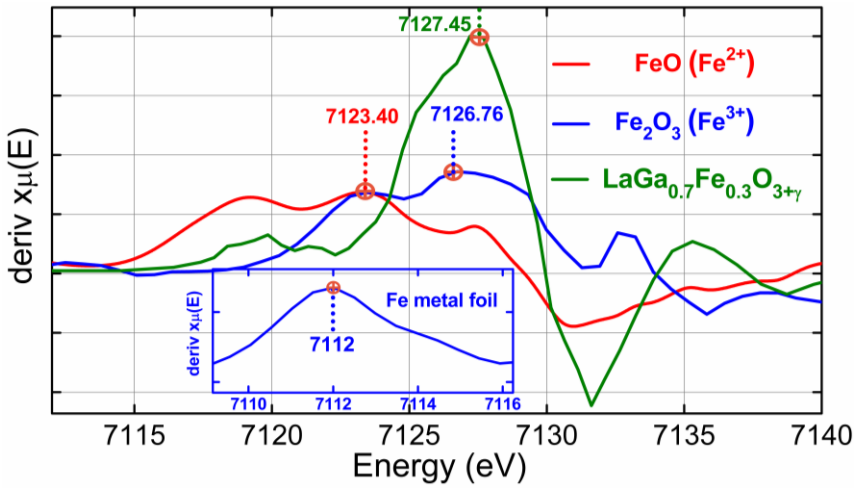

Figure 5.3: Estimation of absorption K-edge energy. The first derivative of μ(E) versus E curve for standards and $LaGa_{0.7}Fe_{0.3}O_{3+\gamma}$. For clarity the data of Fe metal foil is shown separately in the inset. The energy coordinate of small circle indicates corresponding K-edge energy.

Table 5.1: Fe K-edge absorption energies, for sample and standards i.e., Fe metal foil (Fe^0), FeO (Fe^{2+}) and Fe_2O_3 (Fe^{3+}), estimated through first order derivative of μ(E) versus E curves by means of XANES data (Figure 5.3).

Sample/standard	K-edge energy (eV)
Fe metal foil (Fe^0)	7112.00
FeO (Fe^{2+})	7123.40
Fe_2O_3 (Fe^{3+})	7126.76
$LaGa_{0.7}Fe_{0.3}O_{3+\gamma}$	7127.45

In order to obtain a precise value of oxidation setae of Fe in $LaGa_{0.7}Fe_{0.3}O_{3+\gamma}$, the calculated edge energies of FeO (Fe^{2+}), Fe_2O_3 (Fe^{3+}) along with that of the Fe metal foil (Fe^0) are then plotted as a function of corresponding charge states (i.e. 0, 2+ and 3+) as shown in the inset of Figure 5.2. This data is then fitted with a 2nd order polynomial [105] of the following form

$$y = B_1 x^2 + B_2 x + Intercept \qquad (5.1)$$

here, x represents Fe charge state whereas y is the corresponding K-edge energy. Thus, to estimate the charge state of Fe in

$LaGa_{0.7}Fe_{0.3}O_{3+\gamma}$, the corresponding K-edge energy i.e., y=7127.45 eV (see Figure 5.3 or Table 5.1) along with the values of B1 (-0.78), B2 (7.26) and intercept (7112) as obtained from the table of fitting parameters, is substituted in above polynomial i.e., $7127.45 = -0.78x^2 + 7.26x + 7112$. After solving this quadratic equation, the oxidation state of Fe in $LaGa_{0.7}Fe_{0.3}O_{3+\gamma}$, is estimated between +3 and +4 (i.e. $x = 3.29$). This coexistence of Fe^{3+} and Fe^{4+} is attributed to oxygen off-stoichiometry (oxygen excess) in the sample. By using this value (3.29) in the following charge neutrality condition -

$$La^{3+}Ga_{0.7}^{3+}Fe_{0.3}^{3.29+}O_{(3+\gamma)}^{2-} = 0$$

$$(3\times1)+(3\times0.7)+(3.29\times0.3)-2\times(3+\gamma)=0$$

$$\text{OR} \qquad 3+2.1+0.987-6-2\gamma=0$$

$$\text{OR} \qquad 0.087-2\gamma=0$$

$$\text{OR} \quad \gamma=\frac{0.087}{2}=0.0435$$

the value of gamma (γ) is found to be 0.0435 which is closely consistent with that of the value (0.044) obtained through titration experiments. Hence, the charge state of Fe and concentration of Fe^{3+}/ Fe^{4+} in $LaGa_{0.7}Fe_{0.3}O_{3+\gamma}$ sample calculated through both, XANES and titration experiments, are consistent with each other. It is to be noted that the oxygen excess has not been verified thorough present XRD results because the data is recorded at Lab source and hence, refining occupation factor for a low Z element like oxygen may lead to wrong information. In this regard, neutron diffraction measurements will be very useful as the oxygen excess in $LaMnO_{3.12}$ has already been studied by using neutron diffraction data [139,140] and explained in terms of cation vacancies [139,140].

5.3.4 Room temperature magnetodielectric (RTMD) response

A significant RTMD effect of ~ 15% is observed for $LaGa_{0.7}Fe_{0.3}O_{3+\gamma}$ sample when measured at a probing frequency of ~100 kHz with a magnetic field (H) of 1 T (>20% with H=1.2 T). The RT frequency dependence of ε' and loss tangent ($tan\delta$) for $LaGa_{0.7}Fe_{0.3}O_{3+\gamma}$ is shown in Figure 5.4 and 5.5 respectively. These measurements were carried

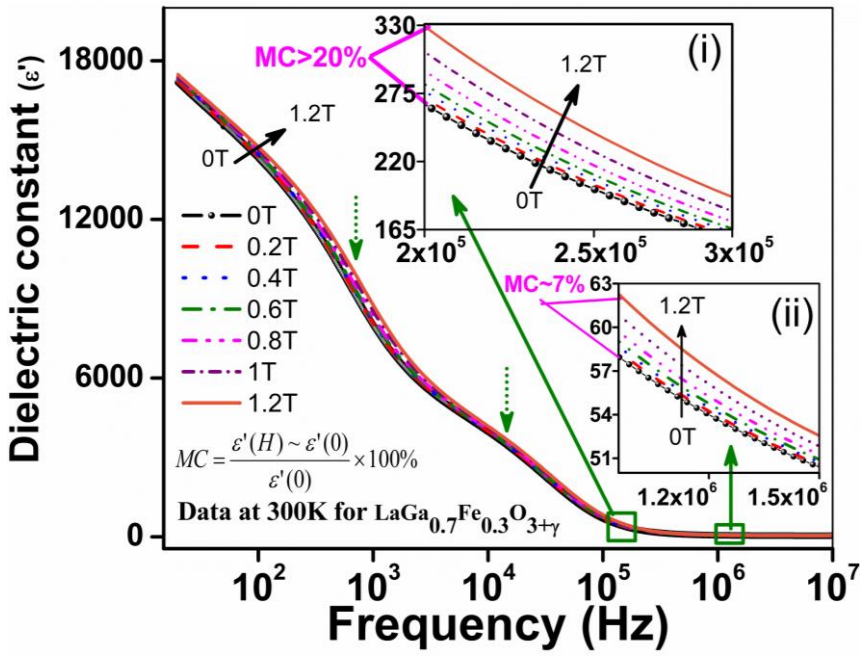

Figure 5.4: Room temperature dielectric constant (ε') as a function of frequency measured in the absence (H=0.0T) and presence (H=0.2T to 1.2T) of magnetic field for $LaGa_{0.7}Fe_{0.3}O_{3+\gamma}$. Insets show magnified view of data at corresponding frequency ranges.

out in the absence (H=0 T) and presence of magnetic field (0.2 T to 1.2T) for a frequency range of 20 Hz to 10 MHz. A noticeable change (upsurge) in the value of ε' due to the application of magnetic field (0.2T to 1.2T) is clearly evident over the entire range of proving frequencies as depicted in in Figure 5.4 and its insets. This observed MD effect is strong at low frequencies and significant even at higher probing frequencies. Interestingly, at ~100 kHz, this observed change is found to be >20% for H=1.2, ~ 15% with H=1T and ~5% even at H=0.5T (Figure 5.4 and its insets) which is comparable with the MD effect reported by others at same/lower probing frequency in different

materials [19,46,47,59,155] but, with the application of similar [155]/relatively higher magnetic field [19,46,47,59] and at low temperatures [47,59]. Inset (ii) of Figure 5.4, shows that the change is ~7% even at a high frequency of 1 MHz with H=1.2T (~5% with H=1T; not marked). These changes in the value of RT ε' due to the application of different magnetic fields are tabulated in Table 5.2 for probing frequencies of 100 kHz and 1 MHz respectively. It should be noted that this observed change in ε' is well above the sum of

Table 5.2: The Change observed in the value of room temperature ε' (in %) due to the application of different magnetic fields ranging from 0.2T to 1.2T.

Frequency	% Change observed in the value of room temperature ε' due to the application of different magnetic fields					
	0.2 T	**0.4 T**	**0.6 T**	**0.8 T**	**1 T**	**1.2 T**
100 kHz	**1.74**	**3.71**	**5.68**	**9.13**	**14.97**	**21.21**
1 MHz	**0.59**	**1.20**	**1.82**	**2.99**	**4.99**	**7.42**

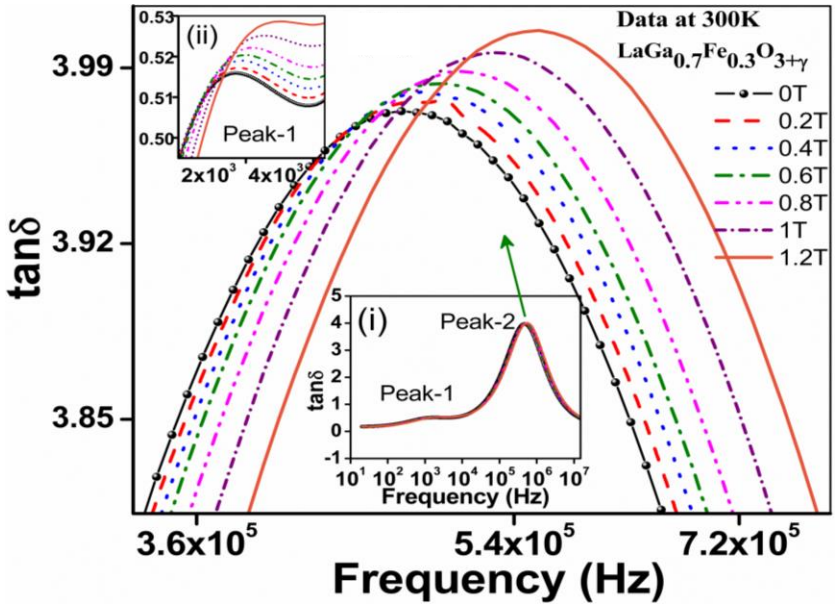

Figure 5.5: Room temperature loss tangent (*tanδ*) as a function of frequency measured in the absence (H=0.0T) and presence (H=0.2T to 1.2T) of magnetic field for $LaGa_{0.7}Fe_{0.3}O_{3+\gamma}$. The data corresponding to entire range of probing frequencies is shown in the inset (i) and high frequency data is magnified as main panel for clarity. Inset (ii) displays magnified view of first broad peak.

instrumental and statistical error bar, even at the highest probing frequency of 10 MHz. Moreover, *tanδ* also increases over the entire range of probing frequency due to the application of magnetic field as shown in Figure 5.5, its inset (ii) and Figure 5.6 by magnifying the corresponding frequency ranges. Further, two broad peaks, indicated as

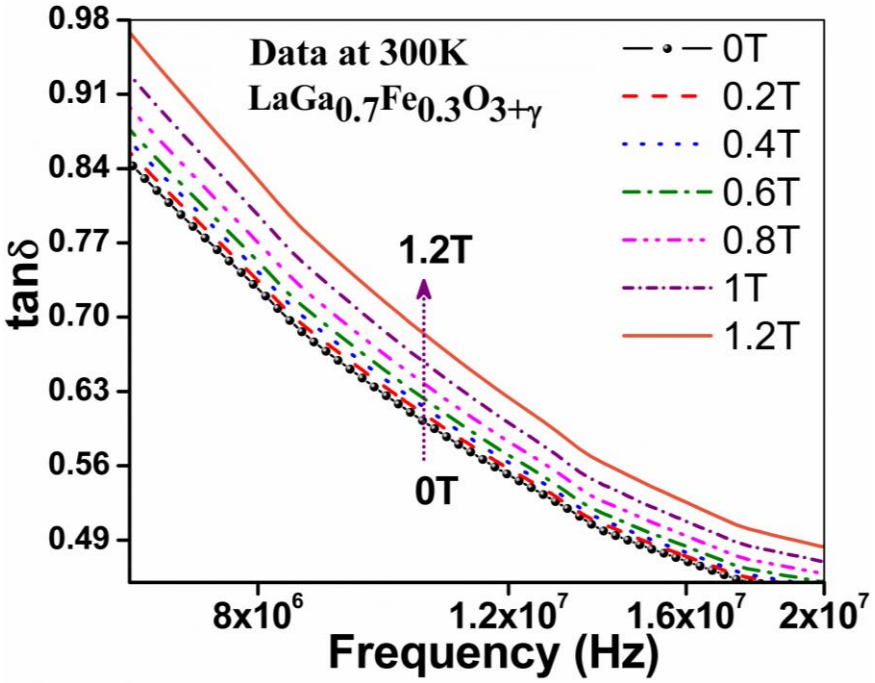

Figure 5.6: Room temperature loss tangent (*tanδ*) as a function of frequency measured in the absence (H=0.0T) and presence (H=0.2T to 1.2T) of magnetic field for $LaGa_{0.7}Fe_{0.3}O_{3+\gamma}$. The data is shown only for higher frequencies to demonstrate that the value of *tanδ* increases with increasing magnetic field even at the frequencies of > 1 MHz and its value remains <1 even at such high frequencies.

peak-1 and peak-2, have been observed in *tanδ* as shown in the inset (i) of Figure 5.5. Peak-2 is prominent in height whereas peak-1 is relatively much broader and smaller in height. These characteristic *tanδ*-peaks are corresponding to the diffusive anomalies in ε' (indicated by two dotted down arrows in the Figure 5.4) observed across the same range of probing frequencies. These two peaks (diffusive anomalies) in *tanδ* (ε') indicate the presence of two dielectric relaxation processes in presently studied LGFO sample. It may be interesting to explore these peaks in future from relaxation viewpoint. In addition to RTMD response, temperature dependent ε' is also recorded with and without

magnetic field for $LaGa_{0.7}Fe_{0.3}O_{3+\gamma}$ sample. Figure 5.7 shows ε' -*T* data recorded in the absence (H=0 T) and presence of magnetic field (H=1.2T). The value of ε' is increasing due

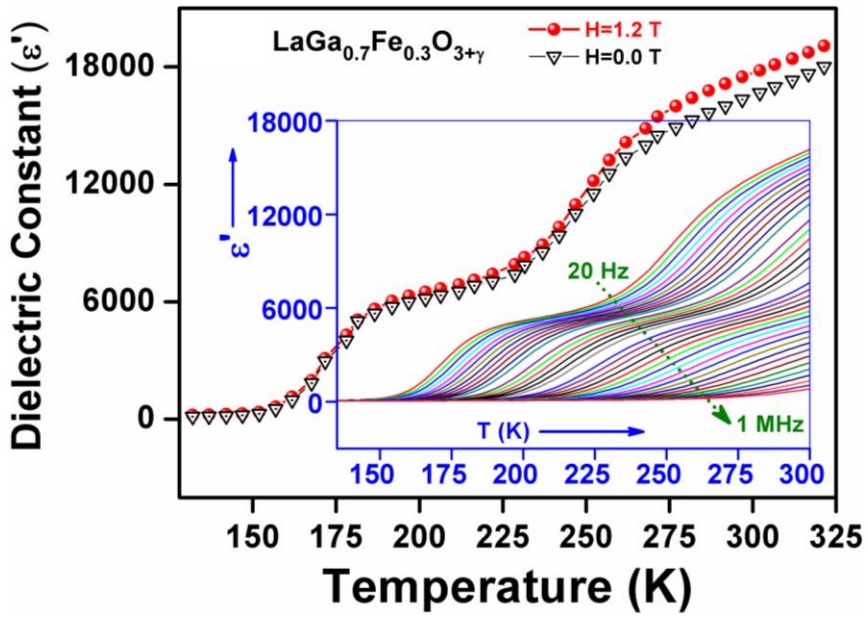

Figure 5.7: Room Temperature dependent ε' at a fixed frequency (20 Hz) recorded in the absence (H=0.0 T) and presence of magnetic field (H=1.2 T) for $LaGa_{0.7}Fe_{0.3}O_{3+\gamma}$. Inset shows temperature dependent dielectric dispersion under zero magnetic field.

to magnetic field even at the lowest temperature (132 K for present case) and hence, the on-set of present temperature dependent MD response can be expected at a temperature lower than 132K. The inset of Figure 5.7 shows ε' of $LaGa_{0.7}Fe_{0.3}O_{3+\gamma}$ as a function of temperature under zero magnetic field for probing frequencies ranging from 20 Hz to 1MHz. Above 150 K, a large dielectric dispersion and frequency dependence of ε' is evident from the inset of Figure 5.7. The appearance of similar temperature dependent MD response in $LuFe_2O_4$ has been attributed to change in polarizability associated with the ordering of coexisting Fe charge sates and charge fluctuations on Fe sites [21], whereas, similar large dielectric dispersion (Figure 1.7) was attributed to order-disorder ferroelectricity (ferroelectric domain boundary motion) generated due to ordering of mixed Fe valences [21,90]. Ultimately, following four major observations (considering MD phenomenon) are noticeable from Figure 5.4 to 5.7 – (i) a

significant RTMD effect is appearing at a low magnetic field. (ii) Both ε' and *tanδ* are increasing with increasing magnetic field over entire range of probing frequencies. This same trend indicates that the observed low field RTMD effect should be an intrinsic property of $LaGa_{0.7}Fe_{0.3}O_{3+\gamma}$ sample as the same is suggested [9]/pointed out [46]/shown [46,47,155] by others. (iii) The peak positions of both broad *tanδ*-peaks are clearly visible to be shifted towards higher frequency side with the application of magnetic field. (iv) *tanδ* increases with increasing magnetic field even at the frequencies $>10^6$ Hz (Figure 5.6). Since, contrary to Point (ii), the last two observations point towards the magneto resistive origin (negative dc MR) [9] of presently observed RTMD phenomenon [9], therefore, magneto-capacitance (MC%) and magneto-loss (ML%) have also been analyzed to get a better insight about the intinsicality of present MD response. Besides the same trend of change observed in ε' and *tanδ* due to magnetic field (Figure 5.4 and 5.5), the trends observed in MC% and ML% (both increase with increasing magnetic field at high frequencies ≥1MHz as shown in Figure 5.8 (a) and (b)), suggest that the presently

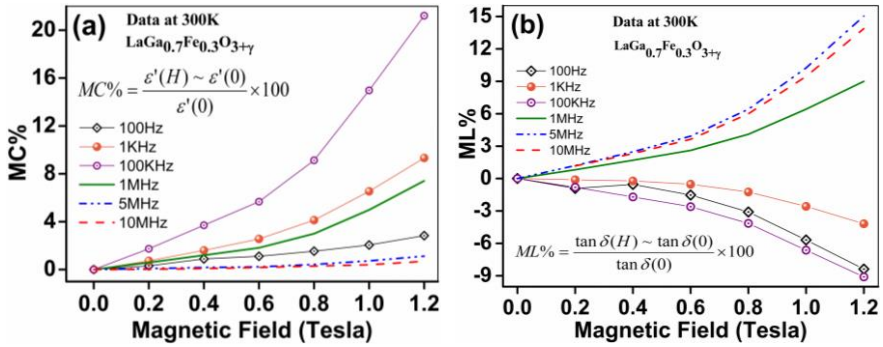

Figure 5.8: The trends of room temperature (a) magneto-capacitance (MC%) and (b) magneto-loss (ML%) as a function of applied magnetic field for $LaGa_{0.7}Fe_{0.3}O_{3+\gamma}$ measured at selected frequencies from 100 Hz to 10 MHz. Both MC% and ML% are increasing with magnetic field for probing frequency of $\geq 10^6$Hz. On the other hand at frequencies $<10^6$ Hz, MC% and ML% are changing oppositely due to increasing magnetic field. Both MC% and ML% have been calculated by using the formula shown in the corresponding Figure. Where, $\varepsilon'(0)$/*tanδ*(0) and ε'(H)/*tanδ*(H) is the value of dielectric constant/*tanδ* correspondingly in the absence (H=0.0T) and presence of magnetic field (H=0.2T to1.2T).

observed low field RTMD effect should be MR unaffected and possibly intrinsic nature of presently studied $LaGa_{0.7}Fe_{0.3}O_{3+\gamma}$ sample at frequencies ≥1MHz as the same is proposed by G. Catalan [9,46]. On the other hand, at frequencies < 1MHz the effect appears to be MR dominated as the trends observed in MC% and ML% are opposite at these frequencies (MC% is increasing and ML% is decreasing with increasing magnetic field). Moreover, MC% has been plotted as function of frequency under different magnetic fields as depicted in Figure 5.9. Two broad

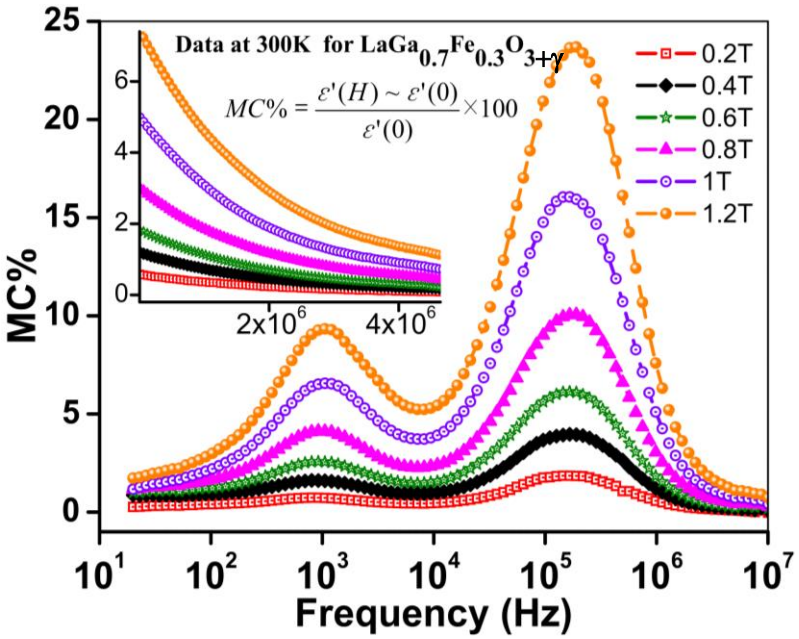

Figure 5.9: Room temperature MC% of $LaGa_{0.7}Fe_{0.3}O_{3+\gamma}$, plotted as a function of probing frequency for different magnetic fields. Inset displays MC% data at higher frequencies (≥10^6Hz) to show that the observed MD effect is significant even at such high frequencies. MC% has been calculated by using the formula shown in Figure. Where, $\varepsilon'(0)$ and $\varepsilon'(H)$ are the dielectric constant correspondingly in the absence (H=0.0T) and presence of magnetic field (H=0.2T to1.2T).

peaks in the MC% vs frequency plot are clearly visible across the frequencies corresponding to peaks (diffusive anomalies) in $tan\delta$ (ε') for all values of applied magnetic field. The MC% is found to be increased with increasing magnetic field even upto MHz frequencies (inset of Figure 5.9) i.e. over the entire range of probing frequencies. It is to be noted here, that the appearance of peak(s) in MC% versus

frequency data (i.e. the value of MC% is high) at the frequencies corresponding to relaxation peaks (inset (i) of Figure 5.5) indicate that the MC% is not a monotonic function of frequency. Since, the application of magnetic field makes the hopping of electron easier between Fe^{3+} and Fe^{4+} sites (as proposed in case of Mn doping; Figure 3.10), therefore, conductivity is increased which turns into the apparent decrease in dielectric thickness. This results into magnetic field induced apparently high value of ε' (considering the parallel plate capacitor geometry) especially at these relaxation frequencies which might be the possible reason for non-monotonic behavior of MC% as function of frequency (Figure 5.9). Further, the position of both the broad MC% peaks appears to be almost unaltered due to the application of different magnetic fields ranging from 0.2 T to 1.2 T. However, a careful analysis revealed that the frequency corresponding to MC% maximum is changing with applied magnetic field; the same is tabulated in Table 5.3. This behavior points toward the possibility of field- induced dipoles as an origin of presently observed RTMD effect in $LaGa_{0.7}Fe_{0.3}O_{3+\gamma}$ as Chandrasekhar et al. [161] have suggested that - to ruled out the possibility of field-induced dipolar relaxation, the said

Table 5.3: Frequencies corresponding to maximum value observed in broad peak of MC% for different magnetic fields (Figure 5.9).

Broad peak in MC%	Frequency (kHz) corresponding to MC% maximum for different magnetic fields (Figure 5.9)					
	0.2 T	0.4 T	0.6 T	0.8 T	1 T	1.2 T
Peak-1	0.85	0.80	0.88	0.96	1.05	1.03
Peak-2	163	163	166	180	151	180

MC% peak position should not be changed with the application of magnetic field. Eventually, similar to the trends of magnetic field dependent change ε' and $tan\delta$, the analysis of MC% and ML% also, provides mixed or contradictory information indicating intrinsic and resistive origin together.

5.3.5 *dc* MR and impedance spectroscopy (FDMR)

In order to further examine that whether the presently observed MD effect is MR dominated or it is completely MR unaffected, firstly RT dc MR has been recorded by means of I-V measurements as plotted in Figure 5.10. A small positive dc MR has been observed as the voltage

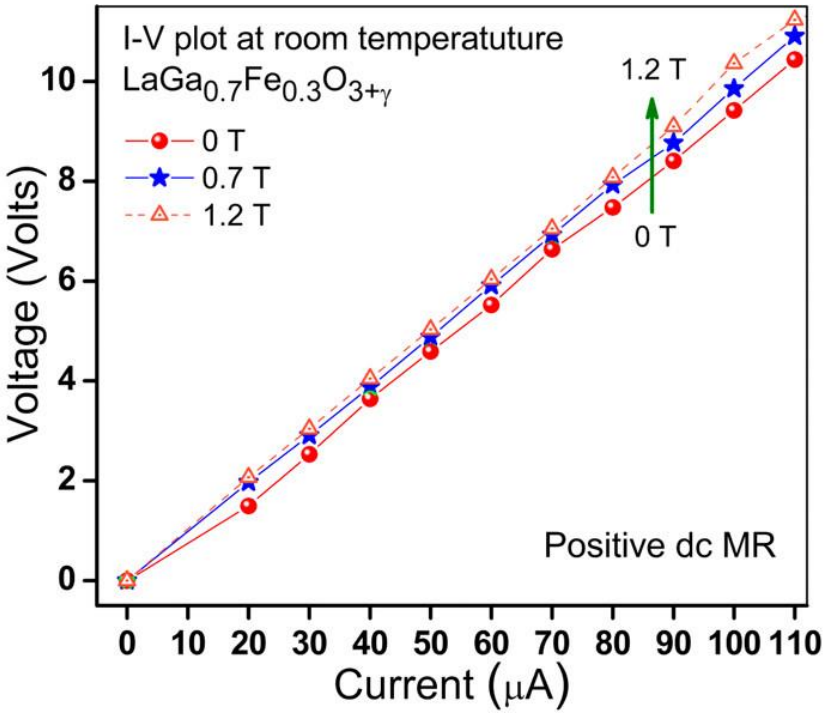

Figure 5.10: Room temperature I-V plot drawn by measuring the voltage for different values of current in the absence (H=0.0T) and presence (H=0.2T to1.2T) of magnetic field by using standard four-probe method.

across each value of current is found to be slightly increased due to increasing magnetic field as shown in I-V plot (Figure 5.10). Since no negative dc MR (which is expected as the MC% is increasing with magnetic field) is observed, therefore, present MD effect appears to be dc MR free. However, (i) as the observed shifting of *tanδ*-peak position towards higher frequency due to applied field (H=0.2T to 1.2T) is indicating towards the presence of resistive component [9] and (ii) since FDMR measurements are supposed to be more sensitive in such a case, therefore, to get a better view about the contribution of MR in observed effect, FDMR (20 Hz to 10 MHz) has also been analyzed by means of MRIS (MR via impedance spectroscopy)

measurements. These RT measurements are performed in the absence (H=0.0T) and presence of magnetic field (H=0.2T to 1.2T) to record

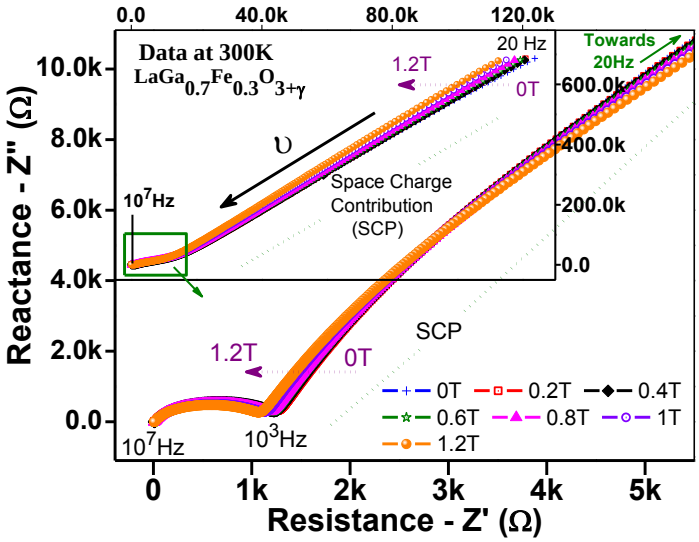

Figure 5.11: Room temperature *Cole-Cole* plot recorded for $LaGa_{0.7}Fe_{0.3}O_{3+\gamma}$ in the absence (H=0.0T) and presence (H=0.2T to 1.2 T) of magnetic field. For clarity, the data corresponding to entire range of probing frequencies is shown in the inset, whereas mid-high range frequency data (enclosed by a rectangular green box in the inset) is magnified as main panel. To visualise the effect of magnetic field with more clarity, this mid-high range frequency data is further magnified and shown accordingly in Figure 5.12 and 5.13. *Note*- For convenience, the data on y-axis is multiplied by minus one.

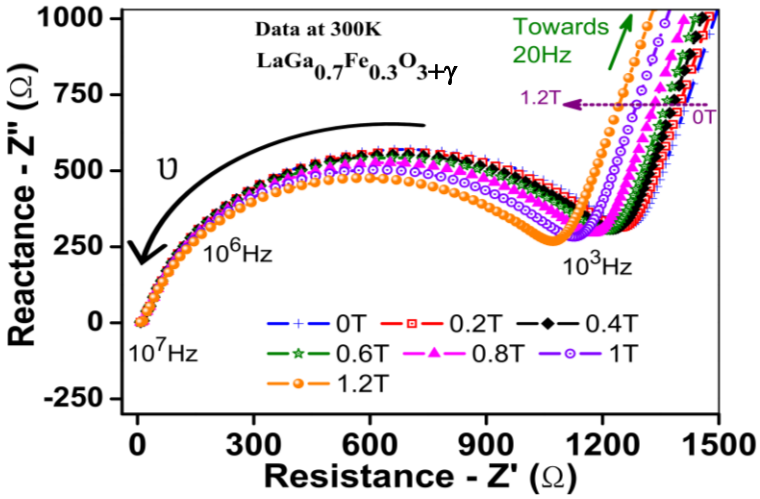

Figure 5.12: Room temperature *Cole-Cole* diagram of $LaGa_{0.7}Fe_{0.3}O_{3+\gamma}$. For clarity, the data corresponding to entire range of probing frequencies is shown separately in the inset of Figure 5.11 and only mid-high range frequency data is magnified here as main panel. The data is measured in the absence (H=0T) and presence of magnetic field (0.2T to 1.2T). *Note*- For convenience, the data on y-axis is multiplied by minus one.

the real (Z′) and imaginary (Z″) part of impedance. The data of these MRIS measurements for $LaGa_{0.7}Fe_{0.3}O_{3+\gamma}$ sample is shown as a Cole-Cole (Nyquist) plot in Figure 5.11. For clarity, entire range of probing frequencies is depicted in the inset whereas mid to high range frequency data is shown as main panel (Figure 5.11). To show the effect of magnetic field clearly, this main panel data (Figure 5.11) is further magnified in Figure 5.12. Whereas, Figure 5.13 shows fit of Nyquist plot only for Z-Z″ data corresponding to H=0.2T (for the data range, shown in Figure 5.12). It is clear from Figure 5.11 and 5.12 that

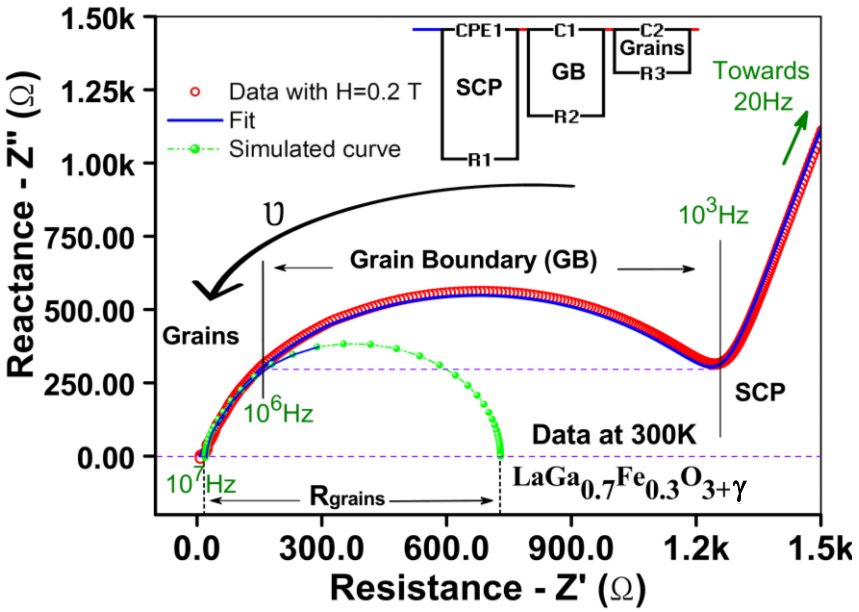

Figure 5.13: Fit of *Cole-Cole* plot for $LaGa_{0.7}Fe_{0.3}O_{3+\gamma}$ (at H=0.2T) by considering the circuit model shown in the figure. The open red symbols (circles) are representing experimental data whereas solid blue line and green balls are presenting fitted and simulated pattern respectively. The frequency segments corresponding to SCP (space charge polarization), GB (grain boundary) and grains were identified by fitting and simulating this data with the displayed circuit model. *Note*- For convenience, the data on y-axis is multiplied by minus one.

at the frequencies corresponding to space charge and grain boundary contributions i.e. at low and mid-range of probing frequencies (20 Hz to $<10^6$ Hz), the value of Z′ (resistance) decreases significantly due to increasing magnetic field as indicated by dotted arrow. This suggests that the large MD effect observed at these frequencies (Figure 5.4) is MR affected/dominated. This frequency dependent negative MR can

be attributed to the hopping of electrons between Fe^{3+} and Fe^{4+} via intermediate oxygen by following the double exchange mechanism. The magnetic field makes this exchange further easier [29] and consequently Z' and Z'', both, decrease i.e., negative MR takes place, which (along with non-intrinsic interface effects; arises due to the accumulation of free charges at interface between different grains within the bulk itself and at the electrode-sample interface which are recognized as Maxwell-Wagner and space charge polarizations respectively), appears to be responsible for presently observed large (significant) MD effect at low (mid) frequencies. Moreover, as the magnetic field makes the said exchange further easier, therefore, the dynamic dipole (Fe^{3+}/Fe^{4+}) starts oscillating with a higher frequency and hence *tanδ*-peak(s) corresponding to this characteristic frequency is (are) observed to be shifted towards higher frequency side due to the increasing magnetic field (Figure 5.5). Ultimately, the magnetic field dependent shifting of *tanδ*-peak position toward higher frequency can be credited to negative FDMR. Nevertheless, the MD effect is expected to be MR free or even intrinsic when it is measured at probing frequencies higher (presently $\geq$ 100 kHz) to characteristic frequency [9] (the frequency of electron hopping between Fe^{3+} and Fe^{4+} sites) because at such high probing frequencies the hopping charge transport (ultimately FDMR) gets suppressed as the carriers have no chance to jump between hopping cites [9,115] (presently Fe^{3+} and Fe^{4+}), therefore, at these frequencies, only grain contribution is expected with a low value of *tanδ* [115] (presently <1; as shown in the Figure 5.6). Further, as shown in Figure 5.11, at frequencies corresponding to grain contributions i.e., $\geq 10^6$ Hz, neither part of impedance is changing due to the application of magnetic field. This discards any contribution of MR in the observed MD coupling at these high frequencies (Figure 5.4 and Table 5.2). It is worth mentioning that the different frequency segments corresponding to SCP (space charge polarization), GB (grain boundary) and grains contribution are identified by fitting Z' -Z'' data for H=0T to H=1.2T (for the data

range, depicted in Figure 5.12) with the circuit model depicted in Figure 5.13. The data is fitted with the help of EIS (Electrochemical Impedance Spectroscopy) Spectrum Analyzer software. The results of fitting are shown in Figure 5.13 only for the data (Z'-Z'') corresponding to H=0.2T as a representative. The data is fitted over the entire range (the range shown in Figure 5.12) of probing frequency considering a series of three capacitors (each having a resistance in parallel individually). The first capacitor-CPE1 represents constant phase element. The contributions of grains, GB and bulk-electrode interface/ SCP have been separated with the help of this fitted data (Figure 5.13). It is known that SCP appears at low frequencies, therefore, the first parallel combination (CPE1-R1) is representing SCP region as low frequency (500 Hz to 1 kHz) data was fitted and simulated by varying the values of mainly CPE1 and R1. It appears that the large semicircular arc (10^3 Hz to 10^7 Hz) has only a single curvature but actually it consists of two curvatures and it is alone fitted with a series combination of two capacitors; each having a resistance in parallel individually (i.e.,C1-R2 and C2-R3). In this regard, a segment of this arc was fitted and simulated separately for a parallel combination of a capacitor and a resistor (C2-R3). Consequently, a new simulated smaller semicircle (green balls), corresponding to 'C2-R3', is observed as shown in Figure 5.13. Since, this small segment is corresponding to higher range of probing frequency (10^6 Hz to 10^7 Hz), hence, it has been recognized as the region corresponding to grains contribution. The remaining segment corresponding to midrange of probing frequency (10^3 Hz to 10^6 Hz), fitted mainly with the variation in C1 and R2, was assigned as the GB region. In this way, in $LaGa_{0.7}Fe_{0.3}O_{3+\gamma}$ sample, three different capacitance regions have been identified. These were separated on the basis of corresponding frequency range and hence recognized as SCP (CPE1-R1), GB (C1-R2) and grains (C2-R3) contributions accordingly. Now, as far as the effect of magnetic field is concern, FDMR analysis reveals that the resistance corresponding to grain contribution (R_{grain}) is found to be

almost equal in the absence (H=0T) and presence (H=0.2T to H=1.2 T) of magnetic field, suggesting that the MD coupling at frequencies $\geq 10^6$ Hz is MR-unaffected. Whereas, the resistance corresponding to both SCP and GB is decreasing with increasing magnetic field which is clearly distinguishable also in Figure 5.11 and 5.12. Since the comparison of resistance in the absence (H=0T) and presence (H=0.2T to H=1.2T) of magnetic field is the main concern of present MRIS study,—therefore, present IS analysis is limited only upto the identification of above mentioned regions (i.e. SCP (CPE1-R1), GB (C1-R2) and grains (C2-R3)) which are contributing to observed magneto capacitance at corresponding frequencies.

5.3.6 Impact and origin of excess oxygen

It can be clearly seen from Figure 5.13 that in present $LaGa_{0.7}Fe_{0.3}O_{3+\gamma}$ compound, grains are less insulating (Note-the difference of x-axis intersects of corresponding semicircular arc gives the value of resistance associated with particular contribution) as compare to GB. In presently studied $LaGa_{0.7}Fe_{0.3}O_{3+\gamma}$ compound, oxygen excess (i.e. presence of Fe^{4+}along with Fe^{3+}) can be considered as one of the causes responsible for low resistivity of grains (owing to hopping charge transport facilitated through Fe^{3+}-O-Fe^{4+} Fe^{3++}-O-Fe^{4+}….path) as the similar enhancement of grains conductivity has been attributed to oxygen vacancies in different compounds [29,169,170]. From application point of view, this low resistivity or high dielectric loss of $LaGa_{0.7}Fe_{0.3}O_{3+\gamma,}$ makes it difficult for this material to be used in microelectronic devices because such devices require a material with very low *tanδ* (low leakage). As the leakage is associated with the coexistence of Fe^{3+} and Fe^{4+} in $LaGa_{0.7}Fe_{0.3}O_{3+\gamma}$, the value *tanδ* can be further minimized by making the samples with better oxygen stoichiometry (i.e. either with Fe^{3+} alone or with Fe^{4+} alone) by means of annealing of these samples in a proper gas environment under precisely controlled and calibrated gas flow. As far as the origin of present MD effect is concern (particularly MR free contribution, which

may be present also at lower frequencies but might have gone suppressed due to the dominance of extrinsic effects), the observed increase in ε' under H=0.2T to 1.2T can be understood in terms of change in orthorhombic strain which may appear in LGO due to the doping of Fe at Ga site similar to that in $LaMn_{1-x}Ga_xO_3$ [94]. The evolution of such orthorhombic strain in $LaMn_{1-x}Ga_xO_3$, is discussed by Farrell *et al.* [94] in terms of transformation/rotation of Mn - $(3x^2 - r^2)/(3y^2 - r^2)$ orbital into the $(3z^2 - r^2)$ state due to replacement of Mn^{3+} with Ga^{3+} because Mn^{3+} is Jahn-Teller (JT) distorted [158] and its long Mn-O (2.18 Å) [94] distance is significantly larger than the Ga-O (1.97 Å) [94] or Mn-O short bond (1.90 Å) [94]. In present $LaGa_{0.7}Fe_{0.3}O_{3+\gamma}$ sample, 29% of total Fe is in its 4+ state which is JT distorted [171] (similar to JT active Mn^{3+} ion, Fe^{4+} also has 4 electrons in its *d* orbital). Owing to that, Fe^{4+} forms two long (short) Fe-O bonds and four short (long) Fe-O bonds with octahedrally connected oxygen [171]. It is to be noted that the ionic radius of Ga^{3+} (0.62 Å) [94,157] is smaller than that of the Fe^{3+} (0.645Å) [157] whereas it is significantly larger to that of Fe^{4+} (0.585 Å) [157]. Thus by considering all these parameters, the evolution of orthorhombic strain in present $LaGa_{0.7}Fe_{0.3}O_{3+\gamma}$ system appears reasonable by means of arrangement of Fe orbitals, transforming due to the replacement of non-JT active Ga^{3+} ions with strongly (weakly) JT distorted Fe^{4+} (Fe^{3+}) ion in a similar manner to that reported for $LaMn_{1-x}Ga_xO_3$ [94]. It is important to mention that for such highly correlated electron systems, spin and orbital degrees of freedoms are strongly coupled with each other. Thus, as the application of magnetic field (H=0.2T to 1.2T), aligns magnetic moments related to Fe ions in $LaGa_{0.7}Fe_{0.3}O_{3+\gamma}$, therefore, readjustment of already transformed Fe orbitals is quite possible which may lead to a change in the above discussed orthorhombic strain and hence in ε'. Ultimately, presently observed change in ε' under the influence of external magnetic field can be considered as magnetostriction (phenomenon [94,132,172] associated with the change in lattice parameters and/or bond distances/bond angles due to the magnetic

field) originated which needs to be explored in detail to confirm our speculation. It is clear from above results and analysis that existence of Fe^{4+} (oxygen excess) has a significant and mixed impact on dielectric (*tanδ* or leakage) and MD properties of studied $LaGa_{0.7}Fe_{0.3}O_{3+\gamma}$ compound. The presence of Fe^{4+} is good as it is relatively a stronger Jahn-Teller active ion [171] than that of the Fe^{3+} i.e., octahedron around Fe^{4+} possess relatively lower symmetry and hence may contribute in enhancing the magnitude of MD coupling whereas it is a bad character because it provides path for leakage (i.e, Fe^{3+}-O-Fe^{4+} Fe^{3++}-O-Fe^{4+}…).

It is to be noted that the 4+ state of Fe ion is not observed so often, but, has been observed and reported in specific compounds even at ambient conditions [105,157,171,173,174] and interestingly also in the same series of samples i.e., LGFO compound [175] as confirmed through XPS (X-ray photoelectron spectroscopy). Even though the 4+ state of Fe is reported for LGFO series itself [175], the stability of Fe^{4+} can be a matter of concern and we have tried to understand this existence of Fe^{4+}on the basis of observed excess oxygen. We propose that the excess oxygen in present LGFO sample can be attributed to (i) it's adsorption at the surface [138,139] and/or (ii) vacancies at A (La) and/or B (Ga/Fe) cation sites considering ABO_3 structure [139,140]. The first situation is discussed in detail elsewhere for other ABO_3 structures [138,139]. In order to understand the second situation (vacancy at cation site) [139,140], we have performed 'bond-valance-sum' calculations in FullProf suit. In these calculations, in order to account the oxygen excess, we deliberately created vacancy at cation cite by assuming following three situations (considering a slightly lower value of occupancy than its actual value for corresponding element) –

(i) Deficiency of only La atom (s)

(ii) Deficiency of only Ga atom (s)

(iii) Deficiency of only Fe atom (s).

It is noticeable that the deficiency of a combination of either any two or all three cations is supposed to further increase the oxygen excess, therefore, these combinations have not been considered for calculations. Present 'bond-valance-sum' analysis reveals (Table 5.4) that amongst all present cations (La, Ga, Fe), the charge state of Fe ion is affected most due to the vacancies at any cationic site. Moreover, the oxidation state of Fe exceeds owing to the cation deficiency and affected most for the La vacancy. In order to further confirm the

Table 5.4: Charge on cation/anion calculated (by considering cation vacancy) through 'bond-valance-sum' calculations in FullProf suit.

Vacant cation site	charge on cation/anion				
	La	Ga	Fe	O_1	O_2
Ideal case (No vacancy)	2.999	2.942	3.182	2.0048	1.998
Vacancies at only La site	3.051	3.073	3.324	2.026	2.075
Vacancies at only Ga site	2.961	3.033	3.281	1.998	2.021
Vacancies at only Fe site	2.960	3.032	3.280	1.997	2.023

same, the Bader charge on La, Fe, Ga and Oxygen ions was determined using DFT (density functional theory) based first principles calculations. For this purpose, we have investigated 25% Fe-doped $LaGaO_3$ i.e., $LaGa_{0.75}Fe_{0.25}O_3$ (as for $LaGa_{0.7}Fe_{0.3}O_{3+\gamma}$ composition, 30% Fe doping involves large number of atoms whereas doping of 25% Fe is achieved only with 20 atoms in a supercell) system. We have used spin-polarized DFT calculations as implemented in the Vienna Ab initio Simulation Package (VASP) [141]. Projector augmented wave (PAW) method [142,143] is employed using an energy cut-off of 470 eV to describe the electronic wave functions. The local density approximation (LDA) + U method [144] is used to account the strong on-site correlated electrons in the partially filled *d* orbitals. We have employed correlation energy (U) of 4 eV and exchange energy (J) of 1 eV for Fe *d*-orbitals [144]. These U and J values have been well tested and used in similar systems [145,146]. A 20 atom (2×2×1) supercell is used to study $LaGa_{0.75}Fe_{0.25}O_3$. The Monkhorst-pack [147] generated set of 7×7×7 (for 20 atoms supercell) K-points are used to optimize the structures. The convergence criteria

for energy and force are set at 10^{-6} eV and 10^{-3} eV/Å respectively. We have calculated La, Ga and Fe defect formation energy in $LaGa_{0.75}Fe_{0.25}O_3$ system to understand that which cation-defect, amongst La, Ga and Fe, is most favorable. Figure 5.14 shows the structure with La-defect as a representative case. The defect formation energy (E_f) is calculated using the following equation:

$$E_f = [E_D + E_\mu] - E_p$$

where, E_D and E_P represent total energies of defected and pure $LaGa_{0.75}Fe_{0.25}O_3$ systems. E_μ represents chemical potential of lanthanum (μ_{La}), gallium (μ_{Ga}) and iron (μ_{Fe}) in their respective bulk structures. The chemical potential energy is calculated from their most

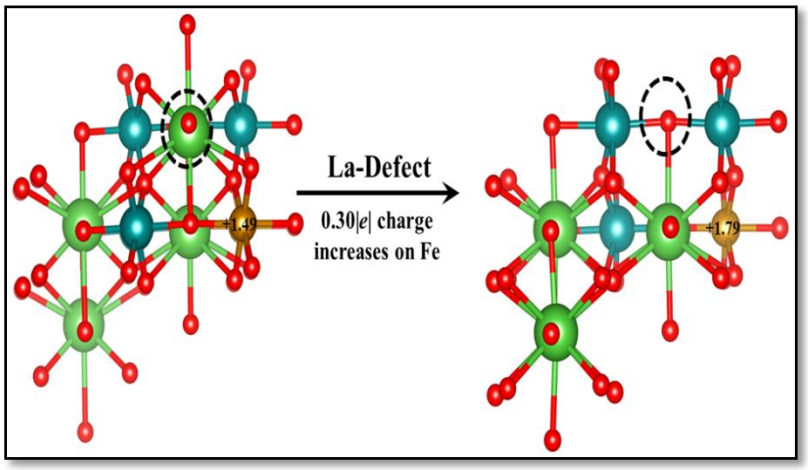

Figure 5.14: The change in Bader charge on Fe atom due to the La-defect in $LaGa_{0.75}Fe_{0.25}O_3$. Here, green, blue, golden and red color balls denote La, Ga, Fe and O atoms, respectively.

stable crystal structure such as La in hexagonal close-packed (hcp) `, Ga in orthorhombic [149], and Fe in body-centred cubic (bcc) [176] respectively. Present defect formation energy calculations reveal that La-defect (E_f = 1.02 eV) formation is energetically favorable compared to Fe (5.61 eV) and Ga (7.85 eV) defects. Therefore, the La-defected structure is considered for the Bader charge analysis. The Bader charge analysis [150,151] is performed using the Henkelman program [152] with near-grid algorithm refine-edge method. From our Bader charge analysis, we find that Fe losses 0.30|*e*| (Table 5.5) due to the La-defect

(Figure 5.14), whereas charges on other atoms are almost unchanged. Thus, Fe gains more positive charge due to the La-

Table 5.5: Average Bader charges (total electrons) on La defected $LaGa_{0.75}Fe_{0.25}O_3$ structure. Net effective charges (average) are given in parenthesis.

Pure (No defect)	Defect (cation vacancy)
La= 8.95 (+2.05)	La= 8.92 (+2.08)
Ga= 1.31 (+1.69)	Ga=1.32 (+1.68)
Fe = 6.51 (+1.49)	Fe = 6.21 (+1.79)
O = 7.23 (-1.23)	O = 7.09 (-1.09)

In this way, present 'bond-valance-sum' and Bader charge analysis (DFT) are found to be consistent with each other and the La-defect formation appears to be responsible for making the oxidation state of Fe more than 3+.

5.3.7 Evidence of intrinsic nature of observed MD coupling: Magnetic field dependent Raman spectroscopy

Magnetic field dependent Raman spectra for $LaGa_{0.7}Fe_{0.3}O_{3+\gamma}$ were recorded between 300 to 3000 cm^{-1} and the results are shown in Figure 5.15. Note that similar to undoped/doped $LaFeO_3$ and $La(TM)O_3$ systems [97,168,177,178], the observed Raman spectrum is basically dominated by the FeO_6 octahedral vibrational modes. Using previous conventions, the spectral structures between or around 400-500 and 600 cm^{-1}, (Figure 5.15) were respectively assigned as bending (*B*) or Jahn-teller asymmetric stretching (*JT-AS*) and symmetric stretching (*SS*) FeO_6 octahedral Raman modes [177,178]. Note that the *SS* FeO_6 Raman mode appears around 625 cm^{-1} in $LaFeO_3$ [177,178] and becomes harder i.e., peaks shifts towards higher frequency with doping [177,178], therefore, its appearance at 655 cm^{-1} in $LaGa_{0.7}Fe_{0.3}O_{3+\gamma}$ sample is reasonable due to Ga substitution at Fe site (considering $LaFeO_3$ as parent compound). Similarly features corresponding to 441 and 503 cm^{-1} are also appearing at higher wavenumber relative to $LaFeO_3$ (parent) i.e., 431 and 486 cm^{-1}[177,178]. It is to be noted that at/around 440 and 500 cm^{-1} (Figure 5.15 (b)), the phonon peak of *JT*

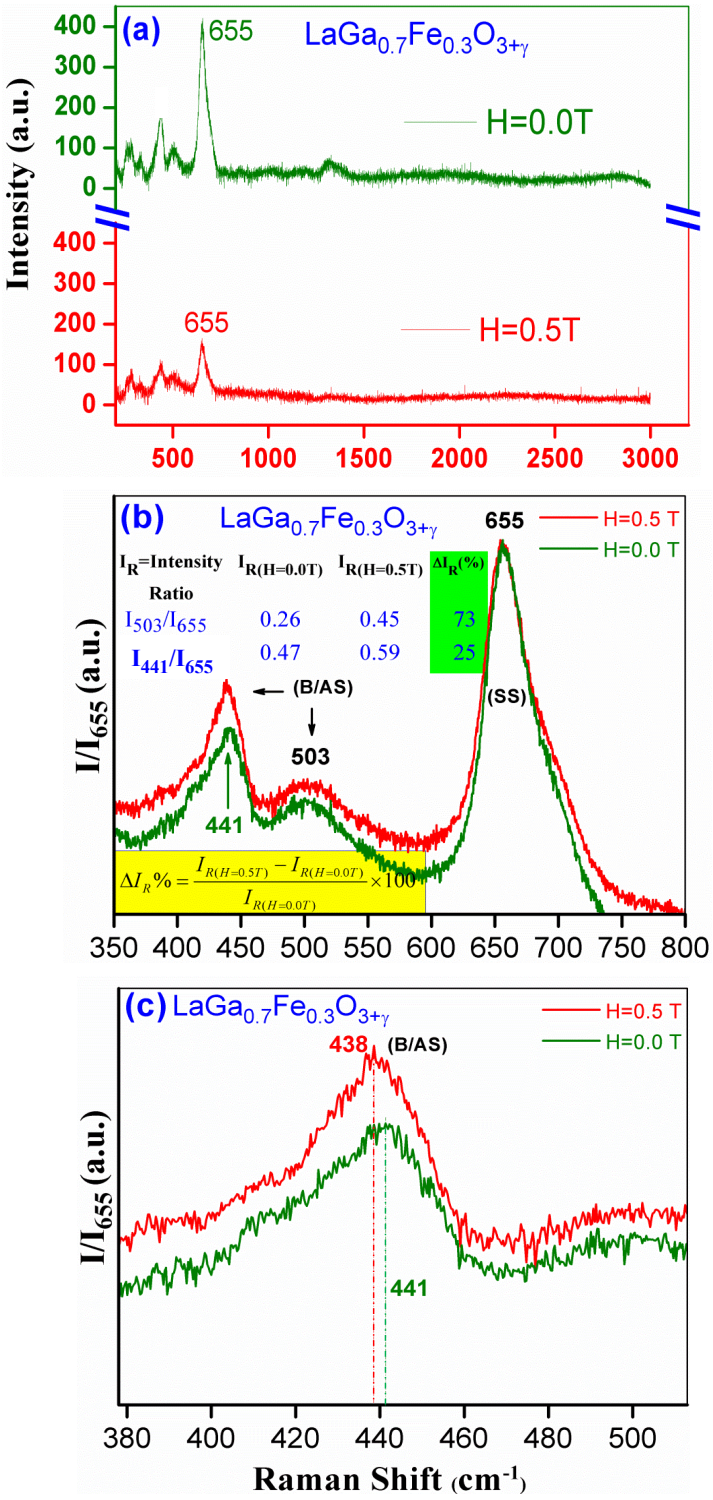

Figure 5.15: (a) Room temperature Raman spectra of $LaGa_{0.7}Fe_{0.3}O_{3+\gamma}$ recorded between 300cm^{-1} to 3000 cm^{-1} in the absence (H=0.0T) and presence (H =0.5T) of magnetic field. (b) Magnified view across the peaks corresponding to 441, 503 and 655 cm^{-1}. (c) Shifting of 441 peak towards lower frequency side. In (b) and (c), the intensity is scaled by the intensity of peak corresponding to 655 cm^{-1}. Table enclosed in (b) represents change in relative intensity under a magnetic field of H=0.5T. This change is calculated by using the formula shown in (b).

(Jahn-Teller) active anti-symmetric stretching (*AS*) mode related to TMO_6 tilting angle, also coexist along with the above mentioned bending FeO_6/TMO_6 octahedral modes [97,168,177]. Interestingly for $LaGa_{0.7}Fe_{0.3}O_{3+\gamma}$, due to the application of external magnetic field, the relative intensity ratio I_R is changed significantly (Figure 5.15 (b) and enclosed Table), indicating that the bending and/or *JT-AS* FeO_6 octahedral modes are sensitive to externally applied magnetic field. Figure 5.15 (c) shows the magnified view around the peaks corresponding to 441 cm^{-1}. Interestingly, a significant red shift from 441 cm^{-1} to 438cm^{-1} due to the application of magnetic field is clearly visible. This shifting of peak (*B/JT-AS*) to lower wave-number side signifies softening of *B/AS* FeO_6 octahedral modes/frequencies, indicates expansion of material [97] (i.e., magnetostriction) because, an exactly opposite behavior i.e. hardening of *SS* modes has been reported as signature of volume compression in $LaMn_{1-x}Ga_xO_3$ compound [97]. As a result of this volume expansion (considering uniform expansion for a circular pellet), the observed increase in ε' i.e., positive MC%, appears justified in accordance to relation (3.1) as in case of a circular pellet sample, ε' scales with *A* (for uniform magnetic expansion /compression). This analysis reveals that the observed MD coupling is an intrinsic nature of $LaGa_{0.7}Fe_{0.3}O_{3+\gamma}$ sample. This analysis supports our prediction (section **5.3.6**) as the spin-phonon coupling induced magnetostriction mechanism appears responsible for intrinsic part of observed RTMD effect in $LaGa_{0.7}Fe_{0.3}O_{3+\gamma}$. It is important to note that FeO_6 is a centrosymmetric octahedron consisting of a weak *JT* active Fe^{3+} ion at its center, but, in $LaGa_{0.7}Fe_{0.3}O_{3+\gamma}$ sample, 29% of total Fe is in its 4+ state which is strong *JT* active [171] and it forms relatively a distorted/asymmetric FeO_6 octahedron. The magnetic field dependent shifting of peak corresponding to *AS* (441 cm^{-1}) indicates softening of frequency modes of an asymmetric FeO_6 octahedron consisting *JT* active Fe^{4+} ions. Which could be the possible reason of magnetic expansion induced MD effect observed in $LaGa_{0.7}Fe_{0.3}O_{3+\gamma}$. This

suggests that in the observed MD coupling, Fe^{4+} is contributing significantly.

5.4 Summary

Room temperature MD effect with a low magnetic field was observed in $LaGa_{0.7}Fe_{0.3}O_{3+\gamma}$. The trends of changes observed in dielectric constant (ε'), *tanδ*, MC% and ML% due to the application of magnetic field have been analyzed systematically. Similar to Mn doped LGO (chapter 3 and 4), present trend analysis also provides contradictory information about the resistive (MR) contributions in MD coupling. In this regard, analysis of RT frequency dependent MRIS provided better and conclusive information, suggesting that at frequencies ≥1MHz the observed MD coupling is MR-unaffected. However, at lower frequencies, the presently observed MD phenomenon appears MR dominated which has been attributed to the electron hopping between Fe^{3+} and Fe^{4+} sites along with space charge polarizations. The MR-unaffected part of observed MD effect has been first speculated as magnetostriction originated and then evidenced with magnetic field dependent Raman spectroscopy. The excess of oxygen i.e., the coexistence of Fe^{3+} and Fe^{4+} along with the charge state of Fe 3.29 (> 3) in the studied $LaGa_{0.7}Fe_{0.3}O_{3+\gamma}$ sample was established through iodometric titration and XANES. The stability of Fe^{4+} ion (s) in $LaGa_{0.7}Fe_{0.3}O_{3+\gamma}$ sample is credited to the oxygen excess/excess of charge (>3) on Fe ion. This oxygen excess/excess of charge (>3) on Fe ion i.e., the stability of Fe^{4+} ion (s) in the studied $LaGa_{0.7}Fe_{0.3}O_{3+\gamma}$ system, has been understood in terms of cation vacancies by means of 'bond-valance-sum' and Bader charge analysis (DFT based first principles calculations). In summary, a significant RTMD effect is observed in $LaGa_{0.7}Fe_{0.3}O_{3+\gamma}$ and the origin of oxygen excess (presence of Fe^{4+}), along with its impact upon dielectric and MD properties is understood. We have considered a possibility that the low frequency intrinsic part of observed RTMD coupling might have been suppressed by dominating FDMR effect and could not be detected as the system

was probed only with electrical measurement technique(s). Thus, in this regard, in order to concretely justify the intrinsicality of present MD coupling, magnetic field dependent measurements using a non-electrical characterization technique (where, electrical resistance does not contribute in signal; Raman spectroscopy) has been employed. The results of magnetic field dependent Raman spectroscopy suggest that the observed MD coupling is intrinsic and magnetostriction (magneto expansion) meditated. This magnetic expansion in $LaGa_{0.7}Fe_{0.3}O_{3+\gamma}$ has been attributed to the reorientation/retransformation of spin-coupled Fe orbitals. In this way, our assumption that for MD and MR being electrical measurements, the intrinsic part of observed MD coupling at low frequencies might have gone suppressed due to the dominance of FDMR is found reasonable. Present in-depth MD study on Fe doped LGO supports our proposal (s) or conclusive arguments given in section **4.4.** Ultimately, RTMD effect in terms of its observation, evidence and origin has been systematically explored in Mn/Fe doped LGO (chapter 3 to 5). Our analysis (chapter 3 to 5) reveals that- (i) for analyzing resistive origin of MD coupling, measuring only dc MR or investigating only trends of magnetic field dependent change in ε'/C and $tan\delta$, are not sufficient. FDMR measurements in this regard provide better information and hence should necessarily be employed to analyze the resistive contribution in MD effect. (ii) The intrinsic MD coupling can be realized also in a compound which expands/shrinks in response to an externally applied magnetic field. (iii) Mn/Fe doped LGO shows scope for MD applications especially in samples with better stoichiometry. In addition to observed RTMD effect, the studied Mn doped LGO samples have been probed also to check the possibility of (i) multiferroicity (type-I or type-II [8]) by recording *P-E* and *M-H* loops, and (ii) direct MD coupling i.e., direct correlation between ε' and magnetic moment M (by recording temperature dependent dielectric and magnetic response with an expectation of coinciding anomalies in ε'-*T* (under zero magnetic field) and *M-T* data; similar to that shown in Figure 1.9).

Chapter 6

Large Dielectric Permittivity, Dielectric Dispersion and Possibility of Multiferroicity in Mn doped $LaGaO_3$

In the first half of this chapter, an observation of large dielectric permittivity in Mn doped $LaGaO_3$ (LGO) and its analysis is presented. The other half covers a study on temperature dependent dielectric behavior (under zero magnetic field) of Mn doped LGO and possibility of multiferroicity in these compounds. The results of this chapter are published in peer reviewed journals[††‡‡%]

[††] *H.M. Rai et al., RSC Adv.* **6** *(2016) 26621-26629.*
[‡‡] *H.M. Rai et al., J. Mater. Chem. C* **4** *(2016) 10876-10886.*
[%] *H.M. Rai et al., AMPT* ***3*** *(2017) 1-11.*

6.1 Introduction

Recently the search for new multiferroic and/or magnetoelectric materials triggered intense scientific research worldwide [179]. In this connection the lead free and bismuth based materials are investigated to a large extent [38,180] and the high k dielectric materials such as $BaTiO_3$, $SrTiO_3$ etc. were doped with magnetic impurities to achieve the above said properties [181]. Further the effect of doping on the occurrence of large ('colossal') dielectric permittivity (ε') has been vastly investigated in single layer and double layered perovskite oxides [182–188] due to their possible potential applications in electronic industries [189] and also due to their interesting physics [182]. The large value of ε' may be an intrinsic property of these materials which is originated due to the dipolar effects (ferroelectricity) associated with structural distortions (like presence of non-centro symmetric octahedron in different perovskite oxides) [31,182,190] and also due to order-disorder ferroelectricity (ferroelectric domain boundary motion) associated with ordering of mixed TM (transition metal) valences [21,90]**.** Additionally, this effect may appear also due to extrinsic processes such as hopping charge transport mechanism and inter-face effects associated with the Maxwell-Wagner (M-W) type heterogeneous structures [9,182–184] which are discussed in detail along with charge-density waves and metal-insulator transition, by Lunkenheimer *et al.* [182]**,** as existing possible mechanisms responsible for the occurrence of high ε' in different materials. The occurrence of large ε' and temperature dependent ε' dispersion of dielectric anomalies is reported also in various other systems like- rare-earth tungstate $CoEu_4W_3O_{16}$ [191], A/B co-substituted $Bi_{0.5}Na_{0.5}TiO_3$ perovskite [192], barium strontium titanate $Ba_{0.85}Sr_{0.15}TiO_3$ [193] etc.. The appearance of large ε', in some compounds having unfilled and unscreened subshells such as rare-earth metal tungstates, has been attributed to the field induced polarization [191,194]. Under present research work, in addition to RTMD effect (chapter 3 and 4), large ε',

temperature dependent dielectric dispersion and possibility of multiferroicity have also been explored in Mn doped lanthanum gallate (LGO). The observed results have been examined by means of room temperature (RT) impedance spectroscopy, XANES analysis, *P-E* (polarization versus electric field) and *M-H* (magnetization versus magnetic field) hysteresis loops, and temperature dependent magnetization measurements in ZFC and FC modes.

6.2 Experimental

Polycrystalline samples of Mn doped $LaGa_{1-x}Mn_xO_3$ (LGMO), with x=0, 0.05, 0.1, 15, 0.2 and 0.3 were prepared by conventional solid-state reaction route by following the process described in section **2.1.1**. The starting materials were La_2O_3 (99.999%), Ga_2O_3 (99.999%), and MnO_2 (99.99%). In order to examine the phase purity of the prepared samples the powder X-ray diffraction (XRD) experiments were carried out in angle dispersive mode using Huber 5020 diffractometer at BL-12 XRD beam line on Indus-2 synchrotron radiation source. The energy of the incidence X-ray beam was kept at 15 keV. [105]**.** FullProf Rietveld refinement package was used for refining XRD data [101,195]. For dielectric measurements single phase powdered samples were pelletized at a high pressure of 15 ton to form 1 mm thick circular discs of 12 mm diameter and these pellets were sintered in air at 1400 ^oC for 24 hours. Capacitance of prepared pellets has been measured at RT for a frequency range of 20Hz to 10 MHz by using Wynne Kerr 65120B precision impedance analyzer. Moreover, in order to demonstrate the effect of temperature on ε' and loss tangent ($tan\delta$), temperature dependent dielectric measurements were carried out in a temperature range of 120-430 K with the frequencies ranging from 100 Hz to 1 MHz. Mn K-edge XANES measurements have been carried out on the scanning extended X-ray absorption fine structure (EXAFS) beamline [134] (BL-9) of Indus-2 synchrotron source, in transmission mode. The beamline consists of Rh/Pt coated meridional cylindrical mirror for collimation and Si (111) based double crystal

monochromator (DCM) to select excitation energy. The second crystal of the DCM is a sagittal (bent in the direction perpendicular to the beam) cylinder with radius of curvature in the range 1.28-12.91 meters which provides horizontal focusing to the beam. The energy range of XANES was calibrated using Mn foil. The RT and low temperature (LT) *M-H* measurements along with *M-T* measurements in FC-ZFC mode were carried out on a quantum-design SQUID magnetometer. RT ferroelectric hysteresis *P-E* loops were recorded by using precision material analyzer (Radiant Technologies INC).

6.3 Results and discussions

This section is divided into five subsections; first two parts present the analysis for structural phase purity by XRD along with the validation of oxygen access (coexistence of Mn^{3+} and Mn^{4+}) in LGMO samples by means of XANES analysis. The third and fourth subsections respectively cover room temperature and temperature dependent dielectric studies for selected LGMO compositions. In last subsection, the status of magnetic and ferroelectric ordering is discussed for Mn doped LGO samples and possibility of multiferroicity is predicted.

6.3.1 XRD

Figure 6.1 (a) shows the powder XRD pattern for LGMO samples whereas Figure 6.1 (b) shows the refined XRD pattern for $LaGa_{0.7}Mn_{0.3}O_3$ as a representative of prepared LGMO samples. XRD patterns were refined considering orthorhombic structure with *Pnma* space group. The value for the goodness of fit was found to be ~1.45 for all samples. It should be noted that the absence of any unaccounted peak in the refined XRD patterns confirms the phase purity of LGMO samples. Rest of the other measurements was performed on these compounds by making circular pellets.

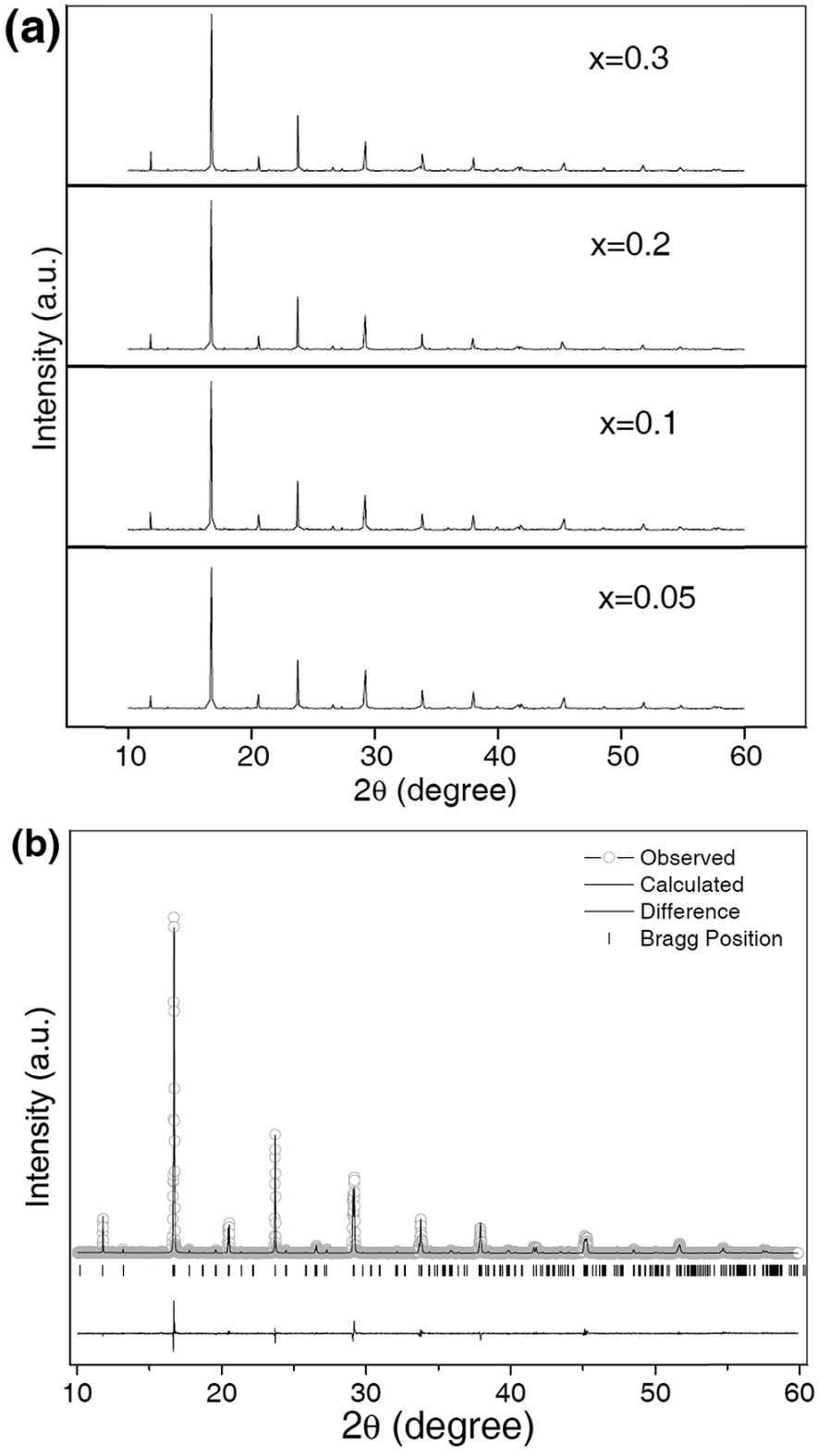

Figure 6.1: (a) X-ray diffraction data of $LaGa_{1-x}Mn_xO_3$ (LGMO) powder samples collected by using indus-2 synchrotron radiation source. (b) Rietveld refined X-ray diffraction data for $LaGa_{0.7}Mn_{0.3}O_3$ as a representative of studied LGMO samples. The absence of any unaccounted peak confirms the purity of structural phase of prepared samples.

6.3.2 XANES analysis

It is known for ABO_3 type oxides, that the presence of mixed charge states of B site cation significantly contributes to the dielectric nature (i.e. ε', $tan\delta$ and relaxation behavior [90,155,196–198]) of these materials therefore, in order to explain dielectric response of studied LGMO samples, charge states of Mn is estimated using XANES (X-ray absorption near edge structure) measurements [105–107,199] which were carried out with K-edge (Mn) energy of 6539 eV and the observed results are shown in Figure 6.2. The energies corresponding

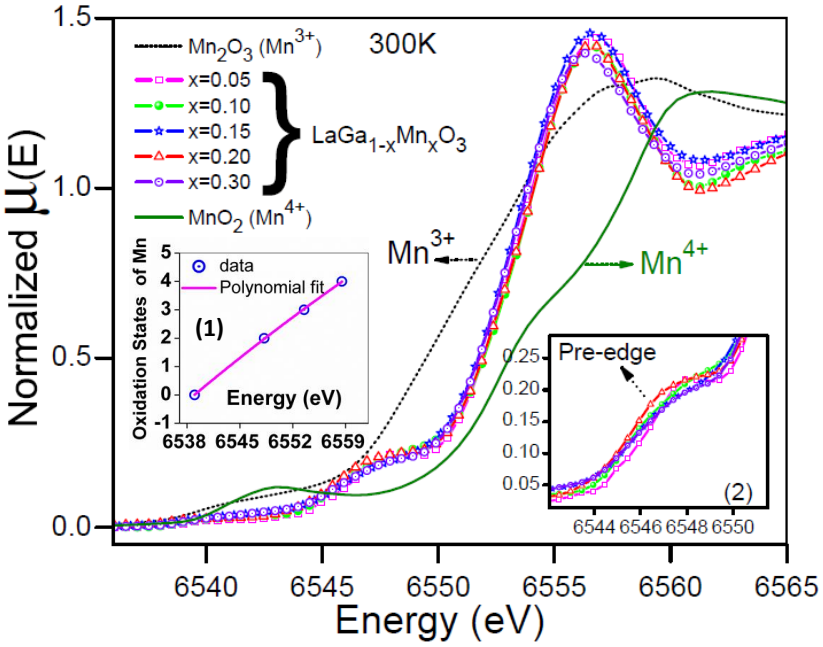

Figure 6.2: Room temperature XANES data carried out at Mn k-edge for $LaGa_{1-x}Mn_xO_3$ samples and two references corresponding to Mn^{3+} (Mn_2O, black dotted curve) and Mn^{4+} (MnO_2, green smooth curve) charge states. Mixed charge state of Mn in all presently studied LGMO samples is observed as the corresponding edge energies for all LGMO samples are found to be situated between the edge energies of Mn^{3+} and Mn^{4+} references. Inset-1 shows oxidation states of Mn references (i.e., 0, 2+, 3+ and 4+) as a function of corresponding K-edge energies. In that inset, pink curve is displaying 2nd order polynomial fit of this data. Inset-2 highlights pre-K-edge features for all LGMO samples.

to absorption edge of pure Mn metal foil (Mn^0) and powders of MnO (Mn^{2+}), Mn_2O_3 (Mn^{3+}) and MnO_2 (Mn^{4+}) have been used as references/standards. Figure 6.2 compares the normalized XANES

spectra of LGMO (x=0.05 to x=0.3) samples with Mn^{3+} and Mn^{4+} references. With an obviously noticeable chemical shift, absorption edge of all Mn doped LGO samples is found to be situated between Mn^{3+} and Mn^{4+} which points towards the presence of mixed Mn charge states in all the studied LGMO samples. Moreover, the oxidation states of Mn references (i.e., 0, 2+, 3+ and 4+) are plotted as a function of corresponding K-edge energies as shown in the inset (1) of Figure 6.2. This data is fitted with a 2^{nd} order polynomial [105] and by using fitting parameters oxidation states of Mn for all LGMO (x=0.05 to x=0.3) samples were estimated to be ranging between +3 and +4. These values of oxidation states suggest coexistence of Mn^{3+} and Mn^{4+} in all present LGMO samples (x=0.05 to x=0.3) which might be appearing due to oxygen off-stoichiometry i.e., due to excess of oxygen. This excess of oxygen and hence the coexistence of Mn^{3+} and Mn^{4+} in case of LGMO samples (x=0.2 to x=0.6) has been further validated through iodometric titration method (section **3.3.2**) and found reasonably consistent with the XANES results. The amount of excess oxygen, Mn charge state and relative percentage of Mn^{3+} and Mn^{4+}, for selected LGMO compositions determined through XANES analysis (determined in the same way as described in section **2.2.2.1, 3.3.2** and **3.3.3**) are tabulated in Table B-1 of Appendix B. Except x=0.2 and x=0.6, the tabulated values (Table B-1 of Appendix B) for all other LGMO compositions are yet to be verified/supported through some other technique like iodometric titration or XPS (X-ray photoelectron spectroscopy). The observed multivalence of Mn may lead to Jahn – Teller (JT) polaron hopping in these samples via Mn^{3+}- O^{2-}- Mn^{4+} path. It is well known that Mn^{3+} is an JT active/distorted ion [158] therefore it is noticeable that when an electron hop from Mn^{3+} to Mn^{4+} ion; then acceptor cation site becomes Mn^{3+} and carries the JT distortion i.e. the octahedron around donor (acceptor) Mn ion only shrinks (expands) as a whole, while its shape remains normal, mimicking the movement of breathing. This movement of electron by carrying JT distortion in company suggests the manifestation of polaron hopping mechanism

[196,200,201] in present LGMO system. In addition, since the chemical potential of Mn^{3+} is different to that of Mn^{4+}, therefore, a pair of nearest Mn^{3+} and Mn^{4+} can be treated jointly as an electric dipole (or Mn^{3+}/Mn^{4+} localized dipole; see Figure 3.9) with finite local polarization similar to Fe^{2+}/Fe^{3+} [29,155] and Mn^{3+}/Mn^{4} dipoles [196]. Due to the application of an electric field , when an electron jumps between Mn^{3+} and Mn^{4+} via O^{2-}; this polaron hopping is considered to be analogous to the flipping of Mn^{3+}/Mn^{4+} dipole which contributes significantly to the dielectric behavior of the material [29].

6.3.3 Room temperature dielectric response and its analysis

The high purity samples in the form of circular pellets were used for dielectric measurements. The RT frequency response of dielectric constant/dielectric permittivity (ε') for undoped LGO and $LaGa_{1-x}Mn_xO_{3+\gamma}$ (x=0.05, 0.1, 0.15, 0.2, and 0.3) is shown in Figure 6.3. It

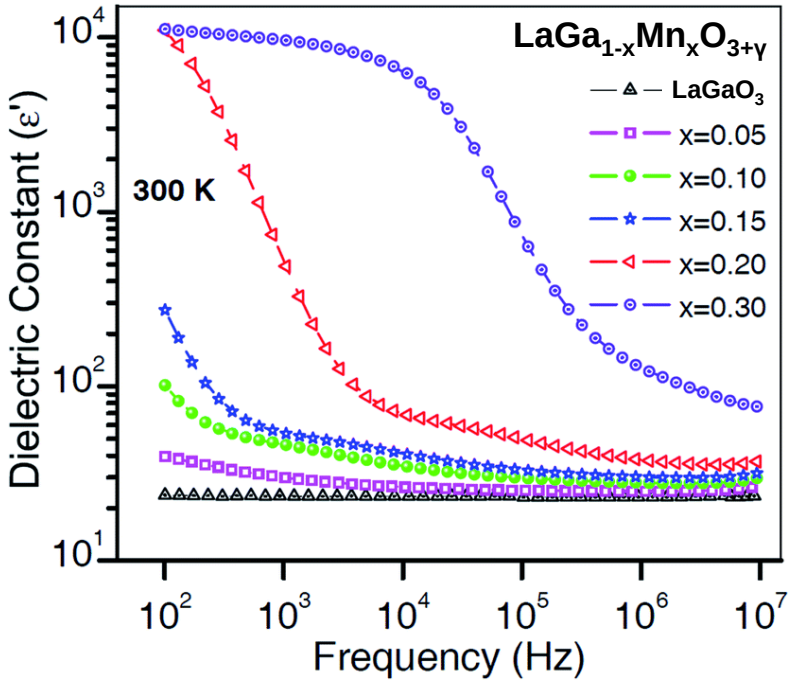

Figure 6.3: Room temperature frequency response of dielectric constant (ε') for undoped LGO and $LaGa_{1-x}Mn_xO_{3+\gamma}$ samples with x=0.05, 0.1, 0.15, 0.2 and 0.3.

can be clearly seen that the value of RT ε' (~24) for undoped LGO remains almost unaffected over the entire range of probing frequency

whereas for Mn doped samples (x≥0.1) the value of ε' decreases rapidly with increasing frequency in lower frequency region and decreases marginally in higher frequency region. Further; the value of ε' at RT increases significantly with increasing Mn doping throughout the frequency range. Interestingly a very large value of ε' (of the order of 10^4) is observed for samples with x=0.2 and x=0.3. Moreover, a diffused anomaly in ε' versus frequency data starts appearing with 5% doping of Mn and it is clearly visible for samples with higher percentage of Mn doping (≥10%). The presence of such an anomaly,

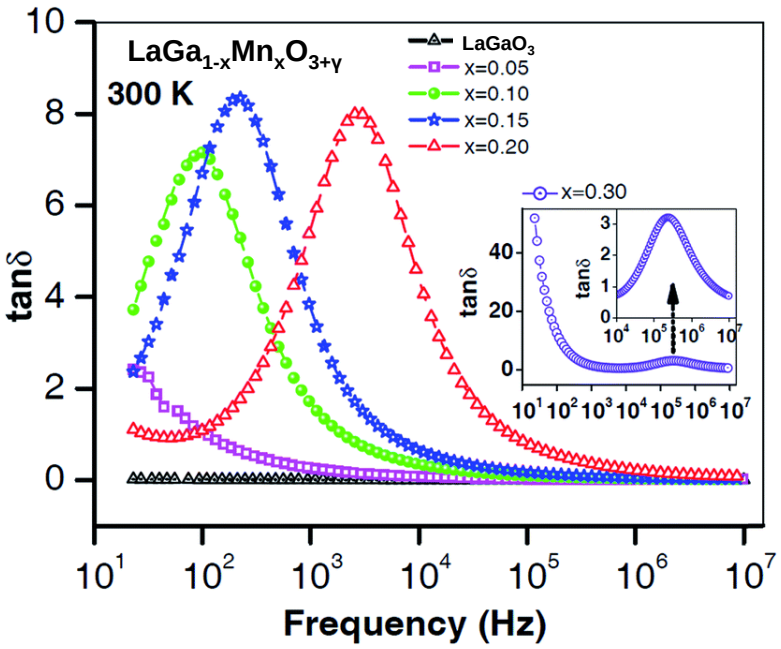

Figure 6.4: Room temperature frequency dependence of loss tangent (*tanδ*) for undoped LGO and $LaGa_{1-x}Mn_xO_{3+\gamma}$ samples with x=0.05, 0.1, 0.15, 0.2 and 0.3 samples. In order to keep the Figure in a presentable format, the data corresponding to x=0.3 is displayed separately in two insets (also see Figure 6.5). The bigger inset shows complete range of probing frequency whereas small inset is showing magnified view of characteristic *tanδ*-peak for corresponding composition.

corresponding to the characteristic frequency, points towards the existence of dielectric relaxation in the present system [110]. It is noticeable that the frequency range, corresponding to this diffused anomaly shifts towards higher frequency side with increasing Mn doping. Figure 6.4 represents RT frequency dependence of loss tangent (*tanδ*) for undoped LGO and $LaGa_{1-x}Mn_xO_{3+\gamma}$ (x=0.05, 0.1, 0.15, 0.2,

and 0.3). It is clear from this Figure that for undoped LGO sample no obvious peak/anomaly in the *tanδ* curve is observed and its value is of the order of 10^{-3} which remains almost unchanged over the entire range of probing frequencies and this is consistent with the stable nature of its ε' (Figure 6.3). Interestingly, a small peak starts emerging in *tanδ* curve at 5% doping of Mn and it becomes prominent in appearance for samples with higher percentage of Mn doping as depicted in Figure 6.4 and its corresponding insets. The loss spectra which is characterized by a prominent peak appearing at characteristic frequency for Mn doped samples is indicating towards the presence of dielectric relaxation in all presently studied Mn doped LGO samples [110,114]. These broad *tanδ*-peaks are equivalent to the diffusive anomaly observed in ε' (Figure 6.3) for corresponding $LaGa_{1-x}Mn_xO_{3+\gamma}$ compositions. It is

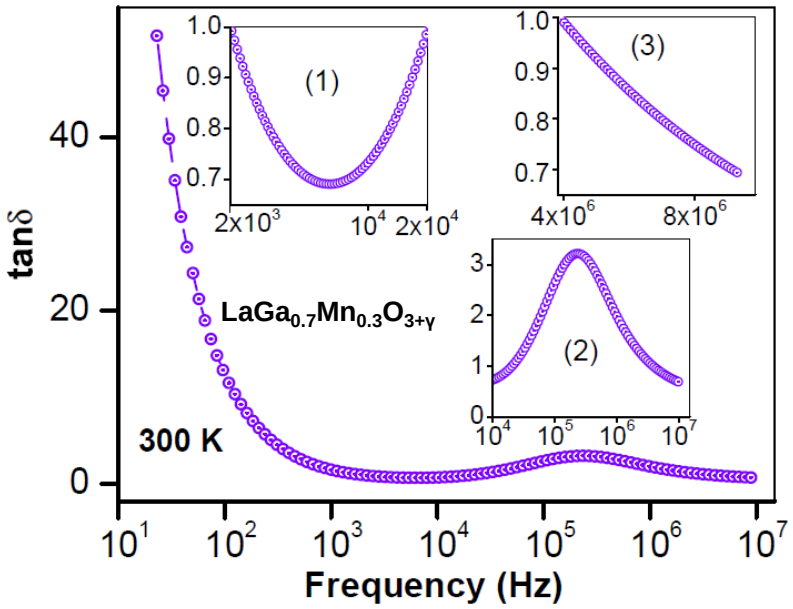

Figure 6.5: Room temperature loss tangent (*tanδ*) of $LaGa_{0.7}Mn_{0.3}O_{3+\gamma}$ plotted as a function of probing frequencies ranging from 20Hz to 10MHz. Inset-1 and 3 show that the value of *tanδ* is <1 for corresponding low (2kHz to 20kHz) and high (>1MHz) frequencies respectively. Inset-2 displays the magnified view of characteristic *tanδ*-peak.

noticeable that analogous to the shifting of this diffusive anomaly in ε' (Figure 6.3), the position of *tanδ*-peaks also shifts towards higher frequency side with increasing percentage of Mn doping. This observed consistency in the results of ε' and *tanδ* is well known for the

compounds which exhibit dielectric relaxation phenomenon [57,110,114,155,196,202,203]. Moreover, large ε' (10^4), observed for LGMO samples with x=0.2 and x=0.3, is comparable with compounds which exhibit colossal dielectric constant (CDC) [182,184,204–207]. Interestingly, the corresponding loss (*tanδ*) for present samples is found to be relatively small as compared with above cited other CDC compounds [182,184,204–207]. In addition, at MHz frequencies (≥1MHz), the value of *tanδ* is found to be fairly small for all presently studied $LaGa_{1-x}Mn_xO_{3+\gamma}$ samples (*tanδ* <1 even in case of $LaGa_{1-x}Mn_xO_{3+\gamma}$ with x=0.3; can be seen also in the inset 3 of Figure 6.5) which makes them useful for high-frequency applications [208], especially $LaGa_{1-x}Mn_xO_{3+\gamma}$ with x=0.3, as its ε' is ~ 90 to 100 at MHz frequencies which is comparable with ε' of titanates [209,210]. It is important to note that for $LaGa_{0.7}Mn_{0.3}O_{3+\gamma}$, the value of tanδ is <1 even at low frequencies ranging from 2 kHz to 20 kHz (inset 1 of Figure 6.5) and the value of its ε' in this frequency range is as high as 10^4.

Now, with the background of Mn mixed valence, Mn^{3+}/Mn^{4+} as a dipole and polaron hopping (section **6.3.2**), the above dielectric response (Figure 6.3 to 6.5) for undoped LGO and $LaGa_{1-x}Mn_xO_{3+\gamma}$ (x=0.05, 0.1, 0.15, 0.2, and 0.3) samples has been explained in the following manner; the RT - (i) large ε' (i.e., frequency response of ε'), (ii) frequency response of *tanδ* and then (iii) shifting of dielectric anomaly.

(i) Large ε' i.e., frequency response of ε' (Figure-6.3): In order to understand the reason for largely enhanced dielectric permittivity with Mn doping, in addition to XANES analysis, the *Cole-Cole* diagram is also plotted between the imaginary and real parts of the impedance for all Mn doped LGO samples as shown in Figure 6.6. Depressed semicircles have been observed for all $LaGa_{1-x}Mn_xO_{3+\gamma}$ samples (see Figure 6.6 and its insets) as the centers of all these semicircles appears to be located below the real axis which points towards the deviation

from a single *Debye* relaxation process [110,114] in all these samples. It is clearly visible from Figure 6.6 and its corresponding insets (see the difference between x-axis intersects of corresponding semicircle and maximum value of curvature along y-axis) that with increasing Mn concentration from 5% to 30%, the maximum value of both real and imaginary parts of impedance, by taking all three contributions i.e. space-charge polarization (SCP), grain boundaries (GB) and grains into account, decreases enormously by order of magnitude (i.e., from MΩ to kΩ). Our analysis reveals that with higher percentage of Mn

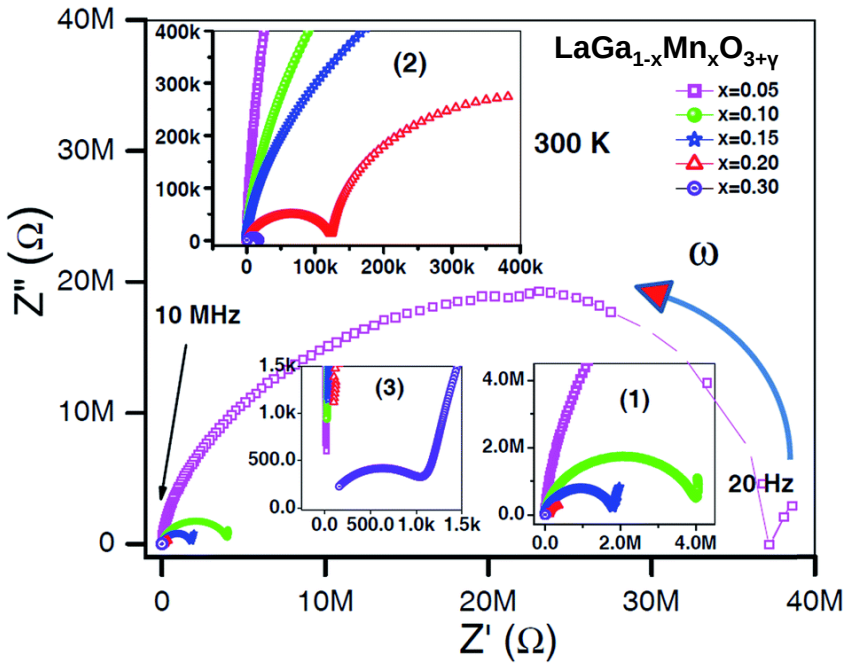

Figure 6.6: Room temperature impedance spectroscopy (*Cole–Cole* plot) for $LaGa_{1-x}Mn_xO_{3+\gamma}$ samples with x=0.05, 0.1, 0.15, 0.2 and 0.3. Inset (1) shows magnified view of the semicircles for $LaGa_{1-x}Mn_xO_{3+\gamma}$ corresponding to x=0.1 and x=0.15 whereas insets (2) and (3) display a magnified view of semicircles for $LaGa_{1-x}Mn_xO_{3+\gamma}$ with x=0.2 and x=0.3 respectively. *Note*- For convenience, the data on y-axis is multiplied by minus one.

doping ac conductivity increases due to the increased concentration of both Mn^{3+} and Mn^{4+} sites (or due to reduction in average distance between Mn ions). As a consequence a large ε' (or capacitance) is observed due to apparently reduced thickness of the sample under study as also discussed by G. Catalan and S. Krohns et al. [9,183] on the basis of parallel plate capacitor model by considering the effective

contributions from GB and electrode–sample interface due to the electrical heterogeneity present in investigated samples especially at low frequency range. Thus, the hopping charge transport mechanism along with additional non-intrinsic interface effects (arises due to the accumulation of free charges at interface between different grains within the bulk itself and at the electrode–sample interface which are recognized as Maxwell-Wagner and space charge polarizations respectively) among five most prominent mechanisms associated with the occurrence of colossal dielectric constant (CDC) (as reported by Lunkenheimer *et al.* [182] for different transition-metal oxides [183,207,211]), seems to be responsible for the observed large ε' specially in low frequency regime. Moreover, it has been already reported in case of tungstates [191,194] that an applied electric field polarizes the compound which contains ions having electrons in their unfilled and unscreened subshells (e.g. Mn for present case), therefore, there is a possibility that presently studied $LaGa_{1-x}Mn_xO_{3+\gamma}$ samples are turned out to be polarized due the application of electric field which may be another possible reason for enormous increase observed in $\boldsymbol{\varepsilon'}$ of LGO after Mn doping.

However, a pre-edge feature in the XANES data [99,212] appearing for all Mn doped LGO samples (inset 2 of Figure 6.2), indicates the presence of noncentro-symmetry (or breaking of inversion symmetry [213]) around Mn considering MnO_6 octahedron [214–216] which points towards the possibility of ferroelectricity associated with dipolar contribution; a mechanism which is accountable for intrinsically enhanced ε' [182]. Similar intrinsic effect has been observed in an extensively explored compound - CCTO ($CaCu_3Ti_4O_{12}$) [217], where it's intrinsic large ε' was attributed to its ferroelectric relaxor behavior associated with the correlated off-center displacement of Ti ions along each single (001) orientation. Moreover, it has been already reported by Y. Joly *et al*. [218] that pre-K-edge features in $A(TM)O_3$ (TM: transition metal ion) oxides are aroused possibly due to the strong mixing of 3*d-states* of neighbouring TM

atoms via hybridization with 2*p-states* of intermediate oxygen which is supported well by other reports [99,212]. This strong mixing of 3*d-states* probably causes local distortions which may lead to the reduction in inversion symmetry around TM atom in $(TM)O_6$ octahedron [212] and consequently gives rise to a net electric dipole moment (Ferro-electricity). It is noticeable that the intensity of pre-K-edge features signifies stronger reduction in centro-symmetry of $(TM)O_6$ octahedron i.e., it is a measure of strongness of above mentioned mixing of 3*d-states* via oxygen 2*p*-states [212,214]. For studied $LaGa_{1-x}Mn_xO_{3+\gamma}$ systems, the observed pre-Kedge features may be credited to 1*s*→3d dipolar (forbidden) and quadrupole (allowed) transitions [99,212]. The contribution of latter transitions is weaker whereas the former ones contribute strongly as they become allowed probably due to the above discussed strong mixing of Mn 3*d-states* via oxygen 2*p*-states [99,212,218]. Besides the pre-K-edge, possibility of order-disorder ferroelectricity (ferroelectric domain boundary motion) associated with ordering of mixed TM valences (presently Mn^{3+} and Mn^{4+}) also may be responsible for dipolar (ferroelectric) contributions [21,90]. In this way, the appearance of large ε', as observed for all $LaGa_{1-x}Mn_xO_{3+\gamma}$ samples especially at MHz frequencies for x=0.3, can be accounted (as a speculation) for intrinsic dipolar contributions. In order to investigate our speculation of possibility of non-centrosymmetry in the sample we have measured the electric polarization as a function of applied electric field (*P-E*) for undoped and 5% Mn doped LGO samples using precision material analyzer (Radiant Technologies INC). Figure 6.7 shows the *P-E* curve for undoped and 5 % Mn doped LGO sample. It is clear that Mn doped sample is showing a hysteresis loop (leaky), which is generally possible for sample having non-centrosymmetric crystallographic structure, hence we have refined the experimental diffraction data obtain for this 5% Mn doped sample with a lower symmetry space group ***Pna2₁***. The refined XRD pattern is shown as unpublished data in Figure A-3 (Appendix A-III). It should be noted that the value of χ^2 is

better as compared to that of orthorhombic structure. Thus, from our analysis it appears that dipolar effect is also contributing in the presently observed large ε'. It is important to note that the dipolar (ferroelectric) contribution may be a little only as the shape of observed *P-E* loop is similar to that of originated due to leaky systems [31,219]. However, corresponding pre-K-edge feature, observed in XANES data (Figure 6.2), points towards the possibility of finite

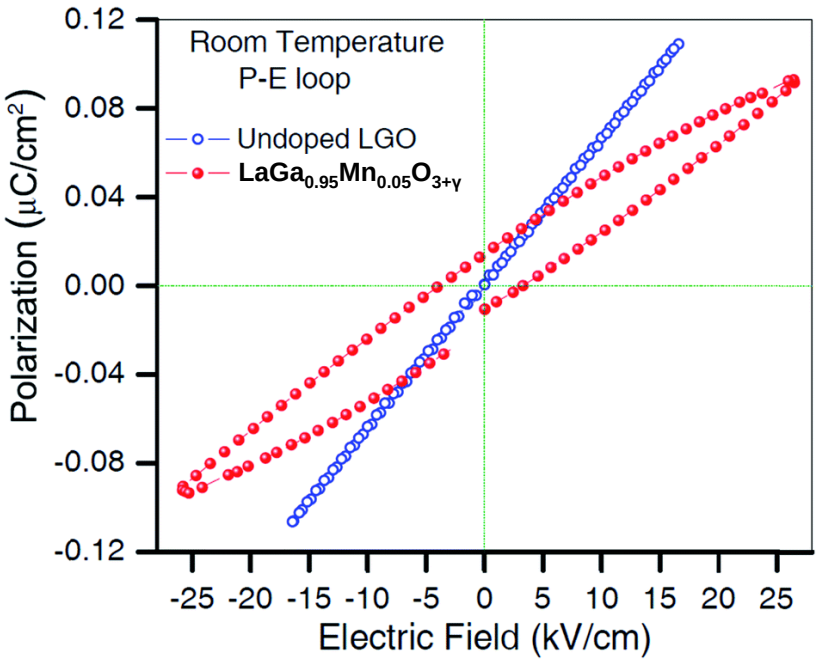

Figure 6.7: Room temperature P–E plot for undoped LGO and $LaGa_{1-x}Mn_xO_{3+\gamma}$ with x = 0.05.

dipolar contribution. Thus, further experimental and theoretical investigations may be interesting and helpful in order to conclude that which one, out of these possible mechanisms is dominatingly responsible for the observed large ε' especially at high frequencies.

(ii) Frequency response of *tanδ* (Figure-6.4 and 6.5): The small values of *tanδ* observed (specifically for the compositions with x<0.3) at low ($<10^2$ Hz) frequencies and also at very high ($\geq 10^4$ Hz) frequencies can be understood, in terms of electron/polaron hopping between Mn^{3+} and Mn^{4+} ions (i.e., in terms of dipolar oscillations of Mn^{3+}/Mn^{4+} dipole), in following manner-

Below characteristic frequency, the frequency of applied ac field is low enough that hopping electron/polaron between Mn^{3+} and Mn^{4+} sites, follows the field, as a result loss tangent (*tanδ*) is found to be small in the frequency range below to characteristic frequency [115,220]. It is noticeable that this *tanδ* (ε') continuously increases (decreases) till characteristic frequency with increasing ω, after that, *tanδ* (ε') starts (continues) decreasing. When the frequency of applied ac electric field is much larger as compared to the frequency of dipolar oscillations of Mn^{3+}/Mn^{4+} dipole then the electrons/polarons have no chance to jump at all thus the loss is found to be very small [115,220] also at frequencies faster to characteristic/cut-off frequency. Further, the emergence of relaxation peak (diffusive anomaly) in *tanδ* (ε') takes place when the frequency of polaron hopping between Mn^{3+} and Mn^{4+} ions at B-sites (ABO_3) matches with the frequency of applied ac electric field [115,221]. It is already known that step-like sharp drop in ε' across the characteristic relaxation frequency represents a single relaxation time which is recognized as *Debye* single relaxation process (*Debye* relaxation) whereas a diffusive feature exhibits a distribution of relaxation time [110,114]. It is thus noticeable that none of the investigated samples (which are showing relaxation like feature) exhibits an ideal *Debye* relaxation character (single relaxation time) as the drop in RT ε' across the characteristic relaxation frequency is diffusive (Figure 6.3) in nature which points towards the distribution of relaxation time.

(iii) Shifting of dielectric anomaly: In order to understand the shifting of characteristic dielectric anomaly towards higher frequency with increasing Mn doping and to address the type of relaxation process present in these Mn doped LGO samples, the data obtained for dielectric constant as a function of frequency (Figure 6.3) has been fitted by using the following *Cole-Cole* relation [57,110,114]

$$\varepsilon(\omega)^* = \varepsilon_\infty + \frac{\varepsilon'_S - \varepsilon'_\infty}{1+(i\omega\tau)^{1-\alpha}}; 0 \leq \alpha \leq 1 \qquad (6.1)$$

where, $\varepsilon(\omega)^* = \varepsilon' + i\varepsilon''$, is the complex dielectric permittivity, ω is the angular frequency, τ is the mean relaxation time, ε_s' and ε_∞' are the values of the dielectric constant in the low-frequency (static) and high-frequency limit respectively, the change $\varepsilon_s'-\varepsilon_\infty' = \Delta\varepsilon'$ is the strength of dielectric relaxation and α is the exponent parameter which is a measure of relaxation broadening (i.e., sharpness in the step-like feature observed in ε' versus frequency plot) and it varies between 0 and 1; for α=0, *Cole-Cole* expression 6.1 reduces to *Debye* single relaxation process [110,114]. Figure 6.8 shows the *Cole-Cole* fitting of ε' versus probing frequency data for $LaGa_{0.8}Mn_{0.2}O_{3+\gamma}$ (as a representative) by using equation 6.1. The data is fitted well over the entire range of probing frequency with the fitting parameters (α and τ),

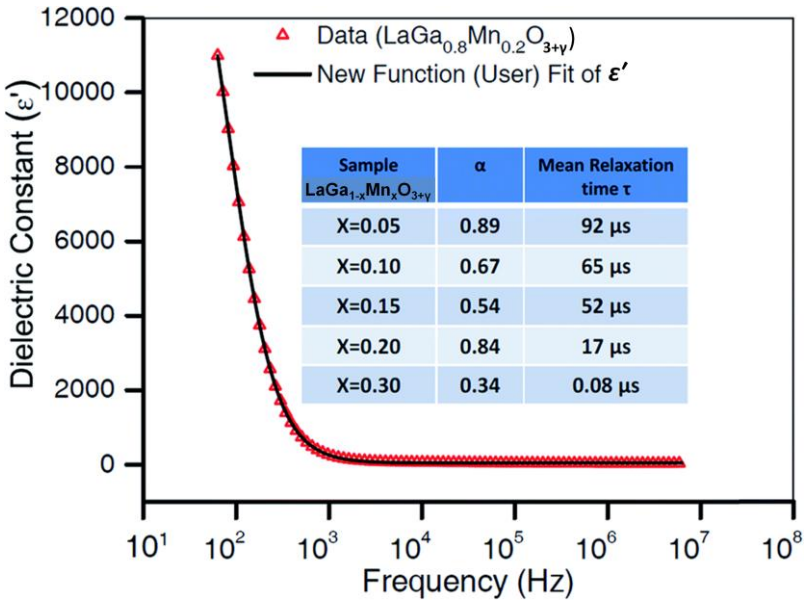

Figure 6.8: Fitting of room temperature ε' versus frequency data for $LaGa_{0.8}Mn_{0.2}O_{3+\gamma}$ (as a representative of the present $LaGa_{1-x}Mn_xO_{3+\gamma}$ series) using the *Cole–Cole* relation which is expressed as equation 6.1. The variation of the fitting parameters, α; the exponent term and τ; the mean relaxation time, are tabulated in the enclosed table for the $LaGa_{1-x}Mn_xO_{3+\gamma}$ samples with x = 0.05, 0.1, 0.15, 0.2 and 0.3.

tabulated in the Table enclosed in Figure 6.8. The perusal of Table reveals that the value of α for Mn doped samples varies from 0.34 to 0.89 which points towards a distribution of relaxation time rather a single relaxation process. Importantly, the value of τ is decreasing with increasing Mn, which suggests that average hopping frequency is

increased possibly due to the presence of increased average number of hopping sites (Mn^{3+} and Mn^{4+} ions). This may be the reason for shifting of dielectric anomaly towards higher frequency side for LGO samples with higher Mn doping. In addition, increased average number of hopping sites leads to increase in conductivity which contributes to the observed large ε' (especially at low-frequencies) by following the hopping charge transport mechanism [182] and interfacial effects [9,183] as discussed above**.**

6.3.4 Temperature dependent dielectric study

In order to investigate the effect of temperature on dielectric response of samples under study (i.e. Mn doped LGO), temperature dependent dielectric measurements were carried out for a temperature range of 120K to 430K, at selected frequencies between 100Hz to 1MHz. Since the results of these temperature dependent measurements for all studied $LaGa_{1-x}Mn_xO_{3+\gamma}$ samples with $x \geq 0.1$ are found to be almost similar in nature (from dielectric relaxation/dispersion perspective), therefore, results (temperature dependent dielectric response) for only $LaGa_{0.8}Mn_{0.2}O_{3+\gamma}$ sample along with undoped LGO are discussed in rest of the text and the same is presented in Figure 6.9. It has been observed that undoped LGO undergoes a phase transition near 418K as shown in the inset of Figure 6.9 (a). This phase transition is structural in nature as it has been already reported by Dube *et al.* [222] that RT orthorhombic symmetry of pure LGO changes to rhombohedral symmetry above 418K. This transition temperature is independent of frequency as no frequency dispersion is observed in ε'- T curve for pure LGO sample (inset of Figure 6.9(a)). This non-dispersion behavior is consistent with the temperature response of $tan\delta$ as it is also found to be independent of probing frequency for the same sample (Figure 6.10 (a)). Additionally, the value of $tan\delta$ for this undoped LGO is of the order of 10^{-3} (i.e., <0.01) which remains almost unchanged over the entire probing frequency range. Such a small value of $tan\delta$ points towards the insulating nature of this sample [223] and hence

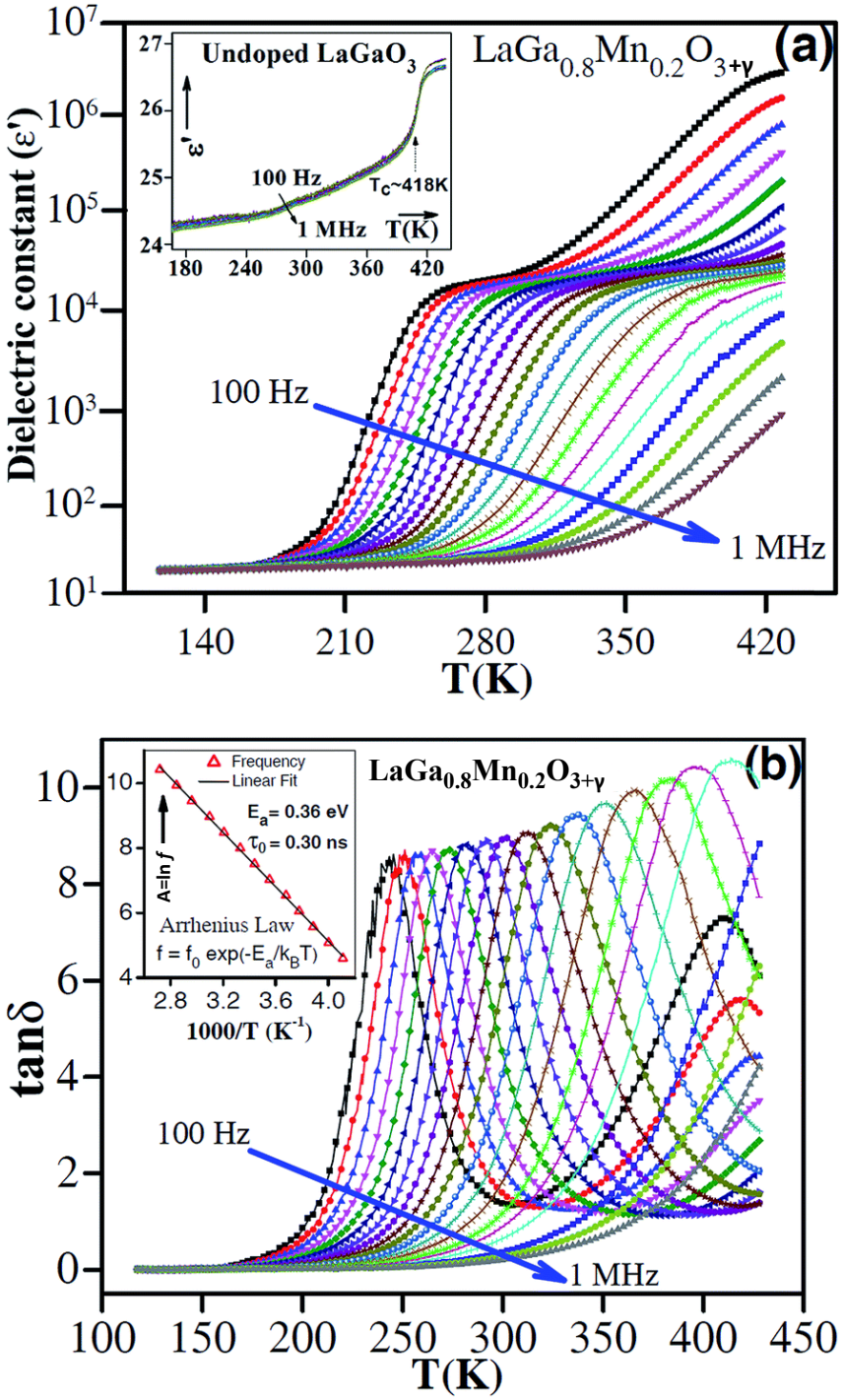

Figure 6.9: Temperature dependent dielectric response of $LaGa_{0.8}Mn_{0.2}O_{3+\gamma}$ (as a representative of the present $LaGa_{1-x}Mn_xO_{3+\gamma}$ series): shifting of characteristic- (a) anomaly in ε' and (b) peak in *tanδ* with increasing temperature for different probing frequencies ranging from 100Hz to 1MHz. The inset of (a) displays the variation of ε' for undoped LGO with increasing temperature over frequencies ranging from 100Hz to 1MHz. The structural phase transition around 418K is indicated through an arrow in the same inset. The inset of (b) shows linear fitting of frequency versus temperature values corresponding to peaks observed in the *tanδ*–*T* curves for different frequencies with the help of Arrhenius law.

makes this undoped LGO a good choice for the applications as a dielectric material. On the other hand in case of Mn doped samples, strong frequency dispersion in ε' and *tanδ* is observed at higher temperature (for $LaGa_{0.8}Mn_{0.2}O_{3+\gamma}$ at T>170 K) whereas both of these (ε' and *tanδ*) are found to be nearly frequency and also temperature independent at lower temperatures (<170K) as shown in figure 6.9 (a) and (b) respectively. In low temperature range (<170K), the static dielectric constant ε_s' and the high-frequency limit dielectric constant ε_∞' reach a common limit value of ~24. It is clear from ε'-*T* and *tanδ* -*T*

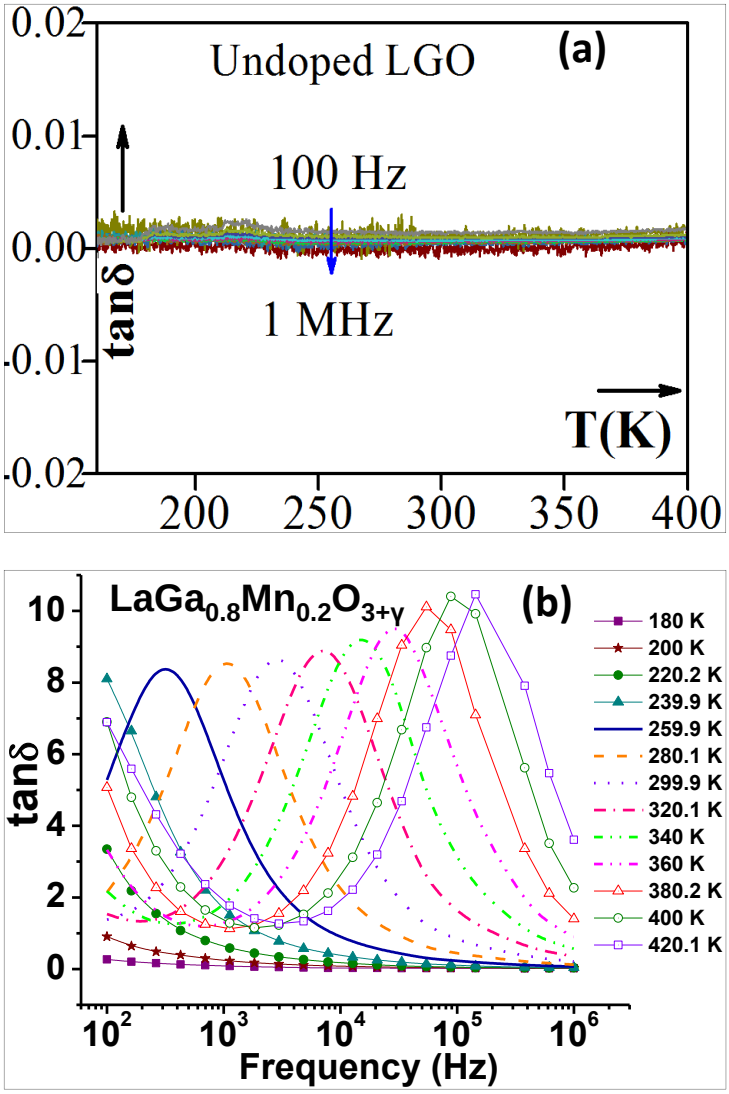

Figure 6.10: (a) Temperature dependence of loss tangent (*tanδ*) for undoped $LaGaO_3$ (LGO) recorded over a frequency range of 100 Hz to 1 MHz. (b) Shifting of characteristic *tanδ* peak frequency with increasing temperature for $LaGa_{0.8}Mn_{0.2}O_{3+\gamma}$ (*tanδ-frequency* form of the data shown in Figure 6.9 (b)).

plots (of $LaGa_{0.8}Mn_{0.2}O_{3+\gamma}$) that the anomaly observed in ε' coincides with the peak observed in *tanδ* and it shifts to higher temperature side

with increasing frequency which is characterized as dielectric relaxation/dispersion. The shifting of ε' anomaly or *tanδ*-peak (Figure 6.9 (a) and (b)) to higher temperature side indicates a thermally activated relaxation process. Moreover, the observed shifting of *tanδ* peak position is credited to the increased kinetic energy of hopping polarons due to the increasing temperature, as a result of which Mn^{3+}/Mn^{4+} dipoles start oscillating at a higher frequency and thus the anomaly (peak) in ε' (*tanδ*) shifts towards higher temperature side with increasing frequency (Figure 6.9 (a) and (b)) or *tanδ* peak shifts to higher frequency with increasing temperature as depicted in Figure 10 (b). This temperature dependent behavior is found to be similar with already reported results for other manganites [57,196,198,200,224–226], ferrites [21,29,90,155] and different perovskite systems [129,130,227–229] and thus attributed to localized hopping of polarons between lattice sites (presently between Mn^{3+} and Mn^{4+}) with a characteristic timescale and also to order-disorder ferroelectricity (ferroelectric domain boundary motion) generated due to ordering of mixed TM valences [21,90]. Beside to this frequency dispersion of dielectric anomalies, an increase in ε' by orders of magnitude is also observed due to increasing temperature (Figure 6.9 (a)) which may be attributed again to a speedy hopping charge transport [182] along with the possibility of electric field induced polarization in LGMO samples probably due to unfilled and unscreened subshells of Mn ions as the same mechanism has already been discussed for tungstates [191,194]. It is worth noticing that a 2^{nd} peak in *tanδ -T* plot is also appearing around 420K for different frequencies (Figure 6.9 (b)). Note that the corresponding temperature is close to that of the structural transition observed in undoped LGO (inset of Figure 6.9 (a)) [222]. It will be interesting to explore these secondary peaks in future for Mn doped LGO samples as the corresponding peak position appears to be shifted with temperature for different probing frequencies. Moreover, it is well established that the effect of temperature on dielectric

relaxation frequency ($1/2\pi\tau_0$) can be described on the basis of following Arrhenius relation [29,115,129,155,196–198,202,206]

$$f = f_0 \exp(-E_a / k_B T) \qquad (6.2)$$

Where, f_0 is the *Debye* relaxation frequency, E_a the activation energy, and k_B is Boltzmann constant. Thus in order to confirm, our speculation of presence of polaron (JT polaron) hopping as a driving mechanism for observed dielectric relaxation in present system, ln(f) is plotted as a function of *tanδ* peak-temperature (10^3/T) as shown in the inset of Figure 6.9 (b). The data for relaxation frequency is fitted well to the Arrhenius relation with fitting parameters τ_0 ($1/2\pi f_0$)=30 ns and E_a=0.36 eV; here, activation energy is calculated from the slope of fitted straight line and τ_0 is determined from the value of intercept on frequency-axis. This value of activation energy (E_a=0.36 eV) is found close to the earlier reported values of E_a correspond to polaron hopping mechanism e.g. 0.33 eVm [196], 0.4 eV [198], 0.30 eV [200] (for the systems with coexistence of Mn^{3+} and Mn^{4+}) and 0.29 eV [90,206], 0.45 eV [129] (for the systems with coexistence of Fe^{2+} and Fe^{3+}). These comparative values of activation energies and co-existence of Mn^{+3} and Mn^{+4} in the present samples suggest that polaron hopping mechanism is responsible for presently observed dielectric relaxation in $LaGa_{0.8}Mn_{0.2}O_{3+\gamma}$. Finally, in Mn doped lanthanum gallate, large RT ε' and dielectric relaxation (or dielectric dispersion) have been observed and analyzed systematically [230].

6.3.5 Possibility of multiferroicity in Mn doped $LaGaO_3$ (LGO)

Multiferroics are the materials which exhibit simultaneous occurrence of at least two ferroic orders among ferroelectricity, ferromagnetism (ferrimagnetic or antiferromagnetic ordering are also accounted) and ferroelasticity. As a part of present research work, from multiferroicity perspective, Mn doped LGO samples were probed to investigate the status of electric and magnetic ordering in these samples. For this purpose, *M-H*/*P-E* measurements have been carried out at RT and low

temperature/at RT. The RT and LT *M-H* plots for $LaGa_{0.9}Mn_{0.1}O_{3+\gamma}$ and $LaGa_{0.8}Mn_{0.2}O_{3+\gamma}$ are displayed in Figure 6.11 and its insets. It has been observed that the RT magnetization increases with magnetic field and it does not saturate even upto a high magnetic field as can be seen

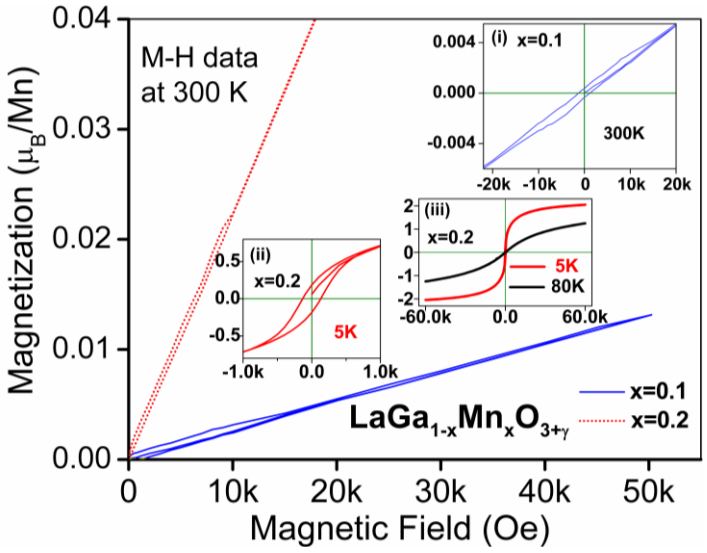

Figure 6.11: Room-temperature (RT) M–H plot for $LaGa_{1-x}Mn_xO_{3+\gamma}$ samples with x=0.1 and 0.2. Inset (i) shows a narrow RT hysteresis loop around the origin of the M–H curve for the $LaGa_{0.9}Mn_{0.1}O_{3+\gamma}$. Insets (ii) and (iii) display a normal hysteresis loop showing saturated magnetization for the $LaGa_{0.8}Mn_{0.2}O_{3+\gamma}$ at a low temperature of 5K. The M–H data recorded at 80K are also shown in inset (iii).

in the main panel of Figure 6.11 (even upto 14 T [231]). However, at RT, the sample is attracted and sticked to the magnetic pole at a low magnetic field of ~0.431T (4310 gauss) and when the field decreases it detaches at a lower magnetic field of 0.305T (see the video at http://www.rsc.org/suppdata/c6/tc/c6tc03641d/c6tc03641d2.mov). This behavior points towards the RT magnetic hysteresis in Mn doped LGO samples. The same is evidenced also by a narrow opening (hysteresis loop) in RT *M-H* curve which is observed around the origin on decreasing the magnetic field as shown in Figure 6.11 and its inset (i). This RT narrow hysteresis *M-H* loop is appearing possibly due to the presence of weak ferromagnetic ordering in $LaGa_{1-x}Mn_xO_{3+\gamma}$ samples (x=0.1 and =0.2) as the similar loops were recognized by others for weak/soft ferromagnetism [39,132,232,233] or due to the coexistence

of para and ferromagnetic phases. Similar hysteresis (*M-H*) loops have also been reported for other MD materials in which the MD effect has been attributed to structural distortion [39]/magnetostriction phenomenon [132,172,232] associated with the change in the lattice parameters or bond angles due to the application of magnetic field. As far as present research work is concern, the same has been evidenced in terms of magnetic field dependent compression/expansion of $LaGa_{1-x}Mn_xO_{3+\gamma}$ samples (x=0.2 and x=0.6) as confirmed through magnetic field dependent Raman spectroscopy (chapter 3 and 4). Nevertheless, at a very LT of 5K, a normal hysteresis loop along with the saturated magnetization is observed for all Mn doped LGO samples as shown in the insets (ii) and (iii) of Figure 6.11 for $LaGa_{0.8}Mn_{0.2}O_{3+\gamma}$, whereas along with other $LaGa_{1-x}Mn_xO_{3+\gamma}$ compositions in Figure B-1 (Appendix B). Further, in order to find out $T_{M/FM}$ (transition temperature for magnetic/ferromagnetic ordering) of $LaGa_{1-x}Mn_xO_{3+\gamma}$ samples, *M-T* measurements are performed in FC (field cooled) and ZFC (zero field cooled) modes and the observed results for

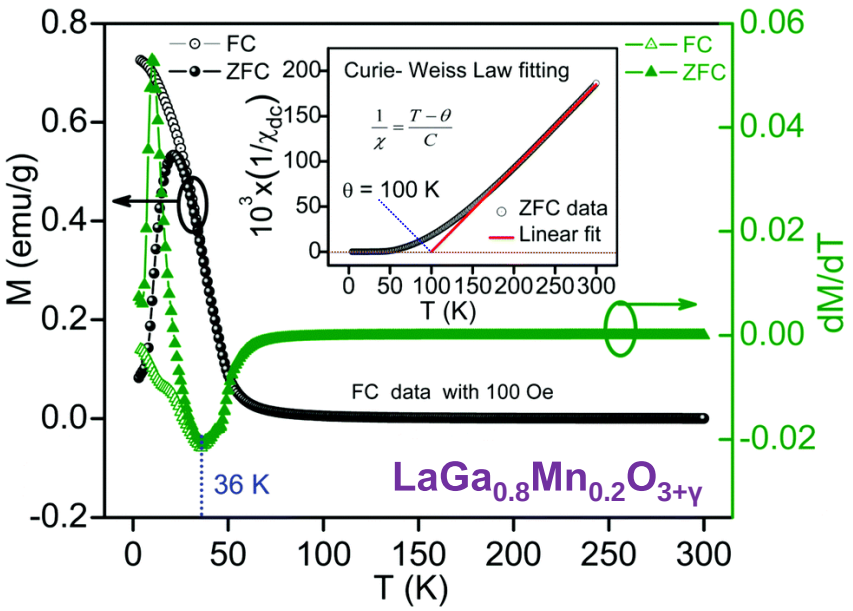

Figure 6.12: Magnetization versus temperature (M–T) curves for $LaGa_{0.8}Mn_{0.2}O_{3+\gamma}$ in FC, ZFC (field-cooled and zero-field-cooled) modes and the first derivatives of both of these M–T curves. In FC mode the sample was cooled by applying a very low magnetic field of 100 Oe and the measuring field was also kept at 100 Oe. Inset shows data for the inverse dc susceptibility versus temperature and its fitting using the Curie–Weiss law.

$LaGa_{0.8}Mn_{0.2}O_{3+\gamma}$ (as a representative) are shown in Figure 6.12, whereas for other selected $LaGa_{1-x}Mn_xO_{3+\gamma}$ compositions in Figure B-2 (Appendix B). A sharp increase appeared in magnetization at LT warrants alignment of magnetic moments and the spin ordering transition is taking place around 36K (T_M) as indicated by a dip appeared in first derivative of both FC and ZFC (M-T) curves as shown for $LaGa_{0.8}Mn_{0.2}O_{3+\gamma}$ (as a representative) in Figure 6.12, whereas for other selected $LaGa_{1-x}Mn_xO_{3+\gamma}$ compositions in Figure B-2 (Appendix B).

It is known that the fitting of inverse susceptibility ($1/\chi$) versus T curve using Curie– Weiss law $1/\chi = (T-\theta/C)$, provides valuable basic information about the magnetic ordering in the material and this method [234] has already been used in the analysis of different other systems [105,235,236]. Note that C is the curie constant and θ is the Curie temperature. Presently, the inverse of dc susceptibility is plotted as a function of temperature as depicted in the inset of Figure 6.12 for $LaGa_{0.8}Mn_{0.2}O_{3+\gamma}$ (as a representative). By fitting the high temperature region with the Curie–Weiss law (inset of Figure 6.12), the Curie-temperature for $LaGa_{0.8}Mn_{0.2}O_{3+\gamma}$ was found θ=100 K (inset of Figure 6.12). This positive value of θ indicates the presence of FM ordering [234] in $LaGa_{0.8}Mn_{0.2}O_{3+\gamma}$. The value of θ for other $LaGa_{1-x}Mn_xO_{3+\gamma}$ compositions have also been determined in the same way and tabulated in the Table B-2 (Appendix B). It is clear from the table that the value of θ is positive for all studied $LaGa_{1-x}Mn_xO_{3+\gamma}$ compounds and thus ferromagnetism is the expected magnetic ordering in all these compounds. It appears that presently studied $LaGa_{1-x}Mn_xO_{3+\gamma}$ samples are showing coexistence of para and FM phases at temperatures higher to T_{FM} as evidenced in the form of *M-H* data recorded at RT and 80K as depicted for selected $LaGa_{1-x}Mn_xO_{3+\gamma}$ compositions in Figure 6.11, its inset (iii) and Figure B-3 (Appendix B). Moreover, a bifurcation in FC and ZFC curves appearing at LT (Figure 6.12) is representing the point of irreversibility of magnetization which is characterized by a parameter known as blocking temperature T_B (or irreversibility

temperature T_{irr}) [237]. T_{irr} is a temperature at which the condition M_{ZFC}-M_{FC} = minimum; but, ≠ zero, is satisfied. It is a function of measuring/cooling magnetic field (presently 100 Oe) and also of material's micro or nanostructural properties. With increasing measuring field it shifts to further lower temperature and it is entirely different from T_{FM} (T_M). Similar bifurcation in FC and ZFC curves has been observed also for other $LaGa_{1-x}Mn_xO_{3+\gamma}$ compounds under investigation as depicted in Figure B-2 (Appendix B) for selected compositions (as representatives). At low temperatures (<T_B), the appearance of bifurcation between FC and ZFC curves can be attributed to the coexistence of FM and AFM phases [238–240] i.e., competing double (Mn^{3+}-O-Mn^{4+}) and super exchange (either Mn^{3+}-O-Mn^{3+} or Mn^{4+}-O-Mn^{4+}) interactions [105,236,238–240]. As far as the status of magnetic phase is concern, Goodenough [238] (Wollan et al. [240]) has reported that in a ABO_3 manganite system with coexisting Mn^{3+} and Mn^{4+}, if the percentage of Mn^{4+} is in the range of 10 to 25% (0 to 25%), simultaneous occurrence of FM and AFM phases is most favorable. Thus the occurrence of such magnetic-phase coexistence in studied $LaGa_{1-x}Mn_xO_{3+\gamma}$ compounds appears reasonable, as for these samples the percentage of Mn^{4+} is found within the said range (Table B-1 of Appendix B). Moreover, in FC mode, cooling of $LaGa_{1-x}Mn_xO_{3+\gamma}$ (especially below T_B) in a very low magnetic field of only 100 Oe, aligns and freezes the magnetic moments (which were frozen randomly/oppositely in ZFC mode as the magnetic moment at lowest temperature is close to zero or very low (ZFC data in Figure 6.12 and Figure B-2 (Appendix B)) along the direction of applied magnetic field and hence gives rise to a significant magnetic moment; clearly visible at the lowest temperature as depicted in FC data (Figure 6.12 and Figure B-2 (Appendix B)). As far as direct MD coupling (coinciding temperature dependent dielectric and magnetic anomalies; similar to that shown in Figure 1.9) is concern, the observed temperature dependent dielectric abnormalities (step like features shown in Figure 6.9 (a)) cannot be assigned as coinciding with the magnetic anomaly

(Figure 6.12; around 36K for representative $LaGa_{0.8}Mn_{0.2}O_{3+\gamma}$ compound) because all Mn doped LGO samples exhibit temperature dependent dielectric dispersion (see Figure 6.9 for representative $LaGa_{0.8}Mn_{0.2}O_{3+\gamma}$ compound). Now, in order to investigate about the correlation of ferroelectric and observed ferromagnetic ordering in $LaGa_{1-x}Mn_xO_{3+\gamma}$ compounds, *P-E* measurements for selected Mn doped

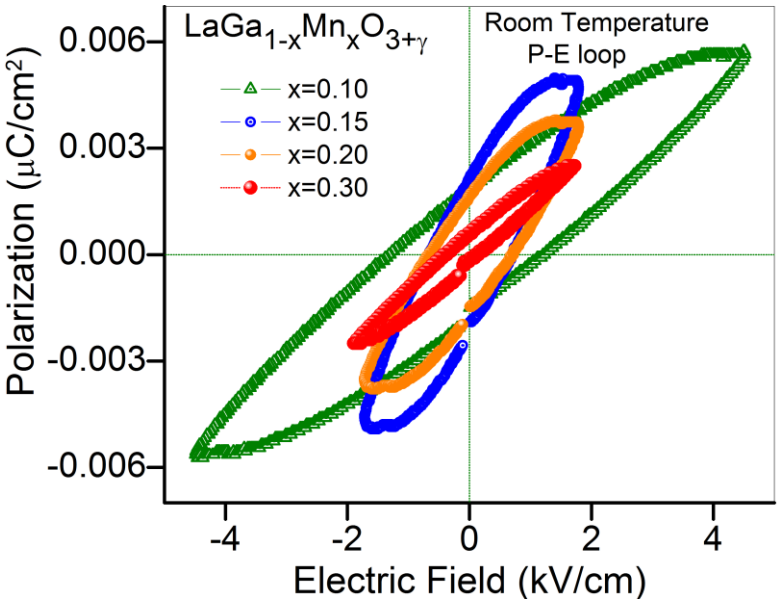

Figure 6.13: Room temperature P–E plots for selected $LaGa_{1-x}Mn_xO_{3+\gamma}$ compositions. The data for undoped LGO and $LaGa_{0.95}Mn_{0.05}O_{3+\gamma}$ samples is shown in Figure 6.7. Note- $LaGa_{1-x}Mn_xO_{3+\gamma}$ samples with x>0.3 were too leaky, therefore *P-E* loops were not observed in presentable form.

LGO compositions were performed at RT and the observed results are shown in Figure 6.7 for undoped and 5% Mn doped LGO whereas in Figure 6.13 for $LaGa_{1-x}Mn_xO_{3+\gamma}$ samples with x=0.1, 0.15, 0.2 and 0.3. It is clear from Figure 6.7 and 6.13, that the undoped LGO displays a linear dielectric behavior whereas all Mn doped LGO samples exhibit a RT hysteresis (*P-E*) loop. It is vital to note that the ferroelectric contribution (intrinsic polarization) is negligible as the shape of the observed *P–E* loops is similar to that appears due to leakage currents [219,230]. Conversely, the corresponding pre-K-edge feature (a signature of breaking of inversion symmetry around TM ion [213]), observed in the XANES data (Figure 6.2), points towards the possibility of a finite ferroelectric contribution associated with the

breaking of inversion symmetry around TM ion [213] (Mn in present case). Additionally, on the basis of available literature, following facts/arguments indicate the possibility of ferroelectric contribution and hence the multiferroicity in the studied $LaGa_{1-x}Mn_xO_{3+\gamma}$ systems. (i) Similar RT *P-E* (even more leaky) and *M-H* loops observed for Ca doped (at Bi site) $BiFeO_3$ have been reported as the signature of Multiferroicity [233]. (ii) $YFeO_3$ having Fe multivalence, has been reported as a multiferroic compound because the similar RT *P-E* loop ($YFeO_3$) was modified with almost 10 times improved polarization when recorded at low temperatures (see Figure 1.8) and assigned as the signature of ferroelectricity [48]. (iii) For present $LaGa_{1-x}Mn_xO_{3+\gamma}$ compounds, the observed temperature dependent dielectric dispersion (Figure 6.9) and coexistence of Mn^{3+} and Mn^{4+} also indicate the possibility of multiferroicity because in the system with similar features (i.e. dielectric dispersion and TM multivalence) para to ferroelectric transition is observed on decreasing the temperature while recording temperature dependent polarization under pyroelectric measurements [21,90] (see Figure 1.6 and 1.7). The order-disorder ferroelectricity (ferroelectric domain boundary motion) in such a system has been attributed to ordering of mixed TM valences [21,90]. By considering these arguments, LT *P-E* measurements (but only upto transition temperature of ferromagnetic ordering (T_{FM}) (because below T_{FM} the ferromagnetic phase is generally supposed to be metallic) will be helpful in order to quantify a genuine polarization as the leakage in the studied Mn doped LGO samples (*tanδ*-peak maximum in Figure 6.10) is supposed to be decreased with decreasing temperatures i.e., for semiconducting systems like $LaGa_{1-x}Mn_xO_{3+\gamma}$, evolution of insulating phase can be expected with decreasing temperature. Further, at LT, it is expected for pairs of neighboring Mn^{3+} and Mn^{4+} ions to form a stable localized dipole (due to difference in their chemical potentials) as the RT electron hopping between Mn^{3+} and Mn^{4+} sites [230] is expected to be ceased at LT [241]. As a whole, since the studied $LaGa_{1-x}Mn_xO_{3+\gamma}$ compounds display FM ordering below T_M (for $T_{M,}$ see Table B-2 of

Appendix B) and may exhibit ferroelectric ordering either at the same temperature i.e., type-II multiferroicity or at a higher temperature i.e., type-I multiferroicity (as below FM phase is generally metallic), therefore, we predict the possibility of multiferroicity in studied samples. Further, in order to comment strongly about the correlation between electric and magnetic orders for studied $LaGa_{1-x}Mn_xO_{3+\gamma}$ systems, temperature dependent *P-E* experiments and/or temperature dependent pyroelectric measurements are required as the transition temperature related to ferromagnetic (T_{FM}) and ferroelectric (T_{FE}) orders will be the deciding factor to classify the presently studied $LaGa_{1-x}Mn_xO_{3+\gamma}$ samples either as type-II (T_M and T_E are same) [8] or type-I multiferroic ($T_E > T_M$) [8].

6.4 Summary

In summary, a large ε' at RT and dielectric relaxation or dielectric dispersion is observed in Mn doped lanthanum gallate. Both of these observed effects have been analyzed by considering inter-site polaron hopping via Mn^{3+}- O^{2-}- Mn^{4+} path and/or a flipping Mn^{3+}/Mn^{4+} dipole under an *ac* electric field as the coexistence of Mn^{3+} and Mn^{4+} charge states is validated through XANES measurements. The appearance of large ε' is attributed to the increased conductivity governed by hopping charge transport mechanism and interface effects along with the possibility of dipolar contributions associated with off-centrosymmetry of MnO_6 octahedron as it has been revealed through systematic analysis of impedance spectroscopy, XANES (pre-K-edge) and *P-E* measurements respectively. The latter effect; presence of dielectric relaxation, is ascribed as a thermally activated relaxation process with the activation energy found to be close to that of polaron hopping 0.36 eV. Ferromagnetic ordering has been observed for all studied Mn doped LGO compounds whereas the order-disorder ferroelectricity (due to the ordering of multivalence of Mn ions) and hence the possibility of multiferroicity has been predicted. Ultimately, The effect of Mn doping on magnetic properties of selected $LaGa_{1-}$

$_xMn_xO_{3+\gamma}$ compositions has been understood in terms of percentage of coexisting Mn^{3+} and Mn^{4+} ions that understanding can be considered only as an initial analysis. In this regard an in-depth analysis is needed to understand the observed magnetic response. For this purpose, as a first attempt, density functional theory (DFT) based spin polarized first principles calculations under local spin density approximation (LSDA) were performed by using the Rietveld refined crystallographic information file (*cif*) in Vienna ab initio simulation package (VASP). Cation vacancies have been considered as the cause responsible for excess oxygen (or for the presence of Mn^{4+}) and hence for the observed magnetic behavior. Density of states (DOS), partial DOS (PDOS) and magnetic ground state (like FM and AFM) have been calculated for un-defected and cation defected $LaGa_{1-x}Mn_xO_{3+\gamma}$ systems. The observed results along with an initial analysis for undoped LGO, un-defected $LaGa_{0.5}Mn_{0.5}O_3$ and La-defected $LaGa_{0.5}Mn_{0.5}O_{3+\gamma}$ systems (as representatives) are presented and discussed in Appendix C.

Chapter 7

Conclusions and Future Scope

7.1 Conclusions

The major findings/conclusions of the research work reported in this thesis are sequentially summarized as follows:

- Magnetodielectric compounds (LGM2O, LGM6O and LGF3O) have been prepared that exhibiting significant MD effect at room temperature by applying a low or moderate magnetic field.

- The resistive contribution (MR) has been analyzed by means of FDMR analysis. The analysis revealed that, at frequencies corresponding to grain contribution the MD effect in LGM2O and LGF3O, is MR-unaffected whereas at lower frequencies it is MR dominated. On the other hand, the MD effect observed in LGM6O is intrinsic over the entire range of probing frequencies.

- In case of LGM2O and LGF3O, low field MD response was also speculated to be intrinsic but suppressed due to the dominance of negative FDMR and could not be extracted as probed with electrical technique where the inclusion of resistance is understandable.

- As a solution, magnetic field dependent Raman spectroscopy; a non-electrical measurement technique (where electrical resistance does not contribute to signals) has been employed to analyze the above speculation.

- The intrinsic nature of MD coupling in all three studied LG(M/F)O compositions was evidenced in terms of magnetic field dependent softening or hardening of $(Mn/Fe)O_6$ octahedral Raman modes.

- The magnetic field dependent Raman analysis suggests that along with the LGM6O, the MD effect of LGM2O and LGF3O is also intrinsic and hence supports our speculation of suppression of intrinsic MD nature due to dominating magnetoresistive artifacts at low frequencies in case of LGM2O and LGF3O.

- The reorientation of spin coupled Mn/Fe-orbitals under the influence of magnetic field was proposed as the mechanism responsible for the compression or expansion of material (i.e. magnetostriction) and ultimately for the observed intrinsic RTMD effect.

- Additionally, large dielectric permittivity (ε') and temperature dependent dielectric dispersion has been observed and studied in selected Mn doped $LaGaO_3$ compounds.

- The appearance of large ε' is attributed to the increased conductivity governed by hopping charge transport mechanism and interface effects along with the possibility of dipolar contributions associated with off-centrosymmetry of MnO_6 octahedron.

- The observed dielectric dispersion has been attributed to localized hopping of polarons between lattice sites (between Mn^{3+} and Mn^{4+}) with a characteristic timescale and also to order-disorder ferroelectricity (ferroelectric domain boundary motion) generated due to ordering of mixed TM valences.

- Possibility of multiferroicity has been predicted in selected Mn doped $LaGaO_3$ compounds which needs further experimental and/or theoretical confirmation.

Ultimately, a magnetodielectric material has been prepared which shows MD effect at room temperature, with a low or moderate magnetic field and the observed effect is MR-unaffected. The intrinsic MD effect has been evidenced in terms of magnetic field dependent shifting of *SS/AS* Raman modes and the mechanism for observed MD phenomenon has been understood in terms of reorientation of spin-coupled TM orbitals. We proposed that MR impedance spectroscopy i.e. MRIS (FDMR measurements) should necessarily be used as an effective experimental technique to detect MR affected and intrinsic contributions of MD effect. Our analysis reveals that MD effect can be realized in strongly correlated compounds that have scope to shrink/expand in response to an externally applied magnetic field.

7.2 Future scope

Present research work is mainly focused on room temperature magnetodielectric (RTMD) and multiferroic studies of bulk Mn doped $LaGaO_3$ (LGO). A significant RTMD effect has been observed and systematically analyzed, but, for recommending these LGM/FO compounds to serve as future MD systems at device level more studies are needed. This opens the possibilities of future research scope in these MD materials. Some of the experiments/studies that can be considered as steps of future research scope for these systems, are mentioned below

- First of all, the intrinsic nature of observed MD effect can be further verified through magnetic field dependent non-electrical measurement techniques like XRD, XANES and DRS (diffuse reflectance spectroscopy).

- For studied LGM/FO materials to be used in microelectronic devices the loss tangent (*tanδ*) should be as low as possible because such devices require a material with very low leakage (low *tanδ*). In the studied LGM/FO systems, *tanδ* is associated with the coexistence of Mn^{3+}/Fe^{3+} and Mn^{4+}/Fe^{4+} and hence can be minimized by making the samples with better oxygen stoichiometry (i.e., samples with single TM valence or with $\gamma=0$ close to zero) by means of annealing of these samples in a proper gas environment under precisely controlled and calibrated gas flow. Additionally, preparing of single crystals of Mn doped LGO may be useful in this regard as the GB effects are negligible (are completely vanished) in case of single crystals.

- Low temperature *P-E* measurements (similar to $YFeO_3$ [48]; see Figure 1.8) and temperature dependent pyroelectric measurements (similar to $LuFe_2O_4$ [21,90]; see Figure 1.6) may provide better hysteresis with improved polarization [48] and para to ferroelectric transition temperature [21,90] respectively. In this way, prediction for the possibly of multiferroicity in Mn doped LGO compounds can be examined.

- As far as device level applications are concern, thin film MD response may be better relative to bulk counterparts (considering magnitude of MC% and the device miniaturization). Thus, RT and temperature dependent MD

response can be investigated by making thin films of Mn doped LGO compounds.

- Neutron diffraction experiments on Mn doped LGM/FO samples will be helpful in order to investigate/confirm the present DFT calculations based assumption of cation vacancies as the source of excess oxygen.

7.3 Our contributions to the field of MDs

On the basis of overall present research work and its analysis-

- We revealed that the existing trend convention (magnetic field dependent change in ε' and $tan\delta$) [46] does not provide correct information every time about the resistive origin of MD effect and hence we reported that it should not be used to interpret MR effects of MD phenomenon.[§]

- We proposed [§] MR impedance spectroscopy i.e. MRIS (FDMR measurements) as an effective experimental technique to detect MR affected and intrinsic contributions.

- We reported that instead of measuring only dc MR, this technique alone can be used as an effective experimental tool to detect and analyze the resistive and intrinsic parts contributing in MD phenomenon and hence should necessarily be used in MD studies. [§]

- We predicted that the intrinsic MD coupling can be realized in strongly correlated compounds that have scope to shrink/expand in response to an externally applied magnetic field. [$]

[§] *H.M. Rai et al., J. Appl. Phys. (under review).*
[$] *H.M. Rai et al., Adv. Mater. (communicated)*

Appendix A-I

Table A-1: Specification of oxides used for preparing $LaGa_{1-x}Mn_xO_{3+\gamma}$ (LGMO) and $LaGa_{1-x}Fe_xO_{3+\gamma}$ (LGFO) compounds.

Oxide	**Physical form**	**Product Code/No.**	**Company**	**Purity (%)**
Lanthanum (III) oxide (La_2O_3)	Powder	11265	Alfa Aesar	99.999
Gallium (III) oxide (Ga_2O_3)	Powder	32102	Alfa Aesar	99.999
Manganese (IV) oxide (MnO_2)	Powder	529664	Sigma Aldrich	99.99
Iron (III) oxide (Fe_2O_3)	Chunks	203513	Sigma Aldrich	99.98

Note- More information about tabulated oxides can be found on the company's website by using the given product code/number.

Table A-2: Sample (pellet) dimensions used to calculate the dielectric constant (ε') from measured capacitance (for LGM2O and LGF3O).

Sample/Pellet	**Thickness (mm)**	**Radius (mm)**	**Area (mm^2)**
$LaGa_{0.8}Mn_{0.2}O_{3+\gamma}$	1.02	5.95	111.22
$LaGa_{0.7}Mn_{0.3}O_{3+\gamma}$	1.03	5.97	111.97

Table A-3: Instrument/set-up accuracy (resolution) for main measurements

Measurement/quantity	**Instrument/set-up accuracy (resolution)**
Capacitance (or ε'), $tan\delta$, MC%, ML%, Z′, Z″	±0.05%
XANES (Edge energy)	$\pm 10^{-4}$ eV
Raman measurements	±0.4 cm^{-1}
M-T measurements	±0.2 K
ε' as a function of temperature (ε'-*T*)	±0.2 K
I-V measurements	±1 nano Volt

Note- In all the measurements the claimed changes are well above to the instrumental accuracy (resolution) and standard error.

Appendix A-II

Primary Ferroics

A primary ferroic material is one which exhibits either a spontaneous polarization, or a spontaneous magnetization, or a spontaneous stain under zero switching force (i.e., electric field *E*, magnetic field *H*, or mechanical stress σ) and exhibits significant remanence even after the compete removal of switching force [242]. Note that the present research work focuses only on magnetic and electric ferroics. Further, these spontaneous order parameters (i.e., polarization (*P*) or magnetization (*M)* or strain (ε) can be reoriented by an external switching force below a characteristic temperature called as Curie temperature or sometimes as Néel temperature [242]. The domains are

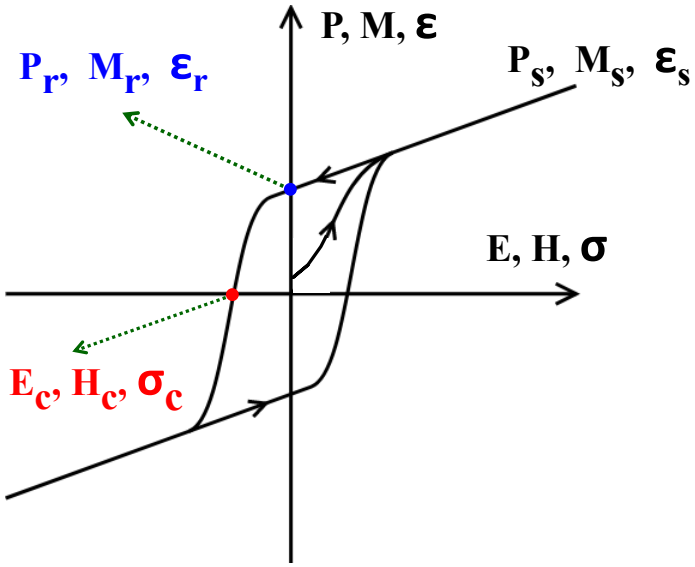

Figure A-1: Schematic of a hysteresis loop showing the coercive field, remanent and saturation in polarization, magnetization and strain for different order parameter [242].

randomly oriented prior to the first application of a switching force (*E or H or* σ) thus; no net order parameter persists in the sample (especially in non-polar systems). As field is applied and increased, the domains aligned with the fields leading to a net order parameter. At higher fields, the order parameter saturates (*Ps*, *Ms*, *εs*) and even if the field is reduced to zero, still there exist a finite order parameter known as remanent order parameter (Pr, Hr, εr). Thus, the M-H/ ε-σ/ P-E

response gives rise to a hysteresis behavior [31]. The primary ferroic materials could be characterized by a hysteresis response in the external switching force as shown in Figure A-1.

Appendix A-III

1) Unpublished XRD Data of $LaGa_{1-x}Fe_xO_3$ Series

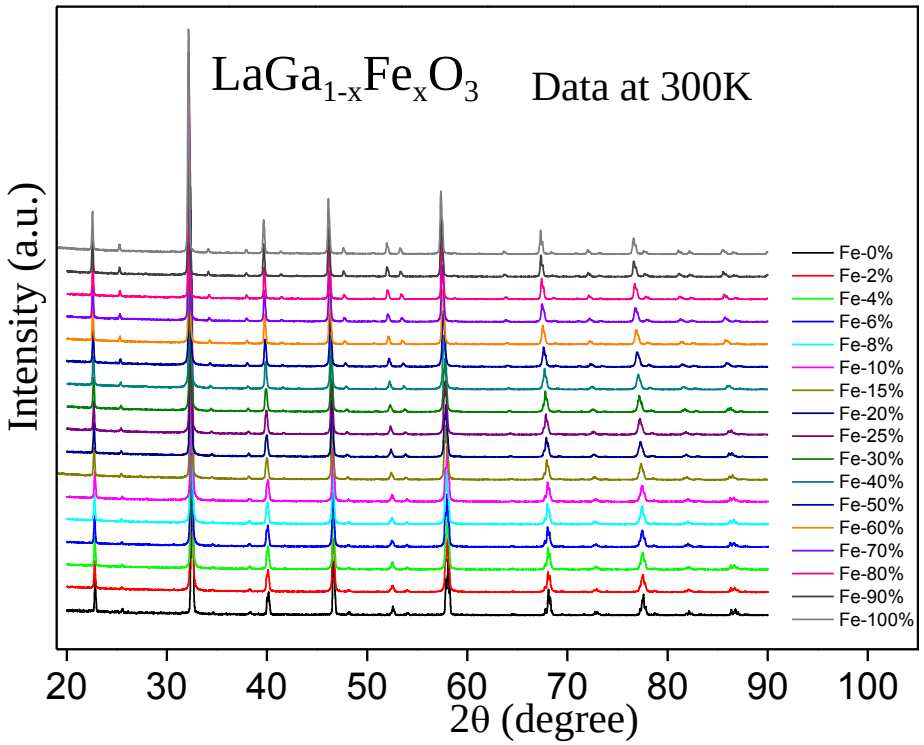

Figure A-2: X-ray diffraction (XRD) data for $LaGa_{1-x}Fe_xO_3$ (LGFO) series. As a representatives of LGFO series, Rietveld refined XRD pattern of $LaGa_{0.7}Fe_{0.3}O_3$ powder sample is shown in Figure 5.1 (chapter 5).

2) Unpublished Rietveld refined XRD Data of $LaGa_{0.95}Mn_{0.05}O_3$

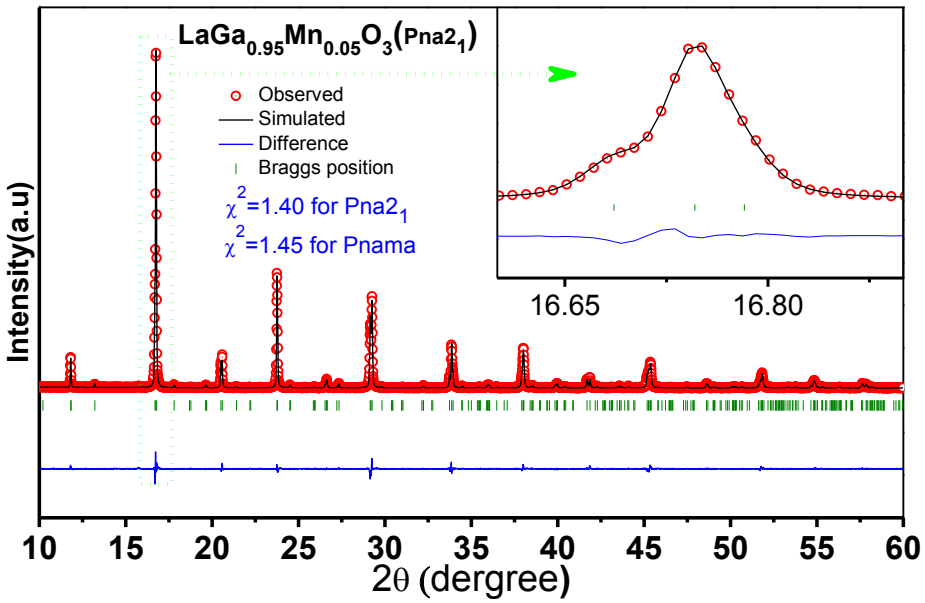

Figure A-3: Rietveld refined X-ray diffraction data for $LaGa_{0.95}Mn_{0.05}O_3$ fitted with ***Pna2₁*** space group (as a representative of ***Pna2₁***and ***Pnma*** space groups). The absence of any unaccounted peak confirms the purity of the structural phase of the prepared sample. Inset displays the magnified view of selected peak to show the quality of fitting.

Appendix B

Magnetic Properties of Mn Doped $LaGaO_3$: Unpublished Results

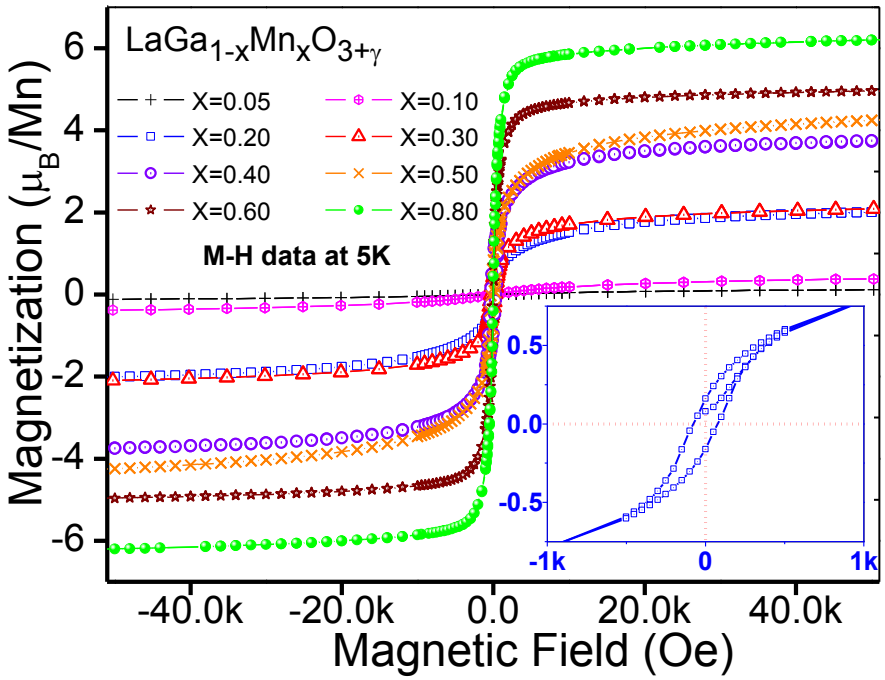

Figure B-1: Low temperature (5K) *M–H* plots for selected $LaGa_{1-x}Mn_xO_{3+\gamma}$ compositions. Inset shows magnified view of *M-H* data for $LaGa_{0.8}Mn_{0.2}O_{3+\gamma}$.

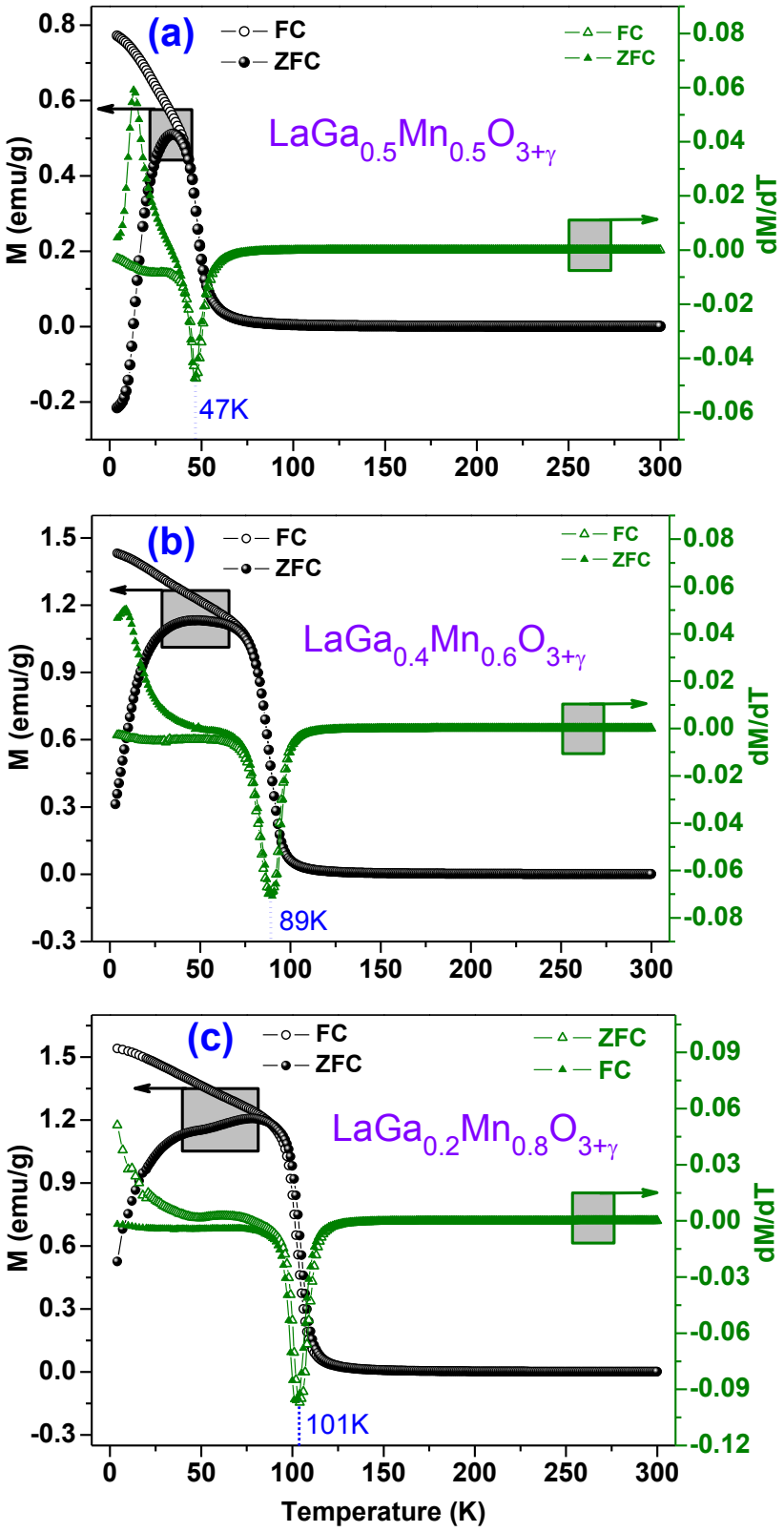

Figure B-2: Magnetization versus temperature (*M*–*T*) curves for selected representative $LaGa_{1-x}Mn_xO_{3+\gamma}$ compositions in FC, ZFC (field-cooled and zero-field-cooled) modes and the first derivatives of both of these *M*-*T* curves. A sharp dip marked as magnetic transition temperature.

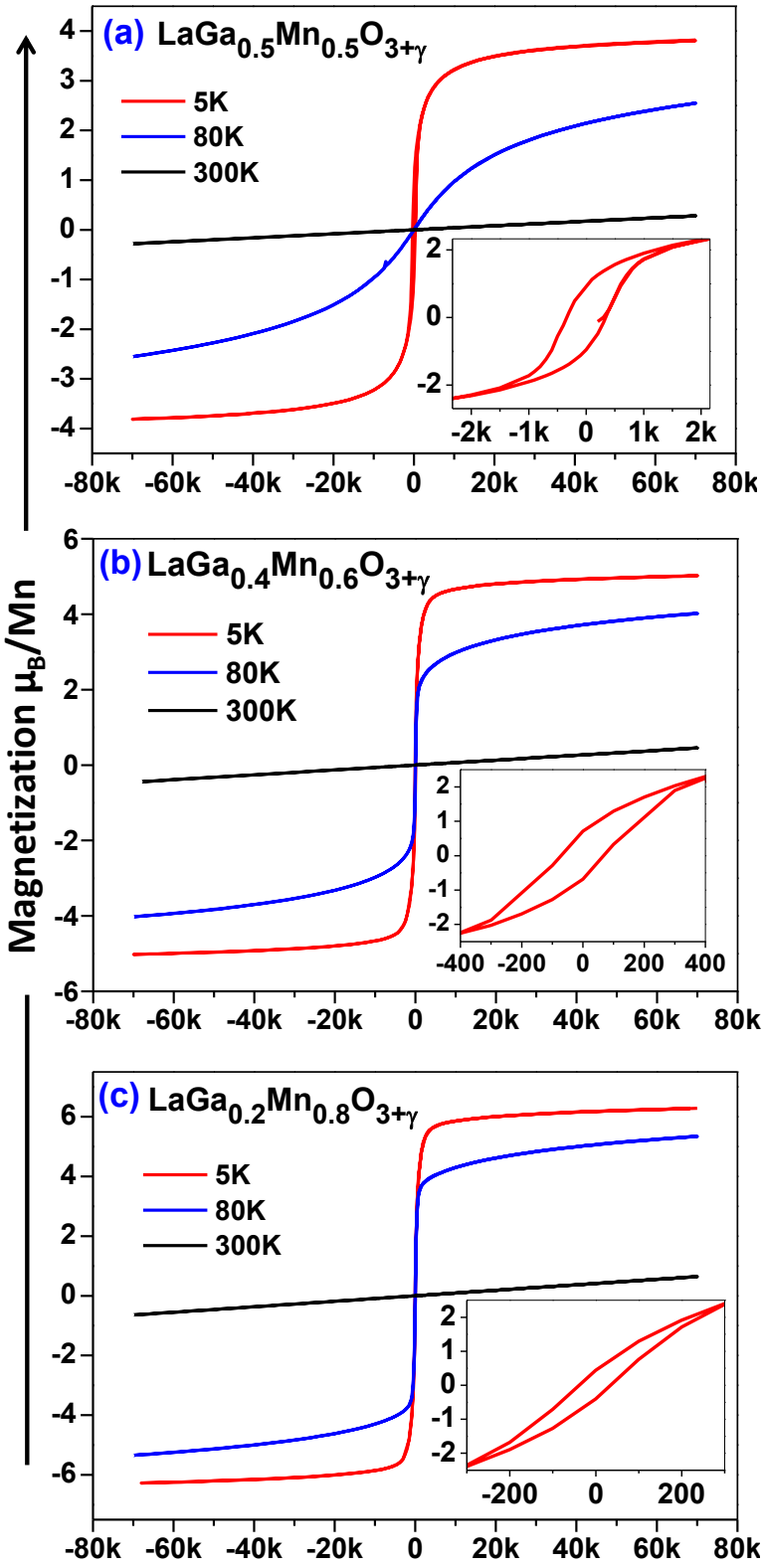

Figure B-3: Magnetization versus magnetic field (*M–H*) curves for selected representative $LaGa_{1-x}Mn_xO_{3+\gamma}$ compositions at three different temperatures.

Table B-1: Charge state of Mn, amount of excess oxygen and percentage of Mn^{3+} and Mn^{4+} for selected $LaGa_{1-x}Mn_xO_{3+\gamma}$ compositions estimated through XANES.

Sample Name	Mn charge state	value of γ	% of Mn^{3+}	% of Mn^{4+}
$LaGa_{0.95}Mn_{0.05}O_{3+\gamma}$	3.07	0.0017	93	07
$LaGa_{0.9}Mn_{0.1}O_{3+\gamma}$	3.08	0.004	92	08
$LaGa_{0.85}Mn_{0.15}O_{3+\gamma}$	3.11	0.008	89	11
$LaGa_{0.8}Mn_{0.2}O_{3+\gamma}$	3.15	0.015	85	15
$LaGa_{0.7}Mn_{0.3}O_{3+\gamma}$	3.13	0.019	87	13
$LaGa_{0.6}Mn_{0.4}O_{3+\gamma}$	3.15	0.030	85	15
$LaGa_{0.5}Mn_{0.5}O_{3+\gamma}$	3.13	0.032	87	13
$LaGa_{0.4}Mn_{0.6}O_{3+\gamma}$	3.14	0.042	86	14
$LaGa_{0.2}Mn_{0.8}O_{3+\gamma}$	3.17	0.068	83	17

Table B-2: Curie temperature (θ), Temperature corresponding to magnetic ordering or magnetic transition (T_C or T_M), and saturated magnetic moment for selected $LaGa_{1-x}Mn_xO_{3+\gamma}$ compositions.

Sample Name	θ (K)	T_C or T_M (K)	μ_{eff}^{sat} (μ_B/Mn)
$LaGa_{0.95}Mn_{0.05}O_{3+\gamma}$	41	-	0.36
$LaGa_{0.9}Mn_{0.1}O_{3+\gamma}$	46	06	0.41
$LaGa_{0.8}Mn_{0.2}O_{3+\gamma}$	100	36	1.80
$LaGa_{0.7}Mn_{0.3}O_{3+\gamma}$	128	30	1.89
$LaGa_{0.6}Mn_{0.4}O_{3+\gamma}$	111	46	3.52
$LaGa_{0.5}Mn_{0.5}O_{3+\gamma}$	119	47	3.89
$LaGa_{0.4}Mn_{0.6}O_{3+\gamma}$	141	89	4.94
$LaGa_{0.2}Mn_{0.8}O_{3+\gamma}$	158	101	6.11

Appendix C

First Principles Study to Understand Magnetic Behavior of Mn Doped $LaGaO_3$ in Terms of Cation Vacancies: Unpublished Results and Anlysis

We have investigated the spin dependent electronic and magnetic properties of pure, Mn-doped and La-defected Mn-doped $LaGaO_3$ (LGO) systems by employing first-principles calculations to understand the observed magnetic behaviour (section **6.3.5** and Appendix B) in terms of cation vacancy (specifically La-defect). For this purpose, along with undoped LGO, 50% Mn-doped $LaGaO_3$ i.e., $LaGa_{0.5}Mn_{0.5}O_3$ system has been carefully chosen; as the study of other systems like $LaGa_{0.8}Mn_{0.2}O_{3+\gamma}$ and $LaGa_{0.4}Mn_{0.6}O_{3+\gamma}$ involves large number of atoms whereas doping of 50% Mn is achieved only with 20 atoms in a supercell. All the calculations were performed by means of spin-polarized density functional theory (DFT) calculations as implemented in the Vienna Ab initio Simulation Package (VASP) [141]. Note that, all these calculations were performed by importing the corresponding refined *crystallographic information file* (.cif) in VASP. Further, projector augmented wave (PAW) method [142,143] is employed using an energy cut-off of 470 eV to describe the electronic wave functions. The local density approximation (LDA) + U method [144] is used to account the strong on-site correlated electrons in the partially filled *d* orbitals. We have employed correlation energy (U) of 4 eV and exchange energy (J) of 1 eV for Mn *d*-orbitals. These U and J values have been well tested and used in similar systems [145,146]. A 20 atoms (2×2×1) supercell is considered to study pure (undoped), Mn doped and cation defected Mn doped LGO systems to achieve 50% Mn-doping and 25% La-defect concentrations. Our optimized structural parameters are very much in agreement with the respective crystal structures. The Monkhorst-pack [147] generated set of 7×7×7 (for 20 atoms supercell) K-points are used to optimize the structures.

The convergence criteria for energy and force are set at 10^{-6} eV and 10^{-3} eV/Å respectively. 15×15×15 Monkhorst-pack generated K-points are used for the spin-polarized density of state calculations (DOS). Following Figure C-1 shows the optimized structure with calculated total DOS and partial DOS (PDOS) for all three considered systems.

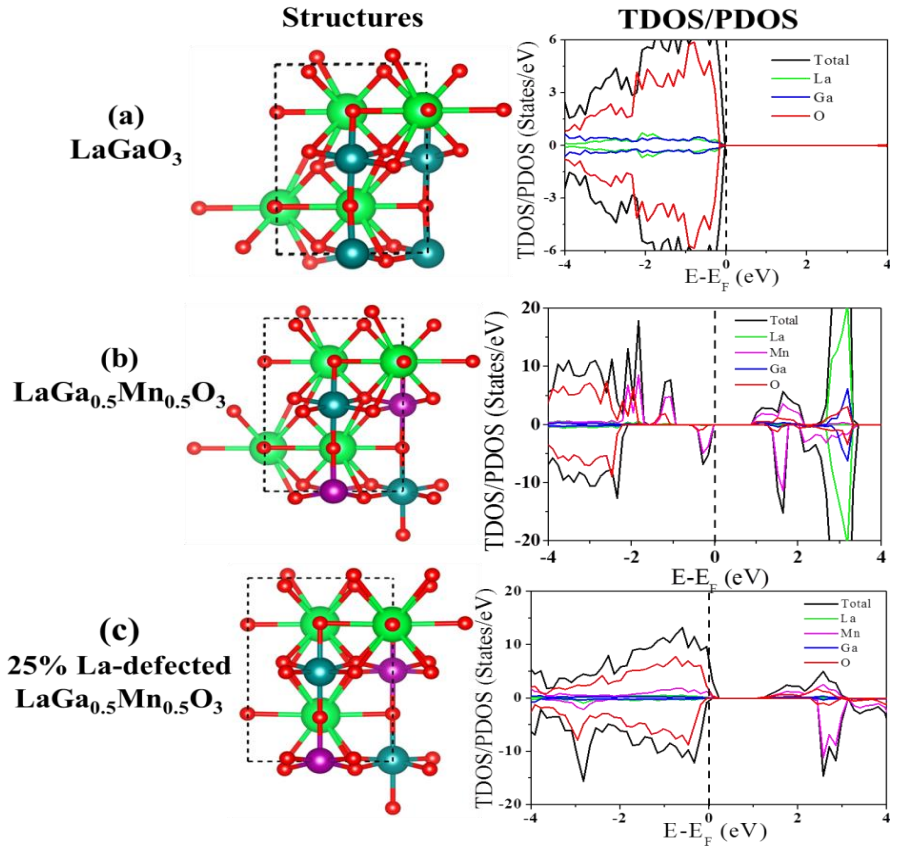

Figure C-1: The optimized structures along with the calculated total DOS and partial DOS (PDOS) for all three considered systems; (a) $LaGaO_3$ (b) 50% Mn-doped $LaGaO_3$, (c) 25% La-defected 50% Mn-doped $LaGaO_3$ ($LaGa_{0.5}Mn_{0.5}O_{3+\gamma}$). Here, green, blue, purple and red color balls denote La, Ga, Mn and O atoms, respectively. The Fermi level is set to zero and indicated by vertical dashed line. Note- the positive (negative) DOS curves are showing the available states for spin up (down) electrons whereas the positive (negative) energy window is corresponding to conduction (valance) band region.

It can be clearly seen that undoped LGO exhibits a wide gap semiconducting nature [243] as the DOS of corresponding spins are well separated across the fermi level (Figure C-1(a)). The mirror symmetry of spin up and down states (Figure C-1(a)) reflects nonmagnetic nature of undoped LGO. As far as the doped system is

concern, Mn states appearing across fermi level suggest the reduction in band gap due to doping of Mn (Figure C-1(b)). This can be attributed to higher energy of Mn 3*d* states than Ga 3*d* states as Ga (1.81) is more electronegative than Mn (1.55) [244]. For Mn doped LGO, anti-parallel arrangement of Mn spins is found energetically more favourable relative to parallel arrangement hence promoting AFM (antiferromagnetic ordering) phase as the magnetic ground state of Mn doped LGO (Figure C-1(b)). However, the breaking of mirror spin symmetry i.e., splitting of spin states across fermi level (Figure C-1(b)) indicates the possibility net magnetic moment in Mn doped LGO. Interestingly, the corresponding calculated magnetic moment (> 3 μB/Mn) supports the splitting of spin states across fermi level. It is known that the magnetic moment for a magnetic system should be zero in its AFM phase. Additionally, according to Goodenough [238] and Wollan et al. [240], even though the magnetic moment is > 3 μB/Mn, the investigated Mn doped LGO configuration cannot be treated as a FM system (especially when two neighbouring Mn^{3+} ions are at 180º via intermediate oxygen ion means the magnetic ground state is an anti-parallel arrangement of spins) as all the Mn ions were considered in their 3+ state only. In such a situation, the observed DFT based theoretical results shown in Figure C-1 (b) (magnetic moment is > 3 μB/Mn and anti-parallel arrangement of spin) can by justified by considering the compound as ferrimagnetic where, a net magnetic moment is obvious with antiparallel arrangement. The similar explanation has been reported by P. Manimuthu *et al.* in the similar situation for $Lu_3Fe_5O_{12-\delta}$ [27]. Ultimately, the initial conclusion is that the Mn doping at Ga site in nom-magnetic (NM) LGO turns it into a ferrimagnetic system.

As far as cation vacancies are concerned, La defect (La vacancy) is found energetically most favourable among La, Ga, and Mn cations (see the section **3.3.4**). The optimized geometry, DOS and PDOS for considered La-defected Mn doped LGO ($LaGa_{0.5}Mn_{0.5}O_{3+\gamma}$)

are depicted in Figure C-1(c). It can be seen that the semiconducting Mn doped LGO (Figure C-1(b)) is transformed into metallic system as evident in the form of crossing of fermi level by total spin up DOS (Figure C-1(c)). Interestingly, a finite separation (band gap) is observed across fermi level for spin down state indicating possibility of spin polarized electronic transport (i.e. half-metallicity) as only spin up states are crossing the fermi level (Figure C-1(c)). It is to be noted that the La vacancy results into excess oxygen and hence in into the

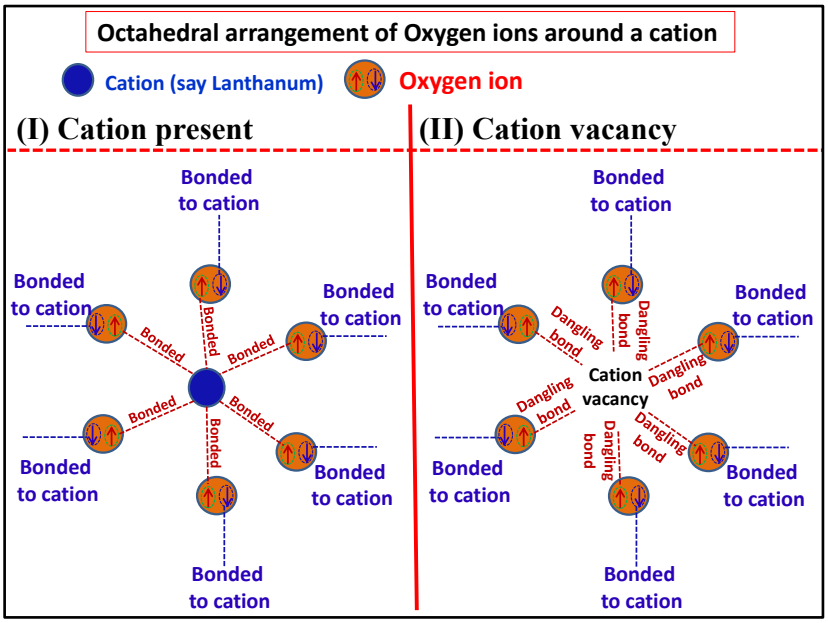

Figure C-2: Schematic situation (I); octahedral arrangement of Oxygen ions around a cation (say La). One of the two electrons of each oxygen ion is bonded with the shown central cation and remaining one is connected to other cation site. Situation (II); shows that due to the removal of La ion (considered La-defect) the up spin Oxygen electron becomes unbound (or the corresponding Oxygen bond remains unsaturated/dangling).

appearance of Mn^{4+} (for better understanding, Table 3.1, Table 3.2 and section **3.3.4** can be seen). Coming back to Figure C-1 ((c)), the transport of only spin up electrons (each spin up oxygen electron, which became unbound due to the missing La atom as shown in schematic situation (II) of Figure C-2) is speculated to be double exchange mediated via Mn^{3+}-O^{2-}-Mn^{4+}- Mn^{3+}-O^{2-}-Mn^{4+}….path (two examples of conduction channel formation are imagined in Figure 3.10 (c) and (d)). This assumed mechanism appears reasonable because the

up spin PDOS corresponding to only Oxygen and Mn are crossing the fermi level (are the only sites responsible for conduction) as depicted in Figure C-1 (c). Similar dangling/unsaturated bond (or unbounded electron) has been predicted as the reason for half-metallicity in completely different systems; edge hydrogenated/fluorinated BN (boron nitride) nanoribbons [245–248]. In case of present La defected LGMO system, further experimental and theoretical studies are needed to confirm present observations. Additionally, the spin mirror symmetry between spin up and spin down DOS/PDOS is broken as evidenced in the form of large splitting of these states across fermi level (Figure C-1(c)). As far as the magnetic state of $LaGa_{0.5}Mn_{0.5}O_{3+\gamma}$ is concern, FM (parallel arrangement of spins) is found as the magnetic ground state with a magnetic moment of ~$4\mu_B$/Mn. This value of theoretically calculated magnetic moment is closely consistent with the experimental value of saturated magnetic moment (Figure B-1 and table B-2 of appendix B). We speculate that in all the studied $LaGa_{1-x}Mn_xO_{3+\gamma}$ systems, the magnetic state (FM, AFM or ferrimagnet), value of θ (Curie temperature), T_C (critical temperature) and saturated magnetization is associated with by the relative number (not the ratio or percentage) of Mn^{3+} and Mn^{4+}. Till now, this analysis of observed magnetic behavior of $LaGa_{1-x}Mn_xO_{3+\gamma}$ systems is only in its initial phase and needs validation through systematic experimental and/or theoretical studies.

Appendix

References

[1] W. Eerenstein, N.D. Mathur, J.F. Scott, Multiferroic and magnetoelectric materials, Nature. 442 (2006) 759–765. doi:10.1038/nature05023.

[2] Y. Tokura, S. Seki, N. Nagaosa, Multiferroics of spin origin, Rep. Prog. Phys. 77 (2014) 076501. doi:10.1088/0034-4885/77/7/076501.

[3] M. Fiebig, Revival of the magnetoelectric effect, J. Phys. Appl. Phys. 38 (2005) R123. doi:10.1088/0022-3727/38/8/R01.

[4] K.F. Wang, J.-M. Liu, Z.F. Ren, Multiferroicity: the coupling between magnetic and polarization orders, Adv. Phys. 58 (2009) 321–448. doi:10.1080/00018730902920554.

[5] N.A. Spaldin, M. Fiebig, The renaissance of magnetoelectric multiferroics, Science. 309 (2005) 391–392. doi:10.1126/science.1113357.

[6] C.N.R. Rao, A. Sundaresan, R. Saha, Multiferroic and Magnetoelectric Oxides: The Emerging Scenario, J. Phys. Chem. Lett. 3 (2012) 2237–2246. doi:10.1021/jz300688b.

[7] N.A. Spaldin, S.-W. Cheong, R. Ramesh, Multiferroics: Past, present, and future, Phys. Today. 63 (2010) 38–43. doi:10.1063/1.3502547.

[8] D. Khomskii, Classifying multiferroics: Mechanisms and effects, Physics. 2 (2009) 20. doi:10.1103/Physics.2.20.

[9] G. Catalan, Magnetocapacitance without magnetoelectric coupling, Appl. Phys. Lett. 88 (2006) 102902. doi:10.1063/1.2177543.

[10] G. Catalan, J.F. Scott, Physics and Applications of Bismuth Ferrite, Adv. Mater. 21 (2009) 2463–2485. doi:10.1002/adma.200802849.

[11] N.A. Hill, Why Are There so Few Magnetic Ferroelectrics?, J. Phys. Chem. B. 104 (2000) 6694–6709. doi:10.1021/jp000114x.

[12] T. Kimura, Spiral Magnets as Magnetoelectrics, Annu. Rev. Mater. Res. 37 (2007) 387–413. doi:10.1146/annurev.matsci.37.052506.084259.

[13] T. Kimura, T. Goto, H. Shintani, K. Ishizaka, T. Arima, Y. Tokura, Magnetic control of ferroelectric polarization, Nature. 426 (2003) 55–58. doi:10.1038/nature02018.

[14] R. Seshadri, N.A. Hill, Visualizing the Role of Bi 6*s* “Lone Pairs” in the Off-Center Distortion in Ferromagnetic $BiMnO_3$, Chem. Mater. 13 (2001) 2892–2899. doi:10.1021/cm010090m.

[15] J.B. Neaton, C. Ederer, U.V. Waghmare, N.A. Spaldin, K.M. Rabe, First-principles study of spontaneous polarization in multiferroic

$BiFeO_3$, Phys. Rev. B. 71 (2005) 014113. doi:10.1103/PhysRevB.71.014113.

[16] R. Ramesh, N.A. Spaldin, Multiferroics: progress and prospects in thin films, Nat. Mater. 6 (2007) 21–29. doi:10.1038/nmat1805.

[17] M. Fiebig, T. Lottermoser, D. Fröhlich, A.V. Goltsev, R.V. Pisarev, Observation of coupled magnetic and electric domains, Nature. 419 (2002) 818–820. doi:10.1038/nature01077.

[18] T. Lottermoser, T. Lonkai, U. Amann, D. Hohlwein, J. Ihringer, M. Fiebig, Magnetic phase control by an electric field, Nature. 430 (2004) 541–544. doi:10.1038/nature02728.

[19] Y. Kitagawa, Y. Hiraoka, T. Honda, T. Ishikura, H. Nakamura, T. Kimura, Low-field magnetoelectric effect at room temperature, Nat. Mater. 9 (2010) 797–802. doi:10.1038/nmat2826.

[20] M.K. Lee, T.K. Nath, C.B. Eom, M.C. Smoak, F. Tsui, Strain modification of epitaxial perovskite oxide thin films using structural transitions of ferroelectric $BaTiO_3$ substrate, Appl. Phys. Lett. 77 (2000) 3547–3549. doi:10.1063/1.1328762.

[21] M.A. Subramanian, T. He, J. Chen, N.S. Rogado, T.G. Calvarese, A.W. Sleight, Giant Room–Temperature Magnetodielectric Response in the Electronic Ferroelectric $LuFe_2O_4$, Adv. Mater. 18 (2006) 1737–1739. doi:10.1002/adma.200600071.

[22] N. Cai, C.-W. Nan, J. Zhai, Y. Lin, Large high-frequency magnetoelectric response in laminated composites of piezoelectric ceramics, rare-earth iron alloys and polymer, Appl. Phys. Lett. 84 (2004) 3516–3518. doi:10.1063/1.1739277.

[23] G. Srinivasan, E.T. Rasmussen, J. Gallegos, R. Srinivasan, Y.I. Bokhan, V.M. Laletin, Magnetoelectric bilayer and multilayer structures of magnetostrictive and piezoelectric oxides, Phys. Rev. B. 64 (2001) 214408. doi:10.1103/PhysRevB.64.214408.

[24] N.D. Mathur, F.M. Grosche, S.R. Julian, I.R. Walker, D.M. Freye, R.K.W. Haselwimmer, G.G. Lonzarich, Magnetically mediated superconductivity in heavy fermion compounds, Nature. 394 (1998) 39–43. doi:10.1038/27838.

[25] N. Hur, S. Park, P.A. Sharma, J.S. Ahn, S. Guha, S.-W. Cheong, Electric polarization reversal and memory in a multiferroic material induced by magnetic fields, Nature. 429 (2004) 392–395. doi:10.1038/nature02572.

[26] L.W. Martin, Engineering functionality in the multiferroic $BiFeO_3$ – controlling chemistry to enable advanced applications, Dalton Trans. 39 (2010) 10813–10826. doi:10.1039/C0DT00576B.

[27] P. Manimuthu, R. Vidya, P. Ravindran, H. Fjellvåg, C. Venkateswaran, Observation of direct magneto-dielectric behaviour in

$Lu_3Fe_5O_{12-\delta}$ above room-temperature, Phys. Chem. Chem. Phys. 17 (2015) 17688–17698. doi:10.1039/C5CP02719E.

[28] L.D. Landau, J.S. Bell, M.J. Kearsley, L.P. Pitaevskii, E.M. Lifshitz, J.B. Sykes, Electrodynamics of Continuous Media, Elsevier, (1984).

[29] Z.X. Cheng, H. Shen, J.Y. Xu, P. Liu, S.J. Zhang, J.L. Wang, X.L. Wang, S.X. Dou, Magnetocapacitance effect in nonmultiferroic $YFeO_3$ single crystal, J. Appl. Phys. 111 (2012) 034103. doi:10.1063/1.3681294.

[30] M. Fiebig, T. Lottermoser, D. Meier, M. Trassin, The evolution of multiferroics, Nat. Rev. Mater. 1 (2016) 16046. doi:10.1038/natrevmats.2016.46.

[31] M.E. Lines and A. Glass, Principle and Application of Ferroelectric and Related Materials,Oxford University Press, Oxford, (2001)

[32] J.F. Scott, Ferroelectric Memories, Springer Science & Business Media, (2000).

[33] W. Eerenstein, F.D. Morrison, J.F. Scott, N.D. Mathur, Growth of highly resistive $BiMnO_3$ films, Appl. Phys. Lett. 87 (2005) 101906. doi:10.1063/1.2039988.

[34] W. Eerenstein, F.D. Morrison, J. Dho, M.G. Blamire, J.F. Scott, N.D. Mathur, Comment on "Epitaxial $BiFeO_3$ multiferroic thin film heterostructures," Science. 307 (2005) 1203. doi:10.1126/science.1105422.

[35] P. Mandal, V.S. Bhadram, Y. Sundarayya, C. Narayana, A. Sundaresan, C.N.R. Rao, Spin-Reorientation, Ferroelectricity, and Magnetodielectric Effect in $YFe_{1-x}Mn_xO_3$ ($0.1 \leq x \leq 0.40$), Phys. Rev. Lett. 107 (2011) 137202. doi:10.1103/PhysRevLett.107.137202.

[36] C.R. Serrao, A. Sundaresan, C.N.R. Rao, Multiferroic nature of charge-ordered rare earth manganites, J. Phys. Condens. Matter. 19 (2007) 496217. doi:10.1088/0953-8984/19/49/496217.

[37] J. Wang, J.B. Neaton, H. Zheng, V. Nagarajan, S.B. Ogale, B. Liu, D. Viehland, V. Vaithyanathan, D.G. Schlom, U.V. Waghmare, N.A. Spaldin, K.M. Rabe, M. Wuttig, R. Ramesh, Epitaxial $BiFeO_3$ Multiferroic Thin Film Heterostructures, Science. 299 (2003) 1719–1722. doi:10.1126/science.1080615.

[38] S.-W. Cheong, M. Mostovoy, Multiferroics: a magnetic twist for ferroelectricity, Nat. Mater. 6 (2007) 13–20. doi:10.1038/nmat1804.

[39] P. Kumar, M. Kar, Effect of structural transition on magnetic and dielectric properties of La and Mn co-substituted $BiFeO_3$ ceramics, Mater. Chem. Phys. 148 (2014) 968–977. doi:10.1016/j.matchemphys.2014.09.007.

[40] P. Padhan, P. LeClair, A. Gupta, G. Srinivasan, Magnetodielectric response in epitaxial thin films of multiferroic Bi_2NiMnO_6, J. Phys.

Condens. Matter. 20 (2008) 355003. doi:10.1088/0953-8984/20/35/355003.

[41] W. Prellier, M.P. Singh, P. Murugavel, The single-phase multiferroic oxides: from bulk to thin film, J. Phys. Condens. Matter. 17 (2005) 7753. doi:10.1088/0953-8984/17/48/C01.

[42] M. Gajek, M. Bibes, S. Fusil, K. Bouzehouane, J. Fontcuberta, A. Barthélémy, A. Fert, Tunnel junctions with multiferroic barriers, Nat. Mater. 6 (2007) 296–302. doi:10.1038/nmat1860.

[43] S. Weber, Colossal Magnetocapacitance and Colossal Magnetoresistance in $HgCr_2S_4$, Phys. Rev. Lett. 96 (2006) 15702. doi:10.1103/PhysRevLett.96.157202.

[44] R.F. Mamin, T. Egami, Z. Marton, S.A. Migachev, Giant dielectric permittivity and magnetocapacitance in $La_{0.875}Sr_{0.125}MnO_3$ single crystals, Phys. Rev. B. 75 (2007) 115129. doi:10.1103/PhysRevB.75.115129.

[45] V. Castel, C. Brosseau, Magnetic field dependence of the effective permittivity in $BaTiO_3$/Ni nanocomposites observed via microwave spectroscopy, Appl. Phys. Lett. 92 (2008) 233110. doi:10.1063/1.2943153.

[46] X. Mao, H. Sun, W. Wang, X. Chen, Y. Lu, Ferromagnetic, ferroelectric properties, and magneto-dielectric effect of $Bi_{4.25}La_{0.75}Fe_{0.5}Co_{0.5}Ti_3O_{15}$ ceramics, Appl. Phys. Lett. 102 (2013) 072904. doi:10.1063/1.4793305.

[47] C.-H. Yang, S.-H. Lee, T.Y. Koo, Y.H. Jeong, Dynamically enhanced magnetodielectric effect and magnetic-field-controlled electric relaxations in La-doped $BiMnO_3$, Phys. Rev. B. 75 (2007) 140104. doi:10.1103/PhysRevB.75.140104.

[48] M. Shang, C. Zhang, T. Zhang, L. Yuan, L. Ge, H. Yuan, S. Feng, The multiferroic perovskite $YFeO_3$, Appl. Phys. Lett. 102 (2013) 062903. doi:10.1063/1.4791697.

[49] L. Lutsev, S. Yakovlev, V. Castel, C. Brosseau, Spin wave dynamics in magnetoelectric Ni/$BaTiO_3$ nanocomposites, J. Phys. Appl. Phys. 43 (2010) 325302. doi:10.1088/0022-3727/43/32/325302.

[50] B. Lorenz, A.P. Litvinchuk, M.M. Gospodinov, C.W. Chu, Field-Induced Reentrant Novel Phase and a Ferroelectric-Magnetic Order Coupling in $HoMnO_3$, Phys. Rev. Lett. 92 (2004) 087204. doi:10.1103/PhysRevLett.92.087204.

[51] S. Dong, J.-F. Li, D. Viehland, Ultrahigh magnetic field sensitivity in laminates of TERFENOL-D and $Pb(Mg_{1/3}Nb_{2/3})O_3$–$PbTiO_3$ crystals, Appl. Phys. Lett. 83 (2003) 2265–2267. doi:10.1063/1.1611276.

[52] R.L. Sandstrom, E.A. Giess, W.J. Gallagher, A. Segmüller, E.I. Cooper, M.F. Chisholm, A. Gupta, S. Shinde, R.B. Laibowitz,

Lanthanum gallate substrates for epitaxial high-temperature superconducting thin films, Appl. Phys. Lett. 53 (1988) 1874–1876. doi:10.1063/1.100485.

[53] V.J. Folen, G.T. Rado, E.W. Stalder, Anisotropy of the Magnetoelectric Effect in Cr_2O_3, Phys. Rev. Lett. 6 (1961) 607–608. doi:10.1103/PhysRevLett.6.607.

[54] G.T. Rado, Magnetoelectric Evidence for the Attainability of Time-Reversed Antiferromagnetic Configurations by Metamagnetic Transitions in $DyPO_4$, Phys. Rev. Lett. 23 (1969) 644–647. doi:10.1103/PhysRevLett.23.644.

[55] D.L. Fox, D.R. Tilley, J.F. Scott, H.J. Guggenheim, Magnetoelectric phenomena in $BaMnF_4$ and $Ba_{0.99}Co_{0.01}F_4$, Phys. Rev. B. 21 (1980) 2926–2936. doi:10.1103/PhysRevB.21.2926.

[56] Z.J. Huang, Y. Cao, Y.Y. Sun, Y.Y. Xue, C.W. Chu, Coupling between the ferroelectric and antiferromagnetic orders in $YMnO_3$, Phys. Rev. B. 56 (1997) 2623–2626. doi:10.1103/PhysRevB.56.2623.

[57] R.S. 44, J.F. Mitchell, P. Schiffer, Magnetodielectric consequences of phase separation in the colossal magnetoresistance manganite $Pr_{0.7}Ca_{0.3}MnO_3$, Phys. Rev. B. 72 (2005) 144429. doi:10.1103/PhysRevB.72.144429.

[58] B. Lorenz, Y.Q. Wang, Y.Y. Sun, C.W. Chu, Large magnetodielectric effects in orthorhombic $HoMnO_3$, Phys. Rev. B. 70 (2004) 212412. doi:10.1103/PhysRevB.70.212412.

[59] M. Sánchez-Andújar, S. Yáñez-Vilar, N. Biskup, S. Castro-García, J. Mira, J. Rivas, M.A. Señarís-Rodríguez, Magnetoelectric behavior in the complex $CaMn_7O_{12}$ perovskite, J. Magn. Magn. Mater. 321 (2009) 1739–1742. doi:10.1016/j.jmmm.2009.02.018.

[60] Y. Yamasaki, Y. Kohara, Y. Tokura, Quantum magnetoelectric effect in iron garnet, Phys. Rev. B. 80 (2009) 140412. doi:10.1103/PhysRevB.80.140412.

[61] N. Hur, S. Park, S. Guha, A. Borissov, V. Kiryukhin, S.-W. Cheong, Low-field magnetodielectric effect in terbium iron garnets, Appl. Phys. Lett. 87 (2005) 042901. doi:10.1063/1.1997272.

[62] T. Kimura, Y. Sekio, H. Nakamura, T. Siegrist, A.P. Ramirez, Cupric oxide as an induced-multiferroic with high-TC, Nat. Mater. 7 (2008) 291–294. doi:10.1038/nmat2125.

[63] J. Hemberger, Multiferroic phases of $Eu_{1-x}Y_xMnO_3$, Phys. Rev. B. 75 (2007) 035118. doi:10.1103/PhysRevB.75.035118.

[64] T. Katsufuji, H. Takagi, Coupling between magnetism and dielectric properties in quantum paraelectric $EuTiO_3$, Phys. Rev. B. 64 (2001) 054415. doi:10.1103/PhysRevB.64.054415.

[65] T. Kimura, S. Kawamoto, I. Yamada, M. Azuma, M. Takano, Y. Tokura, Magnetocapacitance effect in multiferroic $BiMnO_3$, Phys. Rev. B. 67 (2003) 180401. doi:10.1103/PhysRevB.67.180401.

[66] T. Suzuki, T. Katsufuji, Magnetodielectric properties of spin-orbital coupled system Mn_3O_4, Phys. Rev. B. 77 (2008) 220402. doi:10.1103/PhysRevB.77.220402.

[67] G. Lawes, A.P. Ramirez, C.M. Varma, M.A. Subramanian, Magnetodielectric Effects from Spin Fluctuations in Isostructural Ferromagnetic and Antiferromagnetic Systems, Phys. Rev. Lett. 91 (2003) 257208. doi:10.1103/PhysRevLett.91.257208.

[68] J.F. Scott, Applications of Modern Ferroelectrics, Science. 315 (2007) 954–959. doi:10.1126/science.1129564.

[69] N. Ortega, A. Kumar, P. Bhattacharya, S.B. Majumder, R.S. Katiyar, Impedance spectroscopy of multiferroic $PbZr_xTi_{1-x}O_3/CoFe_2O_4$ layered thin films, Phys. Rev. B. 77 (2008) 014111. doi:10.1103/PhysRevB.77.014111.

[70] S. Kamba, D. Nuzhnyy, M. Savinov, J. Šebek, J. Petzelt, J. Prokleška, R. Haumont, J. Kreisel, Infrared and terahertz studies of polar phonons and magnetodielectric effect in multiferroic $BiFeO_3$ ceramics, Phys. Rev. B. 75 (2007) 024403. doi:10.1103/PhysRevB.75.024403.

[71] A. Singh, V. Pandey, R.K. Kotnala, D. Pandey, Direct Evidence for Multiferroic Magnetoelectric Coupling in $0.9BiFeO_3$-$0.1BaTiO_3$, Phys. Rev. Lett. 101 (2008) 247602. doi:10.1103/PhysRevLett.101.247602.

[72] Y. Wang, J. Hu, Y. Lin, C.-W. Nan, Multiferroic magnetoelectric composite nanostructures, NPG Asia Mater. 2 (2010) 61–68. doi:10.1038/asiamat.2010.32.

[73] D.M. Evans, M. Alexe, A. Schilling, A. Kumar, D. Sanchez, N. Ortega, R.S. Katiyar, J.F. Scott, J.M. Gregg, The Nature of Magnetoelectric Coupling in $Pb(Zr,Ti)O_3$–$Pb(Fe,Ta)O_3$, Adv. Mater. 27 (2015) 6068–6073. doi:10.1002/adma.201501749.

[74] W. Qin, X. Chen, H. Li, M. Gong, G. Yuan, J.C. Grossman, M. Wuttig, S. Ren, Room Temperature Multiferroicity of Charge Transfer Crystals, ACS Nano. 9 (2015) 9373–9379. doi:10.1021/acsnano.5b03558.

[75] K. Everschor-Sitte, M. Sitte, A.H. MacDonald, Interaction correction to the magnetoelectric polarizability of Z_2 topological insulators, Phys. Rev. B. 92 (2015) 245118. doi:10.1103/PhysRevB.92.245118.

[76] H.M. Jang, J.H. Park, S. Ryu, S.R. Shannigrahi, Magnetoelectric coupling susceptibility from magnetodielectric effect, Appl. Phys. Lett. 93 (2008) 252904. doi:10.1063/1.3050533.

[77] J.J. Betouras, Multiferroicity Induced by Dislocated Spin-Density Waves, Phys. Rev. Lett. 98 (2007) 257602. doi:10.1103/PhysRevLett.98.257602.

[78] A.B. Harris, Towards a microscopic model of magnetoelectric interactions in $Ni_3V_2O_8$, Phys. Rev. B. 73 (2006) 184433. doi:10.1103/PhysRevB.73.184433.

[79] C. Wang, Ferroelectricity Driven by the Noncentrosymmetric Magnetic Ordering in Multiferroic $TbMn_2O_5$: A First-Principles Study, Phys. Rev. Lett. 99 (2007) 177202. doi:10.1103/PhysRevLett.99.177202.

[80] H. Kimura, S. Kobayashi, S. Wakimoto, Y. Noda, K. Kohn, Magnetically Induced Ferroelectricity in Multiferroic Compounds of RMn_2O_5, Ferroelectrics. 354 (2007) 77–85. doi:10.1080/00150190701454602.

[81] C.D. Hu, Relationship between ferroelectricity and Dzyaloshinskii-Moriya interaction in multiferroics and the effect of bond-bending, Phys. Rev. B. 77 (2008) 174418. doi:10.1103/PhysRevB.77.174418.

[82] I.A. Sergienko, Role of the Dzyaloshinskii-Moriya interaction in multiferroic perovskites, Phys. Rev. B. 73 (2006) 094434. doi:10.1103/PhysRevB.73.094434.

[83] P. Tolédano, Pseudo-proper ferroelectricity and magnetoelectric effects in $TbMnO_3$, Phys. Rev. B. 79 (2009) 094416. doi:10.1103/PhysRevB.79.094416.

[84] A.I. Smirnov, Chiral and Collinear Ordering in a Distorted Triangular Antiferromagnet, Phys. Rev. Lett. 102 (2009) 037202. doi:10.1103/PhysRevLett.102.037202.

[85] H. Katsura, Spin Current and Magnetoelectric Effect in Noncollinear Magnets, Phys. Rev. Lett. 95 (2005) 057205. doi:10.1103/PhysRevLett.95.057205.

[86] M. Mostovoy, Ferroelectricity in Spiral Magnets, Phys. Rev. Lett. 96 (2006) 067601. doi:10.1103/PhysRevLett.96.067601.

[87] Y. Yamasaki, S. Miyasaka, Y. Kaneko, J.-P. He, T. Arima, Y. Tokura, Magnetic Reversal of the Ferroelectric Polarization in a Multiferroic Spinel Oxide, Phys. Rev. Lett. 96 (2006) 207204. doi:10.1103/PhysRevLett.96.207204.

[88] Y. Tokura, N. Kida, Dynamical magnetoelectric effects in multiferroic oxides, Philos. Trans. R. Soc. Lond. Math. Phys. Eng. Sci. 369 (2011) 3679–3694. doi:10.1098/rsta.2011.0150.

[89] G. Lawes, A.B. Harris, T. Kimura, N. Rogado, R.J. Cava, A. Aharony, O. Entin-Wohlman, T. Yildirim, M. Kenzelmann, C. Broholm, A.P. Ramirez, Magnetically Driven Ferroelectric Order in $Ni_3V_2O_8$, Phys. Rev. Lett. 95 (2005) 087205. doi:10.1103/PhysRevLett.95.087205.

[90] N. Ikeda, H. Ohsumi, K. Ohwada, K. Ishii, T. Inami, K. Kakurai, Y. Murakami, K. Yoshii, S. Mori, Y. Horibe, H. Kitô, Ferroelectricity from iron valence ordering in the charge-frustrated system $LuFe_2O_4$, Nature. 436 (2005) 1136–1138. doi:10.1038/nature04039.

[91] A. Kumar, D. Varshney, Crystal structure refinement of $Bi_{1-x}Nd_xFeO_3$ multiferroic by the Rietveld method, Ceram. Int. 38 (2012) 3935–3942. doi:10.1016/j.ceramint.2012.01.046.

[92] B.B. Van Aken, T.T.M. Palstra, A. Filippetti, N.A. Spaldin, The origin of ferroelectricity in magnetoelectric $YMnO_3$, Nat. Mater. 3 (2004) 164–170. doi:10.1038/nmat1080.

[93] J. van den Brink, D.I. Khomskii, Multiferroicity due to charge ordering, J. Phys. Condens. Matter. 20 (2008) 434217. doi:10.1088/0953-8984/20/43/434217.

[94] J. Farrell, G.A. Gehring, Interplay between magnetism and lattice distortions in $LaMn_{1-x}Ga_xO_3$, New J. Phys. 6 (2004) 168. doi:10.1088/1367-2630/6/1/168.

[95] N. Imamura, M. Karppinen, T. Motohashi, D. Fu, M. Itoh, H. Yamauchi, Positive and Negative Magnetodielectric Effects in A-Site Ordered $(BiMn_3)Mn_4O_{12}$ Perovskite, J. Am. Chem. Soc. 130 (2008) 14948–14949. doi:10.1021/ja806487d.

[96] J. Blasco, J. García, J. Campo, M.C. Sánchez, G. Subías, Neutron diffraction study and magnetic properties of $LaMn_{1-x}Ga_xO_3$, Phys. Rev. B. 66 (2002) 174431. doi:10.1103/PhysRevB.66.174431.

[97] M. Baldini, D. Di Castro, M. Cestelli-Guidi, J. Garcia, P. Postorino, Phase-separated states in high-pressure $LaMn_{1-x}Ga_xO_3$ manganites, Phys. Rev. B. 80 (2009) 045123. doi:10.1103/PhysRevB.80.045123.

[98] L. Malavasi, M. Baldini, D. di Castro, A. Nucara, W. Crichton, M. Mezouar, J. Blasco, P. Postorino, High pressure behavior of Ga-doped LaMnO3: a combined X-ray diffraction and optical spectroscopy study, J. Mater. Chem. 20 (2010) 1304–1311. doi:10.1039/B914975A.

[99] M.C. Sánchez, G. Subías, J. García, J. Blasco, Stability of the tetragonal Mn_3O_6 distortions in the $LaMn_{1-x}Ga_xO_3$ series by x-ray absorption spectroscopy, Phys. Rev. B. 69 (2004) 184415. doi:10.1103/PhysRevB.69.184415.

[100] A.R. West, Solid State Chemistry and its Applications, John Wiley and Sons (1991). ISBN: 978-0-471-90874-6.

[101] H. Rietveld, A profile refinement method for nuclear and magnetic structures, J. Appl. Crystallogr. 2 (1969) 65–71. doi:10.1107/S0021889869006558

[102] C.N.R. Rao, B. Raveau, Colossal Magnetoresistance, Charge Ordering and Related Properties of Manganese Oxides, World Scientific Publishing Company, (1998).

[103] I.M. Kolthoff, P.J. Elving, Treatise on Analytical Chemistry,Wiley-Interscience, (1970).

[104] J.H. Kennedy, Analytical Chemistry: Principles, Saunders College Publising, New York, (1990).

[105] A. Sagdeo, K. Gautam, P.R. Sagdeo, M.N. Singh, S.M. Gupta, A.K. Nigam, R. Rawat, A.K. Sinha, H. Ghosh, T. Ganguli, A. Chakrabarti, Large dielectric permittivity and possible correlation between magnetic and dielectric properties in bulk $BaFeO_{3-\delta}$, Appl. Phys. Lett. 105 (2014) 042906. doi:10.1063/1.4892064.

[106] C. Li, X. Han, F. Cheng, Y. Hu, C. Chen, J. Chen, Phase and composition controllable synthesis of cobalt manganese spinel nanoparticles towards efficient oxygen electrocatalysis, Nat. Commun. 6 (2015) 7345. doi:10.1038/ncomms8345.

[107] M. Sikora, C. Kapusta, K. Knížek, Z. Jirák, C. Autret, M. Borowiec, C.J. Oates, V. Procházka, D. Rybicki, D. Zajac, X-ray absorption near-edge spectroscopy study of Mn and Co valence states in $LaMn_{1-x}Co_xO_3$ (x=0-1), Phys. Rev. B. 73 (2006) 094426. doi:10.1103/PhysRevB.73.094426.

[108] E.E. Alp, G.L. Goodman, L. Soderholm, S.M. Mini, M. Ramanathan, G.K. Shenoy, A.S. Bommannavar, A new approach to determining the charge distribution in copper compounds, J. Phys. Condens. Matter. 1 (1989) 6463. doi:10.1088/0953-8984/1/36/014.

[109] B. Roling, What do electrical conductivity and electrical modulus spectra tell us about the mechanisms of ion transport processes in melts, glasses, and crystals?, J. Non-Cryst. Solids. 244 (1999) 34–43. doi:10.1016/S0022-3093(98)00847-3.

[110] A.K. Jonscher, Dielectric Relaxation in Solids, Chelsea Dielectrics Press Ltd, London, (1983).

[111] A.K. Jonscher, Physics of Thin Films 11 (1980) 232.

[112] A.K. Jonscher, Analysis of the alternating current properties of ionic conductors, J. Mater. Sci. 13 (1978) 553–562. doi:10.1007/BF00541805.

[113] J.B. Bates, J.C. Wang, Dielectric response of ionic conductors, Solid State Ion. 28 (1988) 115–119. doi:10.1016/S0167-2738(88)80017-1.

[114] G.G. Raju, Dielectrics in Electric Fields, CRC Press, (2003).

[115] M.A. El Hiti, Dielectric behaviour in Mg–Zn ferrites, J. Magn. Magn. Mater. 192 (1999) 305–313. doi:10.1016/S0304-8853(98)00356-4.

[116] C. Liu, C.A. Angell, Mechanical vs electrical relaxation in Agl-based fast ion conducting glasses, J. Non-Cryst. Solids. 83 (1986) 162–184. doi:10.1016/0022-3093(86)90066-9.

[117] S.W. Martin, C.A. Angell, Dc and ac conductivity in wide composition range $Li_2OP_2O_5$ glasses, J. Non-Cryst. Solids. 83 (1986) 185–207. doi:10.1016/0022-3093(86)90067-0.

[118] D.L. Sidebottom, P.F. Green, R.K. Brow, Comparison of KWW and power law analyses of an ion-conducting glass, J. Non-Cryst. Solids. 183 (1995) 151–160. doi:10.1016/0022-3093(94)00587-7.

[119] K.L. Ngai, J.N. Mundy, H. Jain, O. Kanert, G. Balzer-Jollenbeck, Correlation between the activation enthalpy and Kohlrausch exponent for ionic conductivity in alkali aluminogermanate glasses, Phys. Rev. B. 39 (1989) 6169–6179. doi:10.1103/PhysRevB.39.6169.

[120] F.S. Howell, R.A. Bose, P.B. Macedo, C.T. Moynihan, Electrical relaxation in a glass-forming molten salt, J. Phys. Chem. 78 (1974) 639–648. doi:10.1021/j100599a016.

[121] L.L. Hench, J.K. West, Principles of electronic ceramics, Wiley, (1990).

[122] K.S. Cole, R.H. Cole, Dispersion and Absorption in Dielectrics I. Alternating Current Characteristics, J. Chem. Phys. 9 (1941) 341–351. doi:10.1063/1.1750906.

[123] D.W. Davidson, R.H. Cole, Dielectric Relaxation in Glycerol, Propylene Glycol, and n-Propanol, J. Chem. Phys. 19 (1951) 1484–1490. doi:10.1063/1.1748105.

[124] S. Havriliak, S. Negami, A complex plane representation of dielectric and mechanical relaxation processes in some polymers, Polymer. 8 (1967) 161–210. doi:10.1016/0032-3861(67)90021-3.

[125] A. Chtchelkanova, S. Wolf, Y. Idzerda, Magnetic Interactions and Spin Transport, Springer Science & Business Media, (2003).

[126] R.C. Black, F.C. Wellstood, Measurements of Magnetism and Magnetic Properties of Matter; The SQUID Handbook, Wiley-VCH Verlag GmbH & Co. KGaA, (2006) 391–440. doi:10.1002/9783527609956.ch12.

[127] H.M. Rai, S.K. Saxena, V. Mishra, R. Kumar, P.R. Sagdeo, Observation, Evidence and Origin of Room Temperature Magnetodielectric Effect in Mn doped $LaGaO_3$ arxiv:1705.00184v1 [cond-mat.mtrl-sci] (2017).

[128] T. Bonaedy, Y.S. Koo, K.D. Sung, J.H. Jung, Resistive magnetodielectric property of polycrystalline γ-Fe_2O_3, Appl. Phys. Lett. 91 (2007) 132901. doi:10.1063/1.2790474.

[129] V.G. Nair, A. Das, V. Subramanian, P.N. Santhosh, Magnetic structure and magnetodielectric effect of $YFe_{0.5}Cr_{0.5}O_3$, J. Appl. Phys. 113 (2013) 213907. doi:10.1063/1.4808459.

[130] V.G. Nair, L. Pal, V. Subramanian, P.N. Santhosh, Structural, magnetic, and magnetodielectric studies of metamagnetic $DyFe_{0.5}Cr_{0.5}O_3$, J. Appl. Phys. 115 (2014) 17D728. doi:10.1063/1.4870139.

[131] V. Castel, C. Brosseau, J.B. Youssef, Magnetoelectric effect in $BaTiO_3$/Ni particulate nanocomposites at microwave frequencies, J. Appl. Phys. 106 (2009) 064312. doi:10.1063/1.3225567.

[132] W. Wang, L.-Q. Yan, J.-Z. Cong, Y.-L. Zhao, F. Wang, S.-P. Shen, T. Zou, D. Zhang, S.-G. Wang, X.-F. Han, Y. Sun, Magnetoelectric coupling in the paramagnetic state of a metal-organic framework, Sci. Rep. 3 (2013) 2024.

doi:10.1038/srep02024

[133] D.B. Wiles, R.A. Young, A new computer program for Rietveld analysis of X-ray powder diffraction patterns, J. Appl. Crystallogr. 14 (1981) 149–151. doi:10.1107/S0021889881008996.

[134] S. Basu, C. Nayak, A.K. Yadav, A. Agrawal, A.K. Poswal, D. Bhattacharyya, S.N. Jha, N.K. Sahoo, A comprehensive facility for EXAFS measurements at the INDUS-2 synchrotron source at RRCAT, Indore, India, J. Phys. Conf. Ser. 493 (2014) 012032. doi:10.1088/1742-6596/493/1/012032.

[135] B. Ravel, M. Newville, ATHENA, ARTEMIS, HEPHAESTUS: data analysis for X-ray absorption spectroscopy using IFEFFIT, J. Synchrotron Radiat. 12 (2005) 537–541. doi:10.1107/S0909049505012719.

[136] A. Shahee, R.J. Choudhary, R. Rawat, A.M. Awasthi, N.P. Lalla, Effect of oxygen off-stoichiometry on coupled structural and magnetic phase-transitions in $La_{0.15}Sr_{0.85}MnO_{3-\delta}$ (δ=0.02, 0.14), Solid State Commun. 177 (2014) 84–88. doi:10.1016/j.ssc.2013.10.005.

[137] A. Gaur, B.D. Shrivastava, H.L. Nigam, X-Ray Absorption Fine Structure (XAFS) Spectroscopy–A Review, Proc. Indian Natl. Sci. Acad. 79 (2013) 921–966.

[138] E.A. Kotomin, Y.A. Mastrikov, E. Heifets, J. Maier, First principles modeling of oxygen adsorption on $LaMnO_3$ (001) surface, arxiv08020193 Cond-Mat. (2008).

[139] M.A. Peña, J.L.G. Fierro, Chemical Structures and Performance of Perovskite Oxides, Chem. Rev. 101 (2001) 1981–2018. doi:10.1021/cr980129f.

[140] B.C. Tofield, W.R. Scott, Oxidative nonstoichiometry in perovskites, an experimental survey; the defect structure of an oxidized lanthanum manganite by powder neutron diffraction, J. Solid State Chem. 10 (1974) 183–194. doi:10.1016/0022-4596(74)90025-5.

[141] G. Kresse, D. Joubert, From ultrasoft pseudopotentials to the projector augmented-wave method, Phys. Rev. B. 59 (1999) 1758–1775. doi:10.1103/PhysRevB.59.1758.

[142] J.P. Perdew, J.A. Chevary, S.H. Vosko, K.A. Jackson, M.R. Pederson, D.J. Singh, C. Fiolhais, Atoms, molecules, solids, and surfaces: Applications of the generalized gradient approximation for exchange and correlation, Phys. Rev. B. 46 (1992) 6671–6687. doi:10.1103/PhysRevB.46.6671.

[143] V.I. Anisimov, F. Aryasetiawan, A.I. Lichtenstein, First-principles calculations of the electronic structure and spectra of strongly correlated systems: the LDA + U method, J. Phys. Condens. Matter. 9 (1997) 767. doi:10.1088/0953-8984/9/4/002.

[144] B. Himmetoglu, A. Floris, S. de Gironcoli, M. Cococcioni, Hubbard-corrected DFT energy functionals: The LDA+U description of correlated systems, Int. J. Quantum Chem. 114 (2014) 14–49. doi:10.1002/qua.24521.

[145] K. Sato, L. Bergqvist, J. Kudrnovský, P.H. Dederichs, O. Eriksson, I. Turek, B. Sanyal, G. Bouzerar, H. Katayama-Yoshida, V.A. Dinh, T. Fukushima, H. Kizaki, R. Zeller, First-principles theory of dilute magnetic semiconductors, Rev. Mod. Phys. 82 (2010) 1633–1690. doi:10.1103/RevModPhys.82.1633.

[146] T. Mayeshiba, D. Morgan, Strain effects on oxygen migration in perovskites, Phys. Chem. Chem. Phys. 17 (2014) 2715–2721. doi:10.1039/C4CP05554C.

[147] H.J. Monkhorst, J.D. Pack, Special points for Brillouin-zone integrations, Phys. Rev. B. 13 (1976) 5188–5192. doi:10.1103/PhysRevB.13.5188.

[148] B.J. Beaudry, P.E. Palmer, The lattice parameters of La, Ce, Pr, Nd, Sm, Eu and Yb, J. Common Met. 34 (1974) 225–231. doi:10.1016/0022-5088(74)90163-5.

[149] M. Bernasconi, G.L. Chiarotti, E. Tosatti, Ab initio calculations of structural and electronic properties of gallium solid-state phases, Phys. Rev. B. 52 (1995) 9988–9998. doi:10.1103/PhysRevB.52.9988.

[150] E. Sanville, S.D. Kenny, R. Smith, G. Henkelman, Improved grid-based algorithm for Bader charge allocation, J. Comput. Chem. 28 (2007) 899–908. doi:10.1002/jcc.20575.

[151] R.F.W. Bader, A quantum theory of molecular structure and its applications, Chem. Rev. 91 (1991) 893–928. doi:10.1021/cr00005a013.

[152] W. Tang, E. Sanville, G. Henkelman, A grid-based Bader analysis algorithm without lattice bias, J. Phys. Condens. Matter. 21 (2009) 084204. doi:10.1088/0953-8984/21/8/084204.

[153] K. Manna, R.S. Joshi, S. Elizabeth, P.S.A. Kumar, Evaluation of the intrinsic magneto-dielectric coupling in $LaMn_{0.5}Co_{0.5}O_3$ single crystals, Appl. Phys. Lett. 104 (2014) 202905. doi:10.1063/1.4879642.

[154] J.K. Murthy, K.D. Chandrasekhar, S. Murugavel, A. Venimadhav, Investigation of the intrinsic magnetodielectric effect in La_2CoMnO_6: role of magnetic disorder, J Mater Chem C. 3 (2015) 836–843. doi:10.1039/C4TC01920B.

[155] X. Wu, X. Wang, Y. Liu, W. Cai, S. Peng, F. Huang, X. Lu, F. Yan, J. Zhu, Study on dielectric and magnetodielectric properties of $Lu_3Fe_5O_{12}$ ceramics, Appl. Phys. Lett. 95 (2009) 182903. doi:10.1063/1.3259651.

[156] D.C. Kakarla, K.M. Jyothinagaram, A.K. Das, V. Adyam, Dielectric and Magnetodielectric Properties of R_2NiMnO_6 (R = Nd, Eu, Gd, Dy, and Y), J. Am. Ceram. Soc. 97 (2014) 2858–2866. doi:10.1111/jace.13039.

[157] R.D. Shannon, Revised effective ionic radii and systematic studies of interatomic distances in halides and chalcogenides, Acta Crystallogr. Sect. A. 32 (1976) 751–767. doi:10.1107/S0567739476001551.

[158] J.B. Goodenough, A. Wold, R.J. Arnott, N. Menyuk, Relationship Between Crystal Symmetry and Magnetic Properties of Ionic Compounds Containing Mn3+, Phys. Rev. 124 (1961) 373–384. doi:10.1103/PhysRev.124.373.

[159] R.V. Krishnan, A. Banerjee, Electron transport studies in rhombohedral series of Al-doped $LaMnO_{3+\delta}$: an effective medium approach, J. Phys. Condens. Matter. 12 (2000) 7887. doi:10.1088/0953-8984/12/36/304.

[160] K.D. Chandrasekhar, A.K. Das, C. Mitra, A. Venimadhav, The extrinsic origin of the magnetodielectric effect in the double perovskite La_2NiMnO_6, J. Phys. Condens. Matter. 24 (2012) 495901. doi:10.1088/0953-8984/24/49/495901.

[161] K.D. Chandrasekhar, A.K. Das, A. Venimadhav, Spin glass behaviour and extrinsic origin of magnetodielectric effect in non-multiferroic La_2NiMnO_6 nanoparticles, J. Phys. Condens. Matter. 24 (2012) 376003. doi:10.1088/0953-8984/24/37/376003.

[162] S. Ghara, K. Yoo, K.H. Kim, A. Sundaresan, Capacitive and magnetoresistive origin of magnetodielectric effects in Sm-substituted spiral antiferromagnet $BiMnFe_2O_6$, J. Appl. Phys. 118 (2015) 164103. doi:10.1063/1.4934509.

[163] A. Venimadhav, D. Chandrasekar, J.K. Murthy, Intrinsic and extrinsic contributions to magnetodielectric effect in double perovskite La_2CoMnO_6 nanoparticles, Appl. Nanosci. 3 (2012) 25–28. doi:10.1007/s13204-012-0069-9.

[164] R.A. Mondal, B.S. Murty, V.R.K. Murthy, Origin of magnetocapacitance in chemically homogeneous and inhomogeneous ferrites, Phys.Chem.Chem.Phys. 17 (2014) 2432–2437. doi:10.1039/C4CP04398G.

[165] A. Congeduti, P. Postorino, E. Caramagno, M. Nardone, A. Kumar, D.D. Sarma, Anomalous High Pressure Dependence of the Jahn-Teller Phonon in $La_{0.75}Ca_{0.25}MnO_3$, Phys. Rev. Lett. 86 (2001) 1251–1254. doi:10.1103/PhysRevLett.86.1251.

[166] P. Postorino, A. Congeduti, E. Degiorgi, J.P. Itié, P. Munsch, High-pressure behavior of $La_xSr_{2-x}MnO_4$ layered manganites investigated by Raman spectroscopy and x-ray diffraction, Phys. Rev. B. 65 (2002) 224102. doi:10.1103/PhysRevB.65.224102.

[167] I. Loa, P. Adler, A. Grzechnik, K. Syassen, U. Schwarz, M. Hanfland, G.K. Rozenberg, P. Gorodetsky, M.P. Pasternak, Pressure-Induced Quenching of the Jahn-Teller Distortion and Insulator-to-Metal Transition in $LaMnO_3$, Phys. Rev. Lett. 87 (2001) 125501. doi:10.1103/PhysRevLett.87.125501.

[168] M.N. Iliev, M.V. Abrashev, H.-G. Lee, V.N. Popov, Y.Y. Sun, C. Thomsen, R.L. Meng, C.W. Chu, Raman spectroscopy of orthorhombic perovskitelike $YMnO_3$ and $LaMnO_3$, Phys. Rev. B. 57 (1998) 2872–2877. doi:10.1103/PhysRevB.57.2872.

[169] Priyanka, A.K. Jha, Electrical characterization of zirconium substituted barium titanate using complex impedance spectroscopy, Bull. Mater. Sci. 36 (2013) 135–141. doi:10.1007/s12034-013-0420-0.

[170] E.M. Alkoy, A. Berksoy-Yavuz, Electrical properties and impedance spectroscopy of pure and copper-oxide-added potassium sodium niobate ceramics, IEEE Trans. Ultrason. Ferroelectr. Freq. Control. 59 (2012) 2121–2128. doi:10.1109/TUFFC.2012.2438.

[171] R. Merkle, J. Purans, E.A. Kotomin, J. Maier, O. Mathon, Jahn-Teller distortion around Fe^{4+} in $Sr(Fe_xTi_{1-x})O_{3-\delta}$ from x-ray absorption spectroscopy, x-ray diffraction, and vibrational spectroscopy, Phys. Rev. B. 76 (2007) 174107. doi:10.1103/PhysRevB.76.174107.

[172] B.K. Ponomarev, S.A. Ivanov, B.S. Red'kin, V.N. Kurlov, Magnetoelectrical effect in paramagnetic rare-earth molybdates, Phys. B. 177 (1992) 327–329. doi:10.1016/0921-526(92)90124-B.

[173] P.D. Battle, M.A. Green, M.J. Rosseinsky, L.E. Spring, J.F. Vente, P.D. Battle, M.A. Green, J.L.A. Mihut, L.E. Spring, J. Singleton, Magnetoresistance in high oxidation state iron oxides, Chem. Commun. (1998) 987–988. doi:10.1039/A801220B.

[174] P. Adler, Charge disproportionation in iron(IV) oxides: electronic properties and magnetism in $Sr_3Fe_{2-x}Ti_xO_{7-y}$ annealed at high oxygen pressures, J. Mater. Chem. 9 (1999) 471–477. doi:10.1039/A806772D.

[175] M.M. Natile, A. Ponzoni, I. Concina, A. Glisenti, Chemical Tuning versus Microstructure Features in Solid-State Gas Sensors: $LaFe_{1-x}Ga_xO_3$, a Case Study, Chem. Mater. 26 (2014) 1505–1513. doi:10.1021/cm4018858.

[176] R. Kohlhaas, P. Duenner, N. Schmitz-Pranghe, The temperature-dependence of the lattice parameters of iron, cobalt, and nickel in the high temperature range, Z. Angew. Phys. 23 (1967) 245.

[177] M. Romero, R.W. Gómez, V. Marquina, J.L. Pérez-Mazariego, R. Escamilla, Synthesis by molten salt method of the $AFeO_3$ system (A=La, Gd) and its structural, vibrational and internal hyperfine magnetic field characterization, Phys. B Condens. Matter. 443 (2014) 90–94. doi:10.1016/j.physb.2014.03.024.

[178] M. Popa, J. Frantti, M. Kakihana, Lanthanum ferrite $LaFeO_{3+d}$ nanopowders obtained by the polymerizable complex method, Solid State Ion. 154–155 (2002) 437–445. doi:10.1016/S0167-2738(02)00480-0.

[179] M. Guennou, M. Viret, J. Kreisel, Bismuth-based perovskites as multiferroics, Multiferroic Mater. Heterostruct. Matér. Hétérostructures Multiferroïques. 16 (2015) 182–192. doi:10.1016/j.crhy.2015.01.008.

[180] R. Ramesh, Materials science: Emerging routes to multiferroics, Nature. 461 (2009) 1218–1219. doi:10.1038/4611218a.

[181] T.-L. Phan, P.D. Thang, T.A. Ho, T.V. Manh, T.D. Thanh, V.D. Lam, N.T. Dang, S.C. Yu, Local geometric and electronic structures and origin of magnetism in Co-doped $BaTiO_3$ multiferroics, J. Appl. Phys. 117 (2015) 17D904. doi:10.1063/1.4907182.

[182] P. Lunkenheimer, S. Krohns, S. Riegg, S.G. Ebbinghaus, A. Reller, A. Loidl, Colossal dielectric constants in transition-metal oxides, Eur. Phys. J. Spec. Top. 180 (2010) 61–89. doi:10.1140/epjst/e2010-01212-5.

[183] S. Krohns, P. Lunkenheimer, C. Kant, A.V. Pronin, H.B. Brom, A.A. Nugroho, M. Diantoro, A. Loidl, Colossal dielectric constant up to gigahertz at room temperature, Appl. Phys. Lett. 94 (2009) 122903. doi:10.1063/1.3105993.

[184] S. Krohns, P. Lunkenheimer, S.G. Ebbinghaus, A. Loidl, Broadband dielectric spectroscopy on single-crystalline and ceramic $CaCu_3Ti_4O_{12}$, Appl. Phys. Lett. 91 (2007) 022910. doi:10.1063/1.2757098.

[185] C.M. Rey, H. Mathias, L.R. Testardi, S. Skirius, High dielectric constant and nonlinear electric response in nonmetallic $YBa_2Cu_3O_{6+\delta}$, Phys. Rev. B. 45 (1992) 10639–10646. doi:10.1103/PhysRevB.45.10639.

[186] J. Rivas, B. Rivas-Murias, A. Fondado, J. Mira, M.A. Señarís-Rodríguez, Dielectric response of the charge-ordered two-dimensional

nickelate $La_{1.5}Sr_{0.5}NiO_4$, Appl. Phys. Lett. 85 (2004) 6224–6226. doi:10.1063/1.1834998.

[187] T. Park, Z. Nussinov, K.R.A. Hazzard, V.A. Sidorov, A.V. Balatsky, J.L. Sarrao, S.-W. Cheong, M.F. Hundley, J.-S. Lee, Q.X. Jia, J.D. Thompson, Novel Dielectric Anomaly in the Hole-Doped $La_2Cu_{1-x}Li_xO_4$ and $La_{2-x}Sr_xNiO_4$ Insulators: Signature of an Electronic Glassy State, Phys. Rev. Lett. 94 (2005) 017002. doi:10.1103/PhysRevLett.94.017002.

[188] X.Q. Liu, S.Y. Wu, X.M. Chen, H.Y. Zhu, Giant dielectric response in two-dimensional charge-ordered nickelate ceramics, J. Appl. Phys. 104 (2008) 054114. doi:10.1063/1.2969946.

[189] J. Sebald, S. Krohns, P. Lunkenheimer, S.G. Ebbinghaus, S. Riegg, A. Reller, A. Loidl, Colossal dielectric constants: A common phenomenon in $CaCu_3Ti_4O_{12}$ related materials, Solid State Commun. 150 (2010) 857–860. doi:10.1016/j.ssc.2010.02.006.

[190] L. Liu, H. Fan, X. Chen, P. Fang, Electrical properties and microstructural characteristics of nonstoichiometric $CaCu_{3x}Ti_4O_{12}$ ceramics, J. Alloys Compd. 469 (2009) 529–534. doi:10.1016/j.jallcom.2008.02.042.

[191] T. Groń, E. Tomaszewicz, Z. Kukuła, S. Pawlus, B. Sawicki, Dielectric permittivity of some novel copper/cobalt and rare-earth metal tungstates, Mater. Sci. Eng. B. 184 (2014) 14–17. doi:10.1016/j.mseb.2014.01.006.

[192] X. Liu, H. Fan, J. Shi, Q. Li, Origin of anomalous giant dielectric performance in novel perovskite: $Bi_{0.5-x}LaxNa_{0.5-x}Li_xTi_{1-y}M_yO_3$ (M = Mg^{2+}, Ga^{3+}), Sci. Rep. 5 (2015) 12699. doi:10.1038/srep12699.

[193] Z. Li, H. Fan, Polaron relaxation associated with the localized oxygen vacancies in $Ba_{0.85}Sr_{0.15}TiO_3$ ceramics at high temperatures, J. Appl. Phys. 106 (2009) 054102. doi:10.1063/1.3211308.

[194] Z. Kukuła, E. Tomaszewicz, S. Mazur, T. Groń, H. Duda, S. Pawlus, S.M. Kaczmarek, H. Fuks, T. Mydlarz, Dielectric and magnetic permittivities of three new ceramic tungstates $MPr_2W_2O_{10}$ (M = Cd, Co, Mn), Philos. Mag. 92 (2012) 4167–4181. doi:10.1080/14786435.2012.704427.

[195] J. Rodríguez-Carvajal, Recent advances in magnetic structure determination by neutron powder diffraction, Phys. B Condens. Matter. 192 (1993) 55–69. doi:10.1016/0921-4526(93)90108-I.

[196] Y.Q. Lin, X.M. Chen, Dielectric relaxation and polaronic conduction in double perovskite La_2MgMnO_6, Appl. Phys. Lett. 96 (2010) 142902. doi:10.1063/1.3377906.

[197] Y. Ma, X.M. Chen, Y.Q. Lin, Relaxorlike dielectric behavior and weak ferromagnetism in $YFeO_3$ ceramics, J. Appl. Phys. 103 (2008) 124111. doi:10.1063/1.2947601.

[198] J. Yang, X.J. Meng, M.R. Shen, L. Fang, J.L. Wang, T. Lin, J.L. Sun, J.H. Chu, Hopping conduction and low-frequency dielectric relaxation in 5mol% Mn doped (Pb,Sr)TiO_3 films, J. Appl. Phys. 104 (2008) 104113. doi:10.1063/1.3021447.

[199] K. Olimov, M. Falk, K. Buse, T. Woike, J. Hormes, H. Modrow, X-ray absorption near edge spectroscopy investigations of valency and lattice occupation site of Fe in highly iron-doped lithium niobate crystals, J. Phys. Condens. Matter. 18 (2006) 5135. doi:10.1088/0953-8984/18/22/013.

[200] E. Pollert, S. Krupička, E. Kuzmičová, Structural study of $Pr_{1-x}Ca_xMnO_3$ and $Y_{1-x}Ca_xMnO_3$ perovskites, J. Phys. Chem. Solids. 43 (1982) 1137–1145. doi:10.1016/0022-3697(82)90142-1.

[201] A.J. Millis, P.B. Littlewood, B.I. Shraiman, Double Exchange Alone Does Not Explain the Resistivity of $La_{1-x}Sr_xMnO_3$, Phys. Rev. Lett. 74 (1995) 5144–5147. doi:10.1103/PhysRevLett.74.5144.

[202] Y. González-Abreu, A. Peláiz-Barranco, E.B. Araújo, A.F. Júnior, Dielectric relaxation and relaxor behavior in bilayered perovskites, Appl. Phys. Lett. 94 (2009) 262903. doi:10.1063/1.3168651.

[203] P. Lunkenheimer, V. Bobnar, A.V. Pronin, A.I. Ritus, A.A. Volkov, A. Loidl, Origin of apparent colossal dielectric constants, Phys. Rev. B. 66 (2002) 052105. doi:10.1103/PhysRevB.66.052105.

[204] M. Shah, M. Nadeem, M. Atif, Dielectric relaxation with polaronic and variable range hopping mechanisms of grains and grain boundaries in $Pr_{0.8}Ca_{0.2}MnO_3$, J. Appl. Phys. 112 (2012) 103718. doi:10.1063/1.4767366.

[205] J.R. Sahu, C.R. Serrao, N. Ray, U.V. Waghmare, C.N.R. Rao, Rare earth chromites: a new family of multiferroics, J. Mater. Chem. 17 (2006) 42–44. doi:10.1039/B612093H.

[206] J.M. Costantini, J.P. Salvetat, F. Brisard, Dielectric and transport properties of magnetic insulators irradiated with GeV heavy ions, J. Appl. Phys. 82 (1997) 5063–5071. doi:10.1063/1.366403.

[207] P. Lunkenheimer, R. Fichtl, S.G. Ebbinghaus, A. Loidl, Nonintrinsic origin of the colossal dielectric constants in $CaCu_3Ti_4O_{12}$, Phys. Rev. B. 70 (2004) 172102. doi:10.1103/PhysRevB.70.172102.

[208] K. Fukunaga, Dielectric materials at high frequencies, IEEE Trans. Dielectr. Electr. Insul. 13 (2006) 687–687. doi:10.1109/TDEI.2006.1667725.

[209] R.W. Wolfe, R.E. Newnham, Rare Earth Bismuth Titanates, J. Electrochem. Soc. 116 (1969) 832–835. doi:10.1149/1.2412072.

[210] A. Mishra, N. Mishra, S. Bisen, K.M. Jarabana, Frequency and temperature dependent dielectric studies of $BaTi_{0.96}$ $Fe_{0.04}O_3$, J. Phys. Conf. Ser. 534 (2014) 012011. doi:10.1088/1742-6596/534/1/012011.

[211] P. Lunkenheimer, T. Rudolf, J. Hemberger, A. Pimenov, S. Tachos, F. Lichtenberg, A. Loidl, Dielectric properties and dynamical conductivity of $LaTiO_3$: From dc to optical frequencies, Phys. Rev. B. 68 (2003) 245108. doi:10.1103/PhysRevB.68.245108.

[212] M.C. Sánchez, J. García, G. Subías, J. Blasco, Lack of Jahn-Teller distortion in highly diluted $LaMn_{1-x}Ga_xO_3$ (x>0.6), Phys. Rev. B. 73 (2006) 094416. doi:10.1103/PhysRevB.73.094416.

[213] F.J. Manjón, A. Segura, M. Amboage, J. Pellicer-Porres, J.F. Sánchez-Royo, J.P. Itié, A.M. Flank, P. Lagarde, A. Polian, V. v. Ursaki, I.M. Tiginyanu, Structural and optical high-pressure study of spinel-type $MnIn_2S_4$, Phys. Status Solidi B. 244 (2007) 229–233. doi:10.1002/pssb.200672522.

[214] T.E. Westre, P. Kennepohl, J.G. DeWitt, B. Hedman, K.O. Hodgson, E.I. Solomon, A Multiplet Analysis of Fe K-Edge $1s \rightarrow 3d$ Pre-Edge Features of Iron Complexes, J. Am. Chem. Soc. 119 (1997) 6297–6314. doi:10.1021/ja964352a.

[215] A.L. Roe, D.J. Schneider, R.J. Mayer, J.W. Pyrz, J. Widom, L. Que, X-ray absorption spectroscopy of iron-tyrosinate proteins, J. Am. Chem. Soc. 106 (1984) 1676–1681. doi:10.1021/ja00318a021.

[216] J. Wong, F.W. Lytle, R.P. Messmer, D.H. Maylotte, K-edge absorption spectra of selected vanadium compounds, Phys. Rev. B. 30 (1984) 5596–5610. doi:10.1103/PhysRevB.30.5596.

[217] S. Ke, H. Huang, H. Fan, Relaxor behavior in $CaCu_3Ti_4O_{12}$ ceramics, Appl. Phys. Lett. 89 (2006) 182904. doi:10.1063/1.2374682.

[218] Y. Joly, D. Cabaret, H. Renevier, C.R. Natoli, Electron Population Analysis by Full-Potential X-Ray Absorption Simulations, Phys. Rev. Lett. 82 (1999) 2398–2401. doi:10.1103/PhysRevLett.82.2398.

[219] J.F. Scott, Ferroelectrics go bananas, J. Phys. Condens. Matter. 20 (2008) 021001. doi:10.1088/0953-8984/20/02/021001.

[220] W. David Kingery, H. K. Bowen, Donald R. Uhlmann, Introduction to Ceramics, 2nd Edition, Wiley (1976). ISBN: 978-0-471-47860-7.

[221] V.R.K. Murthy, J. Sobhanadri, Dielectric properties of some nickel-zinc ferrites at radio frequency, Phys. Status Solidi A. 36 (1976) K133–K135. doi:10.1002/pssa.2210360247.

[222] D.C. Dube, H.J. Scheel, I. Reaney, M. Daglish, N. Setter, Dielectric properties of lanthanum gallate ($LaGaO_3$) crystal, J. Appl. Phys. 75 (1994) 4126–4130. doi:10.1063/1.355993.

[223] S. Sharma, T. Basu, A. Shahee, K. Singh, N.P. Lalla, E.V. Sampathkumaran, Multiglass properties and magnetoelectric coupling in the uniaxial anisotropic spin-cluster-glass Fe_2TiO_5, Phys. Rev. B. 90 (2014) 144426. doi:10.1103/PhysRevB.90.144426.

[224] J.L. Cohn, M. Peterca, J.J. Neumeier, Low-temperature permittivity of insulating perovskite manganites, Phys. Rev. B. 70 (2004) 214433. doi:10.1103/PhysRevB.70.214433.

[225] A. Seeger, P. Lunkenheimer, J. Hemberger, A.A. Mukhin, V.Y. Ivanov, A.M. Balbashov, A. Loidl, Charge carrier localization in $La_{1-x}Sr_xMnO_3$ investigated by ac conductivity measurements investigated by ac conductivity measurements, J. Phys. Condens. Matter. 11 (1999) 3273. doi:10.1088/0953-8984/11/16/009.

[226] J.L. Cohn, M. Peterca, J.J. Neumeier, Giant dielectric permittivity of electron-doped manganite thin films, $Ca_{1-x}La_xMnO_3(0\leqslant x\leqslant 0.03)$, J. Appl. Phys. 97 (2005) 034102. doi:10.1063/1.1834976.

[227] O. Bidault, M. Maglione, M. Actis, M. Kchikech, B. Salce, Polaronic relaxation in perovskites, Phys. Rev. B. 52 (1995) 4191–4197. doi:10.1103/PhysRevB.52.4191.

[228] N. Ikeda, K. Kohn, H. Kito, J. Akimitsu, K. Siratori, Dielectric Relaxation and Hopping of Electrons in $ErFe_2O_4$, J. Phys. Soc. Jpn. 63 (1994) 4556–4564. doi:10.1143/JPSJ.63.4556.

[229] E. Iguchi, N. Kubota, T. Nakamori, N. Yamamoto, K.J. Lee, Polaronic conduction in n -type $BaTiO_3$ doped with La_2O_3 or Gd_2O_3, Phys. Rev. B. 43 (1991) 8646–8649. doi:10.1103/PhysRevB.43.8646.

[230] H.M. Rai, S.K. Saxena, R. Late, V. Mishra, P. Rajput, A. Sagdeo, R. Kumar, P.R. Sagdeo, Observation of large dielectric permittivity and dielectric relaxation phenomenon in Mn-doped lanthanum gallate, RSC Adv. 6 (2016) 26621–26629. doi:10.1039/C5RA28074E.

[231] H.M. Rai, R. Late, S.K. Saxena, V. Mishra, R. Kumar, P.R. Sagdeo, Archna Sagdeo, Room temperature magnetodielectric studies on Mn-doped $LaGaO_3$, Mater. Res. Express. 2 (2015) 096105. doi:10.1088/2053-1591/2/9/096105.

[232] A.M. Arévalo-López, J.P. Attfield, Weak ferromagnetism and domain effects in multiferroic $LiNbO_3$-type $MnTiO_3$-II, Phys. Rev. B. 88 (2013) 104416. doi:10.1103/PhysRevB.88.104416.

[233] D. Kothari, V.R. Reddy, A. Gupta, V. Sathe, A. Banerjee, S.M. Gupta, A.M. Awasthi, Multiferroic properties of polycrystalline $Bi_{1-x}Ca_xFeO_3$, Appl. Phys. Lett. 91 (2007) 202505. doi:10.1063/1.2806199.

[234] S. Blundell, Magnetism in Condensed Matter, Oxford University Press Inc., New York, (2001)

[235] M. Oumezzine, S. Kallel, O. Peña, N. Kallel, T. Guizouarn, F. Gouttefangeas, M. Oumezzine, Correlation between structural, magnetic and electrical transport properties of barium vacancies in the $La_{0.67}Ba_{0.33-x\square x}MnO_3$ (x = 0, 0.05, and 0.1) manganite, J. Alloys Compd. 582 (2014) 640–646. doi:10.1016/j.jallcom.2013.08.011.

[236] P.S. Behera, P.A. Bhobe, Crystal structure and magnetic property correlation in (M=Sb, Sn, In), J. Magn. Magn. Mater. 394 (2015) 200–206. doi:10.1016/j.jmmm.2015.06.064.

[237] T.K. Nguyen, Magnetic Nanoparticles: From Fabrication to Clinical Applications, CRC Press. (2012).

[238] J.B. Goodenough, Theory of the Role of Covalence in the Perovskite-Type Manganites [La,M(II)]MnO_3, Phys. Rev. 100 (1955) 564–573. doi:10.1103/PhysRev.100.564.

[239] C. Callender, D.P. Norton, R. Das, A.F. Hebard, J.D. Budai, Ferromagnetism in pseudocubic $BaFeO_3$ epitaxial films, Appl. Phys. Lett. 92 (2008) 012514. doi:10.1063/1.2832768.

[240] E.O. Wollan, W.C. Koehler, Neutron Diffraction Study of the Magnetic Properties of the Series of Perovskite-Type Compounds [(1-x)La, xCa]MnO_3, Phys. Rev. 100 (1955) 545–563. doi:10.1103/PhysRev.100.545.

[241] P.R. Sagdeo, S. Anwar, N.P. Lalla, Strain induced coexistence of monoclinic and charge ordered phases in $La_{1-x}Ca_xMnO_3$, Phys. Rev. B. 74 (2006) 214118. doi:10.1103/PhysRevB.74.214118.

[242] V.K. Wadhawan, Smart Structures: Blurring the Distinction Between the Living and the Nonliving, Oxford University Press, Oxford, New York, 2007.

[243] P. Singh, I. Choudhuri, H.M. Rai, V. Mishra, R. Kumar, B. Pathak, A. Sagdeo, P.R. Sagdeo, Fe doped $LaGaO_3$: good white light emitters, RSC Adv. 6 (2016) 100230–100238. doi:10.1039/C6RA21693E.

[244] L. Pauling, The Nature of the Chemical Bond and the Structure of Molecules and Crystals: An Introduction to Modern Structural Chemistry, Cornell University Press, (1960).

[245] F. Zheng, G. Zhou, Z. Liu, J. Wu, W. Duan, B.-L. Gu, S.B. Zhang, Half metallicity along the edge of zigzag boron nitride nanoribbons, Phys. Rev. B. 78 (2008) 205415. doi:10.1103/PhysRevB.78.205415.

[246] Y. Wang, Y. Ding, J. Ni, Fluorination-induced half-metallicity in zigzag boron nitride nanoribbons: First-principles calculations, Phys. Rev. B. 81 (2010) 193407. doi:10.1103/PhysRevB.81.193407.

[247] H.M. Rai, S.K. Saxena, V. Mishra, R. Late, R. Kumar, P.R. Sagdeo, N.K. Jaiswal, P. Srivastava, Half-metallicity in armchair boron nitride nanoribbons: A first-principles study, Solid State Commun. 212 (2015) 19–24. doi:10.1016/j.ssc.2015.04.003.

[248] H.M. Rai, S.K. Saxena, V. Mishra, R. Late, R. Kumar, P.R. Sagdeo, N.K. Jaiswal, P. Srivastava, Possibility of spin-polarized transport in edge fluorinated armchair boron nitride nanoribbons, RSC Adv. 6 (2016) 11014–11022. doi:10.1039/C5RA21832B.